ISOGEOMETRIC ANALYSIS OF SMALL-SCALE PLATES WITH GENERALISED CONTINUA

HOANG XUAN NGUYEN

PhD

2018

ISOGEOMETRIC ANALYSIS OF SMALL-SCALE PLATES WITH GENERALISED CONTINUA

HOANG XUAN NGUYEN

This dissertation is submitted in partial fulfilment of the requirements of the University of Northumbria at Newcastle for the degree of Doctor of Philosophy

Research undertaken in the Department of Mechanical and Construction Engineering

September 2018

Abstract

Small-scale (micro) structures are increasingly used in variety of engineering fields such as micro- and nano-electro-mechanical system, space and bio-engineering. Reliable numerical prediction of the behaviours of these structures becomes desirable due to costly experiments in micro scales. In structural modelling, it is known that classical continuum theories fail to capture size effects, instead generalised continuum theories which take into account the material length scale should be used.

In this thesis, the behaviours of small-scale plate structures with size-dependent effects are investigated by means of the numerical method of isogeometric analysis and generalised continuum theories of modified couple stress and strain gradient. While the size effects are efficiently captured by the modified couple stress theory and strain gradient theory, the refined plate theory with four variables is employed to establish the displacement fields of plates. The isogeometric analysis in which non-uniform rational B-splines basis function is used for both geometry representation and field approximation is capable of exactly describing the geometry of the domain and efficiently dealing with the high-order element requirements.

The investigation of small-scale plates focuses on the linear analysis, nonlinear analysis, and crack analysis. While linear analysis includes bending, vibration, and buckling responses with a quasi-3D refined plate theory, nonlinear analysis involves the derivation of von Kámán strains and implementation of iterative Newton-Raphson technique. Meanwhile, the vibration responses of cracked plates are assessed in the platform of the strain gradient theory and extended isogeometric analysis where enrichment functions are included to model the discontinuities and improve the solution accuracy around the crack tip.

The successful convergence and comparison studies as well as benchmark results of the analyses of functionally graded small-scale plates ascertain the validity and reliability of the proposed approaches. In addition, a number of parametric studies have been carried out to investigate the effects of material length scale, material and geometrical parameters on the responses of the plates.

The numerical results show that the inclusion of the material length scale which takes into account the size-dependent effects increases the approximated structural stiffness. Consequently, the displacement of the structure is decreased while the fundamental frequency and critical buckling load are increased.

Table of contents

List of tables

List of figures

Acknowledgements

First of all, I would like to thank Dr. Thuc Vo for his supervision and support over the past three years. It is difficult for me to remember a point where he could not find time to discuss a problem that I struggled in my research. Through conversations and discussions with him, I have been given invaluable guidance and advice in my study as well as my life. While he ensured that I was working on the main research topic, he offered me freedom to explore different potential research areas. I also would like to thank my second supervisor, Dr. Keerthan Poologanathan, who was very supportive offering me thoughtful advice regarding my research and future career.

I am grateful to the Faculty of Engineering and Environment for providing financial support via the Researcher Development Framework throughout my time at Northumbria University. Further thanks go to the Santander Universities and Graduate School for their financial support for research travels and conference participations.

I would like to thank Prof. Hung Nguyen-Xuan for his encouragement and discussions regarding the research topic during my PhD. Further thank is reserved for Dr. Elena Atroshchenko for her strong support which resulted in two trips to Chile and a series of fruitful on-going collaborations. Another thank goes to Prof. Stephane Bordas for a short but productive visit to his research group in Luxembourg in 2016.

I would like to thank all of wonderful people that I have met during my PhD study over the past few years.

I would like to thank my parents, Tuyen and Vieng, for their love and constant support. Words are not enough to thank my dearest wife Tuy who has sacrificed her time to always stand by and support me unconditionally. Thank you to my son Nam (Nathan) who teaches me how to be patient and motivates me to be better.

Declaration

I declare that the work contained in this thesis has not been submitted for any other award and that it is all my own work. I also confirm that this work fully acknowledges opinions, ideas and contributions from the work of others.

I declare that the word count of this thesis is 39,905 words.

Hoang Xuan Nguyen

12 September 2018

I would like to dedicate this thesis to my family

Nomenclature

Roman Symbols

$N_{i,p}$	The i^{th} approximation function of order p
$B_\alpha(\mathbf{x})$	Crack-tip enrichment function
P_{cr}	Critical buckling load
$\mathbf{u}$	Displacement vector
$\mathbf{F}$	Global force vector
$H(\mathbf{x})$	Heaviside function
K	Kinetic energy
K_0	Kinetic energy density
$\mathbf{M}$	Global mass matrix
$\mathbf{m}$	Couple stress tensor
p	Polynomial order of a basis function
$\tilde{\mathbf{R}}$	Residual force vector
$\mathbf{K}$	Global stiffness matrix
U	Strain energy
U_0	Strain energy density
$\mathbf{K}_T$	Tangent stiffness matrix
h	Plate's thickness

E	Young's modulus

Greek Symbols

$\boldsymbol{\chi}$	Symmetric curature tensor
ρ	Density
$\boldsymbol{\eta}$	Dipolar stress tensor
ω	Frequency
ξ_i	The i^{th} knot
$\boldsymbol{\Xi}$	Knot vector
λ, μ	Lamé's constants
ν	Poisson's ratio
$\boldsymbol{\sigma}$	Stress tensor
$\boldsymbol{\kappa}$	Strain gradient tensor
$\boldsymbol{\theta}$	Rotation vector
$\boldsymbol{\varepsilon}$	Strain tensor

Other Symbols

ℓ	Material length scale

Acronyms / Abbreviations

CAD	Computer-Aided Design
CAE	Computer-Aided Engineering
CPT	Classical Plate Theory
DOF	Degree of Freedom
FEA	Finite Element Analysis
FEM	Finite Element Method

FGM	Functionally Graded Material
FSDT	First-order Shear Deformation Theory
HSDT	Higher-order Shear Deformation Theory
IGA	Isogeometric Analysis
MCST	Modified Couple Stress Theory
NURBS	Non-Uniform Rational B-splines
RPT	Refined Plate Theory
SGT	Strain Gradient Theory
TSDT	Third-order Shear Deformation Theory
XIGA	eXtended Isogeometric Analysis

Chapter 1

Introduction

1.1 Background of the thesis

Recent advances in technology lead to new industrial fields in which small-scale elements are involved. Such elements have been applied in micro- and nano-electro-mechanical systems [1, 2], actuators [3], space and bio-engineering [4]. These applications encourage new research area that focuses on investigating and predicting the behaviours of such micro structures. A number of approaches have been employed to analyse the characteristics of small-scale structures both experimentally and numerically [5]. Indeed, typical structural sizes range from a few to dozens of polycrystalline grains only, such that the actual local grain morphology has a strong influence on the global structural behaviour [6]. One approach is to handle grains explicitly and represent each of them in the model. This leads to large computational demands because of the lack of scale separation. Such constitutive models must be able to account for size effects which are characteristic of small-scale structures.This is confirmed by a number of theoretical and experimental studies reported by Fleck et al. [7], Stolken and Evans [8], and Lam et al. [9]. From an experimental observation from bending test of epoxy polymeric microbeams, Lam et al. [9] pointed out that the bending rigidity increased 2.4 times as a result of the reduction of the beam thickness from 115 μm to 20 μm.

In order to take into account the size effects, a number theories have been developed including nonlocal elasticity theory [10], strain gradient theory (SGT) [11, 12], and modified couple stress theory (MCST) [13]. In these theories, the material length scale which is used to indicate the size-dependent effects is

taken into account. It is worth noting that the classical elasticity is fundamentally founded by the introduction of the Hooke's Law in which the force and the change in displacement are linearly related via the stiffness of the component where the forces are applied. This physical principle governs the linearly elastic behaviour of materials. Aiming at a more general description of materials' responses, Mindlin and Tiersten [14] and Mindlin [15] developed higher-order theories of elasticity. Based on the employment of deformation metrics, these theories can be classified into two categories: couple stress theory and strain gradient theory. With regards to couple stress theories, both strain and curvature jointly govern the strength of the solid. In addition, while the antisymmetric part of the second-order deformation gradients represent rotation gradients, the symmetric part is generally neglected. Based on the initial ideas of the couple stress theory, a number of attempts have been made to further develop such concepts that are applicable to size-dependent problems. Within the concept of strain gradient theories, the idea was initially proposed in the benchmark study of Mindlin [11]. This theory incorporates both rotation and stretch gradients which enables it becomes more general than the couple stress theory which is only based on the constrained rotation.

However, these generalised continuum theories, when combined with plate theories, usually lead to differential problems with higher-order equations which require elements of high continuities to solve. These requirements may cause serious difficulty in the platform of traditional finite element method (FEM) in which only elements with low continuity can be used. Fortunately, isogeometric analysis (IGA) [16] is able to deal with these requirements naturally and effectively by using highly smooth basis function of non-uniform rational B-splines (NURBS). This basis function is employed to both approximate the unknown field and to exactly represent the geometry domains eliminating the geometry approximation errors that normally occur in FEM.

Therefore, this thesis aims at investigating the behaviours of small-scale plates effectively and comprehensively. This is achieved by conducting linear, nonlinear, and crack analyses of these structures by means of generalised continuum theories and IGA.

1.2 Outline of the thesis

The outline of the remaining of the thesis is as follows

Chapter 2: Generalised continuum theories and their applications to microplates. This chapter provides reviews and formulation of the modified couple stress theory and strain gradient theory which are the two generalised theories that will be used to account for the size-dependent effects. Higher-order shear deformation theories of plate are also discussed in this chapter. It is closed with a review of functionally graded material which is used to form the plate structures.

Chapter 3: Isogeometric analysis. This chapter presents the background and formulation of the IGA including B-splines and NURBS basis functions and there properties. The differences between IGA and FEM is also discussed.

Chapter 4: Linear analysis of small-scale plates. The linear behaviours of small-scale plates including bending, buckling, and vibration are presented in this chapter. Some parametric studies are conducted to show the effects of material length scale ratio, material parameters, and geometric parameters on the plates' responses.

Chapter 5: Geometrically nonlinear analysis of small-scale plates. This chapter investigates the nonlinear behaviours of small-scale plates in which iterative Newton-Raphson algorithm is used to solve for the nonlinear problems.

Chapter 6: Free vibration analysis of cracked small-scale plates. The vibration of small-scale plates with cracks are presented in this chapter. The discontinuities of the cracks are modelled by using enrichment functions within the platform of extended isogeometric analysis (XIGA).

Chapter 7: Conclusion and future work. This final chapter gives conclusions of the studies that have been presented. Some ideas for future outlooks are also proposed in this chapter.

1.3 Publications

The list of papers which have been published in international journals and presented at established conferences are shown below

Journal papers

1. H.X. Nguyen, E. Atroshchenko, H. Nguyen-Xuan, T.P. Vo, *Vibration of cracked functionally graded microplates by the strain gradient theory and extended isogeometric analysis*, Engineering Structures 187, 251-266, 2019.

2. H.X. Nguyen, E. Atroshchenko, H. Nguyen-Xuan, T.P. Vo, *Geometrically nonlinear isogeometric analysis of functionally graded microplates with the modified couple stress theory*, Computers & Structures 193, 110-127, 2017.

3. H.X. Nguyen, T.N. Nguyen, M. Abdel-Wahab, H. Nguyen-Xuan, S.P.A. Bordas, T.P. Vo, *A refined quasi-3D isogeometric analysis for functionally graded microplates based on the modified couple stress theory*, Computer Methods in Applied Mechanics and Engineering 313, 904-940, 2017.

Conference presentations

1. H.X. Nguyen, E. Atroshchenko, H. Nguyen-Xuan, T.P. Vo, *Free vibration of cracked FG plates based on strain-gradient theory*, The 13th World Congress on Computational Mechanics (WCCM XIII), New York, US (2018).

2. H.X. Nguyen, E. Atroshchenko, H. Nguyen-Xuan, T.P. Vo, *Extended isogeometric analysis of gradient-elastic plates with cracks*, The 6th European Conference on Computational Mechanics (ECCM 6), Glasgow, UK (2018).

3. H.X. Nguyen, T.P. Vo, *Isogeometric Analysis for Nonlinear Bending of Microplates*, The 14th U.S. National Congress on Computational Mechanics, Montreal, Canada (2017).

4. H.X. Nguyen, T.P. Vo, *Isogeometric analysis of small-scale plates with nonlinearity*, The 25th UKACM Conference on Computational Mechanics, University of Birmingham, Birmingham, United Kingdom (2017).

5. H.X. Nguyen, T.P. Vo, H. Nguyen-Xuan, *Vibration analysis of functionally graded microplates based on modified couple stress theory*, The 12th World Congress on Computational Mechanics (WCCM XII) and the 6th Asia-Pacific Congress on Computational Mechanics (APCOM VI), Seoul, South Korea (2016).

6. H.X. Nguyen, T.P. Vo, H. Nguyen-Xuan, *Bending and buckling analysis of functionally graded microplates using isogeometric approach*, The 24th UK Conference of the Association for Computational Mechanics in Engineering (ACME-UK 2016), Cardiff University, Cardiff, United Kingdom (2016).

Chapter 2

Generalised continuum theories and their applications to microplates

In this chapter, overview and mathematical formulation of generalised continuum theories including modified couple stress theory and strain gradient theory are presented. It is followed by the derivation of higher order shear deformation theories. Finally, an overview of functionally graded material of which the plate structures are made is presented.

2.1 Modified couple stress theory (MCST)

2.1.1 Background

Yang et al. [13] proposed the MCST which requires only one material length scale parameter in deriving the constitutive equation. It is considered that the equilibrium of moment of couples which was an additional equilibrium relation that forces the couple stress tensor to be symmetric. Therefore, the deformation energy is only influenced by the symmetric part of the rotation gradient and the symmetric part of the displacement gradient. In addition, instead of using two material length scale parameters as needed in the classical couple stress theory, this modified couple stress theory requires only one material length scale parameter to construct the constitutive relation. Park and Gao [17] utilised the principle of minimum total potential energy to develop a variational formulation of the MCST. This method not only derives the equilibrium equations but also forms the introduction of boundary conditions which are not available in Yang's theory [13]. Possessing those beneficial characteristics in which a symmetric

couple stress included and only one material length scale parameter involved, the MCST is considered to have advantages over other size-dependent theories such as classical couple stress theory and nonlocal theory.

Owing to its striking features, the MCST is continuously developed and has its own extensive literature. It has been applied to investigate various behaviours at small-scales. For beam analysis, static bending, buckling, and vibration analysis have been solved using Euler-Bernoulli [18], Timoshenko [19–22], and higher-order beam theories [23]. The MCST was also applied to small-scale plate analyses in several ways, Tsiatas [24] initially employed it to investigate the static bending response of isotropic Kirchhoff microplates. Yin et al. [25] investigated the vibration behaviour of Kirchhoff microplates using the standard separation of variables to derive the closed-form solution for natural frequencies. Bending and vibration behaviours of Mindlin microplates were studied by Ma et al. [26] in which the thickness stretching effect was also taken into account. Chen and Li [27] developed quadrilateral spline element for couple stress elasticity. The MCST has been also applied to investigate the behaviours of beams with different types of theories including Bernoulli-Euler [18, 28], Timoshenko [21] and higher-orders [23, 29]. Employing the MCST, a large volume of record predicting plates' behaviours has been conducted for both linear and nonlinear problems . Thai and Vo [30] paid their attention to the bending and vibration responses of size-dependent microplates. Reddy and his colleagues worked on the nonlinear finite element analysis (FEA) of FG microplates with different geometries and plate theories [31, 32]. Static bending and buckling of FG microbeams were studied by Simsek et al. [33] and Nateghi et al. [34]. Thai and his colleagues utilised the Navier's approach when deriving solutions for FG microplates in which Kirchhoff, Mindlin and sinusoidal plate theories were used [35–37]. Ke et al. [38, 39] employed the p-version of the Ritz method and different quadrature method to solve free vibration, bending, and buckling problems of the rectangular and annular FG Mindlin microplates, respectively. Using the MCST, a refined plate theory was utilised to predict the bending, buckling, and vibration behaviours of FG microplates by He et al. [40] following the Navier approach. Reddy et al. [41, 42, 32, 43] studied the nonlinear behaviour of small-scale FG microplates for different geometries based on FEM with eleven-unknown C^0 element formulation. Most of these efforts followed either analytical approaches being able to solve specific problem for a limit set of boundary conditions or C^0 FEMs with high number of unknowns which are computationally expensive.

2.1.2 Formulation

In the MCST, the strain energy density U_0 for linear isotropic material is a quadratic function of generalised strains [13]

$$U_0 = \frac{1}{2}\lambda\left(\mathrm{tr}\boldsymbol{\varepsilon}\right)^2 + \mu\left(\boldsymbol{\varepsilon}:\boldsymbol{\varepsilon} + \ell^2\boldsymbol{\chi}:\boldsymbol{\chi}\right), \tag{2.1}$$

where λ and μ are Lamé's constants, μ is also known as shear modulus which is often denoted as G, ℓ represents material length scale parameter and the strain tensor $\boldsymbol{\varepsilon}$ and symmetric curvature tensor $\boldsymbol{\chi}$ are defined by

$$\boldsymbol{\varepsilon} = \frac{1}{2}\left[\nabla\mathbf{u} + (\nabla\mathbf{u})^T\right], \tag{2.2a}$$

$$\boldsymbol{\chi} = \frac{1}{2}\left[\nabla\boldsymbol{\theta} + (\nabla\boldsymbol{\theta})^T\right], \tag{2.2b}$$

where $\mathbf{u}$ is the displacement vector and the rotation vector $\boldsymbol{\theta}$ is given by

$$\boldsymbol{\theta} = \frac{1}{2}\mathrm{curl}\left(\mathbf{u}\right). \tag{2.3}$$

The strain energy U stored in a deformed elastic body is then defined as

$$U = \int_V U_0 dV = \int_V \left(\boldsymbol{\sigma}:\boldsymbol{\varepsilon} + \mathbf{m}:\boldsymbol{\chi}\right) dV, \tag{2.4}$$

where $\boldsymbol{\sigma}$ and $\mathbf{m}$ are the symmetric stress tensor and the deviatoric part of the symmetric couple stress tensor, respectively. These components, $\boldsymbol{\sigma}$ and $\mathbf{m}$, which are conjugated to the deformation measures $\boldsymbol{\varepsilon}$ and $\boldsymbol{\chi}$, respectively, are given as

$$\boldsymbol{\sigma}\left(\boldsymbol{\varepsilon}\right) = \lambda\left(\mathrm{tr}\boldsymbol{\varepsilon}\right)\mathbf{I} + 2\mu\boldsymbol{\varepsilon}, \tag{2.5a}$$

$$\mathbf{m}\left(\boldsymbol{\chi}\right) = 2\mu\ell^2\boldsymbol{\chi}, \tag{2.5b}$$

where $\mathbf{I}$ denotes the identity matrix, and $\mathrm{tr}\left(\boldsymbol{\varepsilon}\right)$ is the trace of the strain tensor $\left(\varepsilon_{kk}\right)$. Meanwhile, Lamé's constants λ and μ are calculated by

$$\lambda = \frac{\nu E}{\left(1+\nu\right)\left(1-2\nu\right)}, \tag{2.6a}$$

$$\mu = \frac{E}{2\left(1+\nu\right)}, \tag{2.6b}$$

where E and ν are the Young's modulus and Poisson's ratio, respectively.

In Eq. (2.5), apparently, only one material length scale is needed and the deviatoric couple stress tensor **m** is also symmetric. It is worth commenting that, in MCST, the material length scale parameter ℓ explicitly depends on the material and its specific value can be experimentally determined from either bending tests of thin beams [9] or torsional experiments of slender cylinders [44]. According to Mindlin [45], the material length scale can be also estimated theoretically by taking the square root of the ratio of curvature modulus to shear modulus.

2.2 Strain gradient theory (SGT)

2.2.1 Background

The general SGT with microstructure was initially presented in the benchmark paper of Mindlin [11]. This theory incorporates both rotation and stretch gradients which enables it to more general than the couple stress one which is only based on the constrained rotation. The generalised SGT by Mindlin which is also called, for the lowest-order theory, *dipolar gradient theory* or *grade-two theory* is considered as one of the most effective theory. The fundamental idea of this theory is to incorporate an internal displacement field to each particle of a continuum, i.e. the material particle is considered as a deformable medium. According to this theory, the gradients of strain are included in the strain energy density which implies the appearance of new material constants, in addition to two classical Lamé's constants (λ, μ), and the material characteristic lengths. On the other hand, the expression of the kinetic energy density depends on the *micro-inertia* term leading to the presence of the intrinsic material length which is associated with the material microstructure. It is worth commenting that, at the early stage of the development, the gradient theories were highly complex with many independent parameters which discouraged researchers and engineers to consider it seriously to solve mechanics problems. Later, the theories were simplified by Aifantis [46] and Georgiadis et al. [47] who used just one parameter in addition to the Lamé's constants. These simplifications had opened up a broad field of analytical and numerical solution procedures due to the fact that they greatly reduced complex implementational and mathematical treatments. The comprehensive reviews on the development of the gradient theories can be found in the work of Askes and Aifantis [48] and Gourgiotis et al. [49]. The gradient theories, both the general and the simplified ones, have been widely applied in many problem including stress

concentration [50, 51], wave propagation [52, 53], plasticity [54, 55], fracture mechanics [56, 57], static analysis [58].

2.2.2 Formulation

In the most general case of the SGT, the strain energy density and the kinetic energy density are both formulated in terms of quantities on the microscale and on the macroscale. However, the formulations require in total of eighteen constitutive coefficients. Consequently, experimental identification of these constants is extremely difficult which seriously limits the use of this theory in practical analysis and design. Fortunately, by making a number of assumptions, Mindlin proposed simpler versions of the gradient elasticity theory with less number of constants which allows the strain energy density to be dependent upon the macroscopic displacement only. The simpler versions can be categorised into three forms based on how the microscopic deformation gradient κ_{ijk} and the macroscopic displacement u_i related. While the microscopic deformation gradient is expressed directly in terms of the second gradient of the macroscopic displacement in Form I, $\kappa_{ijk} = u_{k,ij}$, it is defined as the first gradient of the macroscopic strain in Form II, $\kappa_{ijk} = \varepsilon_{jk,i}$. It is worth commenting that, according to the classical continuum, the macroscopic strain is defined as the first gradient of the macroscopic displacement. In Form III, the microscopic deformations are split into the gradient of macroscopic rotation, $\chi_{ij} = \frac{1}{2} e_{jlm} u_{m,il}$, and the symmetric part of the second gradient of macroscopic displacement, $\kappa_{ijk} = \frac{1}{3}\left(u_{i,jk} + u_{j,ik} + u_{k,ij}\right)$ [48].

In this study, a simplified version of the SGT derived from the Form II will be used. As a starting point, the strain energy density is expressed with seven material constants including two Lamé's constants (λ, μ) as follows [11, 52]

$$U_0(\varepsilon, \kappa) = \frac{1}{2}\lambda \varepsilon_{ii}\varepsilon_{jj} + \mu \varepsilon_{ij}\varepsilon_{ij} + a_1 \kappa_{iik}\kappa_{kjj} + a_2 \kappa_{kii}\kappa_{kjj} + a_3 \kappa_{iij}\kappa_{jjk} + a_4 \kappa_{kij}\kappa_{kij} + a_5 \kappa_{kij}\kappa_{jik}, \tag{2.7}$$

where the Latin indices span the range $(1,2,3)$ and the classical strain tensor is defined as the first gradient of the macroscopic displacement

$$\varepsilon_{ij} = \frac{1}{2}\left(u_{j,i} + u_{i,j}\right) = \varepsilon_{ji}, \tag{2.8}$$

and the microscopic deformation gradient or also called the strain gradient tensor are expressed in terms of the first gradient of the macroscopic strain, in turns, the

second gradient of the displacement as follows

$$\kappa_{ijk} = \varepsilon_{jk,i} = \frac{1}{2}\left(u_{k,ji} + u_{j,ki}\right) = \kappa_{ikj}. \tag{2.9}$$

By making further assumptions [59, 47], $a_2 = \frac{1}{2}\lambda\ell^2, a_4 = \mu\ell^2, a_1 = a_3 = a_5 = 0$, where ℓ is the characteristic length or material length scale parameter and ℓ^2 represents the volumetric strain energy gradient, one can obtain a simplified model similar to that suggested by Altan and Aifantis [59]. Consequently, the strain energy density can be expressed with only one additional constant

$$U_0 = \frac{1}{2}\lambda\varepsilon_{ii}\varepsilon_{jj} + \mu\varepsilon_{ij}\varepsilon_{ij} + \ell^2\left(\frac{1}{2}\lambda\varepsilon_{ii,k}\varepsilon_{jj,k} + \mu\varepsilon_{ij,k}\varepsilon_{ij,k}\right). \tag{2.10}$$

Meanwhile, the kinetic energy density in Cartesian coordinate system is given as follow [11, 52]

$$K_0 = \frac{1}{2}\rho\dot{u}_i\dot{u}_i + \frac{1}{6}\rho d^2\frac{\partial\dot{u}_j}{\partial x_i}\frac{\partial\dot{u}_j}{\partial x_i} \tag{2.11}$$

where ρ is the mass density, the time derivative is represented by the superposed dot, and $2d$ is the size of the cube edges of the unit cell [52]. In their study on dispersive Rayleigh-wave propagation, Georgiadis et al. [47] suggested the relation between the material length scale and the size of the cube edges to be $\ell^2 = (0.1d)^2$. The second term of the right-hand-side (RHS) of Eq. (2.11) which is ignored in classical theory represents the micro-inertia of the continuum. This velocity gradient involvement allows the SGT to have a more detailed description of the motion which is used to analyse the vibration of the small-scale structures.

2.3 Plate theories

2.3.1 Background

When attention is turned to plate structures, there is a well established body of work on the development of mathematical models. The most basic plate theory is the classical plate theory (CPT), also known as Kirchhoff-Love plate theory. This theory basically assumes that the cross section perpendicular to the mid-plane before deformation remains normal to the mid-plane after deformation. As CPT neglects shear deformations, it is applicable only to thin plates in which the ratios of length to thickness are large. The first-order shear deformation theory (FSDT),

also known as Reissner-Mindlin plate theory, was developed taking into account the shear deformations. This advantageous feature enables FSDT to yield reliable results for both thin and thick plates. However, the shear locking phenomenon which creates higher stiffness is often cited as a drawback of this theory when the problems are solved numerically by means of traditional FEA. In addition, FSDT fails to predict the distribution of shear strains and stresses through the thickness for structures with traction free surfaces. In order to address this issue, one may need to include shear correction factor when using FSDT. However, this is not a straightforward approach as the shear correction factor does not stay the same for different problems. In order to bypass those shortcomings, Reddy pioneered the third-order shear deformation theory (TSDT) [60] before Soldatos proposed the higher-order shear deformation theory (HSDT) [61]. By making further assumptions to the TSDT, Senthilnathan [62] developed refined plate theory (RPT) which requires only four variables compared to Reddy's original theory with five unknowns.

The attention to the combination of the plate theories and generalised continuum theories including their variations to investigate the behaviours of small-scale plates has been constantly increased over the last few years. The studies of the behaviours of microplates employing MCST and different plate theories have been enriched with a wealth of numerical solutions and analytical approaches. Reddy and his colleagues have successfully developed finite element models to analyse the behaviour of microplates with and without nonlinearity [31, 41, 42]. Similarly, Zhang et al. [63] presented the bending, free vibration, and buckling analyses with MCST by means of C^0 finite element method. Concerning the analytical approaches, Thai and his colleagues [30, 64] investigated the bending and vibration responses of the FG microplates based on the TSDT and sinusoidal plate models with MCST. A size-dependent refined plate model for FG microplates based on MCST has been employed to solve for the closed-form solutions by He et al. [65]. It should be noted that although the RPT which requires only four unknowns owns positive properties compared to other models, it requires C^1-continuity elements which may cause difficulty when the conventional FEA is involved to solve the problem. In order to overcome these continuity issues, some C^0 approximations [66] and Hermite interpolation functions with C^1 elements [67] which involve adding extra variables of derivative of displacement can be adopted.

Regarding the integration of plate theories and strain gradient theory, Papargyri-Beskou and Beskos [58] conducted static, stability and dynamic analysis of Kirchhoff plates using the strain gradient theory with one additional material constant. Zhang et al. [68] utilised the Fourier series to predict the mechanical behaviours of small-scale plate based on Kirchhoff theory. Farzam Dadgar-Rad [69] analysed the strain gradient Reissner-Mindlin plate using C^0 quadrilateral elements. Ji et al. [70] proposed a comparison of strain gradient theories which were used in the analysis of functionally graded (FG) circular plates. Khakalo and Niiranen [71, 72] employed the SGT for the analysis of micro/nano materials and structures as well as stress analysis around cylindrical holes with bi-axial tension. However, in most of the works, the micro-inertia term which appears in the kinetic energy density of the original SGT has been ignored. In addition, the solution procedures involve either analytical approach for limited study or finite element analysis with less requirement on the continuity of the inter-elements. It is worth noting that when a plate theory is combined with the SGT, the resulting equation are of sixth-order leading to third-order derivatives in the weak form, which requires at least C^2-continuity of the basis functions.

2.3.2 Formulation

This section focuses on the formulation of higher-order shear deformation theories with the geometry configuration of the structure shown in Fig. 2.1. The third-order shear deformation model initially proposed by Reddy [60] is widely considered as a reliable theory in which no shear correction factor is required. In Reddy's theory, the displacement field, for $z \in [-h/2; h/2]$, is defined as

$$u(x,y,z) = u_0(x,y) + z\beta_x(x,y) + g(z)\Big(\beta_x(x,y) + w_{,x}(x,y)\Big), \tag{2.12a}$$

$$v(x,y,z) = v_0(x,y) + z\beta_y(x,y) + g(z)\Big(\beta_y(x,y) + w_{,y}(x,y)\Big), \tag{2.12b}$$

$$w(x,y,z) = w_0(x,y), \tag{2.12c}$$

where the comma notation $(_{,x},_{,y})$ indicates a derivative with respect to the spatial variable, $g(z) = -4z^3/(3h^2)$ [60] and the variables $\mathbf{u}_0 = [u_0 \quad v_0]^T$, w_0, and $\boldsymbol{\beta} = [\beta_x \quad \beta_y]^T$ are the membrane displacements, the transverse deflection of the mid-plane surface, and the rotations, respectively. By making further assumptions, $w_0 = w_b + w_s, \beta_x = -w_{b,x}, \beta_y = -w_{b,y}$, to Reddy's theory which contains five unknowns, Senthilnathan [62] proposed the four-variable refined plate theory

which can be expressed in the generalised form as

$$u(x,y,z) = u_0(x,y) - zw_{b,x}(x,y) + g(z)\,w_{s,x}(x,y), \tag{2.13a}$$

$$v(x,y,z) = v_0(x,y) - zw_{b,y}(x,y) + g(z)\,w_{s,y}(x,y), \tag{2.13b}$$

$$w(x,y,z) = w_b(x,y) + w_s(x,y), \tag{2.13c}$$

where w_b and w_s represent bending and shear components of transverse displacement, respectively. The function $g : z \longmapsto g(z) = f(z) - z$ is employed to describe the distribution of transverse shear strains and stresses through the plate's thickness. It is necessary to have the first derivative of f satisfies the tangential zero value at $z = \pm h/2$ such that the traction-free condition at top and bottom surfaces is met. Consequently, the shear correction factor is no longer required for higher-order shear deformation theory and refined plate theory.

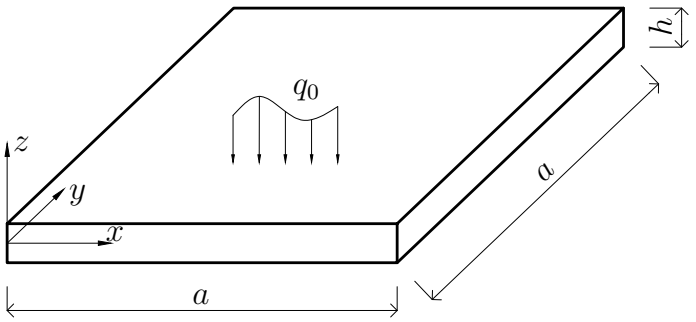

Fig. 2.1 Geometry configuration.

It should be noted that both the higher-order shear deformation theory and refined plate theory fail to capture the thickness stretching effect of normal deformation ($\varepsilon_z \neq 0$) due to the constant deflection through the plate thickness which can be inferred from Eq. (2.13c). In order to bypass this shortcoming, a number of theories which consider the thickness stretching effect have been developed [73–75]. Zenkour [76, 77] proposed the four-variable quasi-3D plate theory accounting for both transverse shear and normal deformations which can be alternatively expressed as follows

$$u(x,y,z) = u_0(x,y) - zw_{b,x}(x,y) + f(z)\,w_{s,x}(x,y), \tag{2.14a}$$

$$v(x,y,z) = v_0(x,y) - zw_{b,y}(x,y) + f(z)\,w_{s,y}(x,y), \tag{2.14b}$$

$$w(x,y,z) = w_b(x,y) + \phi(z)\,w_s(x,y). \tag{2.14c}$$

As can be observed, this quasi-3D model has a similar form to that of the four-variable refined plate theory shown in Eq. (2.13). Indeed, the displacement field based on the refined plate theory can be readily obtained by simplifying those of quasi-3D theory in which f and ϕ are replaced by g and 1, respectively. In addition, this formulation of quasi-3D displacement field requires less number of unknowns than that of existing theories [78–80].

A number of distribution functions, f and ϕ, are available for plates based on higher-order shear deformation theory, refined plate theory, and quasi-3D plate theory. One may find the general framework to construct such polynomial functions in the recent work of Nguyen et al. [81]. In this study, a novel seventh-order function of f and its corresponding function ϕ are proposed for the four-variable refined plate theory and quasi-3D theory. The function f which represents the non-linear distribution of the transverse shear strains and stresses is carefully chosen to satisfy the traction-free boundary conditions, therefore no shear correction factor is required for this refined plate theory. In addition, the function's coefficients are obtained by conducting optimisation procedure in which the minimisation of the differences between the outcome results and the existing analytical solutions is considered as objective functions and the coefficients play roles of design variables. The proposed functions of f and ϕ are presented in Table 2.1.

Table 2.1 Various forms of distribution function used for HSDT, RPT, and quasi-3D theories

Theory	ε_z	$f(z)$	ϕ_z
HSDT [60]	$=0$	$z-\frac{4}{3}\frac{z^3}{h^2}$	-
RPT [82]	$=0$	$\arctan\left(\sin\left(\frac{\pi}{h}z\right)\right)$	-
Quasi-3D [76]	$\neq 0$	$h\sinh\left(\frac{z}{h}\right)-\frac{4z^3}{3h^2}\cosh\left(\frac{1}{2}\right)$	$\frac{1}{12}f'(z)$
Quasi-3D [80]	$\neq 0$	$\frac{h}{\pi}\sin\left(\frac{\pi z}{h}\right)-z$	$f'(z)+1$
Quasi-3D [83]	$\neq 0$	$\frac{\pi}{h}z-\frac{9\pi}{5h^3}z^3+\frac{28\pi}{25h^5}z^5$	$\frac{1}{8}f'(z)$
Present RPT [84]	$=0$	$-8z+\frac{10z^3}{h^2}+\frac{6z^5}{5h^4}+\frac{8z^7}{7h^6}$	-
Present quasi-3D [84]	$\neq 0$	$-8z+\frac{10z^3}{h^2}+\frac{6z^5}{5h^4}+\frac{8z^7}{7h^6}$	$\frac{3}{20}f'(z)$

2.4 Functionally graded materials

Functionally graded materials (FGMs) are composite materials formed of two or more constituent phases in which material properties vary smoothly within

the structure. Consequently, FGMs avoid high interlaminar shear stresses, stress concentration and delamination phenomena which are often cited as shortcomings of laminated composite materials. FGMs consisting of ceramic and metal possess higher thermal resistance and better ductility which are inherited from the ceramic and metal phases, respectively. Owing to these striking features, FGMs are applicable to various fields of engineering including aerospace, nuclear power, chemistry and bio-engineering. FGMs have also been widely studied for various types of structures such as beams [85–88], plates [89–91, 67], and shells [92–94].

FGMs can be homogeneously modelled following either the rule of mixtures (Voigt scheme) [95] or the Mori-Tanaka scheme [96]. Those models assume FGMs to be homogeneous materials with the equivalent effective properties which are calculated from the properties of both, ceramic and metal constituents, depending on their proportions. For the material models, the volume fractions of ceramic phase V_c and metal phase V_m through the structure's thickness h are described by

$$V_c(z) = \left(\frac{1}{2} + \frac{z}{h}\right)^n, \quad V_m = 1 - V_c, \quad -\frac{h}{2} \leq z \leq \frac{h}{2}, \tag{2.15}$$

where n is the material index which indicates the profile of material variation through the thickness. It is worth commenting that $n = 0$ implies a fully homogeneous ceramic material, and the material properties tend to the fully homogeneous metal as n increases towards $+\infty$. The above equation of volume fractions also implies a smooth variation of the material from the bottom surface with metal to the top surface with ceramic.

The effective properties of FGM, according to the rule of mixtures, are calculated as follows

$$E_e = E_m V_m + E_c V_c, \tag{2.16a}$$

$$\nu_e = \nu_m V_m + \nu_c V_c, \tag{2.16b}$$

where E and ν represent the elastic Young's modulus and Poisson's ratio of metal phase (subscript m) and ceramic phase (subscript c), respectively. In spite of the simplicity and ease of implementation, the rule of mixtures model fails to describe the interactions between the constituents. Therefore the Mori-Tanaka scheme was developed taking those interactions into account. This model introduces the

effective bulk modulus K_e and the shear modulus G_e which are expressed as

$$\frac{K_e - K_m}{K_c - K_m} = \frac{V_c}{1 + V_m \frac{K_c - K_m}{K_m + \frac{4}{3}G_m}}, \quad \frac{G_e - G_m}{G_c - G_m} = \frac{V_c}{1 + V_m \frac{G_c - G_m}{G_m + f_1}}, \tag{2.17}$$

where

$$f_1 = \frac{G_m (9K_m + 8G_m)}{6 (K_m + 2G_m)}. \tag{2.18}$$

The effective Young's modulus and Poisson's ratio are then calculated as

$$E_e = \frac{9K_e G_e}{3K_e + G_e}, \quad \nu_e = \frac{3K_e - 2G_e}{2 (3K_e + G_e)}. \tag{2.19}$$

The variations of the former according the two material models are illustrated in Fig. 2.2. It can be seen that although there are differences between the rule of mixtures and Mori-Tanaka scheme, the effective properties including Young's modulus vary smoothly from the bottom surface to the top surface reflecting what expected previously.

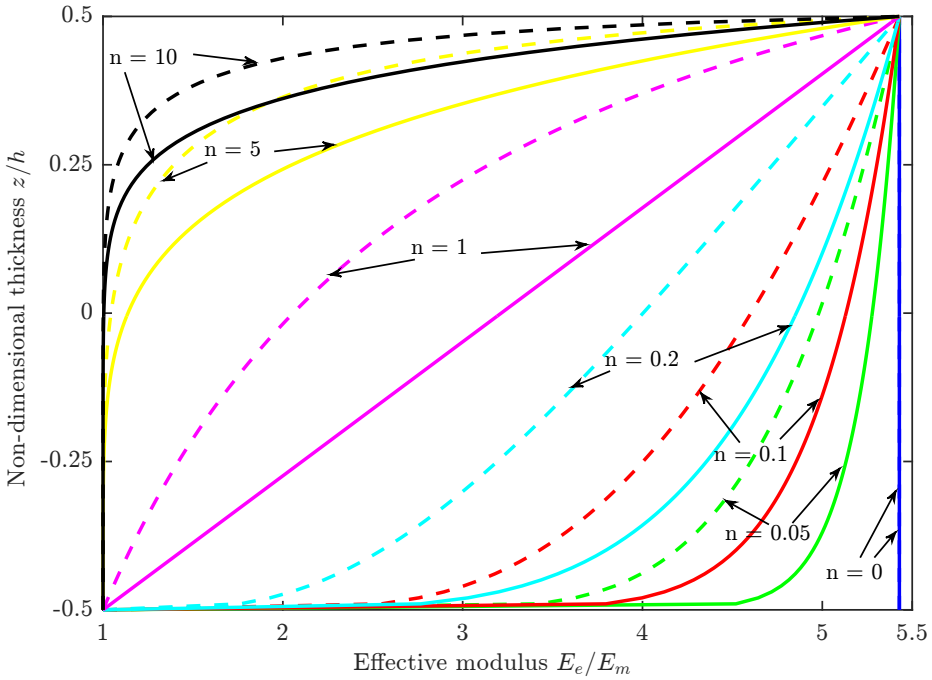

Fig. 2.2 The effective modulus of Al/Al_2O_3 plates according to the rule of mixtures (in solid lines) and Mori-Tanaka scheme (in dash lines).

Chapter 3

Isogeometric analysis

In this chapter, overview and mathematical aspects of the Isogeometric Analysis (IGA) will be presented. The formulation of the B-splines and the non-uniform rational B-splines (NURBS) which will be employed as the basis functions for IGA will also be discussed.

3.1 Introduction

The numercial method of isogeometric analysis has been introduced by Hughes and his co-workers [16]. This method is able to deal with C^1-continuity problem without using any additional variables or Hermite interpolation function . It bridges the existing gap between computer-aided design (CAD) and the fields of FEA. The essential idea of the IGA is that the basis functions, commonly the non-uniform rational B-splines (NURBS), which are employed to exactly describe the geometry domain will also be used for approximations of the unknown fields. In addition, these basic functions are high smoothness and able to tailor the continuity order easily through the domain [16, 97]. With these beneficial features, the NURBS-based IGA appears to be a potential approach in dealing with the C^1 HSDT and RPT problems [82]. One may find the guidance on computer implementation of IGA in the literature [98–100]. IGA has been widely implemented in a number of linearly and non-linearly mechanical and thermal problems such as static, free vibration, and buckling of laminated composite and FG plates with various plate theories including layerwise [101], FSDT [102–104], HSDT [105–107], and RPT [82]. The IGA is also applicable for the analysis of the shell structures [108–110].

3.2 B-splines

3.2.1 Knot vector

The primary point of the B-splines is a knot vector which is a set of non-decreased coordinates in the parameter space, $\boldsymbol{\Xi} = \{\xi_1, \xi_2, ..., \xi_{n+p+1}\}$, where i is the knot index of the i^{th} knot $\xi_i \in \mathbb{R}$, n is the number of basis functions and p represents the polynomial order of the basis function. A knot vector is called *uniform* if its knots are equally spaced, otherwise it is non-uniform. Meanwhile, it is *open* if the first knot and the last knot are simultaneously repeated $p+1$ times. As normally required to indicate the start and end point of a curve, the open knot vectors are used. The knot spans which are bounded by knots define element domains. It is worth noting that even though 1-D basis functions with open knot vectors are interpolatory at the two ends of the space interval, ξ_1 and ξ_{n+p+1}, they are generally not interpolatory at the remaining knots, i.e. interior knots. This property distinguishes the features of the knots from the nodes in the FEA [97].

3.2.2 Basis function

The B-spline basis functions that are constructed by the Cox-de Boor recursion formula, starting with the zeroth order ($p = 0$) are defined by [16, 97]

$$N_{i,0}(\xi) = \begin{cases} 1 & \text{if} \quad \xi_i \leq \xi < \xi_{i+1}, \\ 0 & \text{otherwise}, \end{cases} \tag{3.1a}$$

$$N_{i,p}(\xi) = \frac{\xi - \xi_i}{\xi_{i+p} - \xi_i} N_{i,p-1}(\xi) + \frac{\xi_{i+p+1} - \xi}{\xi_{i+p+1} - \xi_{i+1}} N_{i+1,p-1}(\xi), \text{for } p \geq 1, \tag{3.1b}$$

in which the fraction $0/0$ is defined as zero. While the basis functions are smooth, e.g. C^∞ continuity, within the knot span, they are C^{p-m} continuous across the knots, where m is the multiplicity of the knot. Therefore, for $p \geq 2$, the basis functions are of C^1 continuous at each knot with single multiplicity (single knot) and at the boundary of the knot span. Fig. 3.1 present B-spline basis functions with different knot vector and polynomial order as well as the illustration of how the knots partition the parameter space into elements.

The formulation of B-splines indicates a number of important properties which can be listed as follows

- Partition of unity, i.e. $\sum_{i=1}^{n} N_{i,p}(\xi) = 1, \forall \xi$

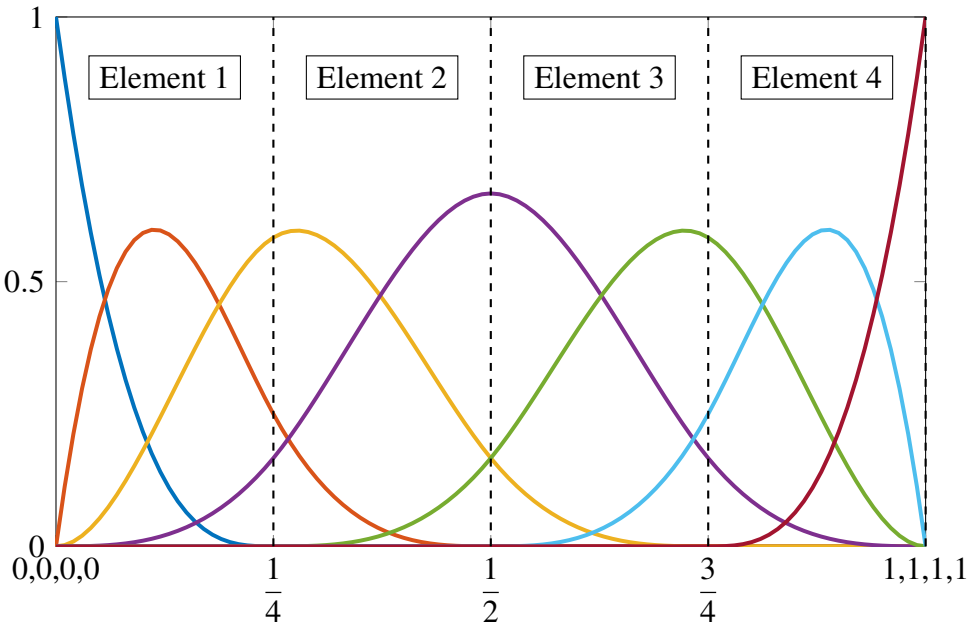

(a) Cubic B-spline basis functions for $\Xi = \left\{0,0,0,0,\frac{1}{4},\frac{1}{2},\frac{3}{4},1,1,1,1\right\}$

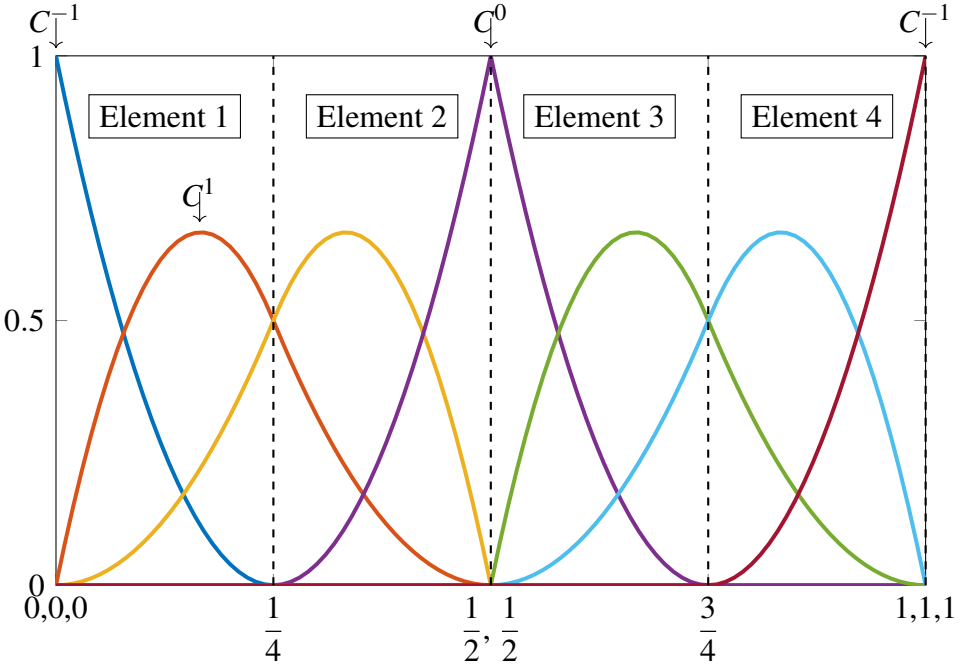

(b) Quadratic B-spline basis functions for $\Xi = \left\{0,0,0,\frac{1}{4},\frac{1}{2},\frac{1}{2},\frac{3}{4},1,1,1\right\}$

Fig. 3.1 One-dimensional B-spline basis functions.

- Pointwise non-negative, i.e. $N_{i,p}(\xi) \geq 0, \forall \xi$
- Highly smooth, i.e. C^{p-m} continuous across the knots

- Local support, i.e. a basis function $N_{i,p}(\xi)$ is non-zero only in the knot span $\left[\xi_i, \xi_{i+p+1}\right]$
- Linear independence, i.e. $\sum_{i=1}^{n} \alpha_i N_{i,p}(\xi) = 0 \Leftrightarrow \alpha_j = 0, \forall j \in \{1,2,3,\ldots,n\}$

Due to the recursive definition of the basis shown in Eq. 3.1, the derivatives of B-spline can be efficiently calculated using the lower-order B-spline terms. Indeed, the first derivative of B-spline basis function with knot vector $\boldsymbol{\Xi}$ of order p is given by

$$\frac{d}{d\xi} N_{i,p}(\xi) = \frac{p}{\xi_{i+p} - \xi_i} N_{i,p-1}(\xi) - \frac{p}{\xi_{i+p+1} - \xi_{i+1}} N_{i+1,p-1}(\xi). \tag{3.2}$$

Furthermore, it can be generalised for higher derivatives as follows

$$\frac{d^k}{d\xi^k} N_{i,p}(\xi) = \frac{p}{\xi_{i+p} - \xi_i} \left(\frac{d^{k-1}}{d\xi^{k-1}} N_{i,p-1}(\xi) \right) - \frac{p}{\xi_{i+p+1} - \xi_{i+1}} \left(\frac{d^{k-1}}{d\xi^{k-1}} N_{i+1,p-1}(\xi) \right). \tag{3.3}$$

For illustration purposes, Fig. 3.2 presents the first and second derivatives of the basis functions which correspond to those shown in Fig. 3.1a.

Two-dimensional B-splines are obtained by introducing a second knot vector $\mathbf{H} = \left\{\eta_1, \eta_2, ..., \eta_{m+q+1}\right\}$ and using the tensor product of $\boldsymbol{\Xi}$ and $\mathbf{H}$ in the parametric dimensions yielding

$$N_{i,j}^{p,q}(\xi, \eta) = N_{i,p}(\xi) M_{j,q}(\eta). \tag{3.4}$$

For illustration purposes, Fig. 3.3 depicts the one- and two-dimensional B-spline basis functions which are generated from the knot vector
$\boldsymbol{\Xi} = \{0,0,0,0,1/4,1/4,1/4,2/4,3/4,1,1,1,1\}$ and its combination with the knot vector $\mathbf{H} = \{0,0,0,0,1/5,2/5,3/5,4/5,1,1,1,1\}$, respectively.

3.2.3 B-spline curve and surface

A B-spline curve of degree p can be calculated by taking the linear combination of the basis functions and control points $\mathbf{P}$ as follow

$$\mathbf{C}(\xi) = \sum_{i=1}^{n} N_{i,p}(\xi) \mathbf{P}_i. \tag{3.5}$$

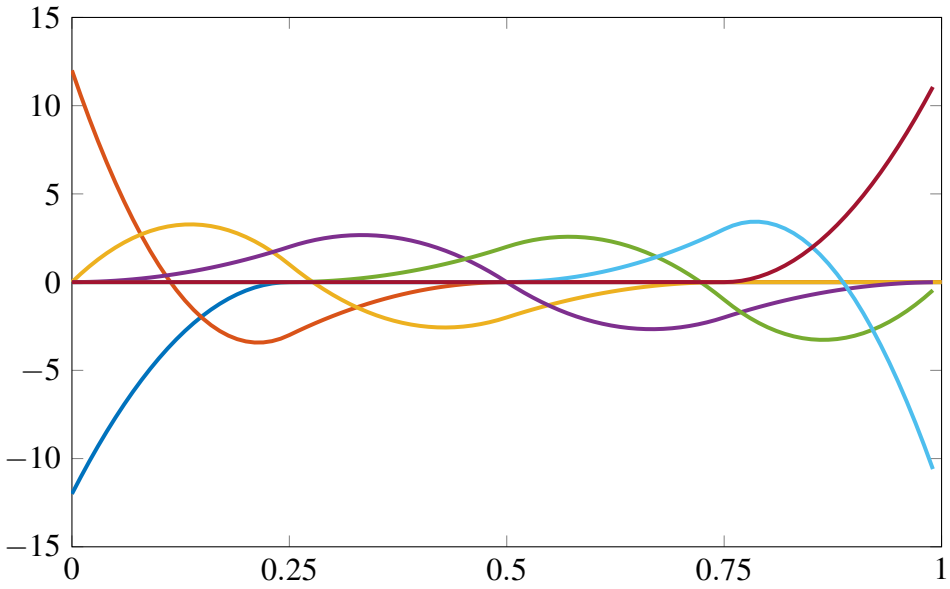

(a) First derivatives

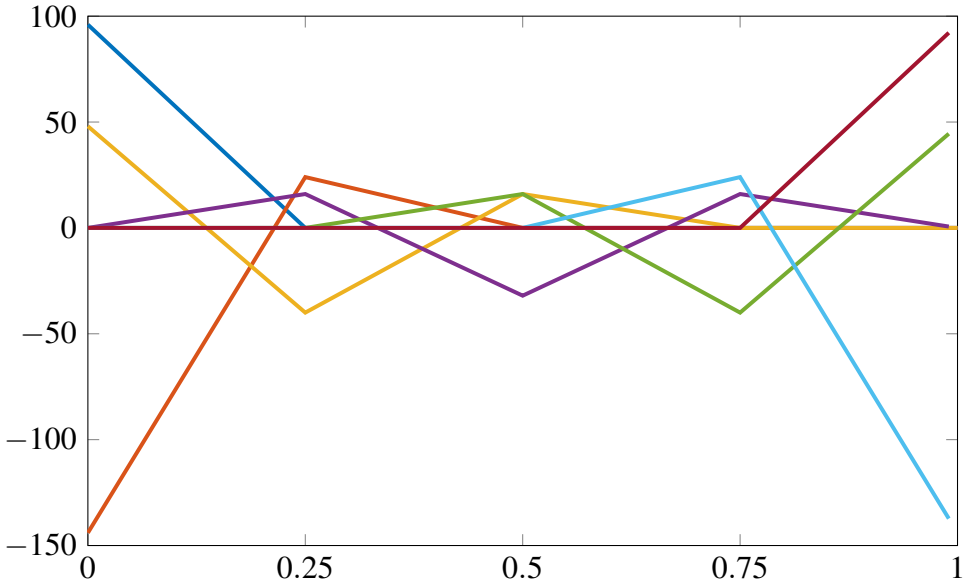

(b) Second derivatives

Fig. 3.2 Derivatives of cubic B-spline basis functions for $\Xi = \left\{0,0,0,0,\frac{1}{4},\frac{1}{2},\frac{3}{4},1,1,1,1\right\}$.

Fig. 3.4 shows the B-spline curves with difference set of control points in which the knot vector is corresponded to those presented in Fig. 3.1b. As can be interpreted, via the B-spline mapping, the boundaries of elements in physical space are the images knot lines. Addition, due to the local support property, only a limited elements are affected when one control point is changed. In this case,

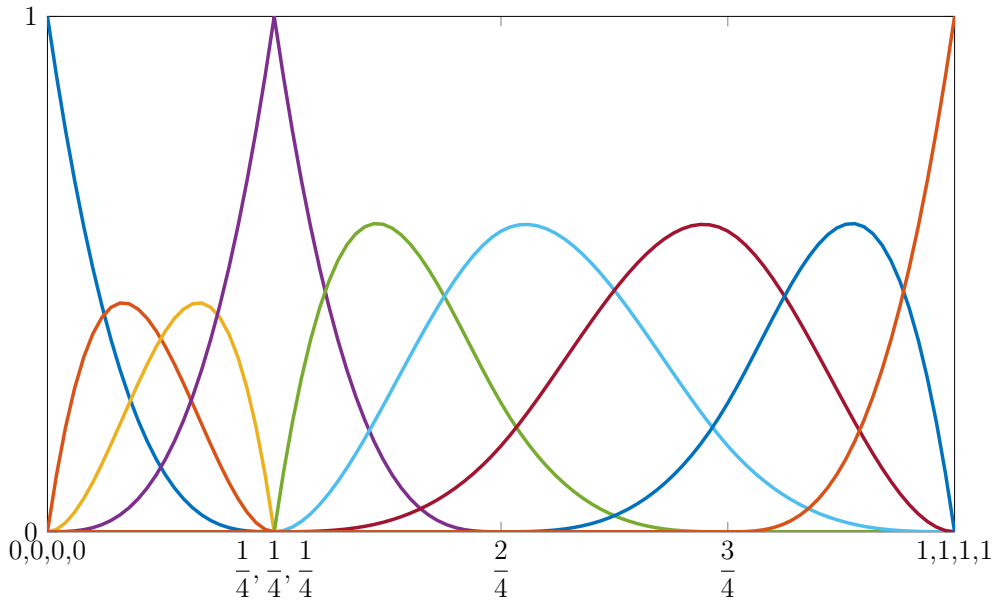

(a) One-dimensional cubic B-spline basis functions corresponding to $\boldsymbol{\Xi} = \left\{0,0,0,0,\frac{1}{4},\frac{1}{4},\frac{1}{4},\frac{2}{4},\frac{3}{4},1,1,1,1\right\}$

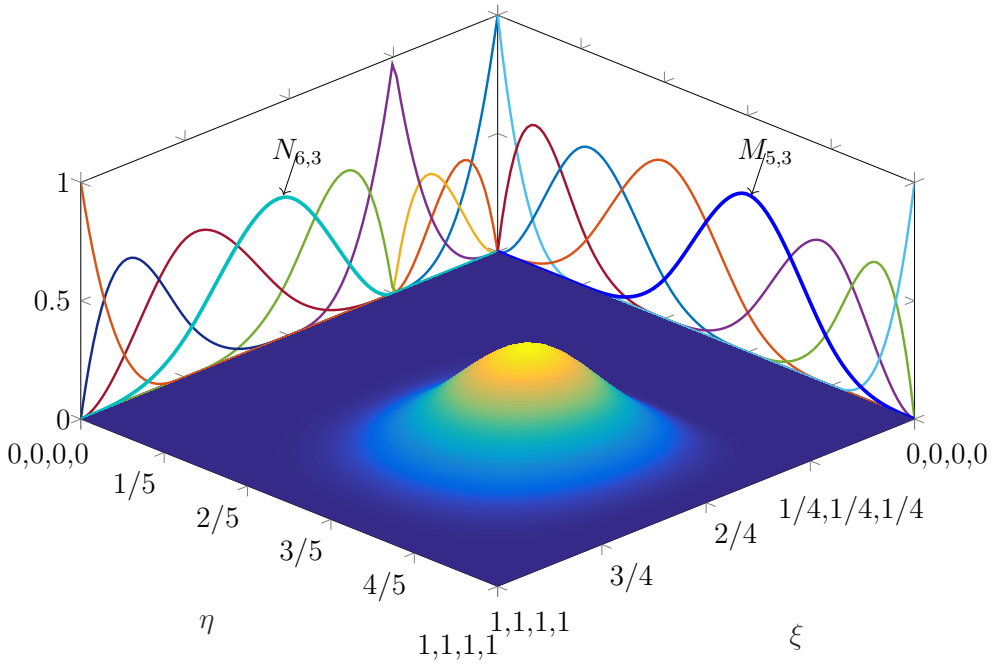

(b) Bivariate B-spline basis functions

Fig. 3.3 One- and two-dimensional B-spline basis functions.

the third and fourth elements are adjusted as a result of the movement of the fifth control point.

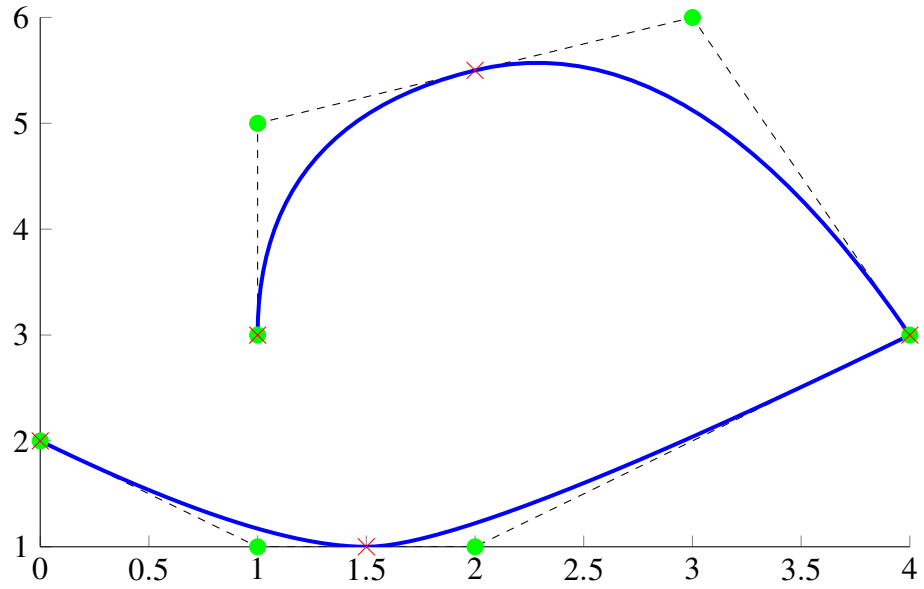

(a) Control point net $P = [0 \quad 2; \quad 1 \quad 1; \quad 2 \quad 1; \quad 4 \quad 3; \quad 3 \quad 6; \quad 1 \quad 5; \quad 1 \quad 3]$

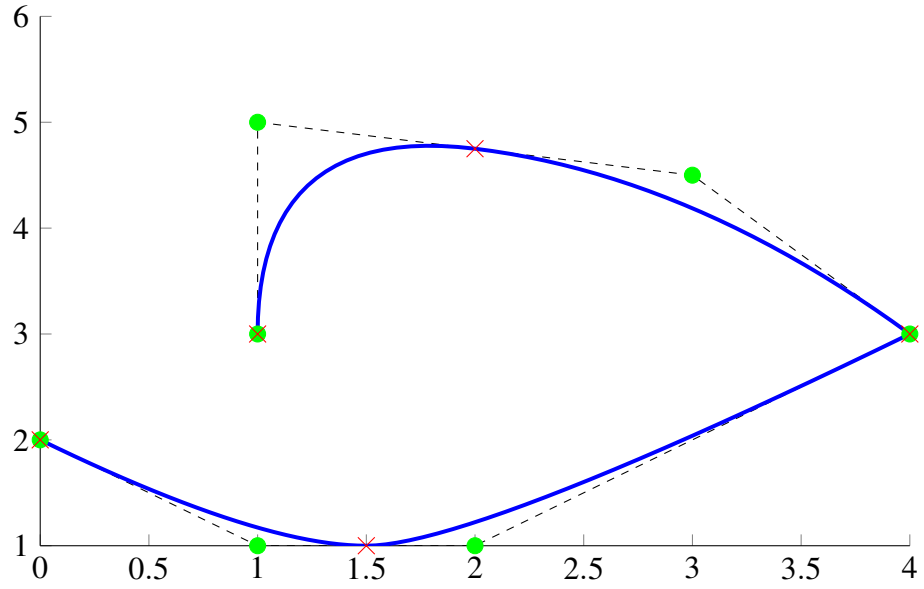

(b) Control point net $P = [0 \quad 2; \quad 1 \quad 1; \quad 2 \quad 1; \quad 4 \quad 3; \quad 3 \quad 4.5; \quad 1 \quad 5; \quad 1 \quad 3]$

Fig. 3.4 Quadratic B-spline curve (solid blue) with 4 segments (elements) bounded by red crosses and control net/polygon (dashed line) with 7 control points (green dot).

Analogous to the B-spline curve, the B-spline surface is computed using two-dimensional B-spline basis functions and a net of $n \times m$ control point $\mathbf{P}$ as follow

$$\mathbf{S}(\xi,\eta) = \sum_{i=1}^{n} \sum_{j=1}^{m} N_{i,p}(\xi) M_{j,q}(\eta) \mathbf{P}_{i,j}. \tag{3.6}$$

It is worth noting that the polynomial order p and q of two basis functions N and M in ξ and η are not necessarily to be the same. A B-spline surface is given in Fig. 3.5 with $\boldsymbol{\Xi} = \{0,0,0,0,1/3,2/3,1,1,1,1\}$ and $\mathbf{H} = \{0,0,0,0,1/3,2/3,1,1,1,1\}$. As can be observed, the element edges in the physical space are defined according to the knot vectors. In addition, since the open knot vectors are used, the vertices of the surface are interpolated while other vertices do not lie on the control net.

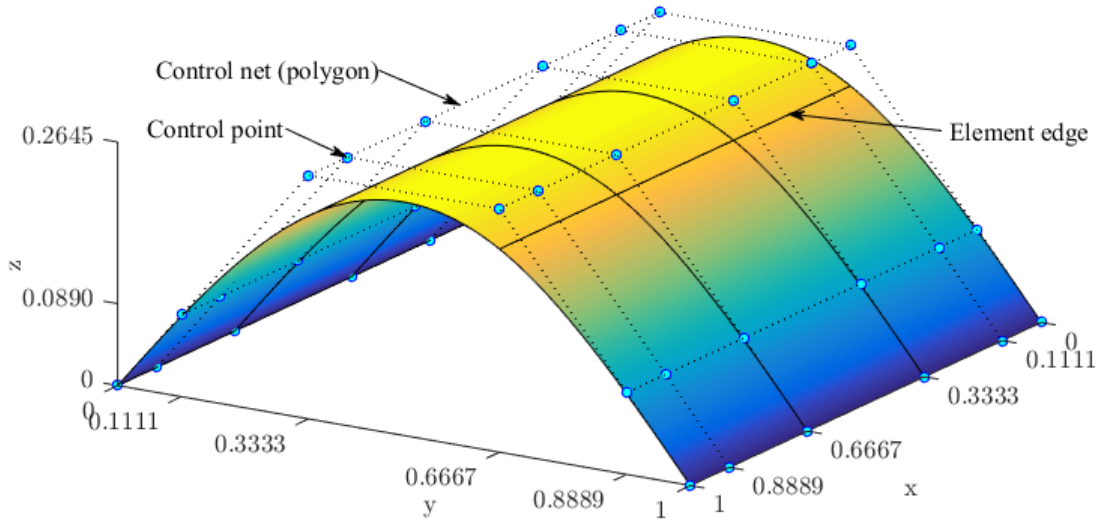

Fig. 3.5 B-spline surface.

3.3 Non-uniform rational B-splines

The NURBS basis functions are then further defined by introducing an additional weight w that associates to each control point. The term *non-uniform* means the knot vectors are generally not uniform while *rational* indicates the basis functions are piecewise rational polynomials. The one- and two-dimensional NURBS are constructed from the B-splines as follows [97]

$$R_i^p(\xi) = \frac{N_i(\xi)\, w_i}{\sum_{\hat{i}=1}^{n} N_{\hat{i},p}(\xi)\, w_{\hat{i}}}, \tag{3.7a}$$

$$R_{i,j}^{p,q}(\xi,\eta) = \frac{N_{i,p}(\xi)\, M_{j,q}(\eta)\, w_{i,j}}{\sum_{\hat{i}=1}^{n}\sum_{\hat{j}=1}^{m} N_{\hat{i},p}(\xi)\, M_{\hat{j},q}(\eta)\, w_{\hat{i},\hat{j}}}. \tag{3.7b}$$

It is worth commenting that B-spline basis function is a special case of NURBS function. Indeed, if all the individual weights corresponding the control points are assigned an equal constant, the NURBS function degenerates to a B-spline function. Additionally, it should be stressed that multi-dimensional NURBS are not tensor products of one-dimensional basis functions but the weighted tensor products of B-splines.

By using NURBS basis functions, the rational curves and surfaces are defined analogously to those of B-splines as follows

$$\mathbf{C}(\xi) = \sum_{i=1}^{n} R_i^p(\xi)\mathbf{P}_i, \tag{3.8a}$$

$$\mathbf{S}(\xi,\eta) = \sum_{i=1}^{n}\sum_{j=1}^{m} R_{i,j}^{p,q}\mathbf{P}_{i,j}. \tag{3.8b}$$

NURBS basis functions inherit all properties of B-splines plus the ability to exactly represent conic geometries, e.g. circles, ellipses.

3.4 Isogeometric analysis based on NURBS

The essential idea of the IGA is that the basis functions, commonly NURBS, which are employed to exactly describe the geometry domain will also be used for approximations of the unknown fields. Even though, other basis functions such as B-splines, T-splines [111, 112], and PHT-splines [113, 114] can be used, NURBS is normally employed since it is the most popular tool used in CAD industry. As a same basis function is used, IGA appears to be an ideal approach to bridge the existing gaps between CAD and the field of FEA, or CEA which is normally used in the industry sector. This integration significantly reduce the time for the creation of analysis-suitable models and mesh generation [97].

In IGA, elements are defined as the knot span as shown in Fig. 3.1. As can also be seen, the basis functions are expanded over multiple elements which is fundamentally different from the definition of elements in FEA. This property allows higher continuities across element boundaries which is essentially needed in higher-order problems.

The refinement processes can be conducted by means of knot insertion and order elevation which are analogous to h-refinement and p-refinement in FEA, respectively. These techniques are demonstrated in Fig. 3.1 where the knot

$\xi = \{1/4, 1/2, 3/4\}$ are inserted to knot vectors $\boldsymbol{\Xi}$ to create new knot spans and increase the number of elements in the domain. Meanwhile, order elevation means the polynomial orders p of the basis functions can be easily controlled by adjusting the multiplicities $p+1$ of the first and last knots of 0 and 1. Another alternative of refinement can be used in IGA but not in FEA is the k-refinement where the order elevation is performed and followed by knot insertion. With these refinement techniques conducted by interfering knot vectors only, IGA offers extremely flexible and efficient ways to control the element polynomials and the mesh size.

As mentioned in the previous section, NURBS-based element is highly smooth which can satisfy C^{∞}-continuity within an element and C^{p-1}-continuity across elements. This striking feature allows NURBS to generally give more accurate results compared to other elements with lower-order basis functions used in FEA. Furthermore, as a role of basis function for analysis, NURBS also possesses other important properties as follows

- Local supports
- Highly smooth
- Linearly independent
- Partition of unity
- DOFs are associated with control points

In order to highlight some of the features of IGA, a comparison between IGA and FEA is summarised in Table 3.1.

Table 3.1 Comparison between IGA and traditional FEA

Isogeometric Analysis	Finite Element Analysis
Control points	Nodal points
Control variables	Nodal variables
NURBS basis functions	Lagrange basis functions
h, p, k-refinement	hp-refinement
High, easily controlled continuity	C^0/C^1-continuity
Exact geometry	Approximate geometry

As NURBS basic functions are highly smooth and able to tailor the continuity order easily through the domain [16, 97], the NURBS-based IGA appears to

be a potential approach in dealing with the C^1 and C^2 plate problems with the presence of generealised continua. These positive properties make the IGA outweighs traditional FEA in many cases. IGA are also widely applied to solve for mechanical and thermal behaviours of complex structures such as plates [82, 102, 105, 115] and shells [108, 116, 109, 117]. There are limited number of works on the implementation of IGA for small-scale plates with generalised continua. Although IGA-based nonlinear analysis for plates has been touched following the works of the researchers in the community including [118–120], there is no reports on the nonlinear analysis of small-scale plates for size-dependent effects using this robust numerical method. In attempts to deal with structure fractures, the ideas of extended finite element method (XFEM) [121] are incorporated in the platform of IGA. While Benson et al. [122] presented the application of XIGA in dealing with the fracture mechanic problems, De Luycker et al. [123] showed the results of XIGA for linear fracture mechanics with good accuracy and better convergence rate. Ghorashi et al. [124] utilised XIGA for the simulation of stationary and propagating cracks.

Chapter 4

Linear analysis of small-scale plates[1]

In this chapter, the linear analyses of microplates based on IGA will be presented. They include static bending analysis, free vibration analysis, and buckling analysis. The chapter starts with the kinematics of microplates where a quasi-3D refined plate theory is employed to model the plates and the modified couple stress theory with one material length scale is used to account for size-dependent effects. It is followed by the NURBS-based formulation of the three aforementioned analyses before the numerical results are presented and discussed.

4.1 A theory for FG microplates

According to the displacement field and the strain-displacement relation, which are presented in Eqs. (2.14) and (2.2a), respectively, and the geometric configuration shown in Fig. 2.1, the following strain expressions can be obtained as

$$\boldsymbol{\varepsilon}(x,y,z) = \boldsymbol{\varepsilon}_0 + z\boldsymbol{\kappa}_b + f(z)\,\boldsymbol{\kappa}_s, \tag{4.1a}$$

$$\boldsymbol{\gamma}(x,y,z) = \left[f'(z) + \phi(z)\right]\boldsymbol{\varepsilon}_s, \tag{4.1b}$$

[1]The results in this chapter have been published in Nguyen et al. [84]

where

$$\boldsymbol{\varepsilon}=\left[\begin{array}{c}\varepsilon_x\\ \varepsilon_y\\ \gamma_{xy}\end{array}\right],\quad \boldsymbol{\varepsilon}_0=\left[\begin{array}{c}u_{0,x}\\ v_{0,y}\\ u_{0,y}+v_{0,x}\end{array}\right],\quad \boldsymbol{\kappa}_b=-\left[\begin{array}{c}w_{b,xx}\\ w_{b,yy}\\ 2w_{b,xy}\end{array}\right],\quad \boldsymbol{\kappa}_s=\left[\begin{array}{c}w_{s,xx}\\ w_{s,yy}\\ 2w_{s,xy}\end{array}\right],$$
$$\boldsymbol{\gamma}=\left[\begin{array}{c}\gamma_{xz}\\ \gamma_{yz}\end{array}\right],\quad \boldsymbol{\varepsilon}_s=\left[\begin{array}{c}w_{s,x}\\ w_{s,y}\end{array}\right],\quad \varepsilon_z=\phi'(z)\,w_s. \tag{4.2}$$

Using Eqs. (2.14), (2.3), and (2.2b), the rotation vector and the curvature vector are expressed as

$$\boldsymbol{\theta}=\left[\begin{array}{c}\theta_x\\ \theta_y\\ \theta_z\end{array}\right]=\frac{1}{2}\left[\begin{array}{c}2w_{b,y}-(f'-\phi)\,w_{s,y}\\ -2w_{b,x}+(f'-\phi)\,w_{s,x}\\ v_{0,x}-u_{0,y}\end{array}\right], \tag{4.3a}$$

$$\boldsymbol{\chi}=\left[\begin{array}{c}\boldsymbol{\chi}_b\\ \boldsymbol{\chi}_s\\ \chi_{zz}\end{array}\right]=\left[\begin{array}{c}\boldsymbol{\chi}_{b0}\\ \boldsymbol{\chi}_{s0}\\ 0\end{array}\right]+\left[\begin{array}{c}f'\boldsymbol{\chi}_{b1}\\ f''\boldsymbol{\chi}_{s2}\\ 0\end{array}\right]+\left[\begin{array}{c}\phi\boldsymbol{\chi}_{b3}\\ \phi'\boldsymbol{\chi}_{s4}\\ 0\end{array}\right], \tag{4.3b}$$

where

$$\boldsymbol{\chi}_b=\left[\begin{array}{c}\chi_{xx}\\ \chi_{yy}\\ \chi_{xy}\end{array}\right],\boldsymbol{\chi}_{b0}=\frac{1}{2}\left[\begin{array}{c}2w_{b,xy}\\ -2w_{b,xy}\\ w_{b,yy}-w_{b,xx}\end{array}\right],\boldsymbol{\chi}_{b1}=\frac{1}{4}\left[\begin{array}{c}-2w_{s,xy}\\ 2w_{s,xy}\\ -w_{s,yy}+w_{s,xx}\end{array}\right],\boldsymbol{\chi}_{b3}=\frac{1}{4}\left[\begin{array}{c}2w_{s,xy}\\ -2w_{s,xy}\\ w_{s,yy}-w_{s,xx}\end{array}\right],$$
$$\boldsymbol{\chi}_s=\left[\begin{array}{c}\chi_{xz}\\ \chi_{yz}\end{array}\right],\boldsymbol{\chi}_{s0}=\frac{1}{4}\left[\begin{array}{c}v_{0,xx}-u_{0,xy}\\ v_{0,xy}-u_{0,yy}\end{array}\right],\boldsymbol{\chi}_{s2}=\frac{1}{4}\left[\begin{array}{c}-w_{s,y}\\ w_{s,x}\end{array}\right],\boldsymbol{\chi}_{s4}=\frac{1}{4}\left[\begin{array}{c}w_{s,y}\\ -w_{s,x}\end{array}\right]. \tag{4.4}$$

According to Eq. (2.5), the constitutive relations for classical and modified couple stress theories can be presented in an explicit form as

$$\left\{\begin{array}{c}\sigma_x\\ \sigma_y\\ \sigma_z\\ \sigma_{xy}\\ \sigma_{xz}\\ \sigma_{yz}\end{array}\right\}=\left[\begin{array}{cccccc}Q_{11}&Q_{12}&Q_{13}&0&0&0\\ &Q_{22}&Q_{23}&0&0&0\\ &&Q_{33}&0&0&0\\ &&&Q_{66}&0&0\\ &&&&Q_{55}&0\\ \text{sym.}&&&&&Q_{44}\end{array}\right]\left\{\begin{array}{c}\varepsilon_x\\ \varepsilon_y\\ \varepsilon_z\\ \gamma_{xy}\\ \gamma_{xz}\\ \gamma_{yz}\end{array}\right\}, \tag{4.5a}$$

$$m_{ij} = 2G_e \ell^2 \chi_{ij}, \tag{4.5b}$$

where, for the quasi-3D theory ($\varepsilon_z \neq 0$), Q_{ij} are the three-dimensional elastic constants given by

$$\begin{aligned} Q_{11} = Q_{22} = Q_{33} &= \frac{(1-\nu_e)E_e}{(1-2\nu_e)(1+\nu_e)}, \\ Q_{12} = Q_{13} = Q_{23} &= \frac{\nu_e E_e}{(1-2\nu_e)(1+\nu_e)}, \\ Q_{44} = Q_{55} = Q_{66} &= \frac{E_e}{2(1+\nu_e)}. \end{aligned} \tag{4.6}$$

However, for the proposed refined plate theory ($\varepsilon_z = 0$), Q_{ij} are reduced plane-stress elastic constants and are expressed as

$$\begin{aligned} Q_{11} = Q_{22} &= \frac{E_e}{1-\nu_e^2}, \\ Q_{12} = Q_{21} &= \frac{E_e \nu_e}{1-\nu_e^2}, \\ Q_{44} = Q_{55} = Q_{66} &= \frac{E_e}{2(1+\nu_e)}, \end{aligned} \tag{4.7}$$

and the shear modulus $G_e = \dfrac{E_e}{2(1+\nu_e)}$.

In this study, the weak form of the static bending, vibration, and buckling problems are derived using the Hamilton's principle and weak formulation. One can find details of these well-known procedures in the literature [125, 82, 83]. Firstly, the weak form of the static bending of the couple-stress-based microplates subjected to transverse load loading q_0 can be expressed in the following compact form

$$\begin{aligned} \int_\Omega \delta \boldsymbol{\varepsilon}_b^T \mathbf{D}^b \boldsymbol{\varepsilon}_b d\Omega + \int_\Omega \delta \boldsymbol{\varepsilon}_s^T \mathbf{D}^s \boldsymbol{\varepsilon}_s d\Omega + \int_\Omega \delta \left(\chi_b^c\right)^T \mathbf{D}_c^b \chi_b^c d\Omega + \int_\Omega \delta \left(\chi_s^c\right)^T \mathbf{D}_c^s \chi_s^c d\Omega \\ = \int_\Omega \left[\delta w_b + \phi\left(\frac{h}{2}\right)\delta w_s\right] q_0 d\Omega \end{aligned}, \tag{4.8}$$

where the strain tensors and material matrices in the first two terms in Eq. (4.8) related to classical elastic theory are

$$\boldsymbol{\varepsilon}_b = \begin{bmatrix} \boldsymbol{\varepsilon}_0 \\ \boldsymbol{\kappa}_b \\ \boldsymbol{\kappa}_s \\ w_s \end{bmatrix}, \quad \boldsymbol{\varepsilon}_s = \begin{bmatrix} w_{s,x} \\ w_{s,y} \end{bmatrix}, \quad \mathbf{D}^b = \begin{bmatrix} \mathbf{A} & \mathbf{B} & \mathbf{E} & \mathbf{X} \\ \mathbf{B} & \mathbf{D} & \mathbf{F} & \mathbf{Y}^b \\ \mathbf{E} & \mathbf{F} & \mathbf{H} & \mathbf{Y}^s \\ \mathbf{X} & \mathbf{Y}^b & \mathbf{Y}^s & Z_{33} \end{bmatrix}, \tag{4.9}$$

in which the material matrices are calculated by

$$(\mathbf{A},\mathbf{B},\mathbf{D},\mathbf{E},\mathbf{F},\mathbf{H}) = \int_{-h/2}^{h/2} \left[1, z, z^2, f(z), zf(z), f^2(z)\right] \bar{\mathbf{Q}} dz, \tag{4.10a}$$

$$\left(\mathbf{X},\mathbf{Y}^b,\mathbf{Y}^s\right) = \int_{-h/2}^{h/2} \left[\phi'(z), z\phi'(z), f(z)\phi'(z)\right] \tilde{\mathbf{Q}} dz, \tag{4.10b}$$

$$Z_{33} = \int_{-h/2}^{h/2} \left[\phi'(z)\right]^2 Q_{33} dz, \tag{4.10c}$$

$$\mathbf{D}^s = \int_{-h/2}^{h/2} \left[f'(z) + \phi(z)\right]^2 \hat{\mathbf{Q}} dz, \tag{4.10d}$$

$$\bar{\mathbf{Q}} = \begin{bmatrix} Q_{11} & Q_{12} & 0 \\ Q_{21} & Q_{22} & 0 \\ 0 & 0 & Q_{66} \end{bmatrix}, \quad \tilde{\mathbf{Q}} = \begin{bmatrix} Q_{13} \\ Q_{23} \\ 0 \end{bmatrix}, \quad \hat{\mathbf{Q}} = \begin{bmatrix} Q_{44} & 0 \\ 0 & Q_{55} \end{bmatrix}, \tag{4.10e}$$

and where the curvature tensors and material matrices in the third and fourth terms in Eq. (4.8) representing the couple stress theory are

$$\boldsymbol{\chi}_b^c = \begin{bmatrix} \boldsymbol{\chi}_{b0} \\ \boldsymbol{\chi}_{b1} \\ \boldsymbol{\chi}_{b3} \end{bmatrix}, \quad \boldsymbol{\chi}_s^c = \begin{bmatrix} \boldsymbol{\chi}_{s0} \\ \boldsymbol{\chi}_{s2} \\ \boldsymbol{\chi}_{s4} \end{bmatrix}, \quad \mathbf{D}_c^b = \begin{bmatrix} \mathbf{A}^c & \mathbf{B}^c & \mathbf{E}^c \\ \mathbf{B}^c & \mathbf{D}^c & \mathbf{F}^c \\ \mathbf{E}^c & \mathbf{F}^c & \mathbf{H}^c \end{bmatrix}, \quad \mathbf{D}_c^s = \begin{bmatrix} \mathbf{X}^c & \mathbf{Y}^c & \mathbf{T}^c \\ \mathbf{Y}^c & \mathbf{Z}^c & \mathbf{V}^c \\ \mathbf{T}^c & \mathbf{V}^c & \mathbf{W}^c \end{bmatrix}, \tag{4.11}$$

in which the material matrices are be defined as

$$(\mathbf{A}^c,\mathbf{B}^c,\mathbf{D}^c,\mathbf{E}^c,\mathbf{F}^c,\mathbf{H}^c) = \int_{-h/2}^{h/2} \left(1, f'(z), \left[f'(z)\right]^2, \phi(z), f'(z)\phi(z), \left[\phi(z)\right]^2\right) \bar{\mathbf{G}} dz, \tag{4.12a}$$

$$(\mathbf{X}^c,\mathbf{Y}^c,\mathbf{Z}^c,\mathbf{T}^c,\mathbf{V}^c,\mathbf{W}^c)=\int_{-h/2}^{h/2}\left(1,f''(z),\left[f''(z)\right]^2,\phi'(z),f''(z)\,\phi'(z),\left[\phi'(z)\right]^2\right)\hat{\mathbf{G}}dz, \tag{4.12b}$$

where

$$\bar{\mathbf{G}}=2G_e\ell^2\begin{bmatrix}1&0&0\\0&1&0\\0&0&1\end{bmatrix},\quad \hat{\mathbf{G}}=2G_e\ell^2\begin{bmatrix}1&0\\0&1\end{bmatrix}. \tag{4.13}$$

The weak form of the free vibration of the couple-stress-based microplates is concisely expressed as

$$\int_\Omega \delta\boldsymbol{\varepsilon}_b^T\mathbf{D}^b\boldsymbol{\varepsilon}_b d\Omega+\int_\Omega \delta\boldsymbol{\varepsilon}_s^T\mathbf{D}^s\boldsymbol{\varepsilon}_s d\Omega+\int_\Omega \delta\left(\boldsymbol{\chi}_b^c\right)^T\mathbf{D}_c^b\boldsymbol{\chi}_b^c d\Omega+\int_\Omega \delta\left(\boldsymbol{\chi}_s^c\right)^T\mathbf{D}_c^s\boldsymbol{\chi}_s^c d\Omega=\int_\Omega \delta\tilde{\mathbf{u}}^T\tilde{\mathbf{m}}\ddot{\tilde{\mathbf{u}}}d\Omega, \tag{4.14}$$

where $\tilde{\mathbf{u}}=\begin{bmatrix}u_0 & -w_{b,x} & w_{s,x} & v_0 & -w_{b,y} & w_{s,y} & w_b & w_s & 0\end{bmatrix}^T$, and the mass matrix $\tilde{\mathbf{m}}$ is defined by

$$\tilde{\mathbf{m}}=\begin{bmatrix}\mathbf{I}_0&0&0\\0&\mathbf{I}_0&0\\0&0&\mathbf{I}_1\end{bmatrix}\quad\text{in which}\quad \mathbf{I}_0=\begin{bmatrix}I_1&I_2&I_4\\I_2&I_3&I_5\\I_4&I_5&I_6\end{bmatrix},\quad \mathbf{I}_1=\begin{bmatrix}I_1&I_7&0\\I_7&I_8&0\\0&0&0\end{bmatrix}, \tag{4.15a}$$

$$(I_1,I_2,I_3,I_4,I_5,I_6,I_7,I_8)=\int_{-h/2}^{h/2}\rho\left[1,z,z^2,f(z),zf(z),f^2(z),\phi(z),\phi^2(z)\right]dz. \tag{4.15b}$$

For buckling analysis, the weak form of the couple-stress-based microplates subjected to in-plane loading is of the form

$$\int_\Omega \delta\boldsymbol{\varepsilon}_b^T\mathbf{D}^b\boldsymbol{\varepsilon}_b d\Omega+\int_\Omega \delta\boldsymbol{\varepsilon}_s^T\mathbf{D}^s\boldsymbol{\varepsilon}_s d\Omega+\int_\Omega \delta\left(\boldsymbol{\chi}_b^c\right)^T\mathbf{D}_c^b\boldsymbol{\chi}_b^c d\Omega+\int_\Omega \delta\left(\boldsymbol{\chi}_s^c\right)^T\mathbf{D}_c^s\boldsymbol{\chi}_s^c d\Omega + \int_\Omega \nabla^T\delta\left[w_b+\phi(0)\,w_s\right]\mathbf{N}_0\nabla\left[w_b+\phi(0)\,w_s\right]d\Omega=0, \tag{4.16}$$

where $\nabla^T = [\partial/\partial x \quad \partial/\partial y]^T$ and $\mathbf{N}_0 = \begin{bmatrix} N_x^0 & N_{xy}^0 \\ N_{xy}^0 & N_y^0 \end{bmatrix}$ are the transpose of gradient operator and matrix of pre-buckling loads, respectively.

4.2 NURBS-based formulation of the modified couple stress theory

By using NURBS basis functions, the displacement variables $\mathbf{u}$ of a microplate can be approximately calculated as follows

$$\mathbf{u}^h(\xi,\eta) = \sum_{A=1}^{n\times m} R_A(\xi,\eta)\mathbf{q}_A, \tag{4.17}$$

where $n \times m$ is the number of basis functions and $\mathbf{q}_A = [u_{0A} \quad v_{0A} \quad w_{bA} \quad w_{sA}]^T$ denotes the vector of degrees of freedom associated with the control point A. By substituting the approximations Eq. (4.17) into the strain-displacement relations Eq. (4.2), the in-plane and shear strains can be obtained

$$\begin{bmatrix}\boldsymbol{\varepsilon}_0^T & \boldsymbol{\kappa}_b^T & \boldsymbol{\kappa}_s^T & \boldsymbol{\varepsilon}_s^T\end{bmatrix}^T = \sum_{A=1}^{n\times m}\begin{bmatrix}(\mathbf{B}_A^m)^T & \left(\mathbf{B}_A^{b1}\right)^T & \left(\mathbf{B}_A^{b2}\right)^T & (\mathbf{B}_A^s)^T\end{bmatrix}^T \mathbf{q}_A, \tag{4.18}$$

where

$$\begin{aligned}
\mathbf{B}_A^m &= \begin{bmatrix} R_{A,x} & 0 & 0 & 0 \\ 0 & R_{A,y} & 0 & 0 \\ R_{A,y} & R_{A,x} & 0 & 0 \end{bmatrix}, \quad \mathbf{B}_A^{b1} = -\begin{bmatrix} 0 & 0 & R_{A,xx} & 0 \\ 0 & 0 & R_{A,yy} & 0 \\ 0 & 0 & 2R_{A,xy} & 0 \end{bmatrix}, \\
\mathbf{B}_A^{b2} &= \begin{bmatrix} 0 & 0 & 0 & R_{A,xx} \\ 0 & 0 & 0 & R_{A,yy} \\ 0 & 0 & 0 & 2R_{A,xy} \end{bmatrix}, \quad \mathbf{B}_A^s = \begin{bmatrix} 0 & 0 & 0 & R_{A,x} \\ 0 & 0 & 0 & R_{A,y} \end{bmatrix},
\end{aligned} \tag{4.19}$$

and the curvatures are obtained by substituting Eq. (4.17) into Eq. (4.4) :

$$\begin{aligned}
&\begin{bmatrix}\boldsymbol{\chi}_{b0}^T & \boldsymbol{\chi}_{b1}^T & \boldsymbol{\chi}_{b3}^T & \boldsymbol{\chi}_{s0}^T & \boldsymbol{\chi}_{s2}^T & \boldsymbol{\chi}_{s4}^T\end{bmatrix}^T \\
&= \sum_{A=1}^{n\times m}\begin{bmatrix}\left(\tilde{\mathbf{B}}_A^{b0}\right)^T & \left(\tilde{\mathbf{B}}_A^{b1}\right)^T & \left(\tilde{\mathbf{B}}_A^{b3}\right)^T & \left(\tilde{\mathbf{B}}_A^{s0}\right)^T & \left(\tilde{\mathbf{B}}_A^{s2}\right)^T & \left(\tilde{\mathbf{B}}_A^{s4}\right)^T\end{bmatrix}^T \mathbf{q}_A,
\end{aligned} \tag{4.20}$$

where

$$\tilde{\mathbf{B}}_A^{b0} = \frac{1}{2}\begin{bmatrix} 0 & 0 & 2R_{A,xy} & 0 \\ 0 & 0 & -2R_{A,xy} & 0 \\ 0 & 0 & \left(-R_{A,xx}+R_{A,yy}\right) & 0 \end{bmatrix}, \quad \tilde{\mathbf{B}}_A^{b1} = \frac{1}{4}\begin{bmatrix} 0 & 0 & 0 & -2R_{A,xy} \\ 0 & 0 & 0 & 2R_{A,xy} \\ 0 & 0 & 0 & \left(R_{A,xx}-R_{A,yy}\right) \end{bmatrix},$$

$$\tilde{\mathbf{B}}_A^{b3} = \frac{1}{4}\begin{bmatrix} 0 & 0 & 0 & 2R_{A,xy} \\ 0 & 0 & 0 & -2R_{A,xy} \\ 0 & 0 & 0 & \left(-R_{A,xx}+R_{A,yy}\right) \end{bmatrix}, \quad \tilde{\mathbf{B}}_A^{s0} = \frac{1}{4}\begin{bmatrix} -R_{A,xy} & R_{A,xx} & 0 & 0 \\ -R_{A,yy} & R_{A,xy} & 0 & 0 \end{bmatrix},$$

$$\tilde{\mathbf{B}}_A^{s2} = \frac{1}{4}\begin{bmatrix} 0 & 0 & 0 & -R_{A,y} \\ 0 & 0 & 0 & R_{A,x} \end{bmatrix}, \quad \tilde{\mathbf{B}}_A^{s4} = \frac{1}{4}\begin{bmatrix} 0 & 0 & 0 & R_{A,y} \\ 0 & 0 & 0 & -R_{A,x} \end{bmatrix}. \tag{4.21}$$

Substituting Eqs. (4.18) and (4.20) into Eqs. (4.8), (4.14), and (4.16), the matrix form of the global equilibrium equations for static bending, free vibration, and buckling can be respectively written as follows

$$\mathbf{K}\mathbf{q} = \mathbf{F}, \tag{4.22a}$$

$$\left(\mathbf{K} - \omega^2\mathbf{M}\right)\mathbf{q} = \mathbf{0}, \tag{4.22b}$$

$$\left(\mathbf{K} - \lambda_{cr}\mathbf{K}_g\right)\mathbf{q} = \mathbf{0}, \tag{4.22c}$$

where the global stiffness matrix $\mathbf{K}$ is the summation of the stiffness matrices corresponding to the classical theory $\mathbf{K}_s$ and the couple stress theory $\mathbf{K}_c$, i.e. $\mathbf{K} = \mathbf{K}_s + \mathbf{K}_c$. These matrices are respectively assembled from the element matrices $\mathbf{K}_s^e$ and $\mathbf{K}_c^e$ of an element Ω_e as follows

$$\mathbf{K}_s^e = \int_{\Omega_e} \left(\begin{Bmatrix} \mathbf{B}^m \\ \mathbf{B}^{b1} \\ \mathbf{B}^{b2} \\ \mathbf{B}^z \end{Bmatrix}^T \begin{bmatrix} \mathbf{A} & \mathbf{B} & \mathbf{E} & \mathbf{X} \\ \mathbf{B} & \mathbf{D} & \mathbf{F} & \mathbf{Y}^b \\ \mathbf{E} & \mathbf{F} & \mathbf{H} & \mathbf{Y}^s \\ \mathbf{X} & \mathbf{Y}^b & \mathbf{Y}^s & Z_{33} \end{bmatrix} \begin{Bmatrix} \mathbf{B}^m \\ \mathbf{B}^{b1} \\ \mathbf{B}^{b2} \\ \mathbf{B}^z \end{Bmatrix} + \left(\mathbf{B}^s\right)^T \mathbf{D}^s \mathbf{B}^s \right) d\Omega_e, \tag{4.23a}$$

$$\mathbf{K}_c^e = \int_{\Omega_e} \left(\begin{Bmatrix} \tilde{\mathbf{B}}^{b0} \\ \tilde{\mathbf{B}}^{b1} \\ \tilde{\mathbf{B}}^{b3} \end{Bmatrix}^T \begin{bmatrix} \mathbf{A}^c & \mathbf{B}^c & \mathbf{E}^c \\ \mathbf{B}^c & \mathbf{D}^c & \mathbf{F}^c \\ \mathbf{E}^c & \mathbf{F}^c & \mathbf{H}^c \end{bmatrix} \begin{Bmatrix} \tilde{\mathbf{B}}^{b0} \\ \tilde{\mathbf{B}}^{b1} \\ \tilde{\mathbf{B}}^{b3} \end{Bmatrix} + \begin{Bmatrix} \tilde{\mathbf{B}}^{s0} \\ \tilde{\mathbf{B}}^{s2} \\ \tilde{\mathbf{B}}^{s4} \end{Bmatrix}^T \begin{bmatrix} \mathbf{X}^c & \mathbf{Y}^c & \mathbf{T}^c \\ \mathbf{Y}^c & \mathbf{Z}^c & \mathbf{V}^c \\ \mathbf{T}^c & \mathbf{V}^c & \mathbf{W}^c \end{bmatrix} \begin{Bmatrix} \tilde{\mathbf{B}}^{s0} \\ \tilde{\mathbf{B}}^{s2} \\ \tilde{\mathbf{B}}^{s4} \end{Bmatrix} \right) d\Omega_e \tag{4.23b}$$

in which $\mathbf{B}_A^z = \begin{bmatrix} 0 & 0 & 0 & R_A \end{bmatrix}$. The load vector $\mathbf{F}$ is given by

$$\mathbf{F} = \int_{\Omega} q_0 \mathbf{R} d\Omega, \tag{4.24}$$

where $\mathbf{R} = \begin{bmatrix} 0 & 0 & R_A & \phi\left(\frac{h}{2}\right) R_A \end{bmatrix}^T$, the global mass matrix $\mathbf{M}$ is assembled from the element mass matrix of an element Ω_e as follow

$$\mathbf{M_e} = \int_{\Omega_e} \tilde{\mathbf{R}}^T \tilde{\mathbf{m}} \tilde{\mathbf{R}} d\Omega_e, \tag{4.25}$$

in which $\tilde{\mathbf{R}} = \begin{Bmatrix} \mathbf{R}_1 & \mathbf{R}_2 & \mathbf{R}_3 \end{Bmatrix}^T$, where

$$\mathbf{R}_1 = \begin{bmatrix} R_A & 0 & 0 & 0 \\ 0 & 0 & -R_{A,x} & 0 \\ 0 & 0 & 0 & R_{A,x} \end{bmatrix}, \quad \mathbf{R}_2 = \begin{bmatrix} 0 & R_A & 0 & 0 \\ 0 & 0 & -R_{A,y} & 0 \\ 0 & 0 & 0 & R_{A,y} \end{bmatrix}, \quad \mathbf{R}_3 = \begin{bmatrix} 0 & 0 & R_A & 0 \\ 0 & 0 & 0 & R_A \\ 0 & 0 & 0 & 0 \end{bmatrix}, \tag{4.26}$$

the geometric stiffness matrix $\mathbf{K}_g$ is assembled from the element geometric stiffness matrix of an element Ω_e as follow

$$\mathbf{K}_g^e = \int_{\Omega_e} (\mathbf{B}^g)^T \mathbf{N}_0 \mathbf{B}^g d\Omega_e, \tag{4.27}$$

where

$$\mathbf{B}^g = \begin{bmatrix} 0 & 0 & R_{A,x} & \phi(0) R_{A,x} \\ 0 & 0 & R_{A,y} & \phi(0) R_{A,y} \end{bmatrix}, \tag{4.28}$$

and ω and λ_{cr} represent the natural frequency and the critical buckling value, respectively.

As can be observed from the expressions of $\mathbf{B}$ and $\tilde{\mathbf{B}}$ matrices in Eqs. (4.19) and (4.21) show the employment of the second-order derivatives of the approximation functions R_A. Consequently, C^1 continuous approximations are required. This requirement may cause difficulties to finite element analysis which can be solved by using the mixed interpolation of tensorial components (MITC) or increasing the degrees of freedom to transform the C^1 problems to C^0 ones [41, 126, 127]. Apparently, these approaches results in higher number of variables and larger computational cost. However, within the platform of isogeometric analysis in

which NURBS basis functions are employed, the C^1-continuity requirement is naturally satisfied for $p \geq 2$ since the basis functions are C^{p-1} continuous across knot spans, i.e. elements. Therefore, the NURBS-based IGA would be a prominent numerical approach to deal with the proposed four-unknown C^1 quasi-3D refined plate theory and modified couple stress theory.

4.3 Numerical examples and discussion

In this section, convergence and validation studies are conducted to demonstrate the accuracy of the novel approaches presented in Section 4.1 and 4.2. In order to illustrate the efficiency of IGA approach in dealing with the MCST, this section is then continued by the computational analysis of FG rectangular and circular microplates with various types of boundary conditions for static bending, free vibration and buckling problems. In these investigations, the FG microplates made of a mixture of metal and ceramic whose material properties are presented in Table 4.1 are used. Throughout the numerical examples, unless otherwise specified, the material length scale ℓ is chosen as 17.6×10^{-6}m which was suggested by Lam et al. [9]. As the results will be presented in the normalised form, the geometric dimensions can be arbitrary. There are two types of boundary conditions considered

Simply supported (S)

$$v_0 = w_b = w_s = 0 \quad \text{at } x = 0,\ a$$
$$u_0 = w_b = w_s = 0 \quad \text{at } y = 0,\ b$$

Clamped (C)

$$u_0 = v_0 = w_b = w_s = 0 \text{ and } w_{b,x} = w_{b,y} = w_{s,x} = w_{s,y} = 0$$

It should be noted that, within the IGA approach, while the homogeneous boundary conditions corresponding to the displacement itself, e.g. u_0, v_0, w_b, w_s, are easily treated in a similar way to the traditional finite element method, those require the first derivative of the displacement components, e.g. $w_{b,x}, w_{b,y}, w_{s,x}, w_{s,y}$, can be enforced by assigning zero values to all displacements of control points which are directly related to clamped edges and their adjacent points [128, 83].

4.3.1 Convergence and validation studies

In order to evaluate the convergence and reliability of the approaches proposed in Sections 4.1 and 4.2, the MCST-based size-dependent analysis of homogeneous

Table 4.1 Material properties of FG plates

Property	Material			
	Al	Al_2O_3	ZrO_2-1	ZrO_2-2
E (GPa)	70	380	200	151
ν	0.3	0.3	0.3	0.3
ρ (kg/m^3)	2707	3800	3000	3000

fully simply-supported (SSSS) square microplate under sinusoidally distributed load which is shown in Fig. 4.1 is conducted using RPT model. Moderately thick plates $(a/h = 20)$ with four different values of material length scale ratio $(\ell/h = 0, 0.2, 0.6, 1)$ are investigated. For each case, eight different finite element meshes are analysed to study the convergence rate of the proposed IGA approach. As can be seen from Table 4.2, while the fast convergence of the analysis for polynomial order $p = 3$ and $p = 4$ is obtained, solutions using quadratic polynomial $p = 2$ experience relatively slower convergence rate toward analytical solutions reported by Thai and Kim [35]. This agrees well with the expectation in which the higher polynomial functions give better solutions in terms of accuracy and convergence rate. Fig. 4.2 presents the convergence study with the relative error of non-dimensional central deflection of homogeneous square microplates with respect to the analytical solutions [35]. Based on the convergence study, the cubic $(p = 3)$ NURBS element mesh of 11×11 is quite sufficient for all analysis cases. Therefore, this mesh whose geometry is shown in Fig. 4.1 will be used throughout the next examples unless otherwise specified.

Further investigation on the accuracy of the proposed method is conducted using FG plates made of aluminum and alumina (Al/Al_2O_3). In this case, without considering couple stress effects, the proposed RPT $(\varepsilon_z = 0)$ and quasi-3D $(\varepsilon_z \neq 0)$ theories are applied to analyses of SSSS square plates using the rule of mixtures. The plates are subjected to uniformly and sinusoidally distributed loads which are defined as q_0 and $q_0 \sin\left(\frac{\pi x}{a}\right) \sin\left(\frac{\pi y}{a}\right)$, respectively. As can be observed in Table 4.3, the present results are in good agreement with those available in published works using various 2-D and quasi-3D theories. It should be noted that some numerical results generated from the proposed IGA approach using the distribution functions from other existing works [60, 76, 83] are also presented in Table 4.3. The above investigations confirm the validity and reliability of the proposed approaches.

Table 4.2 Convergence of non-dimensional central deflections $\bar{w} = \dfrac{10Eh^3}{q_0 L^4} w(a/2, a/2, 0)$ of SSSS homogeneous and isotropic square plate subjected to sinusoidally distributed load ($a/h = 20$)

ℓ/h	p	Element Mesh								Analytical [35]
		3×3	5×5	7×7	9×9	11×11	13×13	15×15	17×17	
0										0.2842
	2	0.2734	0.2799	0.2819	0.2828	0.2833	0.2835	0.2837	0.2838	
	3	0.2823	0.2841	0.2842	0.2842	0.2842	0.2842	0.2842	0.2842	
	4	0.2843	0.2842	0.2842	0.2842	0.2842	0.2842	0.2842	0.2842	
0.2										0.2430
	2	0.2346	0.2397	0.2413	0.2420	0.2424	0.2426	0.2427	0.2428	
	3	0.2415	0.2430	0.2431	0.2431	0.2431	0.2431	0.2431	0.2431	
	4	0.2432	0.2431	0.2431	0.2431	0.2431	0.2431	0.2431	0.2431	
0.6										0.1124
	2	0.1098	0.1115	0.1121	0.1123	0.1125	0.1125	0.1126	0.1126	
	3	0.1120	0.1127	0.1127	0.1127	0.1127	0.1127	0.1127	0.1127	
	4	0.1127	0.1127	0.1127	0.1127	0.1127	0.1127	0.1127	0.1127	
1										0.0542
	2	0.0532	0.0539	0.0541	0.0542	0.0543	0.0543	0.0543	0.0543	
	3	0.0541	0.0544	0.0544	0.0544	0.0544	0.0544	0.0544	0.0544	
	4	0.0544	0.0544	0.0544	0.0544	0.0544	0.1127	0.1127	0.1127	

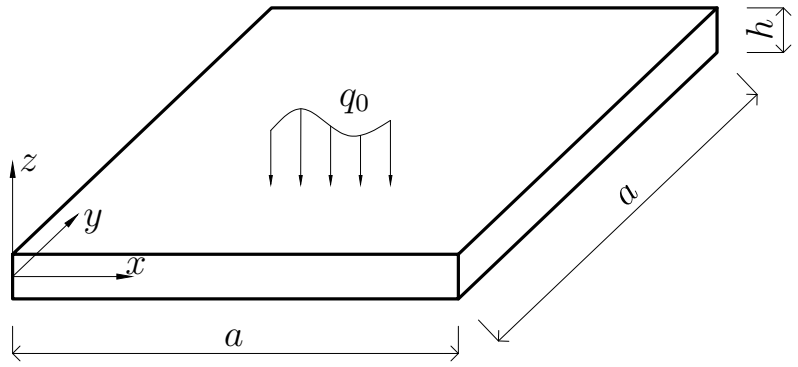

(a) Geometric configuration (replicate from Fig. 2.1).

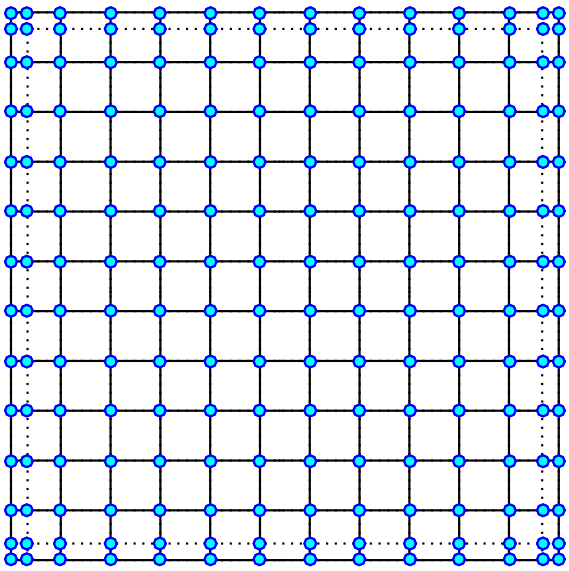

(b) Control point net and 11×11 cubic elements.

Fig. 4.1 Geometry and element mesh of a square microplate.

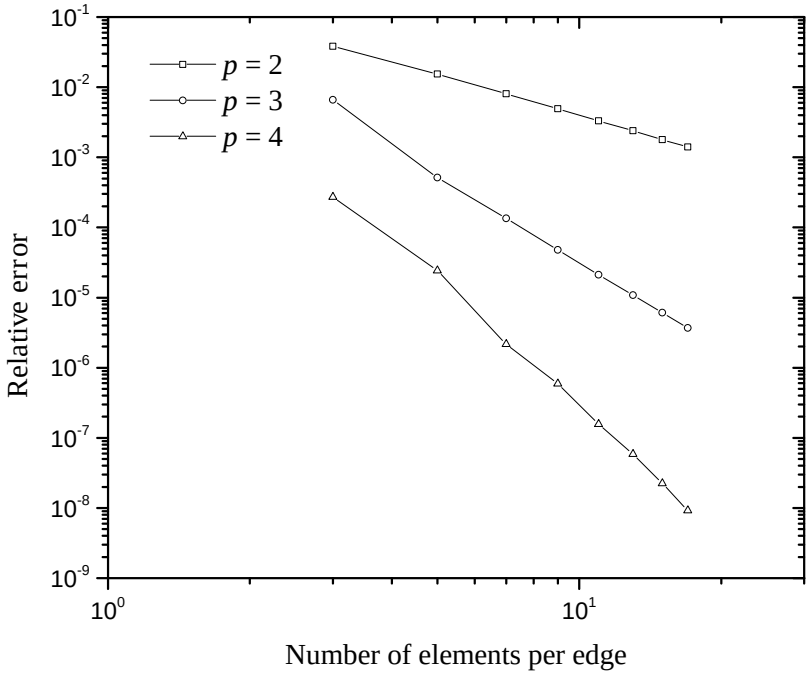

Fig. 4.2 Relative error of non-dimensional central deflection of homogeneous square microplates.

Table 4.3 Comparison of non-dimensional deflections $\bar{w} = \dfrac{10E_c h^3}{q_0 L^4} w(a/2, b/2, 0)$ of SSSS Al/Al_2O_3 square plates (rule of mixtures scheme)

n	Theory	$\varepsilon_z = 0$			$\varepsilon_z \neq 0$		
		$a/h = 4$	$a/h = 10$	$a/h = 100$	$a/h = 4$	$a/h = 10$	$a/h = 100$
Uniformly distributed load							
1	Zenkour [129]	-	0.9287	-	-	-	-
	Akavci and Tanrikulu [130]	-	0.9288	-	-	0.8977	-
	IGA-Reddy [60]	1.1319	0.9288	0.8904	-	-	-
	IGA-Zenkour [76]	1.1319	0.9288	0.8904	1.0611	0.8822	0.8641
	IGA-Nguyen et al. [83]	1.1308	0.9286	0.8904	1.0701	0.8898	0.8582
	IGA-Present [84]†	1.1319	0.9288	0.8904	1.0788	0.8978	0.8642
4	Zenkour [129]	-	1.3890	-	-	-	-
	Akavci and Tanrikulu [130]	-	1.3888	-	-	1.3259	-
	IGA-Reddy [60]	1.7941	1.3884	1.3116	-	-	-
	IGA-Zenkour [76]	1.7942	1.3884	1.3116	1.7020	1.3238	1.2556
	IGA-Nguyen et al. [83]	1.7983	1.3892	1.3116	1.6919	1.3174	1.2464
	IGA-Present [84]†	1.7928	1.3882	1.3116	1.6827	1.3223	1.2556
10	Zenkour [129]	-	1.5876	-	-	-	-
	Akavci and Tanrikulu [130]	-	1.5875	-	-	1.5453	-
	IGA-Reddy [60]	2.1442	1.5872	1.4818	-	-	-
	IGA-Zenkour [76]	2.1442	1.5872	1.4818	2.0656	1.5433	1.4466
	IGA-Nguyen et al. [83]	2.1454	1.5876	1.4818	2.0466	1.5362	1.4397
	IGA-Present [84]†	2.1432	1.5870	1.4818	2.0244	1.5347	1.4454
Sinusoidally distributed load							
1	Zenkour [76]	-	-	-	0.6828	0.5592	0.5624
	Neves et al. [78]	-	-	-	0.6997	0.5845	0.5624
	Mantari and Soares [131]	-	-	-	0.693	0.569	0.545
	Carrera et al. [73]	0.7289	0.5890	0.5625	0.7171	0.5875	0.5625
	Akavci and Tanrikulu [130]	0.7282	0.5889	0.5625	0.6908	0.5691	0.5457
	IGA-Reddy [60]	0.7284	0.5889	0.5625	-	-	-
	IGA-Zenkour [76]	0.7284	0.5889	0.5625	0.6828	0.5592	0.5459
	IGA-Nguyen et al. [83]	0.7275	0.5888	0.5625	0.6880	0.5640	0.5422
	IGA-Present [84]†	0.7284	0.5889	0.5625	0.6935	0.5691	0.5460
4	Zenkour [76]	-	-	-	1.1001	0.8404	0.7933
	Neves et al. [78]	-	-	-	1.1178	0.8750	0.8286
	Mantari and Soares [131]	-	-	-	1.085	0.838	0.793
	Carrera et al. [73]	1.1673	0.8828	0.8286	1.1585	0.8821	0.8286
	Akavci and Tanrikulu [130]	1.1613	0.8818	0.8287	1.0983	0.8417	0.7925
	IGA-Reddy [60]	1.1598	0.8815	0.8287	-	-	-
	IGA-Zenkour [76]	1.1599	0.8815	0.8287	1.1001	0.8404	0.7933
	IGA-Nguyen et al. [83]	1.1625	0.8820	0.8287	1.0931	0.8363	0.7875
	IGA-Present [84]†	1.1590	0.8813	0.8287	1.0868	0.8392	0.7933
10	Zenkour [76]	-	-	-	1.3391	0.9806	0.9140
	Neves et al. [78]	-	-	-	1.3490	0.8750	0.8286
	Mantari and Soares [131]	-	-	-	1.308	0.972	0.911
	Carrera et al. [73]	1.3925	1.0090	0.9361	1.3745	1.0072	0.9361
	Akavci and Tanrikulu [130]	1.3917	1.0089	0.9362	1.3352	0.9818	0.9141
	IGA-Reddy [60]	1.3908	1.0087	0.9362	-	-	-
	IGA-Zenkour [76]	1.3908	1.0087	0.9362	1.3391	0.9806	0.9140
	IGA-Nguyen et al. [83]	1.3914	1.0089	0.9362	1.3260	0.9760	0.9096
	IGA-Present [84]†	1.3902	1.0086	0.9362	1.3116	0.9748	0.9132

†Proposed RPT and quasi-3D models are used for the case of $\varepsilon_z = 0$ and $\varepsilon_z \neq 0$, respectively.

4.3.2 Static bending analysis

In this section, the static bending analysis of FG microplates based on the MCST will be investigated. The SSSS square microplates are assumed to follow the rule of mixtures. The aspect ratio a/h, material length scale ratio ℓ/h, and material index n are taken into account. Table 4.4 presents the comparison of non-dimensional central deflection of an SSSS square plate with those repeated by Thai and Kim [35]. While the results generated from the proposed RPT theory are in very good agreement, quasi-3D theory yields slightly different responses in terms of displacement. This is attributed to the consideration of the thickness stretching effect in the quasi-3D theory.

Table 4.4 Non-dimensional deflection $\bar{w} = \dfrac{10E_c h^3}{q_0 L^4} w(a/2, b/2, 0)$ of SSSS Al/Al_2O_3 square microplates subjected to sinusoidally distributed load (rule of mixtures scheme)

a/h	ℓ/h	$n=0$			$n=1$			$n=10$		
		RPT	Quasi-3D	TSDT[35]	RPT	Quasi-3D	TSDT[35]	RPT	Quasi-3D	TSDT[35]
5	0	0.3433	0.3360	0.3433	0.6688	0.6401	0.6688	1.2271	1.1663	1.2276
	0.2	0.2898	0.2853	0.2875	0.5505	0.5321	0.5468	1.0400	1.0019	1.0247
	0.4	0.1975	0.1965	0.1934	0.3601	0.3537	0.3535	0.7140	0.7043	0.6908
	0.6	0.1292	0.1296	0.1251	0.2288	0.2274	0.2224	0.4694	0.4711	0.4514
	0.8	0.0871	0.0879	0.0838	0.1517	0.1520	0.1464	0.3174	0.3220	0.3052
	1	0.0614	0.0623	0.0588	0.1060	0.1069	0.1017	0.2242	0.2289	0.2158
20	0	0.2842	0.2836	0.2842	0.5689	0.5516	0.5689	0.9537	0.9280	0.9538
	0.2	0.2431	0.2427	0.2430	0.4739	0.4619	0.4737	0.8313	0.8120	0.8303
	0.4	0.1695	0.1694	0.1693	0.3157	0.3105	0.3153	0.6001	0.5906	0.5986
	0.6	0.1127	0.1127	0.1124	0.2029	0.2008	0.2025	0.4102	0.4061	0.4090
	0.8	0.0767	0.0768	0.0765	0.1352	0.1343	0.1349	0.2842	0.2825	0.2834
	1	0.0544	0.0544	0.0542	0.0947	0.0943	0.0944	0.2038	0.2031	0.2033
100	0	0.2804	0.2803	0.2804	0.5625	0.5460	0.5625	0.9362	0.9132	0.9362
	0.2	0.2401	0.2400	0.2401	0.4689	0.4574	0.4689	0.8176	0.8001	0.8176
	0.4	0.1677	0.1677	0.1677	0.3128	0.3076	0.3128	0.5925	0.5833	0.5925
	0.6	0.1116	0.1116	0.1116	0.2012	0.1990	0.2011	0.4062	0.4018	0.4061
	0.8	0.0760	0.0760	0.0760	0.1341	0.1332	0.1341	0.2820	0.2799	0.2820
	1	0.0539	0.0539	0.0539	0.0939	0.0934	0.0939	0.2024	0.2014	0.2024

The bending responses of fully-clamped (CCCC) square Al/Al_2O_3 microplates under sinusoidally and uniformly distributed loads are further studied and presented in Table 4.5. It is noted that since no study on the static behaviours of CCCC microplates using MCST is reported in the literature, the results are compared with those generated from Reddy's HSDT model [60] using the proposed IGA approach. As can be seen, the results based on Reddy's model are in excellent agreement with the proposed RPT-based solutions. Meanwhile, the

difference between those generated from quasi-3D theory and others is due to the fact that thickness stretching effect which is neglected in RPT is accounted in this theory. The effects of material index n and material length scale ℓ on the central displacement of a CCCC square Al/Al_2O_3 plate are depicted in Fig. 4.3 in which data are generated by the proposed RPT and quasi-3D theories for three different ratios ℓ/h of 0, 0.4 and 1.0. As can be observed, an increase in the material index n leads to a rise of the plate's central deflection due to the decrease in the plate's stiffness. On the contrary, the growth of the material length scale ratio ℓ/h is followed by a decline in the displacement. In other words, for specific material length scale ℓ, the thinner the microplate, the higher plate's stiffness. It can be further observed that the discrepancy in terms of central deflection by the proposed RPT and quasi-3D is significantly decreased as ℓ/h increases and vanishes when $\ell/h = 1.0$. Fig. 4.4 depicts the deformed configurations of the Al/Al_2O_3 square microplates with various boundary conditions subjected to a sinusoidally distributed load in which $a/h, \ell/h$ and n are equal to 5, 0.4 and 10, respectively. It should be noted that the deformed shapes of the microplates are scaled up for illustration purposes.

Table 4.5 Non-dimensional deflection $\bar{w} = \dfrac{10E_c h^3}{q_0 L^4} w\,(a/2, b/2, 0)$ of CCCC Al/Al_2O_3 square microplates (rule of mixtures scheme)

a/h	ℓ/h	$n=0$			$n=1$			$n=10$		
		RPT	Quasi-3D	IGA-Reddy	RPT	Quasi-3D	IGA-Reddy	RPT	Quasi-3D	IGA-Reddy
Sinusoidally distributed load										
5	0	0.1601	0.1359	0.1601	0.3021	0.2554	0.3020	0.6111	0.4740	0.6113
	0.2	0.1378	0.1197	0.1377	0.2555	0.2214	0.2554	0.5178	0.4199	0.5183
	0.4	0.0974	0.0883	0.0973	0.1751	0.1586	0.1751	0.3568	0.3132	0.3575
	0.6	0.0655	0.0616	0.0655	0.1151	0.1081	0.1151	0.2358	0.2204	0.2364
	0.8	0.0450	0.0435	0.0449	0.0779	0.0752	0.0779	0.1602	0.1559	0.1606
	1	0.0321	0.0316	0.0320	0.0551	0.0542	0.0551	0.1136	0.1134	0.1139
20	0	0.1035	0.0950	0.1035	0.2065	0.1863	0.2065	0.3505	0.3150	0.3505
	0.2	0.0919	0.0849	0.0919	0.1797	0.1638	0.1797	0.3150	0.2857	0.3151
	0.4	0.0688	0.0645	0.0688	0.1294	0.1204	0.1294	0.2419	0.2237	0.2420
	0.6	0.0485	0.0462	0.0485	0.0882	0.0837	0.0882	0.1746	0.1647	0.1747
	0.8	0.0343	0.0331	0.0343	0.0611	0.0587	0.0611	0.1258	0.1204	0.1258
	1	0.0250	0.0243	0.0250	0.0438	0.0425	0.0438	0.0926	0.0896	0.0926
100	0	0.0999	0.0955	0.0999	0.2003	0.1872	0.2003	0.3336	0.3131	0.3336
	0.2	0.0889	0.0853	0.0889	0.1746	0.1643	0.1746	0.3013	0.2842	0.3013
	0.4	0.0668	0.0646	0.0668	0.1262	0.1204	0.1262	0.2336	0.2228	0.2336
	0.6	0.0473	0.0461	0.0473	0.0863	0.0835	0.0863	0.1701	0.1640	0.1701
	0.8	0.0336	0.0329	0.0336	0.0599	0.0584	0.0599	0.1232	0.1199	0.1233
	1	0.0244	0.0241	0.0244	0.0430	0.0422	0.0430	0.0910	0.0891	0.0910
Uniformly distributed load										
5	0	0.2239	0.1860	0.2238	0.4220	0.3500	0.4219	0.8557	0.6408	0.8559
	0.2	0.1924	0.1641	0.1924	0.3566	0.3040	0.3565	0.7233	0.5701	0.7239
	0.4	0.1358	0.1215	0.1358	0.2443	0.2186	0.2442	0.4976	0.4286	0.4985
	0.6	0.0914	0.0851	0.0913	0.1606	0.1495	0.1605	0.3288	0.3034	0.3295
	0.8	0.0627	0.0602	0.0627	0.1087	0.1041	0.1087	0.2234	0.2154	0.2239
	1	0.0447	0.0439	0.0447	0.0769	0.0752	0.0769	0.1584	0.1570	0.1588
20	0	0.1436	0.1300	0.1436	0.2864	0.2553	0.2864	0.4863	0.4307	0.4863
	0.2	0.1275	0.1164	0.1275	0.2493	0.2248	0.2493	0.4372	0.3912	0.4373
	0.4	0.0956	0.0887	0.0956	0.1797	0.1657	0.1797	0.3360	0.3072	0.3361
	0.6	0.0674	0.0637	0.0674	0.1227	0.1156	0.1227	0.2428	0.2269	0.2429
	0.8	0.0478	0.0457	0.0478	0.0850	0.0813	0.0850	0.1750	0.1664	0.1751
	1	0.0348	0.0336	0.0348	0.0610	0.0589	0.0610	0.1289	0.1240	0.1289
100	0	0.1384	0.1314	0.1384	0.2775	0.2577	0.2775	0.4622	0.4310	0.4622
	0.2	0.1232	0.1174	0.1232	0.2421	0.2265	0.2421	0.4176	0.3915	0.4176
	0.4	0.0927	0.0891	0.0927	0.1751	0.1664	0.1751	0.3242	0.3075	0.3242
	0.6	0.0657	0.0637	0.0657	0.1199	0.1155	0.1199	0.2363	0.2268	0.2363
	0.8	0.0467	0.0456	0.0467	0.0833	0.0810	0.0833	0.1713	0.1661	0.1713
	1	0.0340	0.0334	0.0340	0.0598	0.0586	0.0598	0.1266	0.1236	0.1266

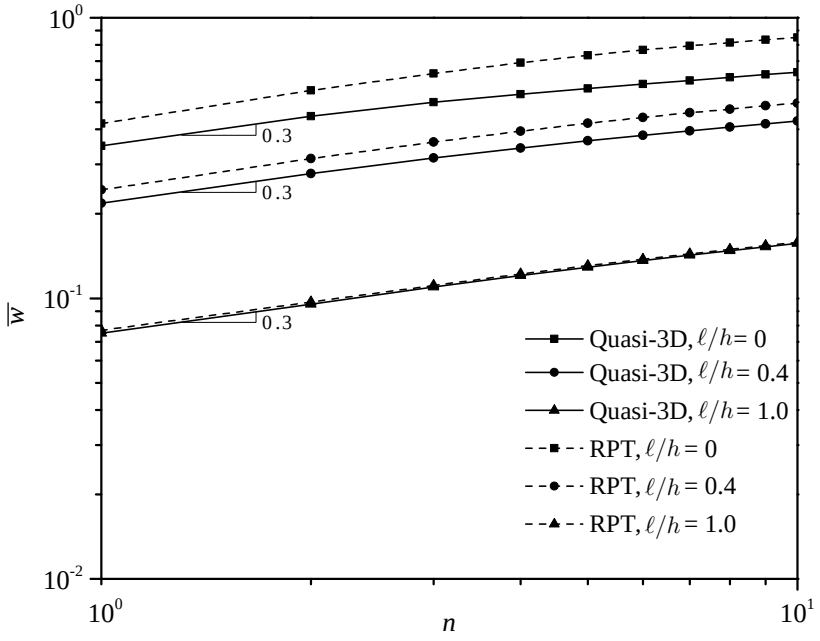

Fig. 4.3 Effects of material index n and material length scale ratio ℓ/h on the central deflection of CCCC Al/Al_2O_3 square microplates subjected to uniformly distributed load, $a/h = 5$ (rule of mixtures scheme).

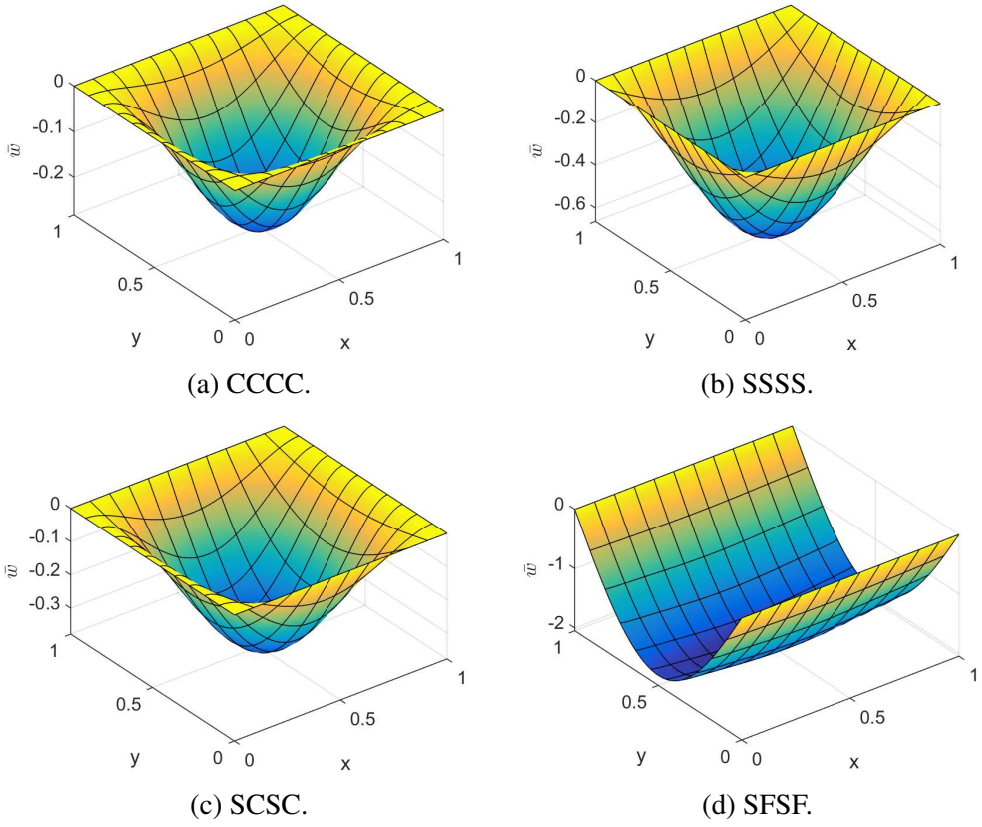

(a) CCCC. (b) SSSS.

(c) SCSC. (d) SFSF.

Fig. 4.4 Deformed configuration of Al/Al_2O_3 square microplates.

4.3.3 Free vibration analysis

In this part, the free vibration analysis of FG microplates based on a MCST is discussed. The proposed quasi-3D model is initially tested for linear elastic SSSS Al/ZrO_2-1 plates with various theories, taking into account the normal shear deformation. It can be seen that the results given in Table 4.6 agree well with other published works. The proposed RPT and quasi-3D models using IGA are further tested for homogeneous square microplates. The results shown in Table 4.7 are compared with analytical solutions generated from CPT by Yin et al. [25] and TSDT by Thai and Kim [35] . As can be observed, while the proposed RPT model yields slight discrepancy with respect to Yin et al.'s [25] due to their CPT assumption neglecting shear deformations, it shows excellent agreement with Thai and Kim [35], especially as plates become thinner, i.e. a/h ratio is relatively large. Due to the consideration of the thickness stretching effects, the proposed quasi-3D model gives slightly different results in comparison with other theories which based on assumption of $\varepsilon_z = 0$.

Table 4.6 Comparison of non-dimensional natural frequencies $\bar{\omega} = \omega \dfrac{a^2}{h}\sqrt{\dfrac{\rho_m}{E_m}}$ of SSSS Al/ZrO_2-1 plates (Mori-Tanaka scheme)

Reference	$n=1$			$a/h=5$		
	$a/h=5$	$a/h=10$	$a/h=20$	$n=2$	$n=3$	$n=5$
Vel and Batra [132]	5.4806	5.9609	6.1076	5.4923	5.5285	5.5632
Matsunaga [133]	5.7123	6.1932	6.3390	5.6599	5.6757	5.7020
Neves et al. [78]	5.4825	5.9600	6.1200	5.4950	5.5300	5.5625
Belabed et al. [134]	5.4800	5.9700	6.1200	5.5025	5.5350	5.5625
Alijani and Amabili [135]	5.4796	5.9578	6.1040	5.4919	5.5279	5.5633
Akavci and Tanrikulu [130]	5.4829	5.9676	6.1160	5.5064	5.5388	5.5644
Present [84]	5.5172	6.0023	6.1505	5.5324	5.5642	5.5886

Table 4.8 presents non-dimensional natural frequency of SSSS Al/Al_2O_3 square microplates. The results are compared with those of Thai and Kim [35] in which an analytical approach based on TSDT model is employed. Thick $(a/h = 5)$, moderately thick $(a/h = 20)$ and thin $(a/h = 100)$ microplates are considered. The results reveal good agreement between the RPT and TSDT [35], especially when the material length scale ratio ℓ/h is small, e.g. 0 or 0.2. On the contrary, the discrepancy becomes larger as ℓ/h gets closer to 1. However, this phenomenon just happens for thick plates and tends to be less pronounced as the plates become thinner. Meanwhile, the quasi-3D gives slightly different

Table 4.7 Comparison of non-dimensional natural frequencies $\bar{\omega} = \omega \frac{a^2}{h}\sqrt{\frac{\rho}{E}}$ of SSSS homogeneous microplates

a/h	Theory	ℓ/h					
		0	0.2	0.4	0.6	0.8	1
5	CPT [25]	5.9734	6.4556	7.7239	9.4673	11.4713	13.6213
	TSDT [35]	5.2813	5.7699	7.0330	8.7389	10.6766	12.7408
	RPT (Present [84])	5.2813	5.7496	6.9667	8.6191	9.8943	9.9791
	Quasi-3D (Present [84])	5.3090	5.7622	6.9438	8.5509	9.8943	9.9791
20	CPT [25]	5.9734	6.4556	7.7239	9.4673	11.4713	13.6213
	TSDT [35]	5.9199	6.4027	7.6708	9.4116	11.4108	13.5545
	RPT (Present [84])	5.9199	6.4009	7.6646	9.4005	11.3945	13.5330
	Quasi-3D (Present [84])	5.9235	6.4030	7.6633	9.3952	11.3854	13.5202
100	CPT [25]	5.9734	6.4556	7.7239	9.4673	11.4713	13.6213
	TSDT [35]	5.9712	6.4535	7.7217	9.4651	11.4689	13.6186
	RPT (Present [84])	5.9712	6.4534	7.7215	9.4646	11.4682	13.6178
	Quasi-3D (Present [84])	5.9723	6.4544	7.7222	9.4650	11.4683	13.6177

results compared to that of RPT model. A general observation from Table 4.8 reveals that the higher material length scale ratio ℓ/h is chosen, the larger the natural frequencies of the plates the plate's stiffness increases. Fig. 4.5 presents the variation of the normalised natural frequency of CCCC Al/Al_2O_3 square microplate with respect to the material length scale parameter ratio ℓ/h, plate's aspect ratio a/h with different values of material index n. As can be seen, the consideration of the size effects, i.e. increasing ℓ/h ratio, yields higher natural frequencies due to the increased structure stiffness. Meanwhile, the increase in material index n results in the decrease of frequencies as the structure has more metal and less ceramic. Fig. 4.6 provides a closer look at the effects of material index n and material length scale ratio ℓ/h on the plate's natural frequencies which are computed using the proposed RPT and quasi-3D models.

Similar to the previous case of bending analysis, the plate's stiffness decreases as a result of rising in material index n and decreasing material length scale ratio ℓ/h which leads to a decrease in natural frequency of the plate. In addition, the discrepancy in terms of frequency results predicted by the proposed RPT and quasi-3D becomes less significant as ℓ/h gets bigger and almost vanish difference when $\ell/h = 1.0$. The first six natural frequencies of Al/Al_2O_3 square microplates with different types of boundary conditions are given in Table 4.9 in which the results are generated for $n = 1$ and $\ell/h = 0.2$. The present quasi-3D results show

good agreement with those of Zenkour's quasi-3D model [76] using the proposed IGA approach. The first six mode shapes corresponding to the quasi-3D vibration analysis of CCCC microplates with $a/h = 10$ are presented in Fig. 4.7. It is worth noting that due to the symmetry, with the same frequency, two mode shapes can be obtained as seen in $\bar{\omega}_2$ and $\bar{\omega}_3$.

Table 4.8 Non-dimensional natural frequency $\bar{\omega} = \omega \dfrac{a^2}{h}\sqrt{\dfrac{\rho_c}{E_c}}$ of SSSS Al/Al_2O_3 square plates (rule of mixtures scheme)

a/h	ℓ/h	$n=0$			$n=1$			$n=10$		
		RPT	Quasi-3D	TSDT[35]	RPT	Quasi-3D	TSDT[35]	RPT	Quasi-3D	TSDT[35]
5	0	5.2813	5.3090	5.2813	4.0781	4.1521	4.0781	3.2519	3.3126	3.2514
	0.2	5.7496	5.7622	5.7699	4.4959	4.5542	4.5094	3.5312	3.5740	3.5548
	0.4	6.9667	6.9438	7.0330	5.5620	5.5865	5.6071	4.2584	4.2627	4.3200
	0.6	8.6191	8.5509	8.7389	6.9822	6.9681	7.0662	5.2471	5.2115	5.3335
	0.8	9.8943	9.8943	10.6766	8.2313	8.2313	8.7058	5.8571	5.8571	6.4759
	1	9.9791	9.9791	12.7408	8.3019	8.3019	10.4397	5.9073	5.9073	7.6895
20	0	5.9199	5.9235	5.9199	4.5228	4.5919	4.5228	3.7623	3.8129	3.7622
	0.2	6.4009	6.4030	6.4027	4.9556	5.0179	4.9568	4.0299	4.0761	4.0323
	0.4	7.6646	7.6633	7.6708	6.0714	6.1203	6.0756	4.7428	4.7794	4.7488
	0.6	9.4005	9.3952	9.4116	7.5739	7.6107	7.5817	5.7369	5.7640	5.7453
	0.8	11.3945	11.3854	11.4108	9.2768	9.3042	9.2887	6.8914	6.9106	6.9013
	1	13.5330	13.5202	13.5545	11.0882	11.1082	11.1042	8.1384	8.1510	8.1494
100	0	5.9712	5.9723	5.9712	4.5579	4.6263	4.5579	3.8058	3.8533	3.8058
	0.2	6.4534	6.4544	6.4535	4.9922	5.0546	4.9922	4.0724	4.1168	4.0725
	0.4	7.7215	7.7222	7.7217	6.1124	6.1635	6.1126	4.7837	4.8215	4.7840
	0.6	9.4646	9.4650	9.4651	7.6220	7.6630	7.6224	5.7778	5.8090	5.7782
	0.8	11.4682	11.4683	11.4689	9.3339	9.3673	9.3344	6.9341	6.9600	6.9345
	1	13.6178	13.6177	13.6186	11.1554	11.1832	11.1560	8.1842	8.2060	8.1846

In the next step, free vibration of circular plates whose geometry configuration and mesh are shown in Fig. 4.8 are investigated. Since there is no publication on the vibration behaviours of FG circular microplates based on the MCST, the investigation of circular plates in this study can serve as benchmark examples. Table 4.10 presents the fundamental natural frequencies which are firstly tested for homogeneous plates. Natural frequencies of plates without considering size-dependent effects are compared with results reported by Mohammadi et al. [136] and Nguyen et al. [83]. The results show very good agreement between the theories, especially proposed RPT and Nguyen et al.'s [83] which also uses another polynomial-based RPT model. Table 4.11 presents the first six natural frequencies of Al/Al_2O_3 circular plates with simple and clamped supports. The plate's thickness h and material index n are set as $0.2R$ and 1, respectively. As in the previous case of square microplates, Zenkour's quasi-3D model [76] using

Table 4.9 The first six non-dimensional natural frequencies $\bar{\omega} = \omega \frac{a^2}{h}\sqrt{\frac{\rho_m}{E_m}}$ of Al/Al_2O_3 square plates (Mori-Tanaka scheme) ($n = 1$, $\ell/h = 0.2$)

BC	a/h	Theory	Mode					
			1	2	3	4	5	6
SSSS	5	IGA-Zenkour	7.9366	13.8049	13.8049	17.3259	17.3259	19.5422
		Quasi-3D (Present [84])	7.8883	13.8049	13.8049	17.2045	17.2045	19.5422
		RPT (Present [84])	7.7844	13.8049	13.8049	16.9943	16.9943	19.5422
	10	IGA-Zenkour	8.5940	20.3230	20.3230	27.5893	27.5893	31.7475
		Quasi-3D (Present [84])	8.5607	20.2031	20.2031	27.5893	27.5893	31.5547
		RPT (Present [84])	8.4401	19.9188	19.9188	27.5893	27.5893	31.1386
	100	IGA-Zenkour	8.8399	21.7851	21.7851	35.3333	43.0764	43.0764
		Quasi-3D (Present [84])	8.8390	21.7802	21.7802	35.3221	43.0573	43.0573
		RPT (Present [84])	8.7127	21.4598	21.4598	34.8171	42.4074	42.4074
CCCC	5	IGA-Zenkour	12.7213	22.6661	22.6661	27.9021	27.9021	31.1450
		Quasi-3D (Present [84])	13.1029	22.9300	22.9300	27.8791	27.8791	31.3005
		RPT (Present [84])	12.1531	22.0683	22.0683	26.3182	26.3182	30.5398
	10	IGA-Zenkour	15.2379	28.9665	28.9665	41.2221	47.8649	47.9221
		Quasi-3D (Present [84])	15.4413	29.3267	29.3267	41.5955	48.2657	48.4504
		RPT (Present [84])	14.3638	27.8276	27.8276	39.9305	46.0435	46.4772
	100	IGA-Zenkour	16.0795	32.6473	32.6473	48.5912	58.0858	58.3951
		Quasi-3D (Present [84])	16.0540	32.6082	32.6082	48.5477	58.0353	58.3402
		RPT (Present [84])	15.5212	31.5708	31.5708	47.0903	56.2566	56.5207

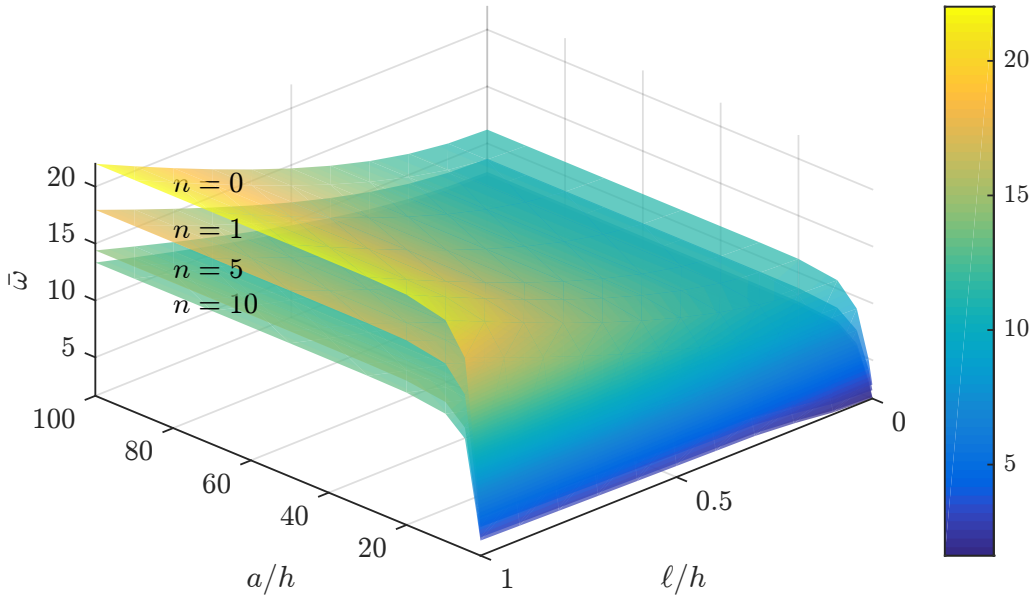

Fig. 4.5 Variation of natural frequency of CCCC Al/Al_2O_3 square microplates (rule of mixtures scheme).

the proposed IGA approach is added for reference purpose since no study can be found for this problem in the literature. The first six vibration mode shapes of clamped plates with $\ell/h = 0.2$ using quasi-3D model are given in Fig. 4.9. As can be seen, the mode frequencies increase through modes as expected and the mode shapes appear to be similar with those of rectangular plates in Fig. 4.7.

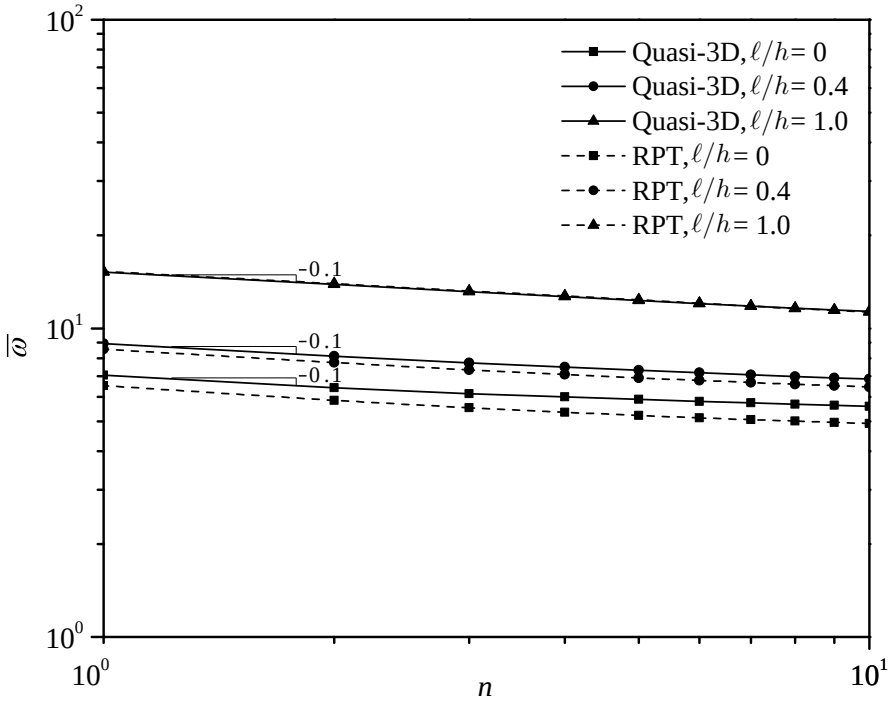

Fig. 4.6 Effects of material index n and material length scale ratio ℓ/h on the natural frequency of CCCC Al/Al_2O_3 square microplates, $a/h = 5$ (rule of mixtures scheme).

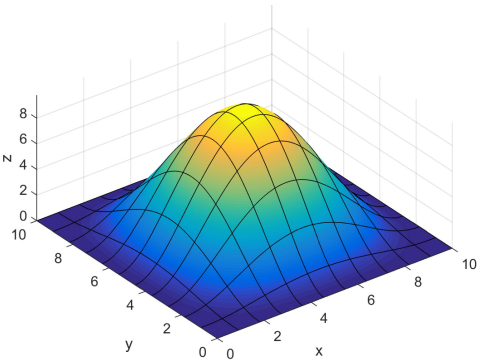

(a) $\bar{\omega}_1 = 15.4413$.

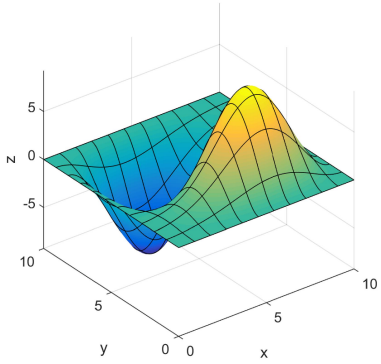

(b) $\bar{\omega}_2 = 29.3267$.

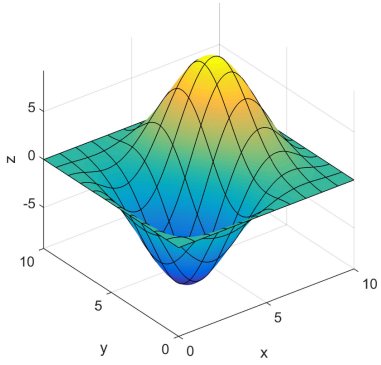

(c) $\bar{\omega}_3 = 29.3267$.

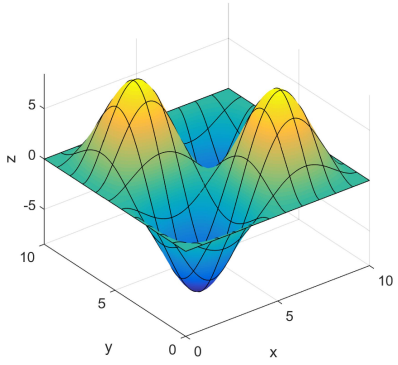

(d) $\bar{\omega}_4 = 41.5955$.

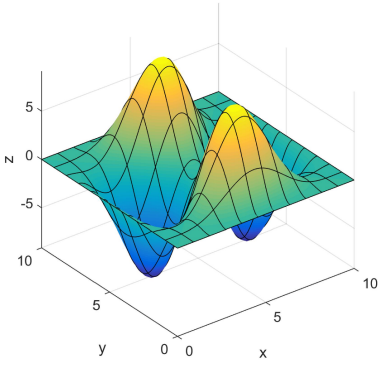

(e) $\bar{\omega}_5 = 48.2657$.

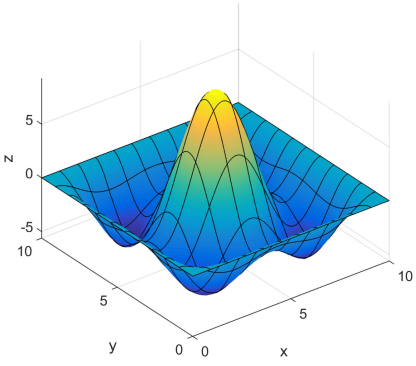

(f) $\bar{\omega}_6 = 48.4504$.

Fig. 4.7 The first six free vibration mode shapes of Al/Al_2O_3 CCCC square microplates.

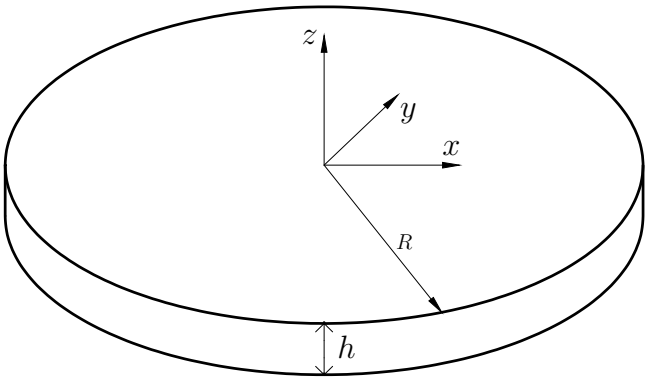

(a) Geometric configuration.

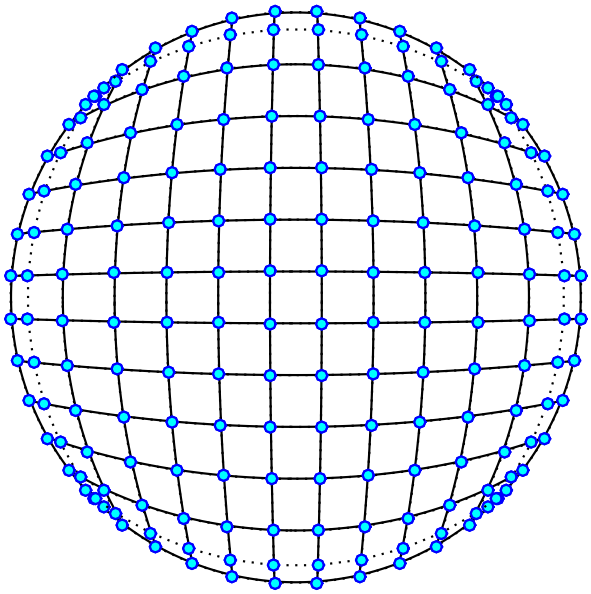

(b) Control point net and 11×11 cubic elements.

Fig. 4.8 Geometry and element mesh of a circular microplate.

Table 4.10 The first six non-dimensional natural frequencies $\bar{\omega} = \omega R^2\sqrt{\frac{\rho h}{D^\dagger}}$ of homogeneous circular microplates

ℓ/h	Theory	Mode					
		1	2	3	4	5	6
Simple support							
0	Mohammadi et al. [136]	4.9345	13.8981	25.6132	29.7198	39.9571	48.4788
	Nguyen et al. [83]	4.9304	13.8587	25.4798	29.5390	39.6331	48.0046
	RPT (Present [84])	4.9304	13.8591	25.4799	29.5456	39.6518	48.0402
	Quasi-3D (Present [84])	4.9385	13.8701	25.4983	29.5691	39.6881	48.0906
0.2	RPT (Present [84])	4.9925	14.5095	26.5426	31.1786	41.8855	50.8427
	Quasi-3D (Present [84])	5.0024	14.5206	26.5613	31.1981	41.9148	50.8808
0.4	RPT (Present [84])	5.1213	16.2743	29.4369	35.5996	47.7406	58.5547
	Quasi-3D (Present [84])	5.1365	16.2857	29.4529	35.6092	47.7542	58.5621
0.6	RPT (Present [84])	5.2422	18.8078	33.6370	41.9096	55.8684	69.6631
	Quasi-3D (Present [84])	5.2649	18.8192	33.6497	41.9065	55.8623	69.6331
0.8	RPT (Present [84])	5.3324	21.8342	38.6993	49.3881	65.3972	82.8177
	Quasi-3D (Present [84])	5.3642	21.8450	38.7080	49.3713	65.3694	82.7497
1	RPT (Present [84])	5.3954	25.1769	44.3292	57.5842	75.8223	97.1772
	Quasi-3D (Present [84])	5.4379	25.1869	44.3335	57.5538	75.7721	97.0720
Clamped support							
0	Mohammadi et al. [136]	10.2158	21.2604	34.8772	39.7706	51.0295	60.8290
	Nguyen et al. [83]	10.1839	21.1433	34.5892	39.3624	50.4385	59.9580
	RPT (Present [84])	10.1842	21.1459	34.5885	39.3832	50.4865	60.0416
	Quasi-3D (Present [84])	10.4466	21.6458	35.2774	40.2833	51.5045	61.3186
0.2	RPT (Present [84])	10.8087	22.4449	36.3961	41.8103	53.5802	63.7743
	Quasi-3D (Present [84])	11.0612	22.9236	37.1800	42.6664	54.5550	64.9738
0.4	RPT (Present [84])	12.4963	25.9527	41.2953	48.3406	61.7419	73.9729
	Quasi-3D (Present [84])	12.7255	26.3811	41.9956	49.0934	62.6149	74.9922
0.6	RPT (Present [84])	14.8897	30.9242	48.3696	57.5674	73.1139	88.5334
	Quasi-3D (Present [84])	15.0927	31.2968	48.9732	58.2073	73.8637	89.3634
0.8	RPT (Present [84])	17.7051	36.7699	56.8123	68.4011	86.4224	105.6689
	Quasi-3D (Present [84])	17.8850	37.0938	57.3265	68.9439	87.0506	106.3411
1	RPT (Present [84])	20.7715	43.1360	66.1009	80.1939	100.9243	124.3039
	Quasi-3D (Present [84])	20.9330	43.4206	66.5388	80.6591	101.4425	124.8498

$^\dagger D = \dfrac{Eh^3}{12(1-\nu^2)}$

Table 4.11 The first six non-dimensional natural frequencies $\bar{\omega} = \omega R^2 \sqrt{\frac{\rho_c h}{D_c^{\dagger}}}$ of Al/Al_2O_3 circular microplates (Mori-Tanaka scheme)

ℓ/h	Theory	Mode					
		1	2	3	4	5	6
Simple support							
0	IGA-Zenkour	3.4629	8.9254	8.9254	12.9890	12.9890	15.4780
	Quasi-3D (Present [84])	3.4132	8.8258	8.8258	12.9916	12.9916	15.3331
	RPT (Present [84])	3.3572	8.6722	8.6722	12.9121	12.9121	15.0490
0.2	IGA-Zenkour	3.5224	9.3961	9.3961	13.1894	13.1894	16.2612
	Quasi-3D (Present [84])	3.4675	9.2928	9.2928	13.1928	13.1928	16.1022
	RPT (Present [84])	3.4118	9.1595	9.1595	13.1037	13.1037	15.8706
0.4	IGA-Zenkour	3.6392	10.6411	10.6411	13.3115	13.3115	18.2644
	Quasi-3D (Present [84])	3.5698	10.5288	10.5288	13.3143	13.3143	18.1203
	RPT (Present [84])	3.5114	10.4415	10.4415	13.2326	13.2326	18.0361
0.6	IGA-Zenkour	3.7577	12.2959	12.2959	13.5601	13.5601	18.4956
	Quasi-3D (Present [84])	3.6687	12.1873	12.1873	13.5445	13.5445	18.4939
	RPT (Present [84])	3.6018	12.1378	12.1378	13.4872	13.4872	18.4475
0.8	IGA-Zenkour	3.8632	13.2220	13.2220	14.8766	14.8766	18.6662
	Quasi-3D (Present [84])	3.7546	13.2030	13.2030	14.7552	14.7552	18.6655
	RPT (Present [84])	3.6721	13.1245	13.1245	14.7850	14.7850	18.6192
1	IGA-Zenkour	3.9548	13.4288	13.4288	17.1268	17.1268	18.8623
	Quasi-3D (Present [84])	3.8303	13.4243	13.4243	16.9751	16.9751	18.8618
	RPT (Present [84])	3.9557	13.5531	13.5531	17.4735	17.4735	18.8633
Clamped support							
0	IGA-Zenkour	6.7718	12.9968	12.9968	19.8267	19.8608	21.9673
	Quasi-3D (Present [84])	6.8745	13.1770	13.1770	20.0202	20.0388	22.2840
	RPT (Present [84])	6.3384	12.4133	12.4133	19.0879	19.1363	20.9877
0.2	IGA-Zenkour	7.2163	13.9289	13.9289	21.1653	21.5889	23.7182
	Quasi-3D (Present [84])	7.3195	14.0950	14.0950	21.3095	21.7503	23.9885
	RPT (Present [84])	6.8208	13.4172	13.4172	20.5401	20.9799	22.8902
0.4	IGA-Zenkour	8.4091	16.4035	16.4035	24.6620	25.9011	25.9011
	Quasi-3D (Present [84])	8.5121	16.5390	16.5390	24.7273	25.8504	25.8504
	RPT (Present [84])	8.0909	16.0391	16.0391	24.2526	24.3345	24.3345
0.6	IGA-Zenkour	10.0860	19.8463	19.8463	25.9424	25.9424	28.6525
	Quasi-3D (Present [84])	10.1880	19.9431	19.9431	25.8948	25.8948	28.6525
	RPT (Present [84])	9.8463	19.6321	19.6321	24.3655	24.3655	28.6525
0.8	IGA-Zenkour	12.0447	23.8379	23.8379	25.9920	25.9920	28.9380
	Quasi-3D (Present [84])	12.1441	23.8850	23.8850	25.9507	25.9507	28.9380
	RPT (Present [84])	11.8741	23.7016	23.7016	24.4627	24.4627	28.9380
1	IGA-Zenkour	14.1674	26.0476	26.0476	28.1435	28.1435	29.3010
	Quasi-3D (Present [84])	14.2615	25.9953	25.9953	28.1492	28.1492	29.3010
	RPT (Present [84])	14.0568	24.4150	24.4150	28.2217	28.2217	29.3010

$^{\dagger} D_c = \dfrac{E_c h^3}{12(1-\nu_c^2)}$

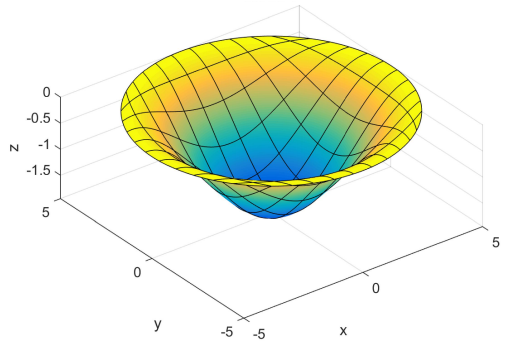

(a) $\bar{\omega}_1 = 7.3195$.

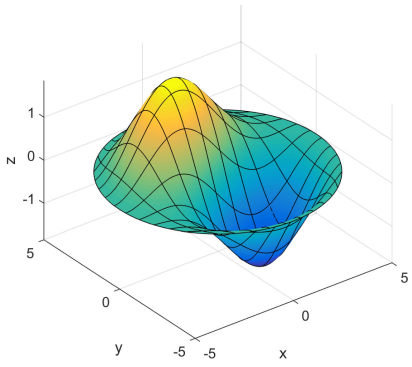

(b) $\bar{\omega}_2 = 14.0950$.

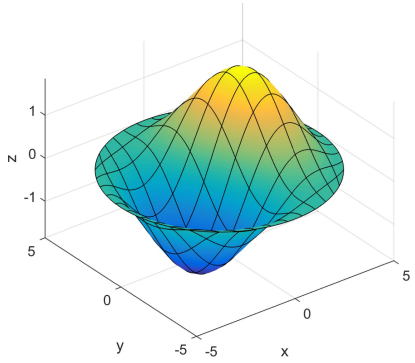

(c) $\bar{\omega}_3 = 14.0950$.

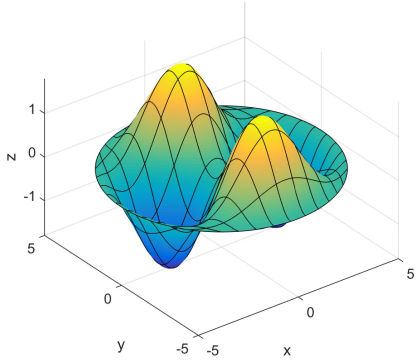

(d) $\bar{\omega}_4 = 21.3095$.

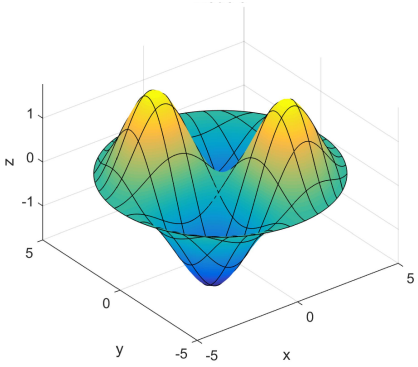

(e) $\bar{\omega}_5 = 21.7503$.

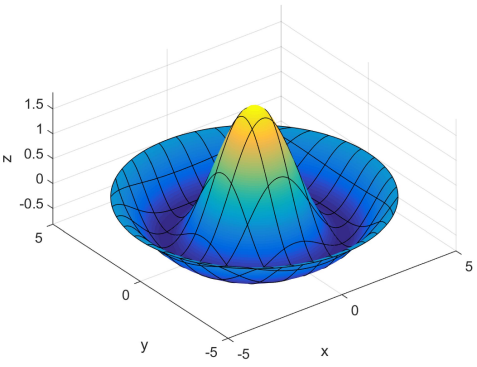

(f) $\bar{\omega}_6 = 23.9885$.

Fig. 4.9 The first six free vibration mode shapes of clamped Al/Al_2O_3 circular microplates.

4.3.4 Buckling analysis

The buckling behaviour of square and circular FG microplates is discussed. In order to validate the proposed method and models in dealing with buckling analysis, the critical buckling load of SSSS FG microplates bearing in-plane biaxial loads is firstly calculated. The results are compared with analytical solutions based on the CPT and the FSDT by Thai and Choi [36] and refined plate theory by He et al. [40]. For comparison purposes, the same material properties are used, $E_1 = 14.4$GPa, $\rho_1 = 12.2 \times 10^3$kg/m^3, $E_2 = 1.44$GPa, $\rho_2 = 1.22 \times 10^3$kg/m^3, $\nu_1 = \nu_2 = 0.38$. As can be seen in Table 4.12, although there is discrepancy for the case of thick microplates $(a/h = 5)$, the results predicted by proposed RPT theory are in good agreement with those calculated by FSDT [36] and RPT [40] as plates become thinner. On the other hand, while CPT-based solutions are significantly different compared to that of FDST and RPTs due to the ignorance of shear deformations, especially for thick plates, the proposed quasi-3D theory which takes into account normal deformation yields similar results with respect to those of shear deformable theories of FSDT and RPTs.

Table 4.13 presents the biaxial buckling analysis results of Al/Al_2O_3 square microplates. The results are calculated based on the proposed RPT and quasi-3D theories which can serve as benchmark examples for future references since no result exists in the literature. The first six non-dimensional biaxial buckling loads of Al/Al_2O_3 square plates are reported in Table 4.14 for $n = 10$ and $\ell/h = 0.2$. While the results generated from the proposed quasi-3D and IGA-based Zenkour's quasi-3D theories [76] are relatively close to each other for both types of boundary conditions, the RPT's show a clear discrepancy to the other theories, especially for the CCCC plates. This is due to the consideration of normal deformation of the quasi-3D theories. For $a/h = 5$, the first six buckling mode shapes of CCCC plates based on the proposed quasi-3D theory which are scaled up for illustration purposes are presented in Fig. 4.10.

Finally, this section ends with a number of investigations on buckling of circular FG microplates. Table 4.15 presents the results of the critical buckling loads of CCCC Al/ZrO_2-2 circular plates without considering couple stress effects. It should be noted that, for this particular attempt of comparison purpose, the material volume fractions are defined as $V_m = (0.5 - z/h)^n$ and $V_c = 1 - V_m$ [137, 138, 82, 139]. The comparison reveals that the results generated from proposed RPT are in good agreement with those of other shear deformation

Table 4.12 Comparison of non-dimensional critical buckling loads $\bar{P}_{cr} = \dfrac{P_{cr}a^2}{E_2h^3}$ of square FG microplates (rule of mixtures scheme)

ℓ/h	Theory	$a/h=5$			$a/h=10$			$a/h=20$		
		$n=0$	$n=1$	$n=10$	$n=0$	$n=1$	$n=10$	$n=0$	$n=1$	$n=10$
0	CPT [36]	19.2255	8.2145	3.8359	19.2255	8.2145	3.8359	19.2255	8.2145	3.8359
	FSDT [36]	15.3228	6.8576	2.9979	18.0746	7.8273	3.5853	18.9243	8.1142	3.7700
	RPT [40]	15.3322	6.8611	2.7672	18.0754	7.8276	3.4969	18.9243	8.1142	3.7450
	RPT (Present [84])	15.3321	6.8610	2.7702	18.0756	7.8277	3.4982	18.9244	8.1143	3.7454
	Quasi-3D (Present [84])	15.3629	7.3905	3.0118	18.1561	8.5396	3.8921	18.9675	8.8639	4.1850
0.2	CPT [36]	22.0863	9.7879	4.3560	22.0863	9.7879	4.3560	22.0863	9.7879	4.3560
	FSDT [36]	17.6150	8.1715	3.4076	20.7607	9.3241	4.0710	21.7387	9.6675	4.2809
	RPT [40]	18.0422	8.3399	3.3619	20.9025	9.3767	4.0513	21.7771	9.6815	4.2752
	RPT (Present [84])	17.8878	8.2820	3.2917	20.8497	9.3581	4.0246	21.7628	9.6766	4.2677
	Quasi-3D (Present [84])	17.7286	8.7153	3.4728	20.8583	10.0344	4.3958	21.7852	10.4160	4.7009
0.4	CPT [36]	30.6685	14.5082	5.9164	30.6685	14.5082	5.9164	30.6685	14.5082	5.9164
	FSDT [36]	24.2899	11.9922	4.6013	28.7478	13.7742	5.5151	30.1625	14.3167	5.8102
	RPT [40]	26.1539	12.7754	5.0407	29.3735	14.0232	5.6631	30.3324	14.3832	5.8505
	RPT (Present [84])	25.5457	12.5322	4.8371	29.1700	13.9459	5.5925	30.2773	14.3626	5.8312
	Quasi-3D (Present [84])	24.8060	12.6741	4.8557	28.9624	14.5168	5.9066	30.2381	15.0722	6.2486
0.6	CPT [36]	44.9723	22.3753	8.5171	44.9723	22.3753	8.5171	44.9723	22.3753	8.5171
	FSDT [36]	34.7856	17.9838	6.4804	41.8271	21.0597	7.8802	44.1369	22.0292	8.3472
	RPT [40]	39.6393	20.1658	7.7001	43.4732	21.7657	8.2906	44.5855	22.2188	8.4589
	RPT (Present [84])	38.2867	19.5858	7.3772	43.0329	21.5846	8.1871	44.4673	22.1708	8.4312
	Quasi-3D (Present [84])	36.5415	19.2256	7.1597	42.4620	21.9814	8.4246	44.3258	22.8320	8.8281
0.8	CPT [36]	64.9976	33.3892	12.1581	64.9976	33.3892	12.1581	64.9976	33.3892	12.1581
	FSDT [36]	48.2915	25.6654	8.9020	59.6657	30.9928	11.1065	63.5656	32.7517	11.8745
	RPT [40]	58.4862	30.5105	11.3322	63.1958	32.6036	11.9349	64.5348	33.1882	12.1011
	RPT (Present [84])	56.0961	29.4240	10.9005	62.4358	32.2693	11.8036	64.3321	33.0999	12.0666
	Quasi-3D (Present [84])	52.8623	28.3151	10.3843	61.3467	32.4199	11.9498	64.0474	33.6948	12.4394
1	CPT [36]	90.7444	47.5499	16.8393	90.7444	47.5499	16.8393	-	-	-
	FSDT [36]	63.8913	34.4981	11.7042	81.8269	43.3274	15.1152	-	-	-
	RPT [40]	82.6938	43.8094	15.9522	88.5416	46.5372	16.6033	90.1804	47.2914	16.7793
	RPT (Present [84])	78.9675	42.0388	15.4071	87.3775	45.9981	16.4431	89.8715	47.1494	16.7376
	Quasi-3D (Present [84])	73.6925	39.8872	14.5287	85.6043	45.8223	16.4819	89.4018	47.6596	17.0825

Table 4.13 Non-dimensional critical buckling load $\bar{P}_{cr} = \dfrac{P_{cr}a^2}{D_m^{\dagger}}$ of Al/Al_2O_3 square microplates (Mori-Tanaka scheme)

BC	a/h	ℓ/h	$n=0$		$n=1$		$n=10$	
			RPT	Quasi-3D	RPT	Quasi-3D	RPT	Quasi-3D
SSSS	5	0	87.4747	86.5475	35.0795	35.6610	21.7236	21.7189
		0.2	103.6359	101.8797	42.3816	42.6185	25.4909	25.2307
		0.4	152.0215	147.6312	64.2668	63.3902	36.7873	35.7417
		0.6	232.4351	223.1633	100.6957	97.7189	55.6034	53.1891
		0.8	344.7280	327.6683	151.6424	145.2904	81.9336	77.4961
		1	488.8378	460.3907	217.0988	205.8260	115.7764	108.5941
	20	0	105.6668	105.6221	42.0033	43.4065	27.5182	27.8578
		0.2	123.5339	123.4102	49.9504	51.3272	31.5521	31.8705
		0.4	177.1295	176.7715	73.7907	75.0881	43.6520	43.9085
		0.6	266.4425	265.6972	113.5226	114.6856	63.8152	63.9707
		0.8	391.4648	390.1733	169.1451	170.1141	92.0401	92.0558
		1	552.1931	550.1813	240.6580	241.3659	128.3267	128.1618
	100	0	107.0958	107.1271	42.5423	44.0165	27.9978	28.3566
		0.2	125.0926	125.1206	50.5370	52.0102	32.0486	32.4065
		0.4	179.0825	179.1009	74.5212	75.9913	44.2009	44.5563
		0.6	269.0653	269.0682	114.4947	115.9596	64.4546	64.8061
		0.8	395.0406	395.0223	170.4576	171.9154	92.8097	93.1557
		1	557.0082	556.9633	242.4098	243.8584	129.2661	129.6052
CCCC	5	0	178.2578	188.3478	72.2150	78.0421	42.1220	45.4860
		0.2	206.9297	215.7331	85.4028	90.6731	49.1101	52.1032
		0.4	292.6287	295.5433	124.8630	127.4320	69.9984	71.1001
		0.6	435.0030	424.8837	190.5274	187.0650	104.7011	101.8084
		0.8	633.8611	601.6084	282.3839	268.7548	153.1709	144.0664
		1	889.1171	823.8983	400.4310	371.8457	215.3906	197.7752
	20	0	273.9507	288.6976	109.0237	117.3906	70.8926	75.2177
		0.2	308.7803	323.9291	124.5481	133.0578	78.8262	83.2085
		0.4	413.0833	429.0109	171.0330	179.8054	102.5575	107.0378
		0.6	586.6304	603.0356	248.3764	257.2793	141.9833	146.4815
		0.8	829.3607	845.5938	356.5558	365.3387	197.0586	201.4295
		1	1141.2885	1156.5929	495.5793	503.9582	267.7793	271.8584
	100	0	283.7646	292.2008	112.7294	119.3117	74.1644	77.0743
		0.2	319.1326	327.9091	128.4414	135.1344	82.1289	85.1055
		0.4	425.0550	434.6081	175.4917	182.4322	105.9838	109.1182
		0.6	601.2918	611.6685	253.7742	260.9696	145.6726	148.9836
		0.8	847.7694	858.8291	363.2623	370.6627	201.1735	204.6383
		1	1164.4998	1176.0787	503.9643	511.5167	272.4865	276.0730

$^{\dagger}D_m = \dfrac{E_m h^3}{12(1-\nu_m^2)}$

Table 4.14 The first six non-dimensional buckling loads $\bar{P} = \dfrac{Pa^2}{D_m}$ of Al/Al_2O_3 square microplates, $n = 10$, $\ell/h = 0.2$ (Mori-Tanaka scheme)

BC	a/h	Theory	Mode					
			1	2	3	4	5	6
SSSS	5	IGA-Zenkour	25.4064	47.0158	47.0158	62.7947	66.4706	66.4706
		Quasi-3D (Present [84])	25.2307	46.2828	46.2828	61.4689	64.8256	64.8256
		RPT (Present [84])	25.4909	47.9306	47.9306	64.7895	68.7456	68.7456
	10	IGA-Zenkour	30.3554	67.5835	67.5835	101.6321	115.5866	115.5866
		Quasi-3D (Present [84])	30.2890	67.2254	67.2254	100.9300	114.4706	114.4706
		RPT (Present [84])	30.1012	67.3570	67.3570	101.9693	116.1512	116.1512
	20	IGA-Zenkour	31.8815	76.0319	76.0319	121.4313	143.5095	143.5095
		Quasi-3D (Present [84])	31.8705	75.8988	75.8988	121.1662	143.0021	143.0021
		RPT (Present [84])	31.5521	75.2628	75.2628	120.4131	142.2468	142.2468
	100	IGA-Zenkour	32.3844	79.0722	79.0722	129.2976	155.1773	155.1773
		Quasi-3D (Present [84])	32.4065	79.1198	79.1198	129.3662	155.2457	155.2457
		RPT (Present [84])	32.0486	78.2296	78.2296	127.9519	153.4678	153.4678
CCCC	5	IGA-Zenkour	50.6557	66.0350	66.0350	78.0114	80.2597	84.0819
		Quasi-3D (Present [84])	52.1032	66.3156	66.3156	77.2179	78.9774	84.1043
		RPT (Present [84])	49.1101	66.7907	66.7907	80.3088	82.9464	85.5400
	10	IGA-Zenkour	74.8665	114.2196	114.2196	146.4170	160.1781	172.6816
		Quasi-3D (Present [84])	75.4661	115.7598	115.7598	147.8696	161.3725	174.2442
		RPT (Present [84])	70.1001	110.6293	110.6293	144.4919	158.8413	167.4729
	20	IGA-Zenkour	83.8952	140.5084	140.5084	191.9601	219.4306	239.0973
		Quasi-3D (Present [84])	83.2085	140.4610	140.4610	192.6237	220.3776	239.1104
		RPT (Present [84])	78.8262	133.9531	133.9531	185.0964	211.8925	227.4324
	100	IGA-Zenkour	85.2475	149.0723	149.0723	210.8794	246.4373	267.8293
		Quasi-3D (Present [84])	85.1055	148.8861	148.8861	210.7133	246.2408	267.4391
		RPT (Present [84])	82.1289	143.8128	143.8128	203.9109	237.9639	257.7571

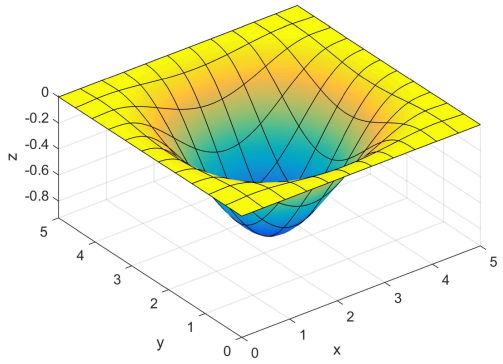

(a) $\bar{P}_1 = 52.1032$.

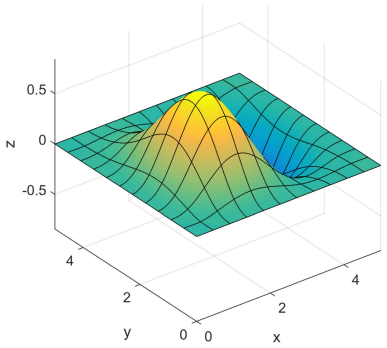

(b) $\bar{P}_2 = 66.3156$.

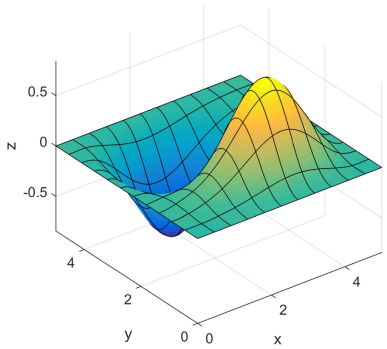

(c) $\bar{P}_3 = 66.3156$.

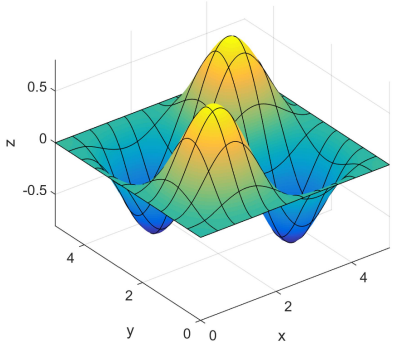

(d) $\bar{P}_4 = 77.2179$.

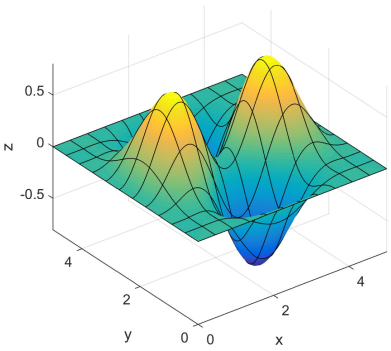

(e) $\bar{P}_5 = 78.9774$.

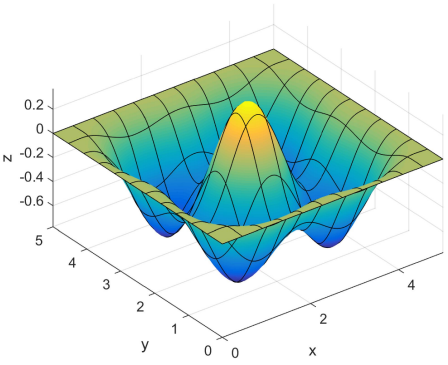

(f) $\bar{P}_6 = 84.1043$.

Fig. 4.10 The first six buckling mode shapes of Al/Al_2O_3 CCCC square microplates.

theories even with relatively thick and thick plates. The proposed quasi-3D approach yields slightly different results in all cases.

Table 4.16 presents the non-dimensional critical buckling loads of Al/Al_2O_3 circular microplates with various boundary conditions based on the proposed RPT and quasi-3D theories. The difference between the two theories is relatively small for both boundary conditions. The effects of the material index n and material length scale ratio ℓ/h on the critical buckling loads of simple and clamped supports of Al/Al_2O_3 circular microplates with $h/R = 0.2$ are illustrated in Fig. 4.11. Fig. 4.12 presents the variation of the normalised critical buckling loads of simply-supported Al/Al_2O_3 circular microplates with respect to the material length scale ratio ℓ/h and plate's aspect ratio a/h with different value of material index n.

The first six buckling loads of Al/Al_2O_3 circular microplates with various aspect ratios for $n = 1$ and $\ell/h = 0.6$ along with the results generated from Zenkour's quasi-3D theory [76] using proposed IGA approach are reported in Table 4.17. The first six buckling mode shapes corresponding to simply-supported circular microplates for $h/R = 0.2$ based on proposed quasi-3D theory are presented in Fig. 4.13.

Table 4.15 Comparison of non-dimensional critical buckling loads $\bar{P_{cr}} = \dfrac{P_{cr}R^2}{D_m}$ of CCCC Al/ZrO_2-2 circular plates (rule of mixtures scheme)

n	Theory	h/R			
		0.1	0.2	0.25	0.3
0	TSDT [137]	14.089	12.574	11.638	10.670
	UTSDT [138]	14.089	12.575	11.639	10.670
	TSDT [139]	14.1089	12.5914	11.6540	10.6842
	RPT [82]	14.2023	12.7281	11.8143	10.8666
	RPT (Present [84])	14.0932	12.5776	11.6409	10.6719
	Quasi-3D (Present [84])	14.8264	13.4557	12.4564	11.3775
0.5	TSDT [137]	19.411	17.311	16.013	14.672
	UTSDT [138]	19.413	17.310	16.012	14.672
	TSDT [139]	19.4391	17.3327	16.0334	14.6910
	RPT [82]	19.5663	17.5180	16.2506	14.9381
	RPT (Present [84])	19.4169	17.3133	16.0153	14.6740
	Quasi-3D (Present [84])	20.5166	18.6074	17.2206	15.7222
2	TSDT [137]	23.074	20.803	19.377	17.882
	UTSDT [138]	23.075	20.805	19.378	17.881
	TSDT [139]	23.1062	20.8319	19.4033	17.9060
	RPT [82]	23.2592	21.0569	19.6687	18.2099
	RPT (Present [84])	23.0809	20.8088	19.3812	17.8848
	Quasi-3D (Present [84])	24.4332	22.3510	20.8035	19.1161
5	TSDT [137]	25.439	22.971	21.414	19.780
	UTSDT [138]	25.442	22.969	21.412	19.778
	TSDT [139]	25.4743	22.9992	21.4407	19.8043
	RPT [82]	25.6418	23.2426	21.7268	20.1313
	RPT (Present [84])	25.4469	22.9742	21.4168	19.7813
	Quasi-3D (Present [84])	26.8812	24.6195	22.9303	21.0878
10	TSDT [137]	27.133	24.423	22.725	20.948
	UTSDT [138]	27.131	24.422	22.725	20.949
	TSDT [139]	27.1684	24.4542	22.7536	20.9750
	RPT [82]	27.3429	24.6994	23.0389	21.2986
	RPT (Present [84])	27.1395	24.4287	22.7297	20.9524
	Quasi-3D (Present [84])	28.6197	26.1483	24.3140	22.3196

Table 4.16 Non-dimensional critical buckling loads $\bar{P_{cr}} = \dfrac{P_{cr}R^2}{D_m}$ of Al/Al_2O_3 circular microplates (Mori-Tanaka scheme)

h/R	ℓ/h	$n=0$		$n=1$		$n=10$	
		RPT	Quasi-3D	RPT	Quasi-3D	RPT	Quasi-3D
Simple support							
0.1	0	22.5182	22.6953	9.5368	9.7960	5.9574	6.0309
	0.2	23.0489	23.2627	9.8179	10.0793	6.0876	6.1617
	0.4	24.1022	24.4172	10.3474	10.6292	6.3543	6.4360
	0.6	25.0682	25.5337	10.8125	11.1391	6.6130	6.7163
	0.8	25.7985	26.4629	11.1543	11.5512	6.8182	6.9619
	1	26.3291	27.2420	11.3981	11.8897	6.9718	7.1752
0.2	0	21.7456	22.0263	9.2059	9.4510	5.6942	5.7510
	0.2	22.2719	22.5928	9.4873	9.7327	5.8318	5.8833
	0.4	23.2739	23.7059	9.9893	10.2520	6.1019	6.1509
	0.6	24.2066	24.8190	10.4423	10.7545	6.3676	6.4377
	0.8	24.9581	25.8386	10.8003	11.2074	6.5891	6.7170
	1	25.5480	26.7897	11.0777	11.6254	6.7647	6.9866
0.3	0	20.5707	20.8606	8.7033	8.9036	5.3041	5.3287
	0.2	21.0993	21.4128	8.9860	9.1777	5.4526	5.4621
	0.4	22.0854	22.4669	9.4810	9.6686	5.7409	5.7276
	0.6	23.0439	23.5641	9.9511	10.1693	6.0352	6.0281
	0.8	23.8746	24.6485	10.3517	10.6610	6.2927	6.3431
	1	24.5707	25.7228	10.6823	11.1443	6.5055	6.6623
Clamped support							
0.1	0	76.5059	80.4859	30.4539	32.7398	19.7743	20.9413
	0.2	86.3696	90.4095	34.8524	37.1578	22.0235	23.1967
	0.4	115.9595	120.0466	48.0474	50.3612	28.7616	29.9236
	0.6	165.2737	169.2564	70.0379	72.3004	39.9728	41.0821
	0.8	234.3115	237.9906	100.8235	102.9597	55.6486	56.6598
	1	323.0727	326.2293	140.4042	142.3316	75.7879	76.6551
0.2	0	68.2782	73.0452	27.3245	29.8617	17.1442	18.6240
	0.2	77.6521	82.3859	31.5460	34.0702	19.3412	20.7979
	0.4	105.7687	110.0650	44.2098	46.5462	25.9122	27.1925
	0.6	152.6199	155.7501	65.3154	67.1544	36.8218	37.7110
	0.8	218.1997	219.2330	94.8629	95.8167	52.0495	52.3297
	1	302.5060	300.3159	132.8523	132.4584	71.5905	71.0373
0.3	0	57.9331	61.7636	23.3438	25.4648	14.0464	15.3047
	0.2	66.6302	70.2136	27.3083	29.3268	16.1359	17.3213
	0.4	92.7032	95.0207	39.2004	40.6571	22.3875	23.1508
	0.6	136.1160	135.6444	59.0182	59.2280	32.7704	32.6634
	0.8	196.8399	191.6493	86.7603	84.8742	47.2643	45.8312
	1	274.8619	262.6208	122.4264	117.4429	65.8628	62.6312

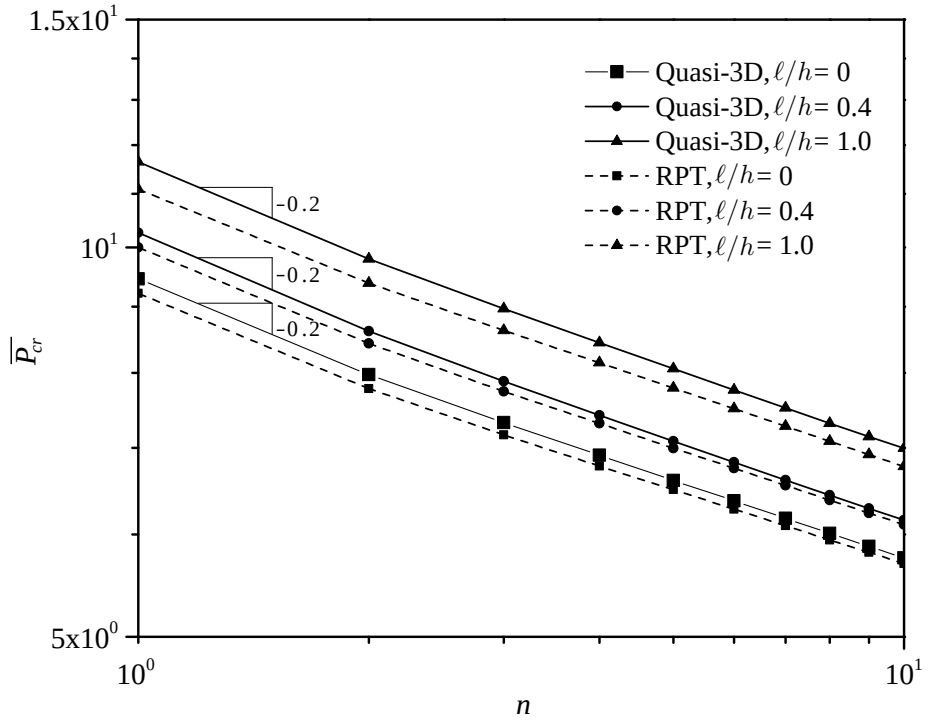

(a) Simply support.

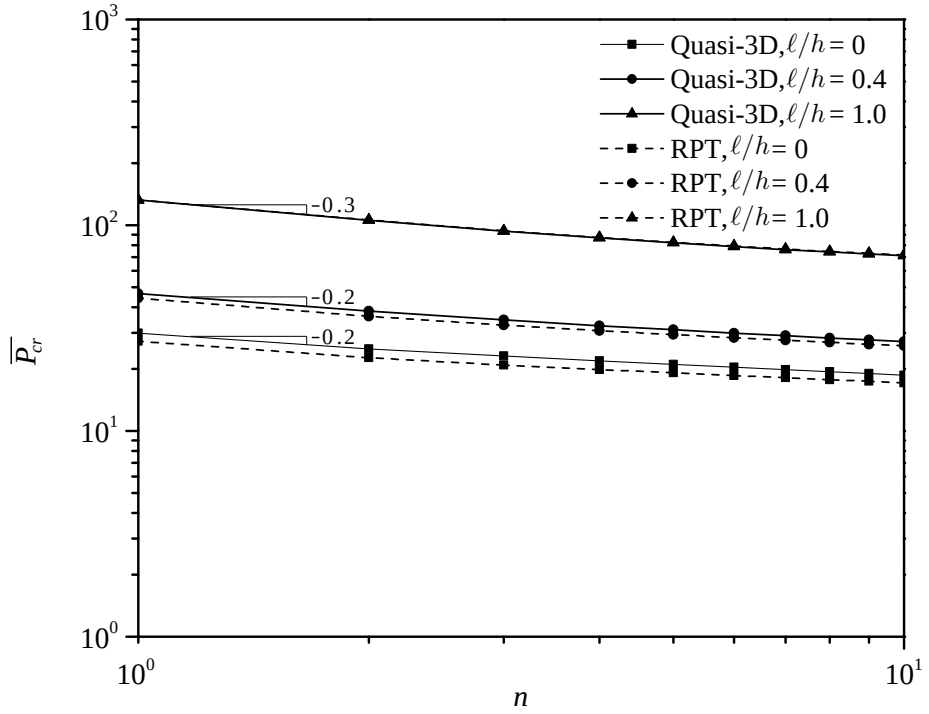

(b) Clamped support.

Fig. 4.11 Effects of material index n and material length scale ratio ℓ/h on the critical buckling loads of Al/Al_2O_3 circular microplates, $h/R = 0.2$ (Mori-Tanaka scheme).

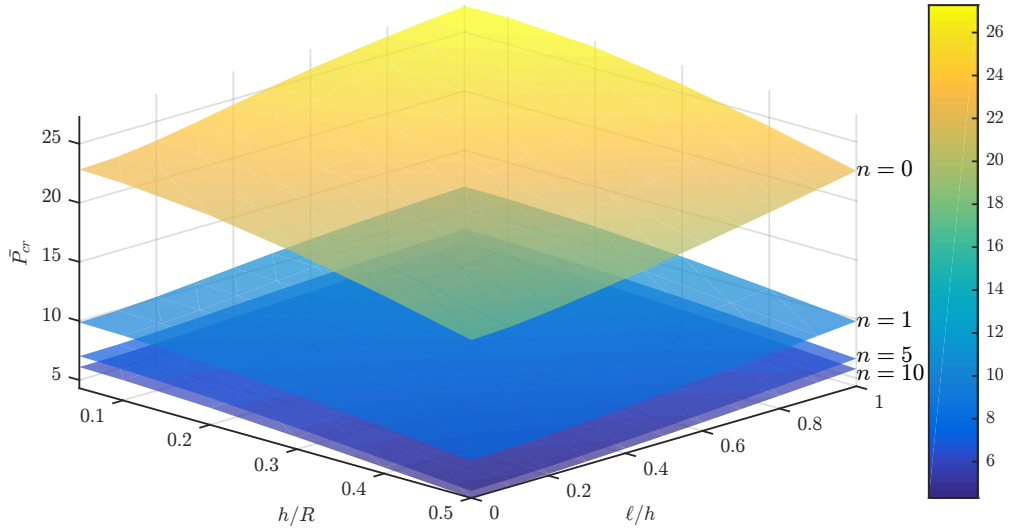

Fig. 4.12 Variation of the critical buckling loads of Al/Al_2O_3 circular microplates (Mori-Tanaka scheme).

Table 4.17 The first six non-dimensional buckling loads $\bar{P} = \dfrac{PR^2}{D_m}$ of Al/Al_2O_3 circular microplates, $n = 1$, $\ell/h = 0.6$ (Mori-Tanaka scheme)

BC	h/R	Theory	Mode					
			1	2	3	4	5	6
Simple support	0.1	IGA-Zenkour	11.4689	54.8031	54.8031	95.3143	123.2488	129.6396
		Quasi-3D (Present [84])	11.1391	54.0884	54.0884	93.7842	122.0854	128.1298
		RPT (Present [84])	10.8125	53.6215	53.6215	93.3944	122.3489	128.3281
	0.2	IGA-Zenkour	11.3113	50.7663	50.7663	83.1176	107.1987	110.9343
		Quasi-3D (Present [84])	10.7545	49.5358	49.5358	80.6606	104.8026	108.1436
		RPT (Present [84])	10.4423	50.2378	50.2378	83.3889	109.1766	112.9355
	0.3	IGA-Zenkour	10.8014	45.2015	45.2015	69.1649	89.4125	90.9795
		Quasi-3D (Present [84])	10.1693	43.6917	43.6917	66.3080	86.1911	87.4685
		RPT (Present [84])	9.9511	45.6739	45.6739	71.5215	93.8041	95.5819
Clamped support	0.1	IGA-Zenkour	72.6509	126.0657	126.0657	172.3464	205.4419	222.4846
		Quasi-3D (Present [84])	72.3004	125.7477	125.7477	171.5372	205.0589	221.0537
		RPT (Present [84])	70.0379	123.1185	123.1185	169.2944	203.3425	218.6139
	0.2	IGA-Zenkour	66.8949	108.9270	108.9270	140.4481	166.8569	175.2599
		Quasi-3D (Present [84])	67.1544	108.3685	108.3685	138.0488	164.4947	172.3137
		RPT (Present [84])	65.3154	109.4813	109.4813	143.4150	171.7706	179.5962
	0.3	IGA-Zenkour	58.9576	90.1444	90.1444	110.5155	131.5270	134.2574
		Quasi-3D (Present [84])	59.2280	88.4285	88.4285	106.6289	127.0395	129.6436
		RPT (Present [84])	59.0182	93.6789	93.6789	117.0824	140.3857	143.1361

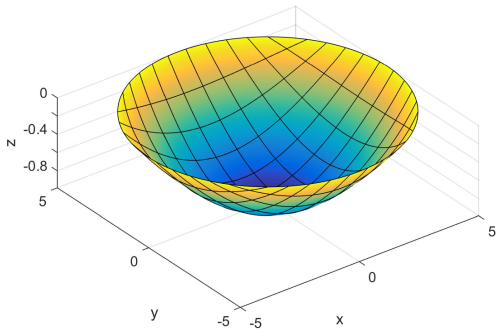

(a) $\bar{P}_1 = 10.7545$.

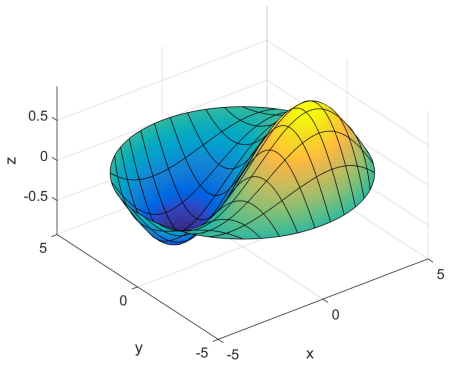

(b) $\bar{P}_2 = 49.5358$.

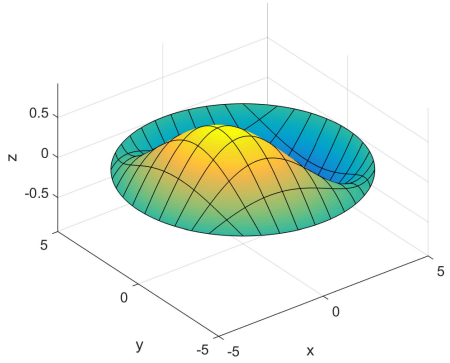

(c) $\bar{P}_3 = 49.5358$.

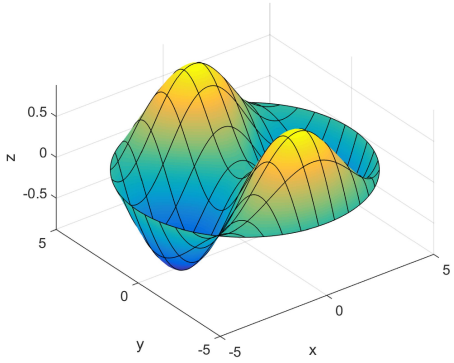

(d) $\bar{P}_4 = 80.6606$.

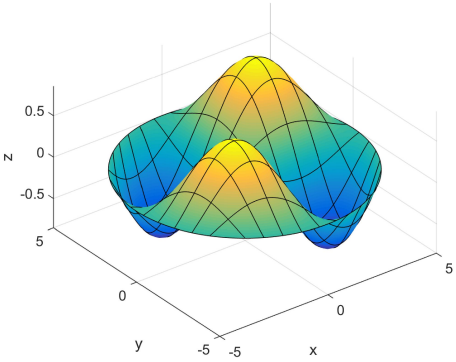

(e) $\bar{P}_5 = 104.8026$.

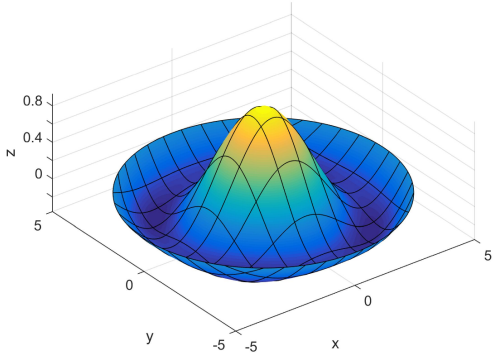

(f) $\bar{P}_6 = 108.1436$.

Fig. 4.13 The first six buckling mode shapes of simply-supported Al/Al_2O_3 circular microplates.

Chapter 5

Geometrically nonlinear analysis of small-scale plates[1]

In this chapter, the geometrically nonlinear analyses of microplates based on IGA will be presented. While the microplates' size-dependent effects are efficiently captured by a simple modified couple stress theory with only one material length scale parameter, the four-unknown refined plate theory is employed to establish the displacement fields of the plates which are eventually used to derive the nonlinear von Kámán strains. The NURBS-based isogeometric analysis is used to construct high-continuity elements that are essentially required in the modified couple stress theory and refined plate theory. The iterative Newton-Raphson algorithm is employed to solve the nonlinear problems. The numerical results include nonlinear analysis of bending problems for different geometry configurations of microplates.

5.1 Kinematics of FG microplates

5.1.1 Geometrically nonlinear refined plate theory

Using similar geometry as shown in Fig. 2.1, the four-unknown displacement field of the plate, for $z \in \left[-\frac{h}{2}, \frac{h}{2}\right]$, can be expressed as

$$u(x,y,z) = u_0(x,y) - z w_{b,x}(x,y) + g(z)\, w_{s,x}(x,y), \tag{5.1a}$$

$$v(x,y,z) = v_0(x,y) - z w_{b,y}(x,y) + g(z)\, w_{s,y}(x,y), \tag{5.1b}$$

[1]The results in this chapter have been published in Nguyen et al. [140]

$$w(x,y,z) = w_b(x,y) + w_s(x,y), \tag{5.1c}$$

The general nonlinear strains can be derived from the displacement fields as

$$\varepsilon_{ij} = \frac{1}{2}\left(u_{i,j} + u_{j,i}\right) + \frac{1}{2}u_{k,i}u_{k,j}. \tag{5.2}$$

If the small strain assumptions are applied, the components of the displacement gradients are neglected. Meanwhile, assuming that the rotations of the transverse normals are moderate, the terms of derivatives of transverse displacement, $(w_{,x})^2, (w_{,y})^2, w_{,x}w_{,y}$, are small but not negligible [141]. In such case, small strains and moderate rotations, the displacement-strain relations associated with the RPT with the von Kármán strains can be expressed as follows

$$\boldsymbol{\varepsilon} = \boldsymbol{\varepsilon}_0 + z\boldsymbol{\kappa}_b + g(z)\,\boldsymbol{\kappa}_s, \tag{5.3a}$$

$$\boldsymbol{\gamma} = \left[1 + g'(z)\right]\boldsymbol{\varepsilon}_s = f'(z)\,\boldsymbol{\varepsilon}_s, \tag{5.3b}$$

where

$$\boldsymbol{\varepsilon} = \begin{bmatrix} \varepsilon_x & \varepsilon_y & \gamma_{xy} \end{bmatrix}^T, \tag{5.4a}$$

$$\boldsymbol{\gamma} = \begin{bmatrix} \gamma_{xz} & \gamma_{yz} \end{bmatrix}^T, \tag{5.4b}$$

and the in-plane, bending and shear strains are expressed as

$$\boldsymbol{\varepsilon}_0 = \boldsymbol{\varepsilon}_0^L + \boldsymbol{\varepsilon}_0^{NL}, \quad \boldsymbol{\kappa}_b = -\begin{bmatrix} w_{b,xx} \\ w_{b,yy} \\ 2w_{b,xy} \end{bmatrix}, \quad \boldsymbol{\kappa}_s = \begin{bmatrix} w_{s,xx} \\ w_{s,yy} \\ 2w_{s,xy} \end{bmatrix}, \quad \boldsymbol{\varepsilon}_s = \begin{bmatrix} w_{s,x} \\ w_{s,y} \end{bmatrix} \tag{5.5}$$

with the linear and nonlinear components of the in-plane strains are defined as

$$\boldsymbol{\varepsilon}_0^L = \begin{bmatrix} u_{0,x} \\ v_{0,y} \\ u_{0,y} + v_{0,x} \end{bmatrix}, \quad \boldsymbol{\varepsilon}_0^{NL} = \frac{1}{2}\mathbf{A}_{\boldsymbol{\vartheta}}\,\boldsymbol{\vartheta}, \tag{5.6}$$

where

$$\mathbf{A}_{\boldsymbol{\vartheta}} = \begin{bmatrix} w_{b,x} + w_{s,x} & 0 \\ 0 & w_{b,y} + w_{s,y} \\ w_{b,y} + w_{s,y} & w_{b,x} + w_{s,x} \end{bmatrix}, \quad \boldsymbol{\vartheta} = \begin{bmatrix} w_{b,x} + w_{s,x} \\ w_{b,y} + w_{s,y} \end{bmatrix}. \tag{5.7}$$

By using Eqs. (2.2b) , (2.3) and (5.1), the couple stress terms of rotation vector and curvature tensor can be obtained as follows

$$\boldsymbol{\theta} = \begin{bmatrix} \theta_1 \\ \theta_2 \\ \theta_3 \end{bmatrix} = \frac{1}{2} \begin{bmatrix} 2w_{b,y} - (g'-1)\, w_{s,y} \\ -2w_{b,x} + (g'-1)\, w_{s,x} \\ v_{0,x} - u_{0,y} \end{bmatrix}, \tag{5.8a}$$

$$\boldsymbol{\chi} = \begin{bmatrix} \boldsymbol{\chi}_b \\ \boldsymbol{\chi}_s \end{bmatrix} = \begin{bmatrix} \boldsymbol{\chi}_{b0} \\ \boldsymbol{\chi}_{s0} \end{bmatrix} + \begin{bmatrix} g'\boldsymbol{\chi}_{b1} \\ g''\boldsymbol{\chi}_{s2} \end{bmatrix}, \tag{5.8b}$$

where

$$\boldsymbol{\chi}_b = \begin{bmatrix} \chi_{11} \\ \chi_{22} \\ \chi_{12} \end{bmatrix}, \quad \boldsymbol{\chi}_s = \begin{bmatrix} \chi_{13} \\ \chi_{23} \end{bmatrix}, \tag{5.9a}$$

$$\boldsymbol{\chi}_{b0} = \frac{1}{4} \begin{bmatrix} 4w_{b,xy} + 2w_{s,xy} \\ -4w_{b,xy} - 2w_{s,xy} \\ 2\left(-w_{b,xx} + w_{b,yy}\right) + \left(-w_{s,xx} + w_{s,yy}\right) \end{bmatrix}, \quad \boldsymbol{\chi}_{b1} = \frac{1}{4} \begin{bmatrix} -2w_{s,xy} \\ 2w_{s,xy} \\ w_{s,xx} - w_{s,yy} \end{bmatrix}, \tag{5.9b}$$

$$\boldsymbol{\chi}_{s0} = \frac{1}{4} \begin{bmatrix} -u_{0,xy} + v_{0,xx} \\ -u_{0,yy} + v_{0,xy} \end{bmatrix}, \quad \boldsymbol{\chi}_{s2} = \frac{1}{4} \begin{bmatrix} -w_{s,y} \\ w_{s,x} \end{bmatrix}. \tag{5.9c}$$

It is worth commenting that in this particular case using the displacement field in Eq. (5.1), the curvature component of χ_{33} is identically zero. Having the strain terms and the curvature tensor derived, the classical and modified couple stress constitutive relations of FG microplates can be obtained as follows

$$\begin{Bmatrix} \sigma_x \\ \sigma_y \\ \sigma_{xy} \\ \sigma_{xz} \\ \sigma_{yz} \end{Bmatrix} = \begin{bmatrix} Q_{11} & Q_{12} & 0 & 0 & 0 \\ Q_{21} & Q_{22} & 0 & 0 & 0 \\ 0 & 0 & Q_{66} & 0 & 0 \\ 0 & 0 & 0 & Q_{55} & 0 \\ 0 & 0 & 0 & 0 & Q_{44} \end{bmatrix} \begin{Bmatrix} \varepsilon_x \\ \varepsilon_y \\ \gamma_{xy} \\ \gamma_{xz} \\ \gamma_{yz} \end{Bmatrix}, \tag{5.10a}$$

$$\left\{\begin{array}{c} m_{11} \\ m_{22} \\ m_{33} \\ m_{12} \\ m_{13} \\ m_{23} \end{array}\right\} = \left[\begin{array}{cccccc} 2G_e\ell^2 & 0 & 0 & 0 & 0 & 0 \\ 0 & 2G_e\ell^2 & 0 & 0 & 0 & 0 \\ 0 & 0 & 2G_e\ell^2 & 0 & 0 & 0 \\ 0 & 0 & 0 & 2G_e\ell^2 & 0 & 0 \\ 0 & 0 & 0 & 0 & 2G_e\ell^2 & 0 \\ 0 & 0 & 0 & 0 & 0 & 2G_e\ell^2 \end{array}\right] \left\{\begin{array}{c} \chi_{11} \\ \chi_{22} \\ \chi_{33} \\ \chi_{12} \\ \chi_{13} \\ \chi_{23} \end{array}\right\}, \tag{5.10b}$$

where

$$Q_{11} = Q_{22} = \frac{E_e(z)}{1-(\nu_e(z))^2}, \quad Q_{12} = Q_{21} = \frac{E_e(z)\,\nu_e(z)}{1-(\nu_e(z))^2}, \quad Q_{44} = Q_{55} = Q_{66} = \frac{E_e(z)}{2(1+\nu_e(z))}, \tag{5.11a}$$

$$G_e = \frac{E_e(z)}{2(1+\nu_e(z))}. \tag{5.11b}$$

Meanwhile, the classical stress resultants are calculated as

$$\left[\begin{array}{c} \mathbf{N} \\ \mathbf{M}^b \\ \mathbf{M}^s \end{array}\right] = \mathbf{D}^b \boldsymbol{\varepsilon}_b, \tag{5.12a}$$

$$\mathbf{Q} = \mathbf{D}^s \boldsymbol{\varepsilon}_s, \tag{5.12b}$$

where

$$\mathbf{N} = \left[\begin{array}{c} N_x \\ N_y \\ N_{xy} \end{array}\right], \quad \mathbf{M}^b = \left[\begin{array}{c} M_x^b \\ M_y^b \\ M_{xy}^b \end{array}\right], \quad \mathbf{M}^s = \left[\begin{array}{c} M_x^s \\ M_y^s \\ M_{xy}^s \end{array}\right], \quad \mathbf{Q} = \left[\begin{array}{c} Q_{xz} \\ Q_{yz} \end{array}\right], \tag{5.13a}$$

$$\boldsymbol{\varepsilon}_b = \left[\begin{array}{c} \boldsymbol{\varepsilon}_0 \\ \boldsymbol{\kappa}_b \\ \boldsymbol{\kappa}_s \end{array}\right], \quad \mathbf{D}^b = \left[\begin{array}{ccc} \mathbf{A} & \mathbf{B} & \mathbf{E} \\ \mathbf{B} & \mathbf{D} & \mathbf{F} \\ \mathbf{E} & \mathbf{F} & \mathbf{H} \end{array}\right], \quad \mathbf{D}^s = \left[\begin{array}{cc} D_{44}^s & 0 \\ 0 & D_{55}^s \end{array}\right], \tag{5.13b}$$

and the components of the material matrices are defined as follows

$$\left(A_{ij}, B_{ij}, D_{ij}, E_{ij}, F_{ij}, H_{ij}\right) = \int_{-h/2}^{h/2} \left[1, z, z^2, g(z), zg(z), g^2(z)\right] \bar{Q}_{ij} dz, \tag{5.14a}$$

$$D_{ij}^{s} = \int_{-h/2}^{h/2} \left[1 + g'(z)\right]^2 \hat{Q}_{ij} dz, \tag{5.14b}$$

$$\bar{\mathbf{Q}} = \begin{bmatrix} Q_{11} & Q_{12} & 0 \\ Q_{21} & Q_{22} & 0 \\ 0 & 0 & Q_{66} \end{bmatrix}, \tag{5.14c}$$

$$\hat{\mathbf{Q}} = \begin{bmatrix} Q_{44} & 0 \\ 0 & Q_{55} \end{bmatrix}. \tag{5.14d}$$

Similarly, the couple stress components are defined by

$$\begin{Bmatrix} \mathbf{N}^c \\ \mathbf{R}^c \end{Bmatrix} = \mathbf{D}_c^b \boldsymbol{\chi}_b^c, \tag{5.15a}$$

$$\begin{Bmatrix} \mathbf{P}^c \\ \mathbf{T}^c \end{Bmatrix} = \mathbf{D}_c^s \boldsymbol{\chi}_s^c, \tag{5.15b}$$

where

$$\boldsymbol{\chi}_b^c = \begin{bmatrix} \boldsymbol{\chi}_{b0} \\ \boldsymbol{\chi}_{b1} \end{bmatrix}, \quad \boldsymbol{\chi}_s^c = \begin{bmatrix} \boldsymbol{\chi}_{s0} \\ \boldsymbol{\chi}_{s2} \end{bmatrix}, \quad \mathbf{D}_c^b = \begin{bmatrix} \mathbf{A}^c & \mathbf{B}^c \\ \mathbf{B}^c & \mathbf{D}^c \end{bmatrix}, \quad \mathbf{D}_c^s = \begin{bmatrix} \mathbf{X}^c & \mathbf{Y}^c \\ \mathbf{Y}^c & \mathbf{Z}^c \end{bmatrix}, \tag{5.16}$$

and the components of the material matrices are calculated as

$$\left(A_{ij}^c, B_{ij}^c, D_{ij}^c\right) = \int_{-h/2}^{h/2} \left(1, g'(z), \left[g'(z)\right]^2\right) \bar{G}_{ij} dz, \tag{5.17a}$$

$$\left(X_{ij}^c, Y_{ij}^c, Z_{ij}^c\right) = \int_{-h/2}^{h/2} \left(1, g''(z), \left[g''(z)\right]^2\right) \hat{G}_{ij} dz, \tag{5.17b}$$

$$\bar{\mathbf{G}} = 2G_e \ell^2 \begin{bmatrix} 1 & 0 & 0 \\ 0 & 1 & 0 \\ 0 & 0 & 1 \end{bmatrix}, \tag{5.17c}$$

$$\hat{\mathbf{G}} = 2G_e \ell^2 \begin{bmatrix} 1 & 0 \\ 0 & 1 \end{bmatrix}. \tag{5.17d}$$

After applying the derivation of the Hamilton's principal and weak formulation, the weak form of the nonlinear bending problem of FG microplates subjected

to transverse load q_0 can be briefly expressed as [84]

$$\int_{\Omega} \delta\boldsymbol{\varepsilon}_b^T \mathbf{D}^b \boldsymbol{\varepsilon}_b d\Omega + \int_{\Omega} \delta\boldsymbol{\varepsilon}_s^T \mathbf{D}^s \boldsymbol{\varepsilon}_s d\Omega + \int_{\Omega} (\delta\boldsymbol{\chi}_b^c)^T \mathbf{D}_c^b \boldsymbol{\chi}_b^c d\Omega + \int_{\Omega} (\delta\boldsymbol{\chi}_s^c)^T \mathbf{D}_c^s \boldsymbol{\chi}_s^c d\Omega = \int_{\Omega} \delta w q_0 d\Omega. \tag{5.18}$$

5.2 NURBS-based approach for nonlinear analysis of FG microplates

5.2.1 NURBS-based formulation of nonlinear microplates with modified couple stress theory

The approximation of the displacement field of a plate in the parametric space can be described as follow

$$\mathbf{u}^h(\xi,\eta) = \sum_{A}^{n\times m} R_A(\xi,\eta)\,\mathbf{q}_A, \tag{5.19}$$

where n and m are the number of control points in the ξ and η directions, respectively, $R_A(\xi,\eta)$ denotes 2-D NURBS basis function. Meanwhile, the vector of nodal degrees of freedom associated with the control point A is given as

$$\mathbf{q}_A = \left\{ \begin{array}{cccc} u_{0A} & v_{0A} & w_{bA} & w_{sA} \end{array} \right\}^T \tag{5.20}$$

By substituting the approximation in Eq. (5.19) into the strains derived in Eqs. (5.3)-(5.7), the strain components can be expressed in terms of NURBS as

$$\boldsymbol{\varepsilon}_b = \boldsymbol{\varepsilon}_b^L + \boldsymbol{\varepsilon}_b^{NL} = \sum_{A}^{n\times m} \left(\mathbf{B}_A^L + \frac{1}{2}\mathbf{B}_A^{NL} \right) \mathbf{q}_A, \tag{5.21a}$$

$$\boldsymbol{\varepsilon}_s = \sum_{A}^{n\times m} \mathbf{B}_A^s \mathbf{q}_A, \tag{5.21b}$$

in which

$$\boldsymbol{\varepsilon}_b^L = \left[\begin{array}{c} \boldsymbol{\varepsilon}_0^L \\ \boldsymbol{\kappa}_b \\ \boldsymbol{\kappa}_s \end{array} \right] = \sum_{A}^{n\times m} \mathbf{B}_A^L \mathbf{q}_A, \quad \boldsymbol{\varepsilon}_b^{NL} = \left[\begin{array}{c} \boldsymbol{\varepsilon}_0^{NL} \\ \mathbf{0} \\ \mathbf{0} \end{array} \right] = \frac{1}{2} \sum_{A}^{n\times m} \mathbf{B}_A^{NL} \mathbf{q}_A, \tag{5.22}$$

where the linear component and the nonlinear component, which contains the solution $\mathbf{q}$, are respectively defined as

$$\mathbf{B}_A^L = \begin{bmatrix} \mathbf{B}_A^m \\ \mathbf{B}_A^{b1} \\ \mathbf{B}_A^{b2} \end{bmatrix}, \quad \mathbf{B}_A^{NL}(\mathbf{q}) = \begin{bmatrix} \mathbf{A}_{\boldsymbol{\vartheta}} \\ \mathbf{0} \\ \mathbf{0} \end{bmatrix} \mathbf{B}_A^g, \tag{5.23}$$

and the linear gradient matrices are expressed as follows

$$\mathbf{B}_A^m = \begin{bmatrix} R_{A,x} & 0 & 0 & 0 \\ 0 & R_{A,y} & 0 & 0 \\ R_{A,y} & R_{A,x} & 0 & 0 \end{bmatrix}, \quad \mathbf{B}_A^{b1} = -\begin{bmatrix} 0 & 0 & R_{A,xx} & 0 \\ 0 & 0 & R_{A,yy} & 0 \\ 0 & 0 & 2R_{A,xy} & 0 \end{bmatrix}, \quad \mathbf{B}_A^{b2} = \begin{bmatrix} 0 & 0 & 0 & R_{A,xx} \\ 0 & 0 & 0 & R_{A,yy} \\ 0 & 0 & 0 & 2R_{A,xy} \end{bmatrix}, \tag{5.24a}$$

$$\mathbf{B}_A^g = \begin{bmatrix} 0 & 0 & R_{A,x} & R_{A,x} \\ 0 & 0 & R_{A,y} & R_{A,y} \end{bmatrix}, \quad \mathbf{B}_A^s = \begin{bmatrix} 0 & 0 & 0 & R_{A,x} \\ 0 & 0 & 0 & R_{A,y} \end{bmatrix}. \tag{5.24b}$$

Meanwhile, the variation of the strain vectors are derived as

$$\delta\boldsymbol{\varepsilon}_b = \delta\boldsymbol{\varepsilon}_b^L + \delta\boldsymbol{\varepsilon}_b^{NL} = \sum_A^{n\times m} \left(\mathbf{B}_A^L + \mathbf{B}_A^{NL}\right) \delta\mathbf{q}_A \tag{5.25}$$

Similarly, by substituting the approximation in Eq. (5.19) into the curvature tensor derived in Eqs. (5.8) and (5.9), the curvature tensor components can be obtained as

$$\boldsymbol{\chi}_b^c = \sum_A^{n\times m} \mathbf{B}_A^{cb} \mathbf{q}_A, \tag{5.26a}$$

$$\boldsymbol{\chi}_s^c = \sum_A^{n\times m} \mathbf{B}_A^{cs} \mathbf{q}_A, \tag{5.26b}$$

where

$$\mathbf{B}_A^{cb} = \begin{bmatrix} \tilde{\mathbf{B}}_A^{b0} \\ \tilde{\mathbf{B}}_A^{b1} \end{bmatrix}, \quad \mathbf{B}_A^{cs} = \begin{bmatrix} \tilde{\mathbf{B}}_A^{s0} \\ \tilde{\mathbf{B}}_A^{s2} \end{bmatrix}, \tag{5.27}$$

in which

$$\tilde{\mathbf{B}}_A^{b0} = \frac{1}{4}\begin{bmatrix} 0 & 0 & 4R_{A,xy} & 2R_{A,xy} \\ 0 & 0 & -4R_{A,xy} & -2R_{A,xy} \\ 0 & 0 & 2\left(-R_{A,xx}+R_{A,yy}\right) & -R_{A,xx}+R_{A,yy} \end{bmatrix}, \quad \tilde{\mathbf{B}}_A^{b1} = \frac{1}{4}\begin{bmatrix} 0 & 0 & 0 & -2R_{A,xy} \\ 0 & 0 & 0 & 2R_{A,xy} \\ 0 & 0 & 0 & R_{A,xx}-R_{A,yy} \end{bmatrix}, \tag{5.28a}$$

$$\tilde{\mathbf{B}}_A^{s0} = \frac{1}{4}\begin{bmatrix} -R_{A,xy} & R_{A,xx} & 0 & 0 \\ -R_{A,yy} & R_{A,xy} & 0 & 0 \end{bmatrix}, \quad \tilde{\mathbf{B}}_A^{s2} = \frac{1}{4}\begin{bmatrix} 0 & 0 & 0 & -R_{A,y} \\ 0 & 0 & 0 & R_{A,x} \end{bmatrix}. \tag{5.28b}$$

The discretised system of equations for the static analysis is

$$\mathbf{K}(\mathbf{q})\,\mathbf{q} = \mathbf{F}, \tag{5.29}$$

where the global stiffness matrix is

$$\mathbf{K}(\mathbf{q}) = \mathbf{K}_L + \mathbf{K}_{NL}(\mathbf{q}), \tag{5.30}$$

in which the global matrices $\mathbf{K}_L$ (linear) and $\mathbf{K}_{NL}$ (nonlinear) are respectively assembled from the element matrices $\mathbf{K}_L^e$ and $\mathbf{K}_{NL}^e$ of the element Ω_e. These matrices can be expressed as follows

$$\mathbf{K}_L^e = \int_{\Omega_e} \left(\mathbf{B}_A^L\right)^T \mathbf{D}^b \mathbf{B}_A^L d\Omega_e + \int_{\Omega_e} \left(\mathbf{B}_A^s\right)^T \mathbf{D}^s \mathbf{B}_A^s d\Omega_e + \int_{\Omega_e} \left(\mathbf{B}_A^{cb}\right)^T \mathbf{D}_c^b \mathbf{B}_A^{cb} d\Omega_e + \int_{\Omega_e} \left(\mathbf{B}_A^{cs}\right)^T \mathbf{D}_c^s \mathbf{B}_A^{cs} d\Omega_e \ , \tag{5.31a}$$

$$\mathbf{K}_{NL}^e(\mathbf{q}) = \int_{\Omega_e} \left(\frac{1}{2}\left(\mathbf{B}_A^L\right)^T \mathbf{D}^b \mathbf{B}_A^{NL} + \left(\mathbf{B}_A^{NL}\right)^T \mathbf{D}^b \mathbf{B}_A^L + \frac{1}{2}\left(\mathbf{B}_A^{NL}\right)^T \mathbf{D}^b \mathbf{B}_A^{NL} \right) d\Omega_e. \tag{5.31b}$$

In addition, the load vector is described as

$$\mathbf{F} = \int_{\Omega} q_0 \mathbf{R} d\Omega \tag{5.32}$$

where

$$\mathbf{R} = \begin{bmatrix} 0 & 0 & R_A & R_A \end{bmatrix}^T \tag{5.33}$$

It can be inferred from Eqs. (5.24) and (5.28) that the second derivatives of the approximation functions are essentially required for the RPT and MCST. Consequently, C^1-continuous elements are needed. These contraints may cause some difficulties in the traditional FEA as the popular Lagrangian elements are C^0 continuous. Another alternative way to bypass this issue is to use mixed formulation. However, this approach involves the use of extra degrees of freedom. Fortunately, by using the proposed IGA-based formulation, the derivatives of the basis functions could be derived easily in a clean and efficient manner. It is also

worth noting that the system of equations includes the nonlinear term $\mathbf{q}$ on the left-hand side of the Eq. (5.29), which contains unknown control variables. As a result, an iterative approach should be considered to solve such a problem.

5.2.2 Newton-Raphson iterative procedure

In the Newton-Raphson procedure, the nonlinear equation in Eq. (5.29) is solved iteratively in which the solutions of the unknowns in the previous step are used to solve for the solution in the current step. These iterations are performed until the solution converges. Following these ideas, the residual force vector is defined as

$$\tilde{\mathbf{R}}(\mathbf{q}) = \mathbf{K}(\mathbf{q})\,\mathbf{q} - \mathbf{F} = (\mathbf{K}_L + \mathbf{K}_{NL}(\mathbf{q}))\,\mathbf{q} - \mathbf{F}. \tag{5.34}$$

Then the improved solution at the end of the $(i+1)^{th}$ iteration is calculated as

$${}^{i+1}\mathbf{q} = {}^{i}\mathbf{q} + \Delta\mathbf{q}, \tag{5.35}$$

where the incremental displacement $\Delta\mathbf{q}$ is given by

$$\Delta\mathbf{q} = \frac{-\tilde{\mathbf{R}}\left({}^{i}\mathbf{q}\right)}{\mathbf{K}_T}, \tag{5.36}$$

in which the tangent stiffness matrix $\mathbf{K}_T$ can be obtained by [142]

$$\mathbf{K}_T = \frac{\partial\tilde{\mathbf{R}}\left({}^{i}\mathbf{q}\right)}{\partial\mathbf{q}} = \mathbf{K}_L + \tilde{\mathbf{K}}_{NL} + \mathbf{K}_g, \tag{5.37}$$

where the nonlinear matrix

$$\tilde{\mathbf{K}}_{NL}(\mathbf{q}) = \int_{\Omega} \left(\left(\mathbf{B}_A^L\right)^T \mathbf{D}^b \mathbf{B}_A^{NL} + \left(\mathbf{B}_A^{NL}\right)^T \mathbf{D}^b \mathbf{B}_A^L + \left(\mathbf{B}_A^{NL}\right)^T \mathbf{D}^b \mathbf{B}_A^{NL} \right) d\Omega, \tag{5.38}$$

and the geometric stiffness matrix

$$\mathbf{K}_g = \int_{\Omega} (\mathbf{B}^g)^T \begin{bmatrix} N_x & N_{xy} \\ N_{xy} & N_y \end{bmatrix} \mathbf{B}^g d\Omega, \tag{5.39}$$

where $\mathbf{B}^g$ is assembled from $\mathbf{B}_A^g$ in Eq. (5.24). The iterations are executed until the difference between the solutions from two consecutive iterations is no greater

than the predefined tolerance ε as described below

$$\frac{\left\| {}^{i+1}\mathbf{q} - {}^{i}\mathbf{q} \right\|}{\| {}^{i+1}\mathbf{q} \|} \leq \varepsilon. \tag{5.40}$$

5.3 Numerical examples

In this section, the numerical results of the nonlinear bending analysis of square, circular and annular plates will be shown. The convergence and validation are first presented to demonstrate the validity and efficiency of the proposed IGA approach for nonlinear problems of plate structures without and with size effects. It should be noted that $\ell/h \equiv 0$ implies no size effect is taken into account. In these investigations, the plates which are made of isotropic material and FGMs with mixtures of ceramic and metal shown in Table 5.1 are used where specific values of properties of Materials I, II, III are simply for comparison purposes. The geometries of square, circular and annular plates employed in this study are shown in Fig. 5.1. It should be noted that, for validation and comparison purposes, the material properties could have different units or without specific unit. For efficient presentation of results, the following normalised formula, unless otherwise specified, are used:

$$P = \frac{q_0 a^4}{E_m h^4}; \quad \bar{w} = \frac{w}{h}; \quad \bar{\sigma}_x = \frac{\sigma_x a^2}{E_m h^2} \tag{5.41}$$

Table 5.1 Material properties

Material	Type	E_c (ceramic)	E_m (metal)	ν_1	ν_2
Material *I* [143]	Isotropic	3×10^7 psi	3×10^7 psi	0.316	0.316
Material *II*[32]	FGM	14.4 GPa	1.44 GPa	0.3	0.3
Material *III* [31]	FGM	1.0×10^6	1.0×10^5	0.25	0.25
Al/Al_2O_3	FGM	380 GPa	70 GPa	0.3	0.3
Al/ZnO_2	FGM	151 GPa	70 GPa	0.3	0.3
Al/SiC	FGM	427 GPa	70 GPa	0.17	0.3

5.3.1 Convergence and validation studies

In order to illustrate the validity and the convergence of the proposed IGA approach and refined plate formulation for nonlinear plate problems with MCST

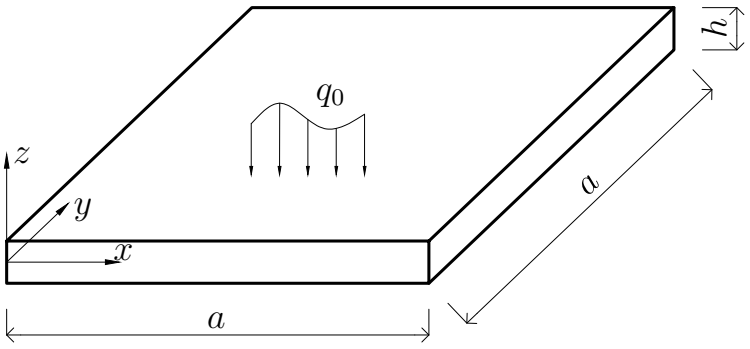

(a) Square plate

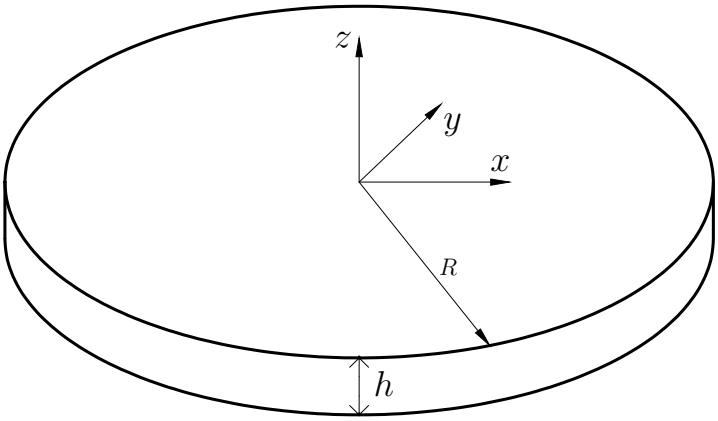

(b) Circular plate

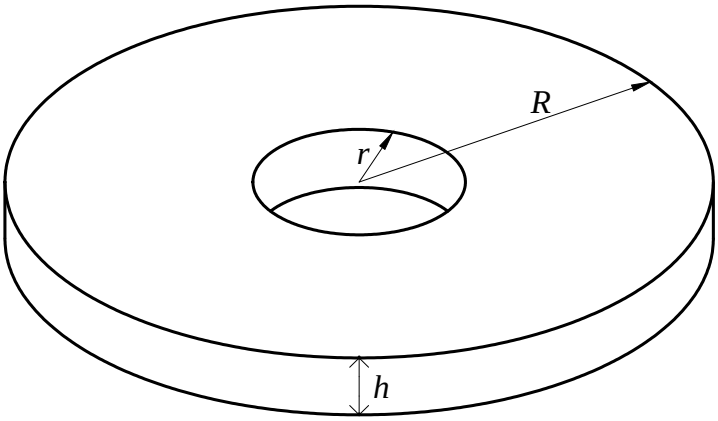

(c) Annular plate

Fig. 5.1 Geometry of different plates.

in Section 5.2, a number of numerical tests have been conducted to deal with the nonlinear bending of isotropic and FG plates. Fig. 5.2 presents the convergence rate of the numerical results toward the analytical solution of Levy [143] whose work is widely considered as a standard reference for nonlinear problems. The analytical reference result is calculated for clamped isotropic square plates with aspect ratio $a/h = 100$ subjected to uniform loading. This figure includes convergences of normalised nonlinear central deflection of clamped isotropic plates (Material *I*) with different element meshes, ranging from 3 to 17 elements per edge, and element polynomial orders, $p = 2, 3$ and 4. As expected, while the quadratic elements ($p = 2$) show slower convergence rate and less accuracy, the higher-order elements ($p = 3$ or $p = 4$) yield better performance in terms of convergences and differences compared to the analytical solution [143]. Having pointed out in the work of Nguyen et al. [84], the meshes of 11×11 cubic ($p = 3$) elements with total of 784 degrees of freedom which are sufficient in between accuracy and computational cost will be used. Table 5.2 shows the complete comparison of the presented numerical linear and nonlinear results of square isotropic plates with those of other researchers including Levy's analytical solution [143], Pica et al.'s FEM with Mindlin formulation [144], Kant and Kommineni's C^0 FEM with high-order formulation [145], Urthaler and Reddy's mixed FEM [146], and Kapoor and Kapania's IGA with first-order formulation [118]. It can be observed that, for all cases of load parameter *P*, the present solutions are in good agreement with the analytical solutions and other published results for both normalised deflection and normal stress. Also, nonlinear displacements are generally smaller than linear displacements due to the fact that in nonlinear analysis von Kámán strains are taken into account which increases the strain energy. For better illustration of the accuracy of the proposed method and differences of linear and nonlinear solutions, all results are plotted in Fig. 5.3.

The validity and accuracy of the proposed IGA with RPT is further investigated for FG square plates. Fig. 5.4 depicts the comparison of the nonlinear central deflection of simply-supported (SSSS) square plates subjected to uniformly distributed load. The plates are made of Al/ZnO_2 in which the material properties are assumed to follow the rule of mixtures. The proposed results with different values of material index *n* are compared to those of Praveen and Reddy [147] using FEM based on 5-DOF FSDT and Phung-Van et al. [119] employing cell-based smoothed three-node plate elements based on 7-DOF HSDT. As can be seen, the presented results are quite close to the others', especially the former

one. This confirms the accuracy and validity of the proposed approach which is applicable not only for isotropic plates but also for the FG plates.

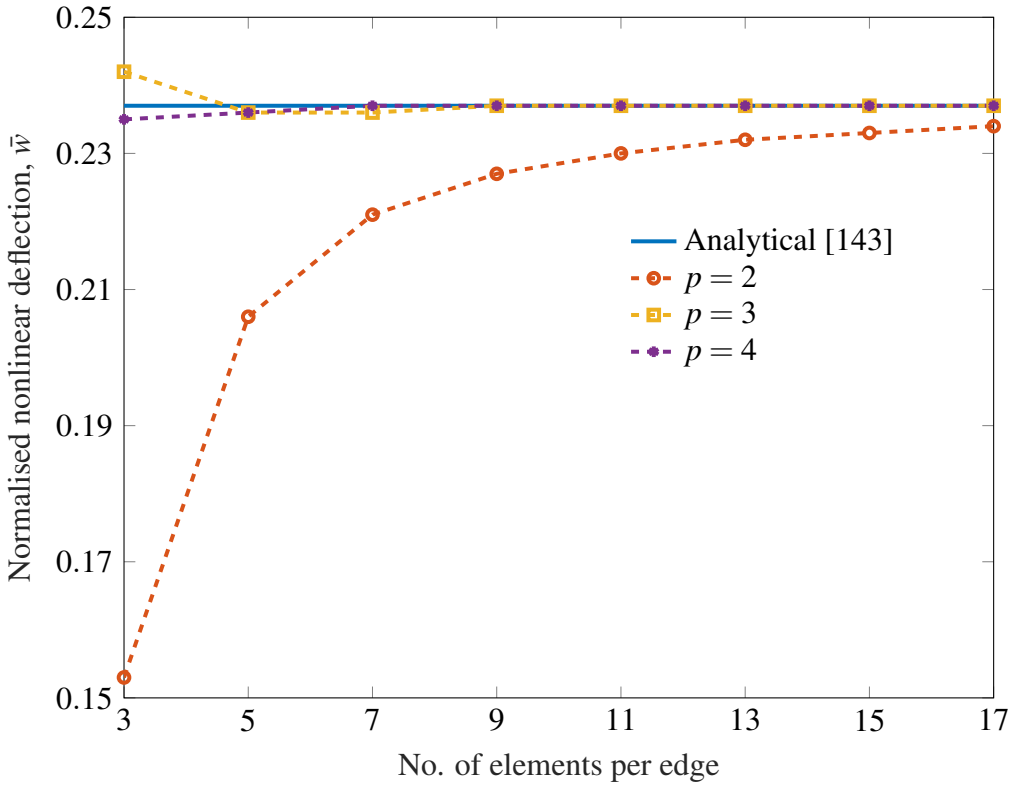

Fig. 5.2 Convergence of nonlinear central deflection of fully clamped isotropic plates with different meshes and polynomial orders, $a/h = 100, a = 300\text{in}, h = 3\text{in}, P = 17.79$ (Material I).

Figures 5.5 and 5.6 depict the bending behaviours including central deflection and normal stress of simply-supported and fully clamped FG microplates with size effects, respectively. The presented results, that are generated from different values of material length scale ratio ℓ/h and material index n, are compared with those reported by Kim and Reddy [32] who employed general third-order theory for element formulation of FG microplates. It is observed that the solutions of the two approaches are in excellent agreement although there are small discrepancy in central displacements of clamped microplates with relatively high material length scale ratio ($\ell/h = 0.5$ and 1). It is worth commenting that Kim and Reddy [32] employed the general third-order shear deformation plate theory (GTPT) with 11 unknowns and 16×16 meshes of conforming cubic elements to analyse the microplates. Meanwhile, the RPT with only 4 variables and meshes of 11×11 cubic elements are used in this study. The comparison of the computational efforts

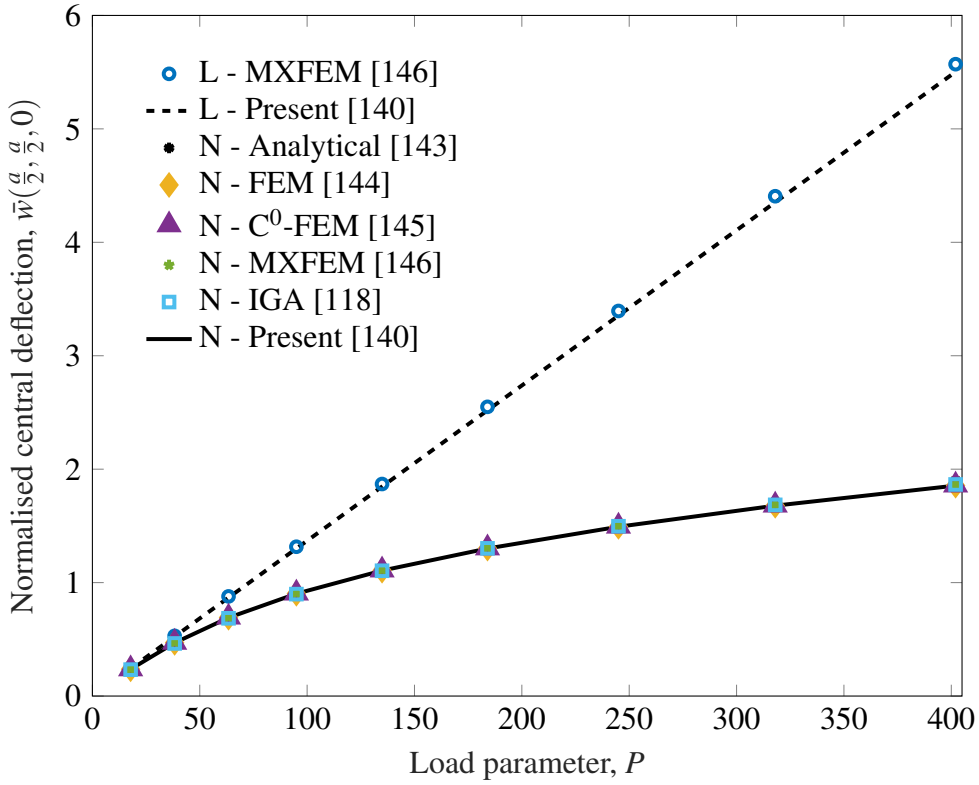

(a) Central deflection

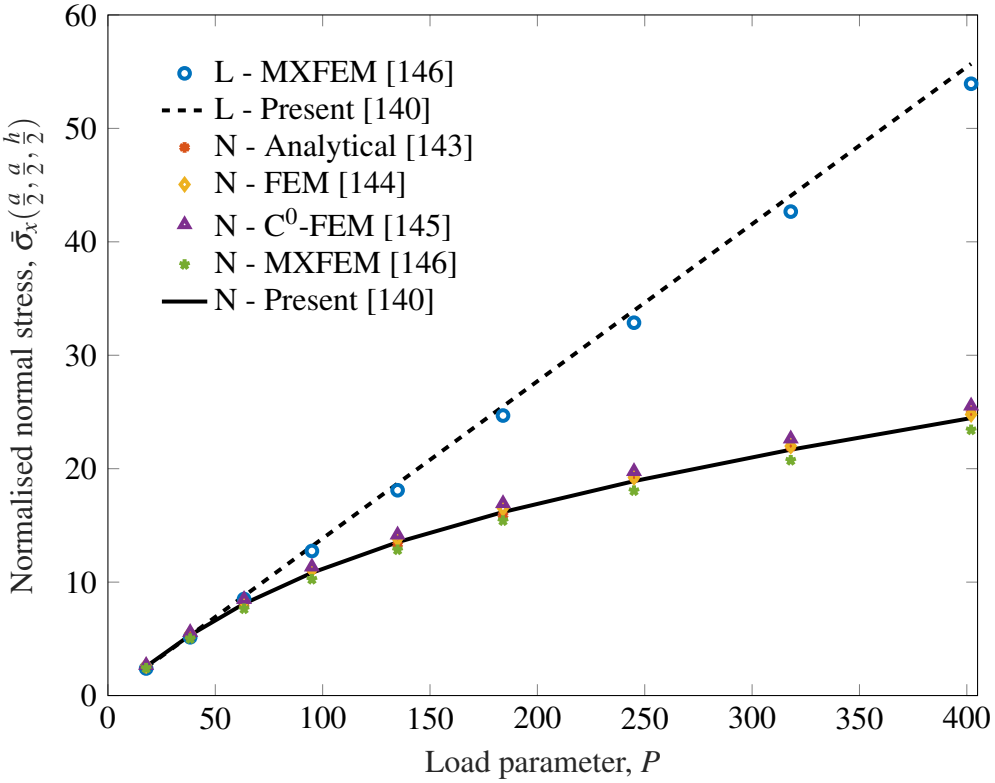

(b) Normal stress

Fig. 5.3 Comparison of nonlinear (a) central deflection and (b) normal stress of fully-clamped isotropic square plates (Material *I*) with existing results. Prefixes L and N denote linear and nonlinear solutions, respectively.

Table 5.2 Comparison of normalised nonlinear deflection $\bar{w}(\frac{a}{2},\frac{a}{2},0)$ and normal stress $\bar{\sigma}_x(\frac{a}{2},\frac{a}{2},\frac{h}{2})$ of clamped isotropic square plates under uniform loading (Material *I*), $a/h = 100$

P	Response	Nonlinear						Linear	
		Present [140]	Analytical [143]	FEM [144]	C^0-FEM [145]	MXFEM [146]	IGA FSDT [118]	Present [140]	MXFEM [146
17.79	$\bar{w}$	0.2365	0.237	0.2368	0.2385	0.2392	0.2328	0.2435	0.2465
	$\bar{\sigma}_x$	2.5602	2.6	2.6319	2.6733	2.414	-	2.4643	2.387
38.3	$\bar{w}$	0.4692	0.471	0.4699	0.4725	0.4738	0.4635	0.5243	0.5307
	$\bar{\sigma}_x$	5.3256	5.2	5.4816	5.5733	5.022	-	5.3054	5.138
63.4	$\bar{w}$	0.6908	0.695	0.6915	0.6948	0.6965	0.6854	0.8678	0.8785
	$\bar{\sigma}_x$	8.0973	8.0	8.3258	8.4867	7.649	-	8.7822	8.510
95.0	$\bar{w}$	0.9024	0.912	0.9029	0.9065	0.9087	0.8985	1.3004	1.3163
	$\bar{\sigma}_x$	10.8248	11.1	11.103	11.3500	10.254	-	13.1595	12.745
134.9	$\bar{w}$	1.1060	1.121	1.1063	1.1100	1.1130	1.1045	1.8466	1.8692
	$\bar{\sigma}_x$	13.5187	13.3	13.827	14.1700	12.850	-	18.6865	18.099
184.0	$\bar{w}$	1.3008	1.323	1.3009	1.3046	1.3080	1.3020	2.5187	2.5495
	$\bar{\sigma}_x$	16.1771	15.9	16.497	16.9367	15.420	-	25.4879	24.686
245.0	$\bar{w}$	1.4926	1.521	1.4928	1.4963	1.5010	1.4969	3.3536	3.3947
	$\bar{\sigma}_x$	18.9019	19.2	19.225	19.7633	18.060	-	33.9377	32.869
318.0	$\bar{w}$	1.6784	1.714	1.6786	1.6820	1.6880	1.6856	4.3529	4.4062
	$\bar{\sigma}_x$	21.6744	21.9	21.994	22.6367	20.741	-	44.0498	42.664
402.0	$\bar{w}$	1.8552	1.902	1.8555	1.8590	1.8660	1.8652	5.5027	5.5702
	$\bar{\sigma}_x$	24.4624	25.1	24.780	25.5367	23.423	-	55.6855	53.933

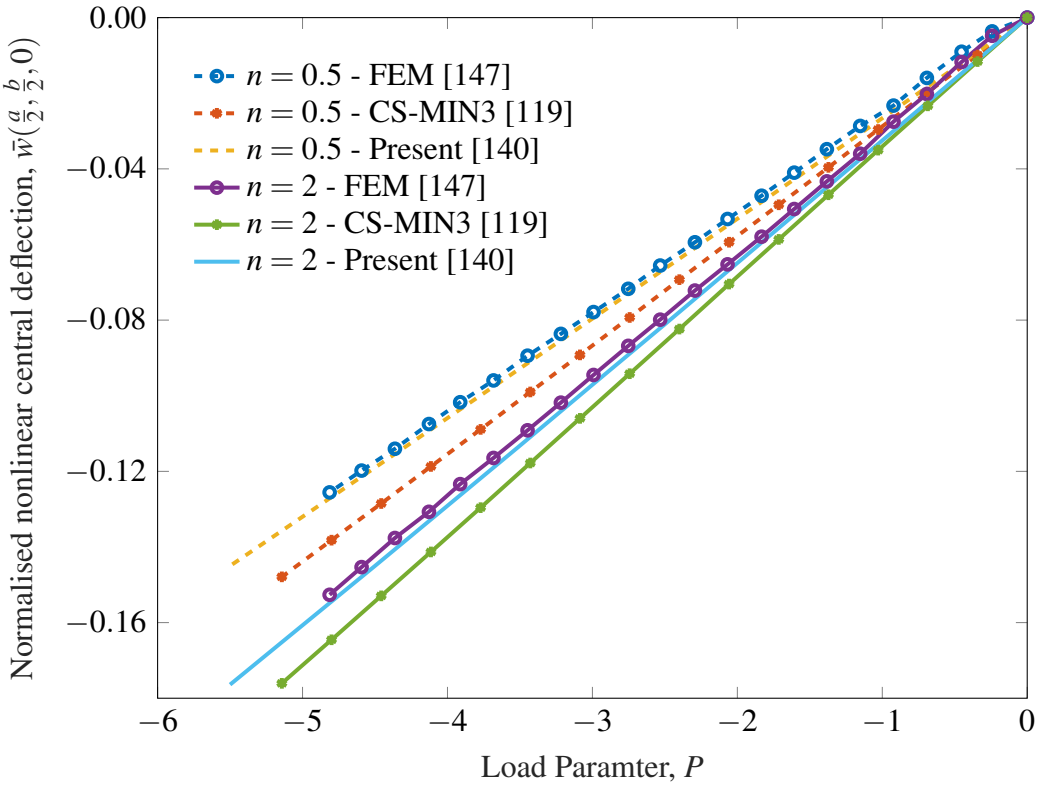

Fig. 5.4 Comparison of nonlinear central deflection of SSSS square Al/ZnO_2 with uniformly distributed load, $a = 0.2$m, $h = 0.01$m (rule of mixtures scheme).

in terms of total number of DOFs between the reference and present approaches is provided in Table 5.3. As can be seen, for a single analysis, the reference approach requires over 16 times as many DOFs as the present approach does. For the nonlinear analysis in which iterative procedures are involved, the difference between the two approaches in terms of computational cost becomes much more significant. As a result, IGA approach performs far better than that of FEM doing in these specific nonlinear problems.

Table 5.3 Degrees of freedom required in FEM and IGA approaches

Approach	# Unknowns	Element type	Mesh	Total DOFs
FEM and GTPT [32]	11	Cubic	16×16	12716
IGA and RPT (present [140])	4	Cubic	11×11	784

The accuracy of the proposed approach is further demonstrated for circular plates in Fig. 5.7 where the proposed solutions are almost coincident with the results published by Reddy et al. [31] for various boundary conditions and material parameters. It should be noted that for the analysis of circular plates, unless otherwise specified, the constrained DOFs of simply-supported boundary conditions are indicated similar to those presented in the work of Reddy et al. [31]. Generally, the positive outcomes confirm the accuracy and validity of the proposed method regardless of material properties, structure scales and geometries.

5.3.2 Nonlinear analysis of square microplates

In this part, a number of numerical studies of the nonlinear behaviour of square FG microplates is conducted to demonstrate the effects of aspect ratio a/h, material length scale ratio ℓ/h, material index n and load parameter P. Table 5.4 and 5.5 present the normalised central deflection and normal stress of simply-supported and fully clamped square Al/Al_2O_3 microplates in which the rule of mixtures is employed to model the material distribution through the thickness. The plates are subjected to either uniformly distributed load, q_0, or sinusoidally distributed load, $q_0 \sin\left(\frac{\pi x}{a}\right)\sin\left(\frac{\pi y}{a}\right)$. The results are generated for different values of a/h, ℓ/h and P, while keeping material index $n = 1$. Similarly, the numerical results for SSSS microplates, which employ the Mori-Tanaka scheme for material modelling, are provided in Table 5.6. These results which have not been reported before could serve as the benchmark examples for the future references. For illustration purposes, Fig. 5.8 depicts the deformed shapes of square microplates under

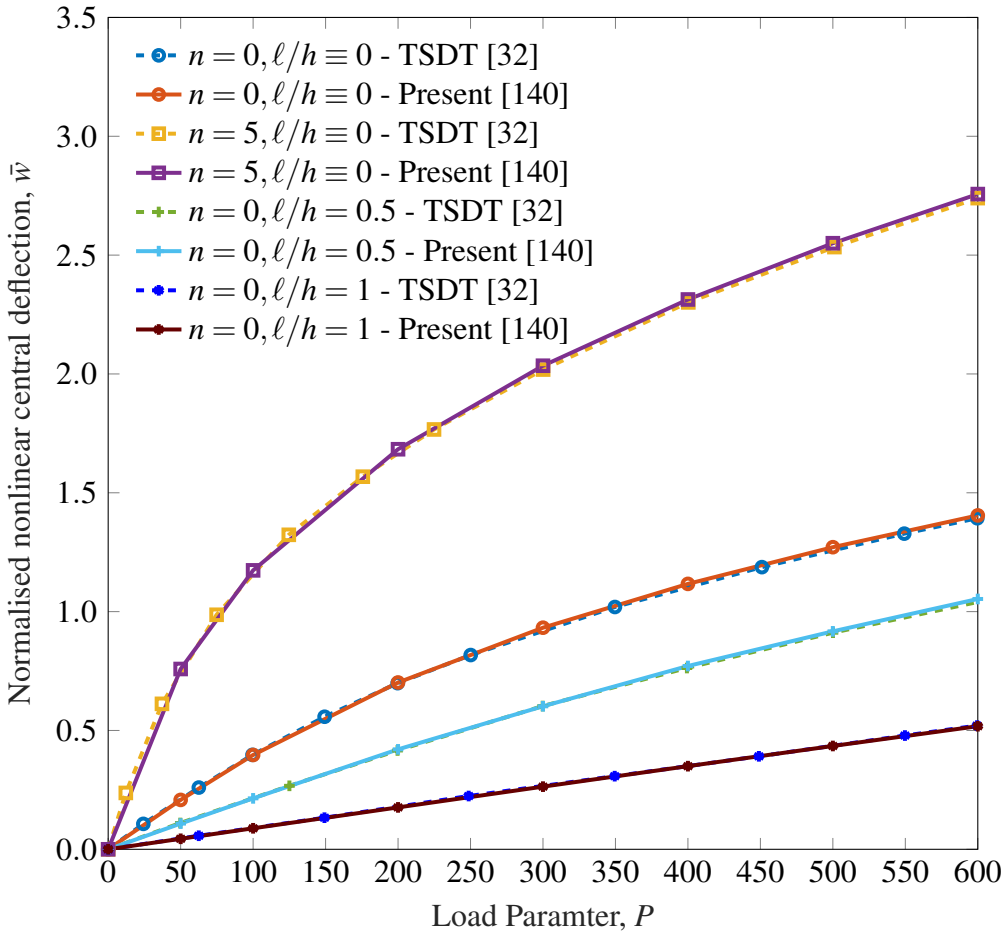

(a) Central deflection $\bar{w}(\frac{a}{2},\frac{a}{2},0)$

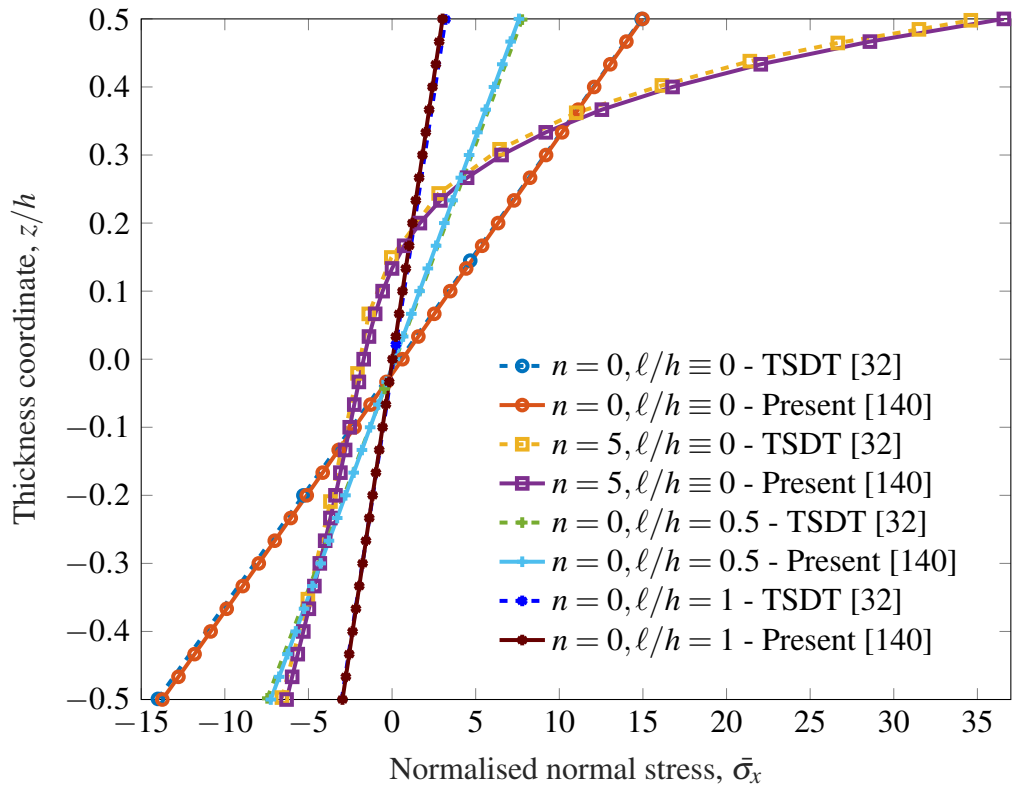

(b) Normal stress $\bar{\sigma}_x(\frac{9a}{16},\frac{9a}{16},z), P=50$

Fig. 5.5 Comparison of nonlinear (a) central deflection and (b) normal stress of SSSS FG square microplates, $a/h=20$, rule of mixtures scheme (Material *II*).

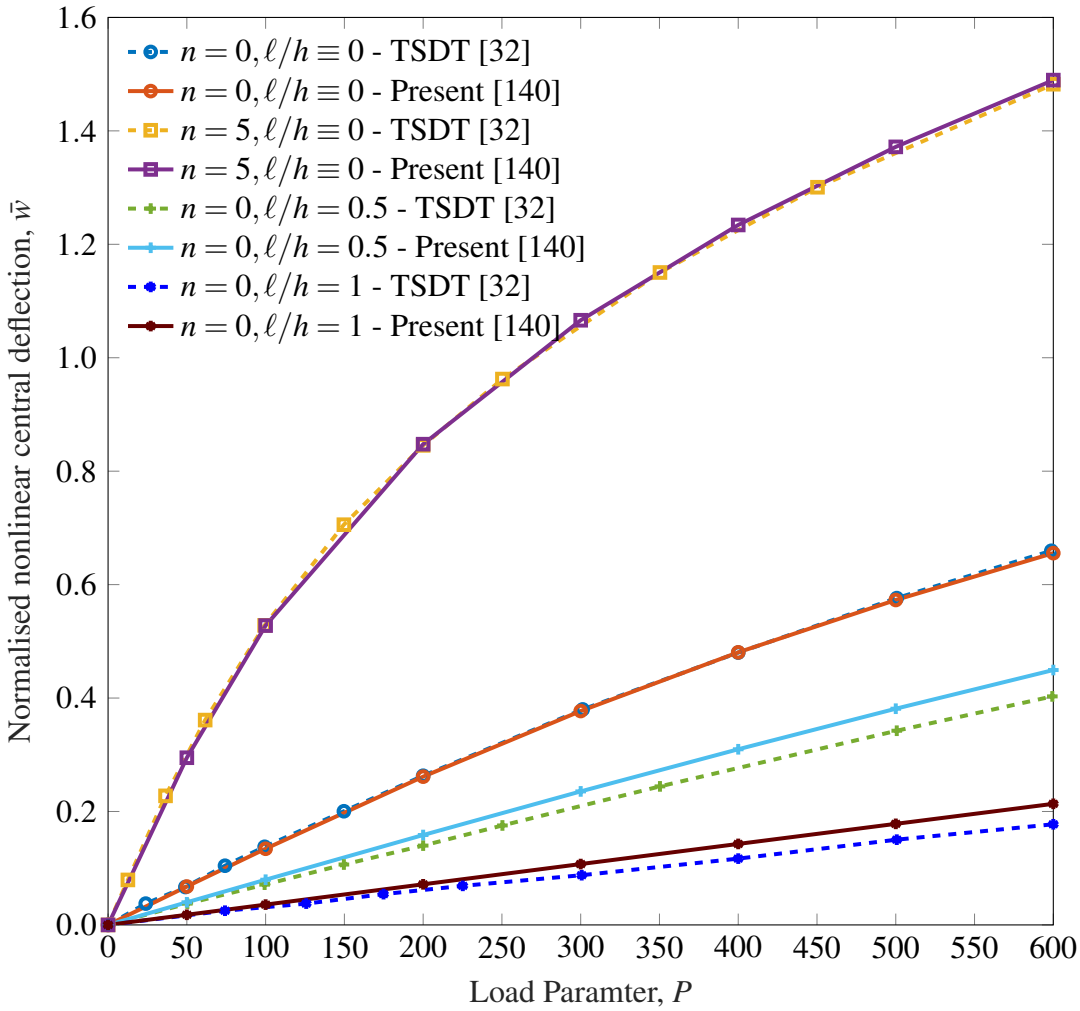

(a) Central deflection $\bar{w}(\frac{a}{2},\frac{a}{2},0)$

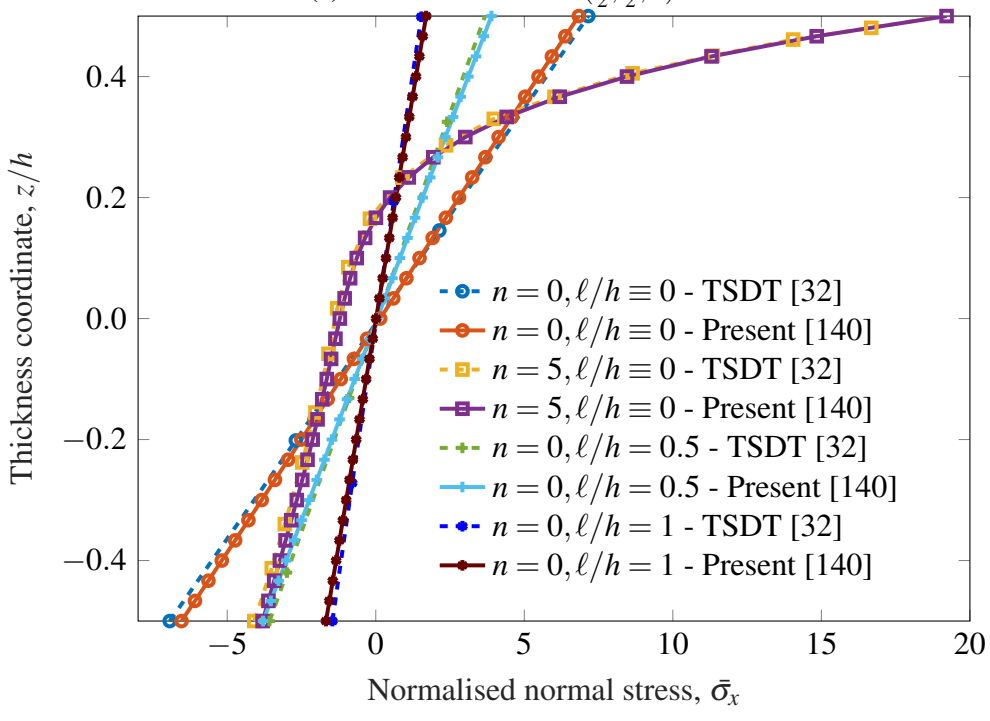

(b) Normal stress $\bar{\sigma}_x(\frac{9a}{16},\frac{9a}{16},z), P=50$

Fig. 5.6 Comparison of nonlinear (a) central deflection and (b) normal stress of CCCC FG square microplates, $a/h=20$, rule of mixtures scheme (Material *II*).

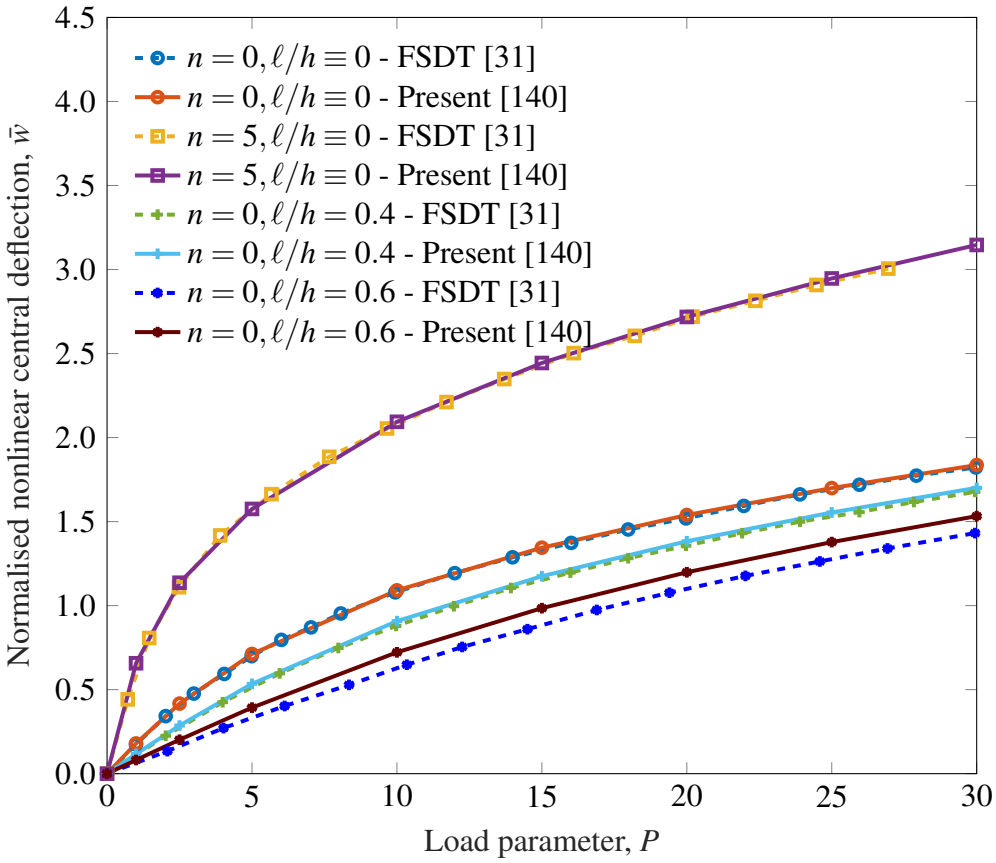

(a) Clamped plates

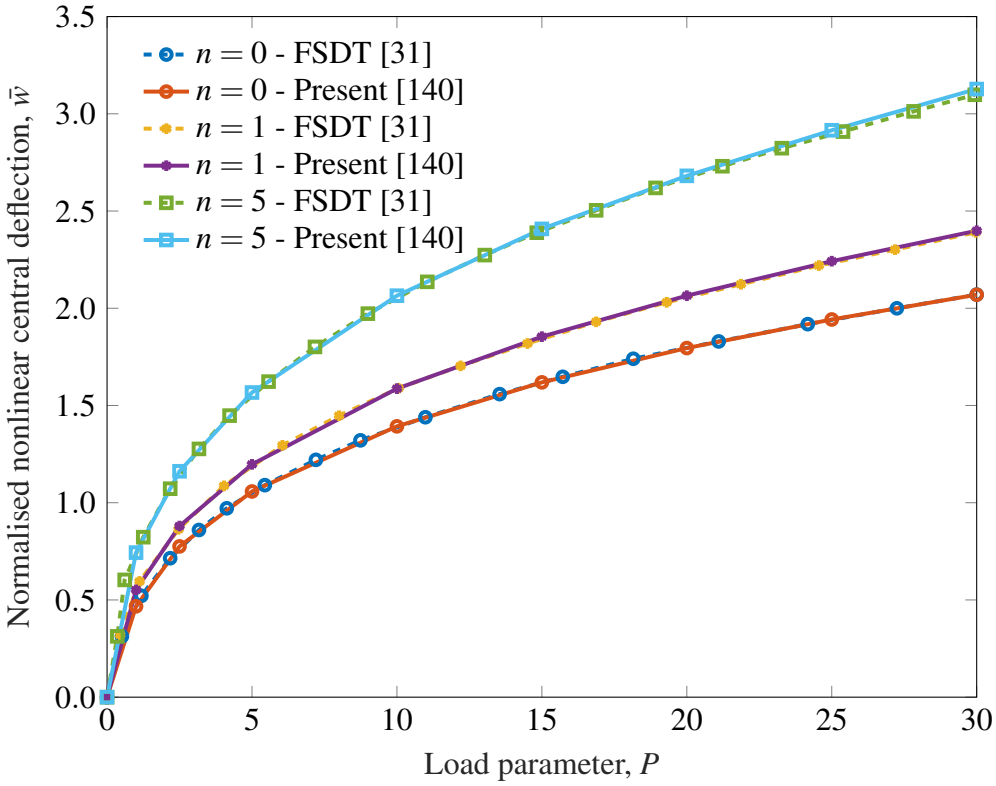

(b) Simply-supported plates, $\ell/h = 0.6$

Fig. 5.7 Comparison of nonlinear central deflection of FG circular microplates subjected to uniformly distributed load, $R = 1$, $h = 0.1$, rule of mixtures scheme (Material *III*), $P = \frac{q_0 R^4}{E_c h^4}$.

uniform load with different boundary conditions. As can be seen, being placed together in the same plots, the nonlinear displacements are always smaller than those of linear counterparts. The reason for this phenomenon is that the nonlinear analysis takes into account the low and higher order terms of the strains while the linear analysis only considers the first order ones. This additional consideration contributes to the increase of the strain energy and the stiffness of the structure correspondingly, which results in smaller displacements for nonlinear cases as presented.

The effects of material index n and material length scale ratio ℓ/h on the nonlinear central deflection and normal stress of fully clamped Al/Al_2O_3 square microplates with different material distribution models are plotted in Fig. 5.9. The results are generated for the plates with aspect ratio $a/h = 5$ and load parameter $P = 100$ and with different values of ℓ/h of 0.0, 0.4, 1.0. It can be observed that the increase of material index n is followed by the increase of central displacement. However, the growth of material length scale ratio ℓ/h leads to a completely different scenario in which the displacement is declined. It is worth commenting that these phenomena are due to the increase of structure stiffness as the material length scale ratio ℓ/h becomes smaller causing the displacement to reduce as expected. In other words, for a specific material length scale ℓ, the thinner the microplate is, the higher the stiffness becomes. For further illustration, Fig. 5.10 presents the variation of nonlinear deflection and normal stress of simply-supported Al/Al_2O_3 square microplates in which the plate's aspect ratio a/h and material length scale ratio ℓ/h are taken into account. As can be seen, the influence of the aspect ratio a/h on the bending responses is remarkable for thin square plates $(a/h \leq 10)$. However, it becomes less pronounced as the square plates get thicker.

5.3.3 Nonlinear analysis of circular microplates

A number of investigations on the nonlinear bending behaviours of circular FG microplates will be presented in this part of the section. Table 5.7 shows the normalised deflection and normal stress of circular Al/ZnO_2 microplates subjected to uniform loading in which the material distribution follows the rule of mixtures. The results are generated for both simply-supported and fully clamped boundary conditions with various values of aspect ratio a/h, material length scale ratio ℓ/h and load parameter P. Since there is no published report for this problem of

Table 5.4 Normalised deflection $\bar{w}(\frac{a}{2},\frac{a}{2},0)$ and normal stress $\bar{\sigma}_x(\frac{a}{2},\frac{a}{2},\frac{h}{2})$ of SSSS square Al/Al_2O_3 microplates (rule of mixtures scheme, $n=1$)

a/h	ℓ/h	$P=1$		$P=50$		$P=100$		$P=200$		$P=300$		$P=400$	
		$\bar{w}$	$\bar{\sigma}_x$	$\bar{w}$	$\bar{\sigma}_x$	$\bar{w}$	$\bar{\sigma}_x$	$\bar{w}$	$\bar{\sigma}_x$	$\bar{w}$	$\bar{\sigma}_x$	$\bar{w}$	$\bar{\sigma}_x$
Uniformly distributed load													
5	0.0	0.0192	0.4585	0.7281	20.2345	1.1161	32.2415	1.6088	48.0796	1.9627	59.8543	2.2512	69.7203
	0.2	0.0158	0.3740	0.6508	17.9251	1.0342	29.9180	1.5183	45.8654	1.8577	57.5988	2.1297	67.3703
	0.4	0.0103	0.2401	0.4792	12.7399	0.8359	23.8318	1.3151	40.0759	1.6491	52.1288	1.9128	62.0664
	0.6	0.0066	0.1497	0.3208	8.1036	0.6069	16.5265	1.0555	31.4986	1.3888	43.7129	1.6541	53.9939
	0.8	0.0043	0.0977	0.2159	5.2192	0.4235	10.9089	0.7952	22.5595	1.1054	33.5254	1.3657	43.4703
	1.0	0.0030	0.0674	0.1514	3.5450	0.3006	7.3965	0.5859	15.6914	0.8470	24.2801	1.0820	32.7521
20	0.0	0.0166	0.4463	0.6703	20.6394	1.0521	33.5078	1.5222	49.6254	1.8445	60.9439	2.0996	70.1634
	0.2	0.0138	0.3690	0.5960	18.1802	0.9745	31.0510	1.4496	47.6881	1.7747	59.3446	2.0306	68.7622
	0.4	0.0092	0.2424	0.4338	12.8277	0.7774	24.4374	1.2547	41.7285	1.5882	54.2994	1.8494	64.3973
	0.6	0.0059	0.1539	0.2890	8.2205	0.5547	16.7933	0.9899	32.4265	1.3230	45.3514	1.5904	56.1730
	0.8	0.0039	0.1018	0.1945	5.3662	0.3837	11.1400	0.7317	23.0212	1.0323	34.3907	1.2901	44.8158
	1.0	0.0027	0.0709	0.1365	3.6877	0.2716	7.6322	0.5331	16.0466	0.7778	24.7742	1.0029	33.4585
Sinusoidally distributed load													
5	0.0	0.0123	0.3175	0.5241	15.4148	0.8496	26.3160	1.2629	41.0497	1.5527	51.8826	1.7860	60.8716
	0.2	0.0101	0.2600	0.4566	13.2402	0.7729	23.7744	1.1849	38.5672	1.4716	49.4606	1.6993	58.4438
	0.4	0.0066	0.1678	0.3201	8.9248	0.5911	17.6100	0.9908	31.8508	1.2783	42.9290	1.5055	52.1164
	0.6	0.0042	0.1050	0.2087	5.5657	0.4064	11.4858	0.7488	23.0488	1.0246	33.3911	1.2513	42.4880
	0.8	0.0028	0.0686	0.1393	3.5870	0.2763	7.4350	0.5358	15.5522	0.7699	23.7339	0.9778	31.6242
	1.0	0.0020	0.0473	0.0975	2.4465	0.1944	5.0419	0.3843	10.5897	0.5663	16.4566	0.7381	22.4713
20	0.0	0.0105	0.3057	0.4691	15.2657	0.7885	26.9596	1.1979	42.7978	1.4782	54.0753	1.6978	63.1780
	0.2	0.0087	0.2544	0.4065	13.0940	0.7125	24.2191	1.1233	40.2018	1.4071	51.7558	1.6293	61.0745
	0.4	0.0058	0.1692	0.2839	8.9138	0.5357	17.7788	0.9266	32.8919	1.2147	44.8087	1.4430	54.6267
	0.6	0.0037	0.1086	0.1856	5.6830	0.3644	11.6787	0.6853	23.5693	0.9539	34.4618	1.1796	44.1625
	0.8	0.0025	0.0723	0.1243	3.7396	0.2472	7.6921	0.4836	15.9740	0.7025	24.3722	0.9017	32.5663
	1.0	0.0017	0.0506	0.0871	2.5916	0.1739	5.3030	0.3450	11.0199	0.5110	17.0156	0.6701	23.1607

Table 5.5 Normalised deflection $\bar{w}(\frac{a}{2},\frac{a}{2},0)$ and normal stress $\bar{\sigma}_x(\frac{a}{2},\frac{a}{2},\frac{h}{2})$ of CCCC square Al/Al_2O_3 microplates (rule of mixtures scheme, $n=1$)

a/h	ℓ/h	$P=1$		$P=50$		$P=100$		$P=200$		$P=300$		$P=400$	
		$\bar{w}$	$\bar{\sigma}_x$	$\bar{w}$	$\bar{\sigma}_x$	$\bar{w}$	$\bar{\sigma}_x$	$\bar{w}$	$\bar{\sigma}_x$	$\bar{w}$	$\bar{\sigma}_x$	$\bar{w}$	$\bar{\sigma}_x$
Uniformly distributed load													
5	0.0	0.0078	0.2252	0.3489	11.8613	0.5859	21.5995	0.8826	35.6241	1.0793	46.2644	1.2298	55.2499
	0.2	0.0066	0.1894	0.3057	10.2216	0.5342	19.4510	0.8349	33.4494	1.0371	44.1720	1.1920	53.2018
	0.4	0.0045	0.1282	0.2192	7.0161	0.4116	14.3554	0.7046	27.4052	0.9158	38.1482	1.0800	47.3132
	0.6	0.0030	0.0830	0.1468	4.4753	0.2873	9.4148	0.5357	19.6087	0.7392	29.2617	0.9073	38.0758
	0.8	0.0020	0.0554	0.0999	2.9290	0.1984	6.1454	0.3864	13.1633	0.5580	20.5329	0.7118	27.8896
	1.0	0.0014	0.0387	0.0708	2.0159	0.1412	4.1914	0.2795	8.9524	0.4127	14.1324	0.5392	19.5814
20	0.0	0.0053	0.2125	0.2533	11.2046	0.4632	21.7147	0.7635	38.0455	0.9728	50.1717	1.1344	59.9860
	0.2	0.0046	0.1827	0.2234	9.6892	0.4181	19.2517	0.7128	35.1496	0.9245	47.4254	1.0892	57.4629
	0.4	0.0033	0.1286	0.1637	6.8102	0.3180	13.9886	0.5819	27.6968	0.7907	39.6071	0.9597	49.8587
	0.6	0.0023	0.0861	0.1126	4.5041	0.2230	9.3278	0.4301	19.3860	0.6139	29.3063	0.7747	38.6670
	0.8	0.0016	0.0588	0.0782	3.0404	0.1559	6.2681	0.3076	13.1496	0.4521	20.3719	0.5875	27.6997
	1.0	0.0011	0.0417	0.0561	2.1404	0.1121	4.3846	0.2230	9.1498	0.3318	14.2196	0.4376	19.5153
Sinusoidally distributed load													
5	0.0	0.0056	0.1796	0.2618	9.5222	0.4645	18.1651	0.7390	31.3879	0.9266	41.4695	1.0713	49.8862
	0.2	0.0047	0.1509	0.2263	8.0842	0.4150	15.9619	0.6869	28.8698	0.8776	38.9915	1.0255	47.4812
	0.4	0.0032	0.1018	0.1591	5.4485	0.3071	11.2496	0.5537	22.3444	0.7445	32.0464	0.8975	40.5132
	0.6	0.0021	0.0657	0.1056	3.4617	0.2089	7.2147	0.4013	15.1395	0.5704	23.0496	0.7171	30.5926
	0.8	0.0014	0.0436	0.0717	2.2683	0.1429	4.6983	0.2817	9.9415	0.4137	15.5190	0.5370	21.2433
	1.0	0.0010	0.0304	0.0507	1.5635	0.1013	3.2135	0.2016	6.7492	0.3000	10.5531	0.3955	14.5666
20	0.0	0.0038	0.1676	0.1861	8.7837	0.3524	17.5107	0.6129	32.4539	0.8047	44.2657	0.9556	53.9954
	0.2	0.0033	0.1445	0.1631	7.5738	0.3138	15.3170	0.5626	29.3711	0.7534	41.0311	0.9059	50.8418
	0.4	0.0024	0.1021	0.1185	5.3225	0.2332	10.9298	0.4420	22.1578	0.6195	32.6175	0.7697	42.0541
	0.6	0.0016	0.0685	0.0811	3.5377	0.1614	7.2664	0.3165	15.0797	0.4610	23.0398	0.5932	30.8616
	0.8	0.0011	0.0469	0.0562	2.4011	0.1123	4.9063	0.2230	10.1790	0.3308	15.7124	0.4346	21.4038
	1.0	0.0008	0.0334	0.0403	1.6974	0.0806	3.4511	0.1607	7.1144	0.2400	10.9624	0.3182	14.9652

Table 5.6 Normalised deflection $\bar{w}(\frac{a}{2},\frac{a}{2},0)$ and normal stress $\bar{\sigma}_x(\frac{a}{2},\frac{a}{2},\frac{h}{2})$ of SSSS square Al/Al_2O_3 microplates (Mori-Tanaka scheme, $n=1$)

a/h	ℓ/h	$P=1$		$P=50$		$P=100$		$P=200$		$P=300$		$P=400$	
		$\bar{w}$	$\bar{\sigma}_x$	$\bar{w}$	$\bar{\sigma}_x$	$\bar{w}$	$\bar{\sigma}_x$	$\bar{w}$	$\bar{\sigma}_x$	$\bar{w}$	$\bar{\sigma}_x$	$\bar{w}$	$\bar{\sigma}_x$
Uniformly distributed load													
5	0.0	0.0246	0.5482	0.8626	23.2446	1.2927	36.4602	1.8441	54.2800	2.2443	67.7888	2.5677	79.1820
	0.2	0.0204	0.4508	0.7837	21.0080	1.2086	34.2580	1.7432	52.0767	2.1203	65.4499	2.4228	76.7142
	0.4	0.0134	0.2935	0.5992	15.6113	1.0078	28.4047	1.5359	46.6052	1.9021	60.1880	2.1913	71.4979
	0.6	0.0086	0.1851	0.4126	10.2260	0.7610	20.6531	1.2738	38.2544	1.6418	52.1977	1.9318	63.8747
	0.8	0.0057	0.1218	0.2807	6.6450	0.5445	13.9813	0.9944	28.6153	1.3510	41.8296	1.6419	53.5045
	1.0	0.0040	0.0845	0.1975	4.5215	0.3904	9.5413	0.7501	20.3799	1.0665	31.3703	1.3416	41.9226
20	0.0	0.0208	0.5316	0.7946	23.9070	1.2144	37.9967	1.7284	55.8226	2.0829	68.6366	2.3647	79.2409
	0.2	0.0175	0.4439	0.7194	21.4738	1.1397	35.7215	1.6590	54.0610	2.0150	67.1516	2.2964	77.9038
	0.4	0.0118	0.2965	0.5445	15.7734	0.9433	29.2949	1.4715	48.5974	1.8353	62.5643	2.1207	73.9078
	0.6	0.0077	0.1905	0.3733	10.3586	0.7017	21.0283	1.2070	39.5113	1.5774	54.2015	1.8705	66.3687
	0.8	0.0051	0.1268	0.2546	6.8097	0.4978	14.2377	0.9269	29.2198	1.2789	42.9825	1.5713	55.2276
	1.0	0.0036	0.0887	0.1797	4.6844	0.3564	9.7958	0.6916	20.7632	0.9944	31.9642	1.2638	42.8335
Sinusoidally distributed load													
5	0.0	0.0158	0.3798	0.6338	18.0329	0.9958	30.0539	1.4525	46.3570	1.7760	58.5463	2.0391	68.7806
	0.2	0.0131	0.3132	0.5622	15.8052	0.9188	27.6207	1.3724	43.9945	1.6886	56.1842	1.9412	66.3525
	0.4	0.0086	0.2049	0.4073	11.0309	0.7295	21.3850	1.1784	37.5949	1.4940	50.0152	1.7428	60.3452
	0.6	0.0055	0.1296	0.2703	6.9968	0.5188	14.4617	0.9260	28.5355	1.2384	40.6386	1.4894	51.0792
	0.8	0.0036	0.0854	0.1815	4.5347	0.3581	9.4848	0.6830	19.8922	0.9637	30.1217	1.2048	39.7251
	1.0	0.0025	0.0593	0.1272	3.1011	0.2531	6.4508	0.4970	13.6998	0.7252	21.3563	0.9351	29.1046
20	0.0	0.0132	0.3639	0.5673	17.9897	0.9251	31.0288	1.3732	48.4600	1.6795	60.9978	1.9206	71.2435
	0.2	0.0111	0.3058	0.5007	15.7108	0.8501	28.3741	1.3019	46.0509	1.6118	58.8559	1.8545	69.2807
	0.4	0.0075	0.2067	0.3612	11.0156	0.6651	21.7013	1.1097	39.0466	1.4270	52.3712	1.6761	63.3102
	0.6	0.0049	0.1342	0.2410	7.1278	0.4680	14.6903	0.8566	29.2710	1.1658	42.0916	1.4182	53.2269
	0.8	0.0033	0.0900	0.1630	4.7134	0.3228	9.7725	0.6234	20.3784	0.8915	30.9239	1.1272	40.9518
	1.0	0.0023	0.0632	0.1148	3.2715	0.2288	6.7474	0.4515	14.1668	0.6635	21.9643	0.8622	29.8852

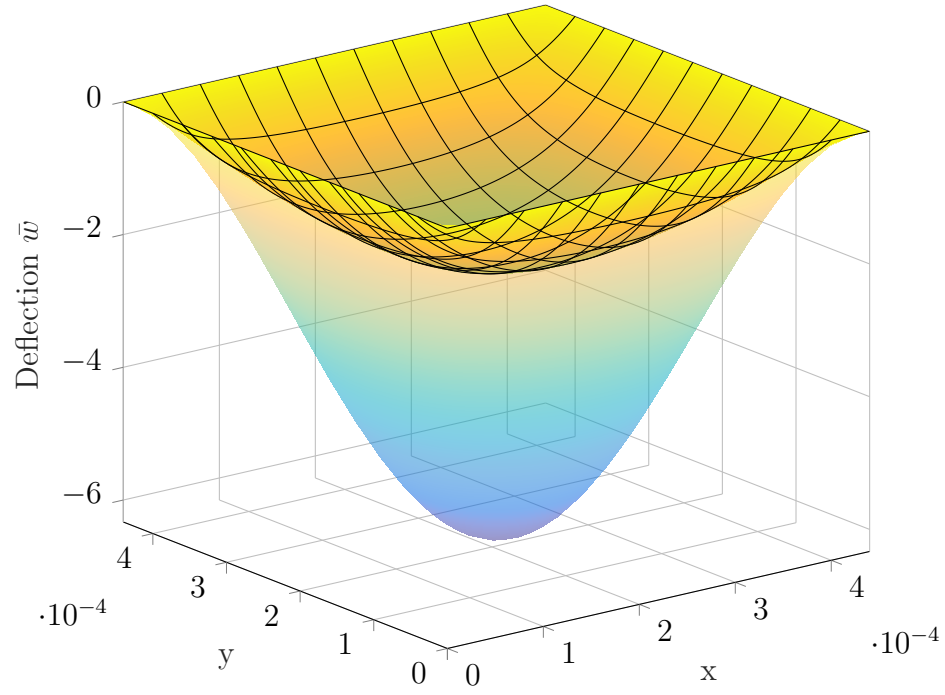

(a) SSSS

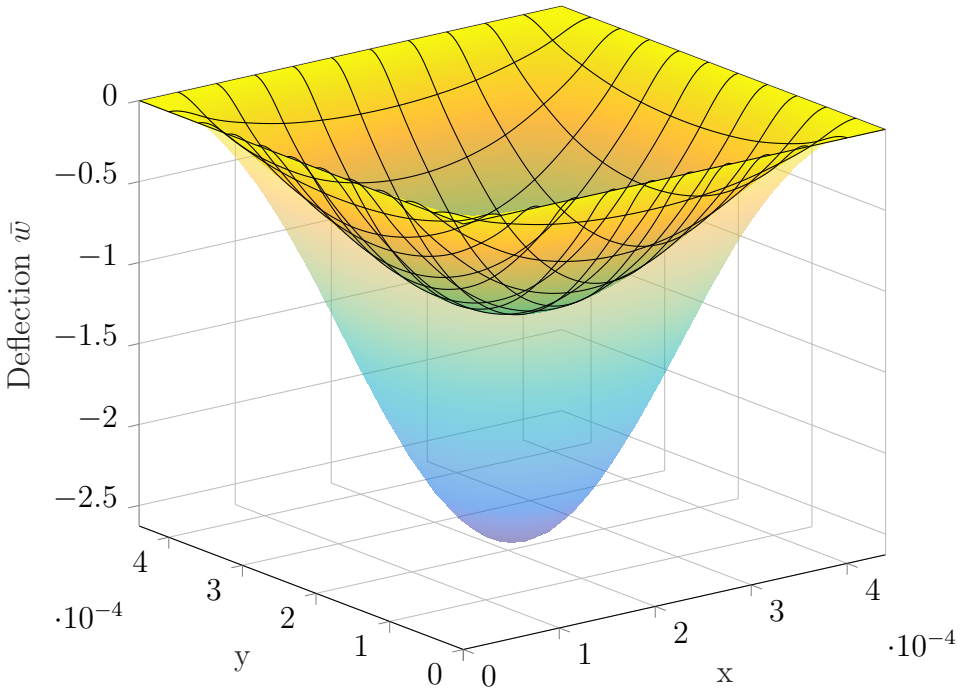

(b) CCCC

Fig. 5.8 Linear (outer) and nonlinear (inner) deformed shape of Al/Al_2O_3 square microplates subjected to uniformly distributed load, $a/h = 5$, $\ell/h = 0.2$, $n = 1$, $P = 400$ (rules of mixtures scheme).

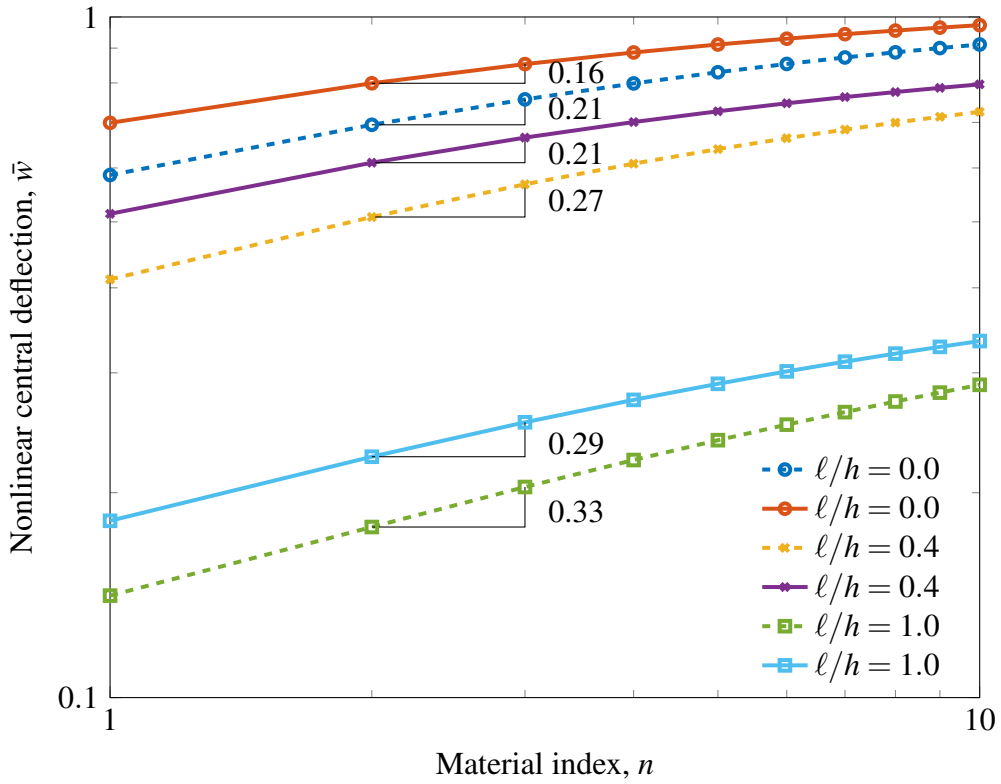

(a) Nonlinear central deflection $\bar{w}(\frac{a}{2}, \frac{a}{2}, 0)$

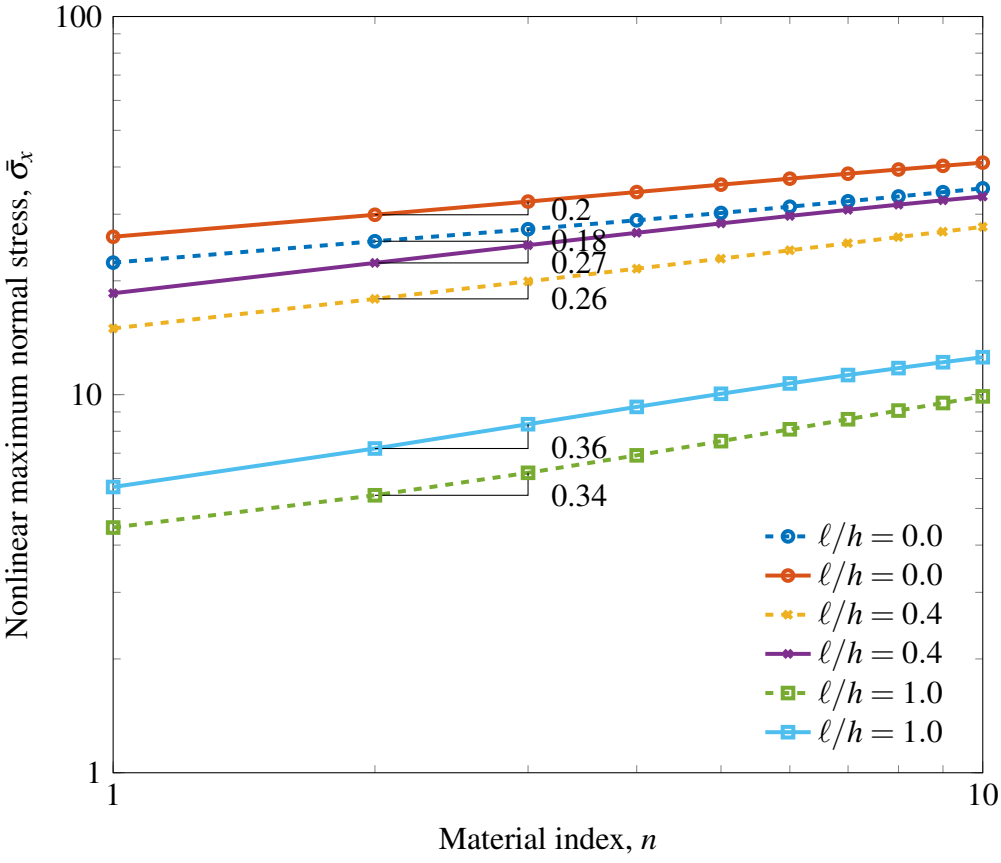

(b) Normal stress $\bar{\sigma}_x(\frac{a}{2}, \frac{a}{2}, \frac{h}{2})$

Fig. 5.9 Effects of material index n and the material length scale ratio ℓ/h on the nonlinear central deflection and normal stress of CCCC Al/Al_2O_3 square microplates, $a/h = 5$, $P = 100$, with the rules of mixtures scheme (dashed line) and Mori-Tanaka scheme (solid line).

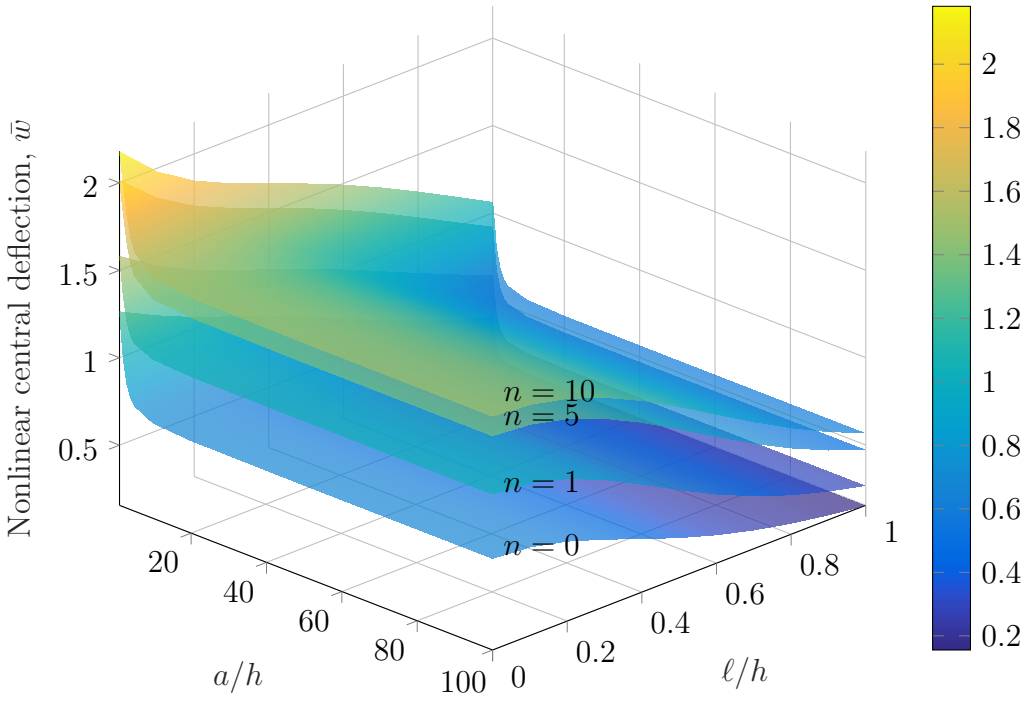

(a) Deflection

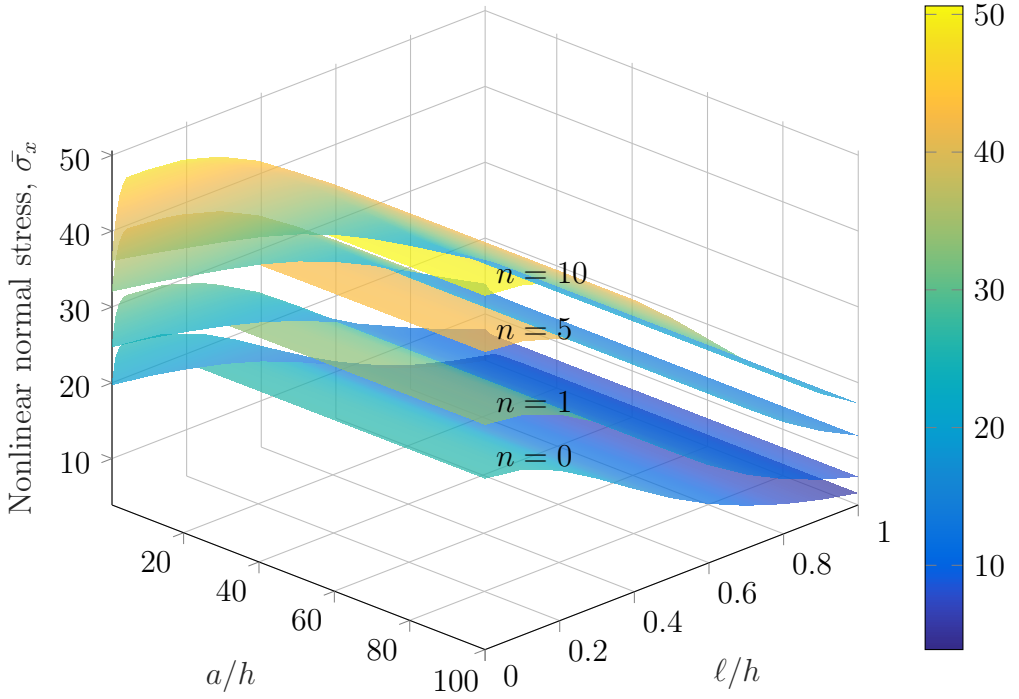

(b) Normal stress

Fig. 5.10 Variation of nonlinear responses of SSSS Al/Al_2O_3 square microplates with respect to a/h and ℓ/h (rule of mixtures scheme), $P = 100$.

nonlinear analysis of FG circular microplates, these numerical results can serve as a benchmark example for future references. Fig. 5.11 provides a visual illustration of the deformed shapes of circular Al/ZnO_2 microplates in which the solutions for linear and nonlinear problems are placed together. The solutions are generated for the specific material and geometry inputs with different boundary conditions.

Fig. 5.12 illustrates the effect of the material index n and material length scale ratio ℓ/h on the nonlinear deflection and normal stress of fully clamped Al/ZnO_2 circular microplates with different material distribution schemes. Similarly to the square microplates, the decline of material index n and the increase of material length scale ratio ℓ/h lead to the strengthening of the plates' stiffness. Consequently, the displacement and normal stress of the plates are both decreased accordingly. However, while the influence of the square plates' aspect ratio a/h on its bending behaviours are different for thin and thick plates, those impacts of the circular plates' aspect ratio h/R on the displacement and normal stress responses remain less pronounced regardless of plates' geometry as shown in Fig. 5.13.

5.3.4 Nonlinear analysis of annular microplates

In this part of the section, a number of analyses are conducted to assess the nonlinear bending behaviours of the annular microplates. The full geometry configuration and element meshes along with control point net of the annular are presented in Fig. 5.1c and Fig. 5.14, respectively. Due to its symmetry, for the sake of computational effort, only a quarter of this cut-out geometry is used for the analysis. The nonlinear bending responses of the annular microplates without considering size effects are compared with the results reported by Golmakani and Kadkhodayan [148]. As can be observed from Fig. 5.15, the results generated from this proposed approach agree well with those published which are based on TSDT theory and the finite difference technique for both fully clamped and simply-supported boundary conditions which are applied at inner and outer circles of the annular microplates.

In order to show the effects of the material length scale to nonlinear bending behaviours of annular microplates, the variations of the vertical displacement through the radius are shown in Fig. 5.16. As expected, when the size-dependent effects are considered, the displacement of the microplate becomes smaller reaching its lowest as the material length scale ratio $\ell/h = 1$. Fig. 5.17 illustrates the

Table 5.7 Normalised deflection $\bar{w}(0,0,0)$ and normal stress $\bar{\sigma}_x(0,0,\frac{h}{2})$ of circular Al/ZnO_2 microplates subjected to uniformly distributed load (rule of mixtures scheme, $n=5$)

h/R	ℓ/h	$P=1$		$P=50$		$P=100$		$P=200$		$P=300$		$P=400$	
		$\bar{w}$	$\bar{\sigma}_x$	$\bar{w}$	$\bar{\sigma}_x$	$\bar{w}$	$\bar{\sigma}_x$	$\bar{w}$	$\bar{\sigma}_x$	$\bar{w}$	$\bar{\sigma}_x$	$\bar{w}$	$\bar{\sigma}_x$
Simply-supported (SSSS, as defined in Reddy et al. [31])													
0.1	0.0	0.3784	1.6354	2.2122	16.6821	2.8106	24.6444	3.5582	36.8432	4.0809	46.8473	4.4966	55.6639
	0.2	0.3722	1.5920	2.2111	16.6896	2.8104	24.6581	3.5585	36.8576	4.0813	46.8609	4.4971	55.6771
	0.4	0.3593	1.4988	2.2083	16.7038	2.8102	24.6960	3.5597	36.9028	4.0829	46.9057	4.4989	55.7212
	0.6	0.3469	1.4084	2.2044	16.7095	2.8098	24.7454	3.5616	36.9742	4.0856	46.9810	4.5020	55.7970
	0.8	0.3372	1.3397	2.2000	16.7014	2.8095	24.7941	3.5641	37.0604	4.0893	47.0794	4.5061	55.8996
	1.0	0.3302	1.2912	2.1957	16.6838	2.8087	24.8329	3.5668	37.1499	4.0934	47.1900	4.5110	56.0201
0.5	0.0	0.4267	1.5608	2.2035	15.8369	2.8018	23.6692	3.5523	35.6463	4.0776	45.4525	4.4954	54.0875
	0.2	0.4194	1.5340	2.2025	15.8886	2.8010	23.7431	3.5515	35.7505	4.0768	45.5786	4.4945	54.2319
	0.4	0.4040	1.4780	2.1999	16.0138	2.7992	23.9233	3.5499	36.0026	4.0750	45.8845	4.4925	54.5829
	0.6	0.3878	1.4219	2.1967	16.1518	2.7974	24.1289	3.5483	36.2909	4.0734	46.2341	4.4908	54.9839
	0.8	0.3737	1.3744	2.1935	16.2643	2.7962	24.3087	3.5479	36.5466	4.0729	46.5443	4.4902	55.3388
	1.0	0.3621	1.3354	2.1905	16.3435	2.7954	24.4455	3.5485	36.7516	4.0739	46.7943	4.4913	55.6260
Fully clamped													
0.1	0.0	0.1383	0.7522	2.0564	15.8791	2.6894	23.3494	3.4603	34.8581	3.9910	44.3909	4.4102	52.8501
	0.2	0.1237	0.6708	2.0281	15.7718	2.6675	23.2474	3.4428	34.7002	3.9760	44.1830	4.3975	52.6031
	0.4	0.0937	0.5053	1.9436	15.3597	2.6037	22.9318	3.3945	34.3111	3.9344	43.6818	4.3595	51.9965
	0.6	0.0667	0.3573	1.8018	14.4121	2.4955	22.2610	3.3141	33.7041	3.8664	42.9934	4.2989	51.2052
	0.8	0.0475	0.2532	1.6082	12.8063	2.3398	21.0101	3.1965	32.7197	3.7685	42.0473	4.2124	50.2166
	1.0	0.0346	0.1842	1.3810	10.7284	2.1391	19.0814	3.0398	31.1718	3.6368	40.6652	4.0962	48.8840
0.5	0.0	0.2722	0.8742	2.1483	14.4573	2.7480	22.0957	3.4935	33.8540	4.0127	43.5197	4.4249	52.0503
	0.2	0.2318	0.7562	2.1289	14.2221	2.7341	21.8094	3.4837	33.5119	4.0050	43.1440	4.4187	51.6510
	0.4	0.1604	0.5263	2.0690	13.7115	2.6901	21.2063	3.4516	32.7902	3.9784	42.3508	4.3953	50.8085
	0.6	0.1051	0.3422	1.9669	12.9403	2.6141	20.4143	3.3948	31.8821	3.9314	41.3505	4.3532	49.7263
	0.8	0.0707	0.2283	1.8198	11.7611	2.5022	19.3106	3.3116	30.7626	3.8612	40.1648	4.2914	48.4734
	1.0	0.0497	0.1597	1.6318	10.1762	2.3529	17.7840	3.1994	29.3084	3.7670	38.7067	4.2082	46.9825

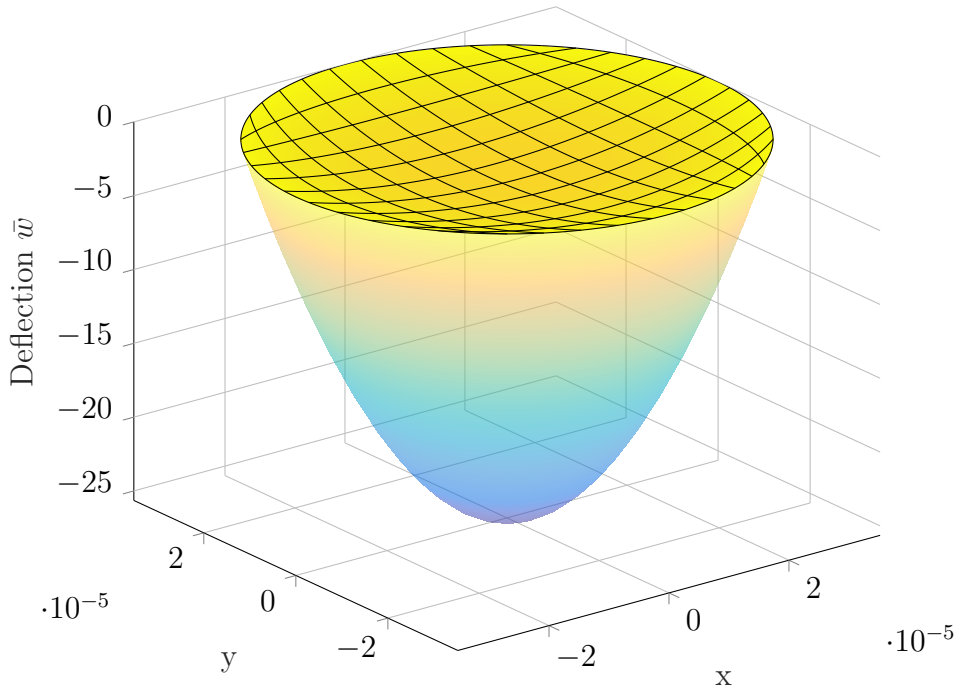

(a) SSSS

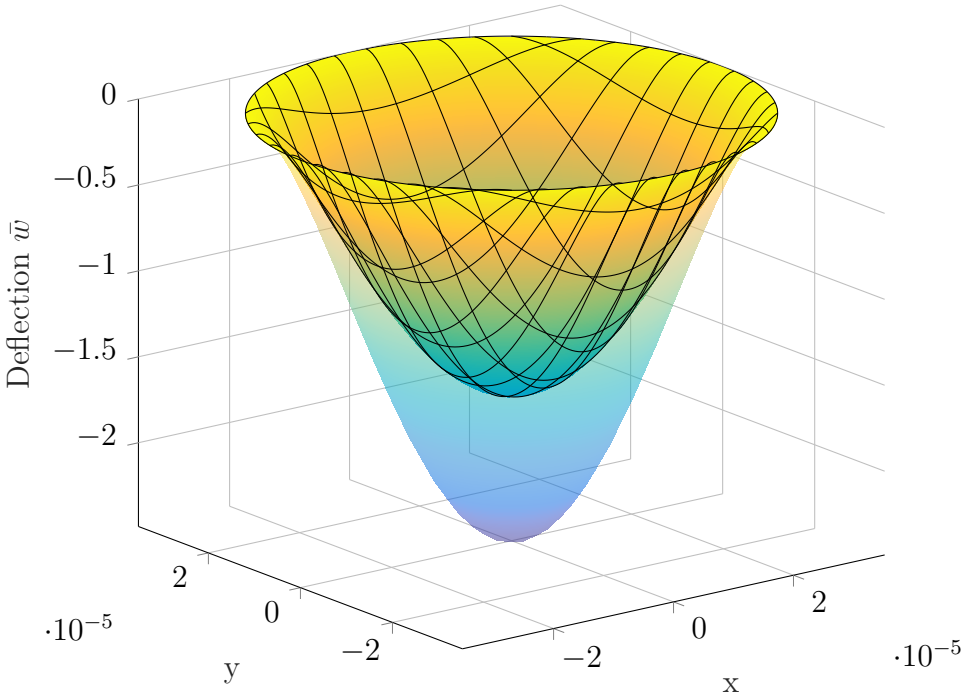

(b) CCCC

Fig. 5.11 Linear (outer) and nonlinear (inner) deformed shape of Al/ZnO_2 circular microplates subjected to uniformly distributed load, $h/R = 0.5$, $\ell/h = 1$, $n = 5$, $P = 50$ (rules of mixtures scheme).

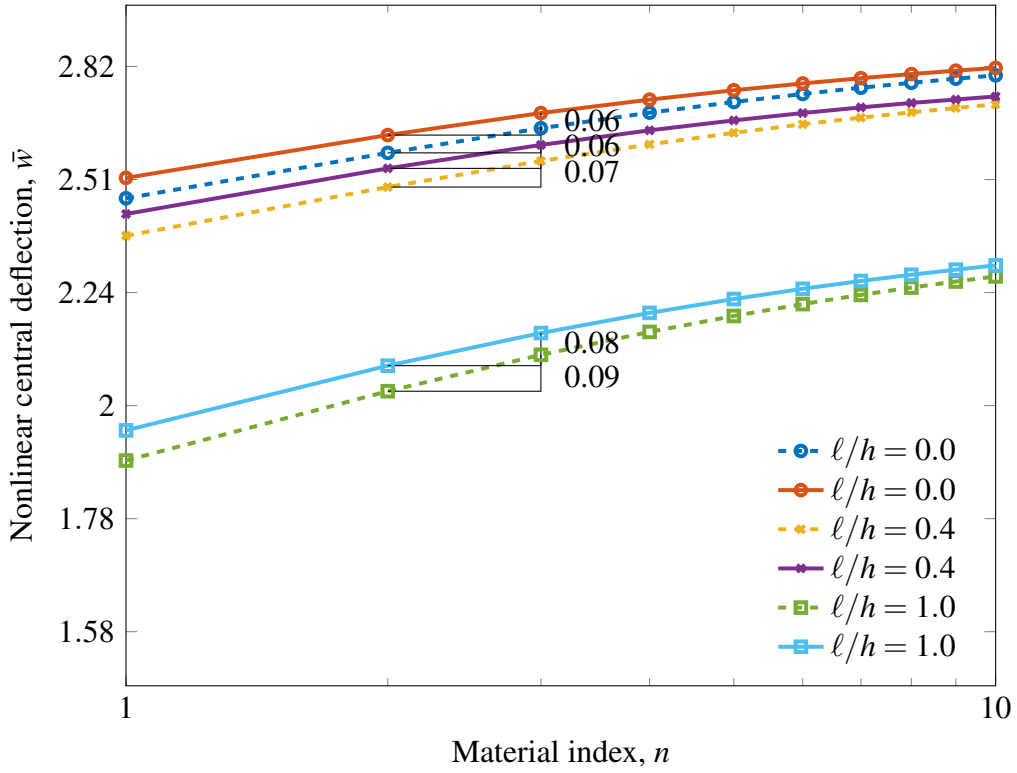

(a) Nonlinear central deflection $\bar{w}(\frac{a}{2}, \frac{a}{2}, 0)$

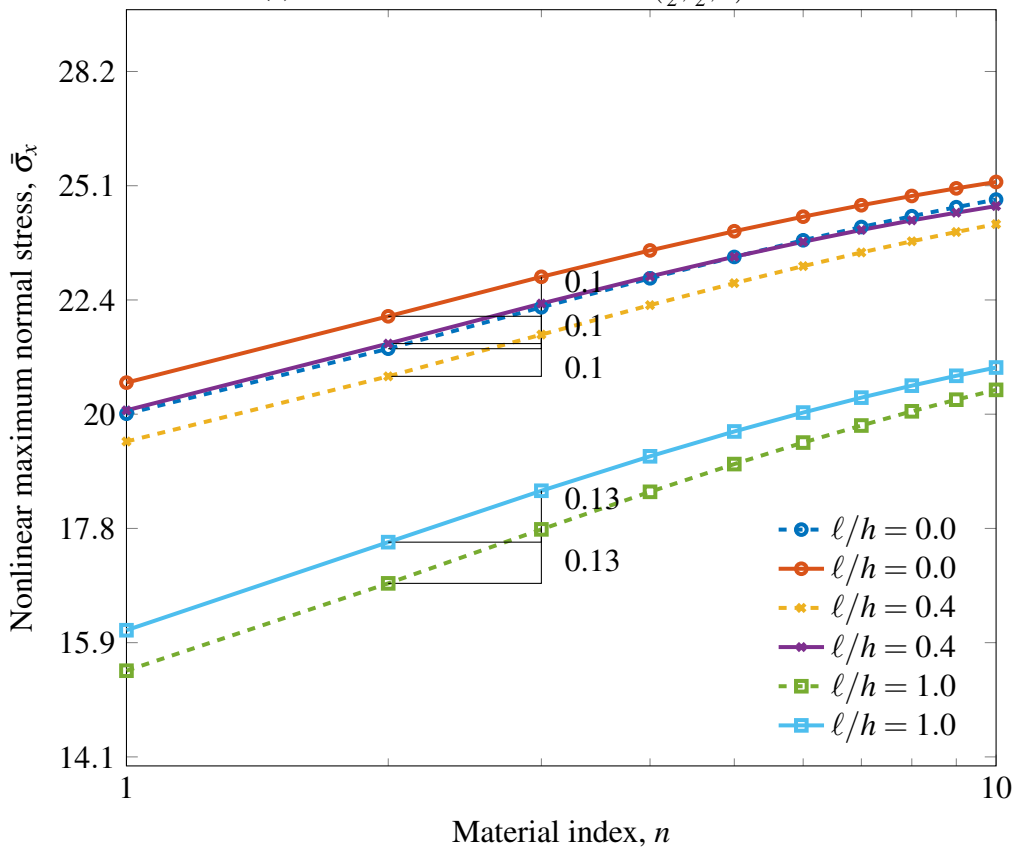

(b) Normal stress $\bar{\sigma}_x(\frac{a}{2}, \frac{a}{2}, \frac{h}{2})$

Fig. 5.12 Effects of the material index n and the material length scale ratio ℓ/h on the nonlinear central deflection and normal stress of fully clamped Al/ZnO_2 circular microplates, $h/R = 0.2, P = 100$, with the rules of mixtures scheme (dashed line) and Mori-Tanaka scheme (solid line).

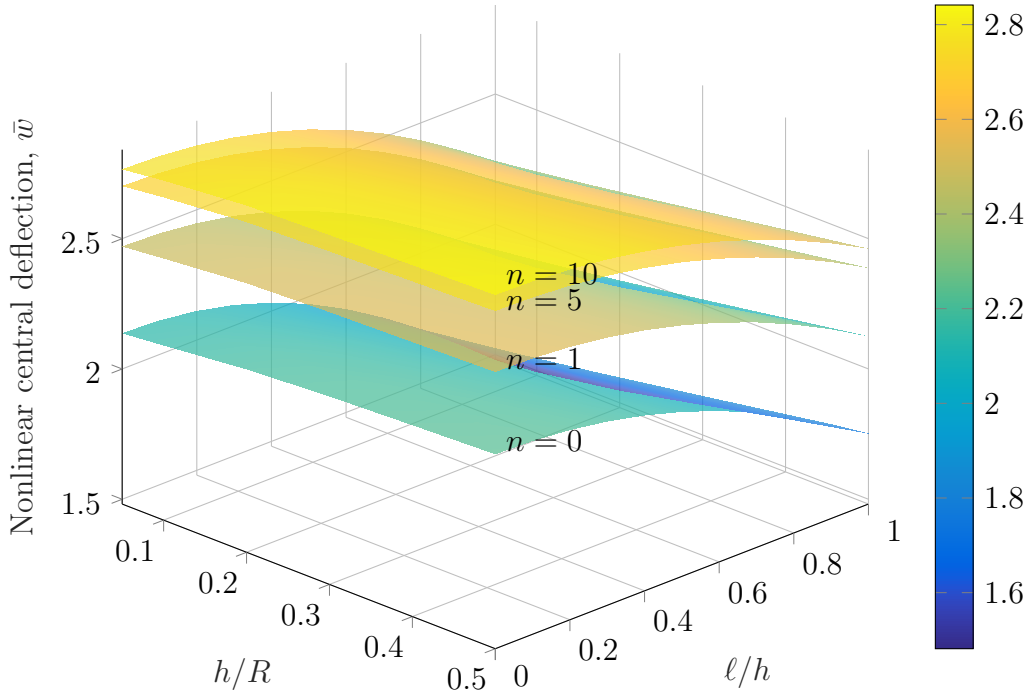

(a) Deflection

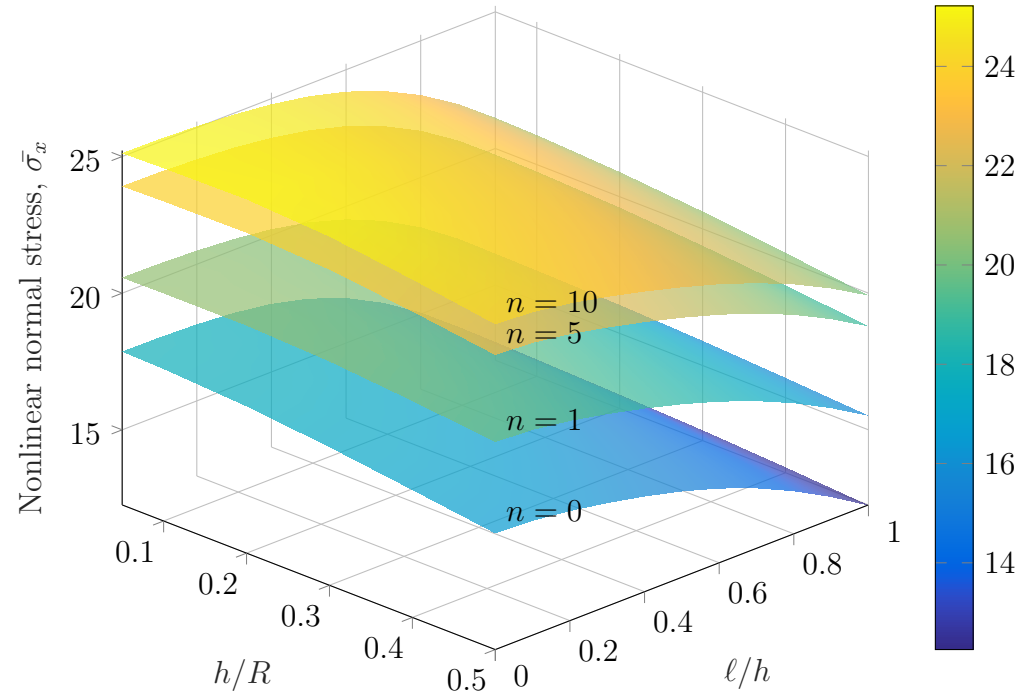

(b) Normal stress

Fig. 5.13 Variation of nonlinear responses of fully clamped Al/ZnO_2 circular microplates with respect to h/R and ℓ/h (Mori-Tanaka scheme), $P = 100$.

deformed shapes of annular microplates for both linear and nonlinear bending cases with same geometry, material and loading inputs. Similarly to other geometries, the linear analysis predicts larger deflections than that of nonlinear case in which von Kármán strains are involved.

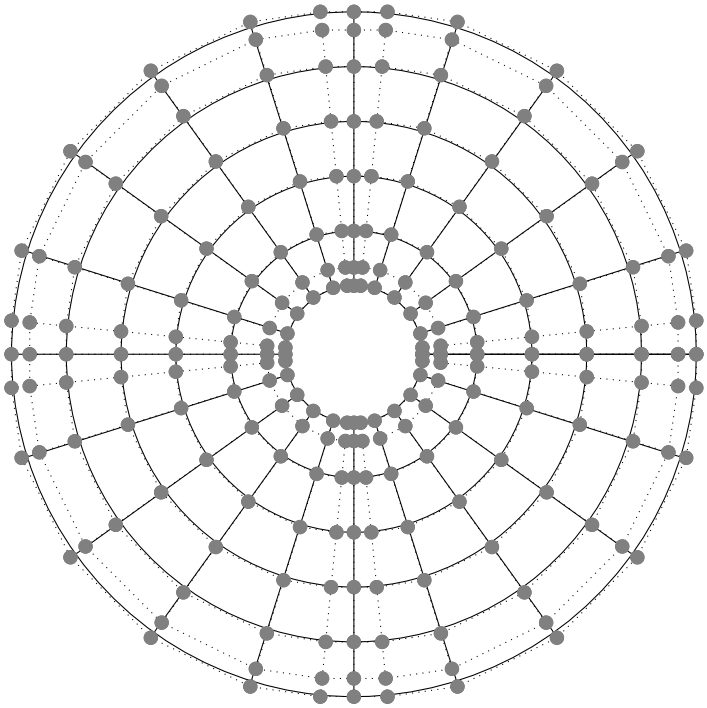

(a) A full annular plate

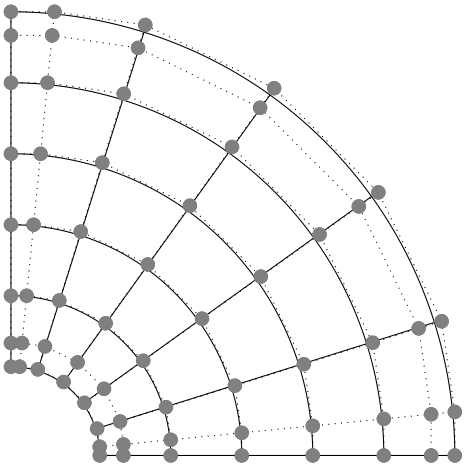

(b) A quarter of an annular plate

Fig. 5.14 Element mesh (solid line), control point (grey dot) and control point net (dotted line).

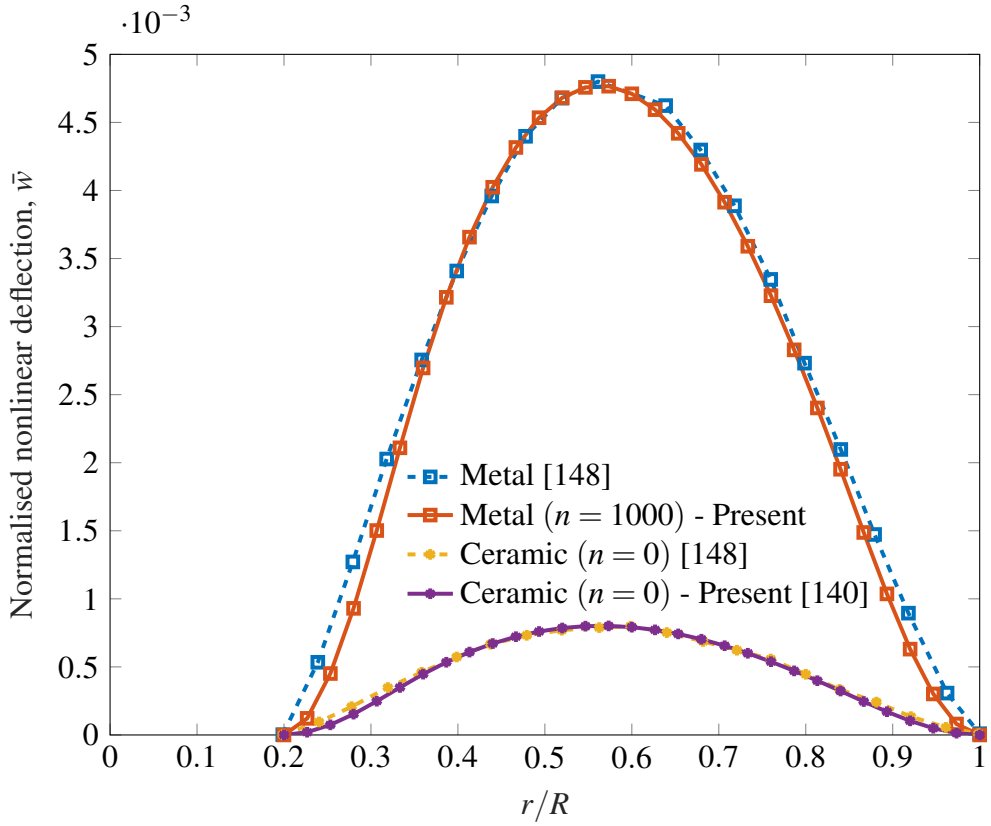

(a) Clamped-clamped plate

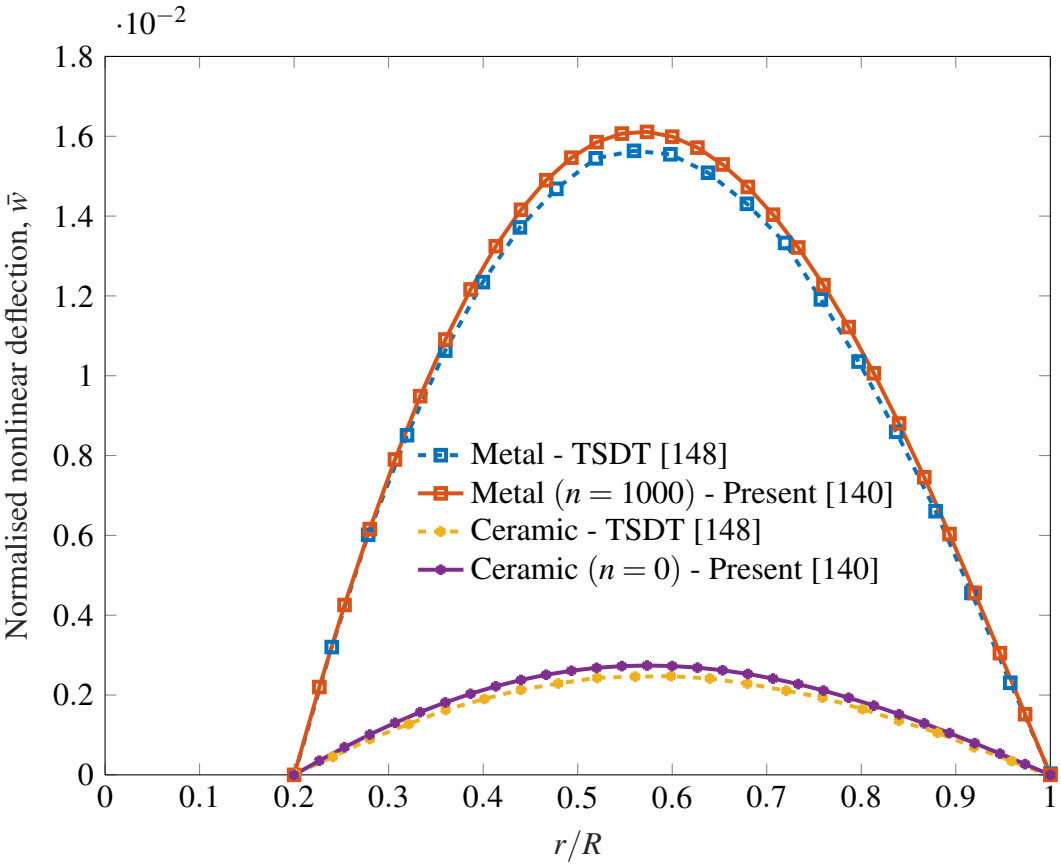

(b) Simply-supported plate

Fig. 5.15 Comparison of nonlinear deflection through radius of Al/SiC annular plates, $h/R = 0.15$.

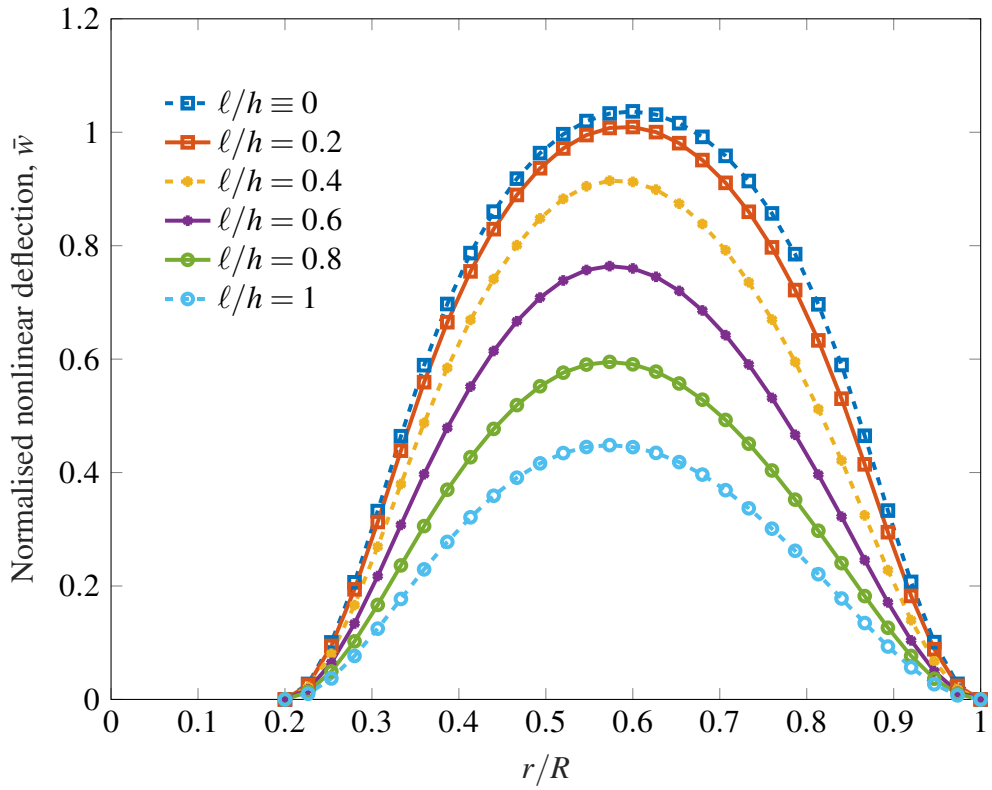

Fig. 5.16 Normalised deflection of CC Al/SiC annular microplates, $h/R = 0.3$, $n = 0$, $P = 600$.

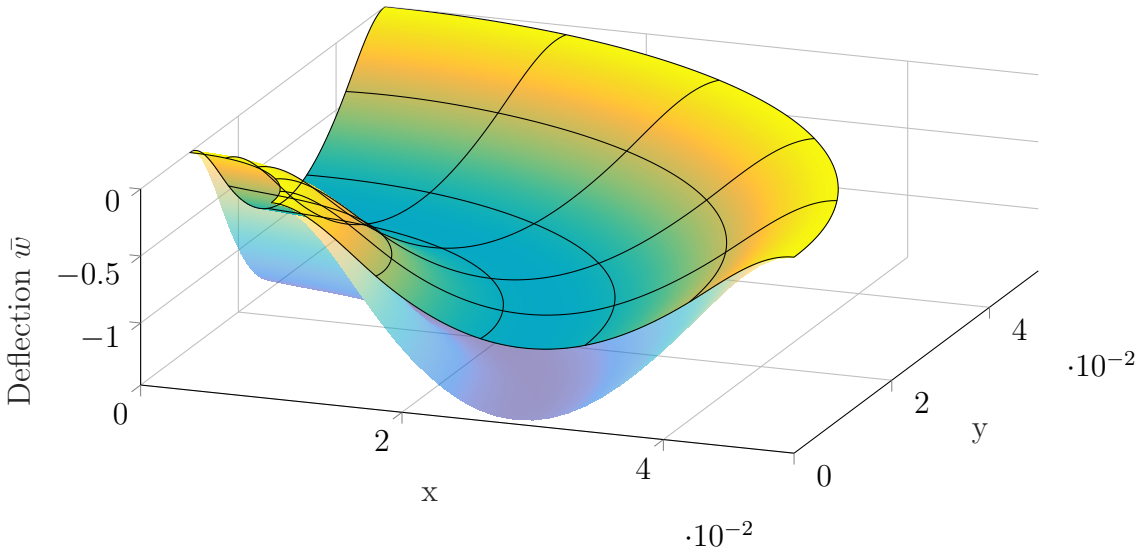

Fig. 5.17 Linear (outer) and nonlinear (inner) deformed shapes of Al/SiC annular microplates subjected to uniformly distributed load, $h/R = 0.15$, $\ell/h = 0.2$, $n = 0$, $P = 600$.

Chapter 6

Free vibration analysis of cracked small-scale plates[1]

In this chapter, the vibration analysis of microplates with cracks will be presented. The simplified strain gradient theory which includes one material length parameter and an additional *micro-inertia* term is employed to capture the size effects. Meanwhile, the extended isogeometric analysis (XIGA) with Heaviside and branch enrichment functions are involved to model the discontinuity along the crack path and increase the solution at the vicinity of the crack tip, respectively. In addition, the IGA approach with highly smooth basis functions of non-uniform rational B-spline (NURBS) ensures a clean and efficient treatment of higher continuity requirements in the strain gradient theory. The benchmark numerical results show significant departure from those analysed by the classical continuum elasticity. Indeed, they reveal strong influences of microstructural characteristics on the vibration responses of microplates which are not shown in the platform of the classical theory and the influences are more pronounced as the size of the plates becomes comparable with the material length parameter.

[1]The results in this chapter have been published in Nguyen et al. [149]

6.1 Strain gradient FG plate formulation

6.1.1 Kinematics of the refined plate theory

Similarly to the previous chapter, the displacement-strain relations associated with the refined plate theory [62] can be explicitly presented as follows

$$\boldsymbol{\varepsilon} = \boldsymbol{\varepsilon}_0 + z\boldsymbol{\kappa}_b + g(z)\,\boldsymbol{\kappa}_s, \tag{6.1a}$$

$$\boldsymbol{\gamma} = \left[1 + g'(z)\right]\boldsymbol{\varepsilon}_s = f'(z)\,\boldsymbol{\varepsilon}_s, \tag{6.1b}$$

where

$$\boldsymbol{\varepsilon} = \begin{bmatrix} \varepsilon_x & \varepsilon_y & \gamma_{xy} \end{bmatrix}^T, \tag{6.2a}$$

$$\boldsymbol{\gamma} = \begin{bmatrix} \gamma_{xz} & \gamma_{yz} \end{bmatrix}^T, \tag{6.2b}$$

and the in-plane, bending and shear strains are expressed as

$$\boldsymbol{\varepsilon}_0 = \begin{bmatrix} u_{0,x} \\ v_{0,y} \\ u_{0,y} + v_{0,x} \end{bmatrix}, \quad \boldsymbol{\kappa}_b = -\begin{bmatrix} w_{b,xx} \\ w_{b,yy} \\ 2w_{b,xy} \end{bmatrix}, \quad \boldsymbol{\kappa}_s = \begin{bmatrix} w_{s,xx} \\ w_{s,yy} \\ 2w_{s,xy} \end{bmatrix}, \quad \boldsymbol{\varepsilon}_s = \begin{bmatrix} w_{s,x} \\ w_{s,y} \end{bmatrix}. \tag{6.3}$$

By using Eqs. (2.9) and (6.1), the strain gradient components can be given in a set of three equations as follows

$$\boldsymbol{\kappa}_i = \boldsymbol{\kappa}_i^0 + z\boldsymbol{\kappa}_i^1 + g(z)\,\boldsymbol{\kappa}_i^2 + g'(z)\,\boldsymbol{\kappa}_i^3 + g''(z)\,\boldsymbol{\kappa}_i^4, \tag{6.4}$$

where i represents three possibilities of $\{x, y, z\}$. The detailed expressions of the strain gradient tensors in terms of macroscopic displacement components can be found in Appendix A.1.

6.1.2 Constitutive relations

In view of Eq. (2.10), the constitutive equation in the classical elasticity theory can be determined as follows

$$\sigma_{ij} = \frac{\partial U_0}{\partial \varepsilon_{ij}} = \lambda\,\delta_{ij}\varepsilon_{kk} + 2\mu\,\varepsilon_{ij}, \tag{6.5}$$

where $\sigma_{ij} = \sigma_{ji}$ are components of monopolar (or Cauchy) stress tensor. Meanwhile, the strain gradient constitutive equations are expressed as

$$\eta_{ijk} = \frac{\partial U_0}{\partial \kappa_{ijk}} = \ell^2 \left(\lambda \delta_{jk} \kappa_{ipp} + 2\mu \kappa_{ijk}\right) = \ell^2 \left(\lambda \delta_{jk} \varepsilon_{pp,i} + 2\mu \varepsilon_{jk,i}\right), \tag{6.6}$$

in which $\eta_{ijk} = \eta_{ikj}$ denote components of dipolar (or double) stress tensor having dimension of [force][length]$^{-1}$. The Lamé's constants λ and μ, which is also known as shear modulus G, are related to the effective Young's modulus E and Poisson's ratio ν.

It should be noted that the effective engineering constants E and ν for the FGMs which is used in this study are varied continuously through the plate's thickness. The estimation of these constants at a specific point can be made following the rules of mixture or the Mori-Tanaka scheme [95, 96]. A review of these estimating models and the properties of the FGMs can be found in Section 2.4.

With the assumption of $\sigma_{zz} = 0$, the monopolar stress components can be written explicitly as follows

$$\begin{Bmatrix} \sigma_x \\ \sigma_y \\ \sigma_{xy} \\ \sigma_{xz} \\ \sigma_{yz} \end{Bmatrix} = \begin{bmatrix} Q_{11} & Q_{12} & 0 & 0 & 0 \\ Q_{21} & Q_{22} & 0 & 0 & 0 \\ 0 & 0 & Q_{66} & 0 & 0 \\ 0 & 0 & 0 & Q_{55} & 0 \\ 0 & 0 & 0 & 0 & Q_{44} \end{bmatrix} \begin{Bmatrix} \varepsilon_x \\ \varepsilon_y \\ \gamma_{xy} \\ \gamma_{xz} \\ \gamma_{yz} \end{Bmatrix} \tag{6.7}$$

where

$$Q_{11} = Q_{22} = \frac{E}{1-\nu^2};\ Q_{12} = Q_{21} = \frac{\nu E}{1-\nu^2};\ Q_{44} = Q_{55} = Q_{66} = \frac{E}{2(1+\nu)} \tag{6.8}$$

Meanwhile, the dipolar stress components are expressed in a set of three equations as follows

$$\begin{Bmatrix} \eta_{ixx} \\ \eta_{iyy} \\ \eta_{iyz} \\ \eta_{ixz} \\ \eta_{ixy} \end{Bmatrix} = \ell^2 \begin{bmatrix} Q_{11} & Q_{12} & 0 & 0 & 0 \\ Q_{21} & Q_{22} & 0 & 0 & 0 \\ 0 & 0 & Q_{44} & 0 & 0 \\ 0 & 0 & 0 & Q_{55} & 0 \\ 0 & 0 & 0 & 0 & Q_{66} \end{bmatrix} \begin{Bmatrix} \kappa_{ixx} \\ \kappa_{iyy} \\ 2\kappa_{iyz} \\ 2\kappa_{ixz} \\ 2\kappa_{ixy} \end{Bmatrix} \tag{6.9}$$

where i is one of the values from the set $\{x,y,z\}$.

6.1.3 Variational formulation

In view of Eqs. (2.10) and (2.11), the strain energy and kinetic energy can be calculated by taking the integration of the energy densities over the volume occupied by the structures as follows

$$U = \int_V U_0 dV = \int_V \boldsymbol{\sigma} : \boldsymbol{\varepsilon} dV + \int_V \boldsymbol{\eta} : \boldsymbol{\kappa} dV \tag{6.10a}$$

$$K = \int_V K_0 dV = \int_V \left(\frac{1}{2}\rho \dot{\mathbf{u}} \cdot \dot{\mathbf{u}} + \frac{1}{6}\rho d^2 \frac{\partial \dot{\mathbf{u}}}{\partial \mathbf{x}} \cdot \frac{\partial \dot{\mathbf{u}}}{\partial \mathbf{x}} \right) dV, \tag{6.10b}$$

where $\boldsymbol{\sigma}$, $\boldsymbol{\varepsilon}$, $\boldsymbol{\eta}$, and $\boldsymbol{\kappa}$ represent monopolar stress, strain, dipolar stress, and strain gradient components, respectively. Meanwhile, $\mathbf{u} = \{u,v,w\}^T$ and $\mathbf{x}$ are displacement and three-dimensional spatial components, and V is the region in $\mathbb{R}^3$ occupied by the body. As can be observed from Eq. (6.10), both strain energy and kinetic energy consist of the classical terms and gradient terms. This inclusion enables the current approach to be able to comprehensively describe the structural behaviours across the scales.

By applying the principle of virtual work, the weak form of the free vibration problem can be expressed as follows

$$\begin{aligned}\left(\int_\Omega \delta\boldsymbol{\varepsilon}_b^T \mathbf{D}^b \boldsymbol{\varepsilon}_b d\Omega + \int_\Omega \delta\boldsymbol{\varepsilon}_s^T \mathbf{D}^s \boldsymbol{\varepsilon}_s d\Omega \right) + \left(\int_\Omega \delta\hat{\boldsymbol{\kappa}}_x^T \hat{\mathbf{D}} \hat{\boldsymbol{\kappa}}_x d\Omega + \int_\Omega \delta\hat{\boldsymbol{\kappa}}_y^T \hat{\mathbf{D}} \hat{\boldsymbol{\kappa}}_y d\Omega + \int_\Omega \delta\hat{\boldsymbol{\kappa}}_z^T \hat{\mathbf{D}} \hat{\boldsymbol{\kappa}}_z d\Omega \right) \\ = \int_\Omega \delta\tilde{\mathbf{u}}^T \tilde{\mathbf{m}} \ddot{\tilde{\mathbf{u}}} d\Omega + \frac{1}{3}d^2 \int_\Omega \left(\delta\tilde{\mathbf{u}}_{,x}^T \tilde{\mathbf{m}} \ddot{\tilde{\mathbf{u}}}_{,x} + \delta\tilde{\mathbf{u}}_{,y}^T \tilde{\mathbf{m}} \ddot{\tilde{\mathbf{u}}}_{,y} + \delta\tilde{\mathbf{u}}_{,z}^T \tilde{\mathbf{m}} \ddot{\tilde{\mathbf{u}}}_{,z} \right) d\Omega\end{aligned} \tag{6.11}$$

where Ω is the domain in $\mathbb{R}^2$ occupied by the mid-plane of the plate ($V = \Omega \times \left[-\frac{h}{2}, \frac{h}{2}\right]$) and the strain tensor as well as the material matrix are

$$\boldsymbol{\varepsilon}_b = \begin{Bmatrix} \boldsymbol{\varepsilon}_0 \\ \boldsymbol{\kappa}_b \\ \boldsymbol{\kappa}_s \end{Bmatrix}, \quad \mathbf{D}^b = \begin{bmatrix} \mathbf{A} & \mathbf{B} & \mathbf{E} \\ \mathbf{B} & \mathbf{D} & \mathbf{F} \\ \mathbf{E} & \mathbf{F} & \mathbf{H} \end{bmatrix}, \tag{6.12}$$

in which matrix components are defined as

$$\left(A_{ij},B_{ij},D_{ij},E_{ij},F_{ij},H_{ij}\right)=\int_{-h/2}^{h/2}\left(1,z,z^2,g,zg,g^2\right)\bar{Q}_{ij}dz, \tag{6.13a}$$

$$D_{ij}^{s}=\int_{-h/2}^{h/2}\left[1+g'(z)\right]^2\hat{Q}_{ij}dz, \tag{6.13b}$$

$$\bar{\mathbf{Q}}=\begin{bmatrix} Q_{11} & Q_{12} & 0 \\ Q_{21} & Q_{22} & 0 \\ 0 & 0 & Q_{66} \end{bmatrix}, \tag{6.13c}$$

$$\hat{\mathbf{Q}}=\begin{bmatrix} Q_{44} & 0 \\ 0 & Q_{55} \end{bmatrix}. \tag{6.13d}$$

Meanwhile, the strain gradient tensor and the material matrices related to the gradient terms are

$$\hat{\boldsymbol{\kappa}}_x=\begin{Bmatrix} \boldsymbol{\kappa}_x^0 \\ \boldsymbol{\kappa}_x^1 \\ \boldsymbol{\kappa}_x^2 \\ \boldsymbol{\kappa}_x^3 \\ \boldsymbol{\kappa}_x^4 \end{Bmatrix},\quad \hat{\boldsymbol{\kappa}}_y=\begin{Bmatrix} \boldsymbol{\kappa}_y^0 \\ \boldsymbol{\kappa}_y^1 \\ \boldsymbol{\kappa}_y^2 \\ \boldsymbol{\kappa}_y^3 \\ \boldsymbol{\kappa}_y^4 \end{Bmatrix},\quad \hat{\boldsymbol{\kappa}}_z=\begin{Bmatrix} \boldsymbol{\kappa}_z^0 \\ \boldsymbol{\kappa}_z^1 \\ \boldsymbol{\kappa}_z^2 \\ \boldsymbol{\kappa}_z^3 \\ \boldsymbol{\kappa}_z^4 \end{Bmatrix},\quad \hat{\mathbf{D}}=\begin{bmatrix} \mathbf{A}^g & \mathbf{B}^g & \mathbf{E}^g & \mathbf{G}^g & \mathbf{M}^g \\ \mathbf{B}^g & \mathbf{D}^g & \mathbf{F}^g & \mathbf{I}^g & \mathbf{N}^g \\ \mathbf{E}^g & \mathbf{F}^g & \mathbf{H}^g & \mathbf{J}^g & \mathbf{P}^g \\ \mathbf{G}^g & \mathbf{I}^g & \mathbf{J}^g & \mathbf{L}^g & \mathbf{Q}^g \\ \mathbf{M}^g & \mathbf{N}^g & \mathbf{P}^g & \mathbf{Q}^g & \mathbf{R}^g \end{bmatrix}, \tag{6.14}$$

in which

$$\begin{aligned}&\left(A_{ij}^g,B_{ij}^g,D_{ij}^g,E_{ij}^g,F_{ij}^g,H_{ij}^g,G_{ij}^g,I_{ij}^g,J_{ij}^g,L_{ij}^g,M_{ij}^g,N_{ij}^g,P_{ij}^g,Q_{ij}^g,R_{ij}^g\right)\\ &=\int_{-h/2}^{h/2}\left(1,z,z^2,g,zg,g^2,g',zg',gg',\left(g'\right)^2,g'',zg'',gg'',g'g'',\left(g''\right)^2\right)Q_{ij}dz.\end{aligned} \tag{6.15}$$

For the terms related to the kinetic energy,

$$\tilde{\mathbf{u}}=\left\{\begin{array}{ccccccccc} u_0 & -w_{b,x} & w_{s,x} & v_0 & -w_{b,y} & w_{s,y} & w_b & w_s & 0 \end{array}\right\}^T,\quad \tilde{\mathbf{m}}=\begin{bmatrix} \mathbf{I}_0 & 0 & 0 \\ 0 & \mathbf{I}_0 & 0 \\ 0 & 0 & \mathbf{I}_1 \end{bmatrix}, \tag{6.16}$$

where

$$\mathbf{I}_0 = \begin{bmatrix} I_1 & I_2 & I_4 \\ I_2 & I_3 & I_5 \\ I_4 & I_5 & I_6 \end{bmatrix}, \ \mathbf{I}_1 = \begin{bmatrix} I_1 & I_1 & 0 \\ I_1 & I_1 & 0 \\ 0 & 0 & 0 \end{bmatrix}, \tag{6.17a}$$

$$(I_1, I_2, I_3, I_4, I_5, I_6) = \int_{-h/2}^{h/2} \rho \left(1, z, z^2, g, zg, g^2\right) dz. \tag{6.17b}$$

6.2 Extended isogeometric analysis discretisation for microplate with cracks

In the platform of the extended isogeometric analysis, the displacements of a plate with cracks are predicted by enriching the standard approximation as follows

$$\mathbf{u}^h(\mathbf{x}) = \sum_{I \in \mathcal{N}} R_I(\mathbf{x})\, \mathbf{q}_I + \sum_{J \in \mathcal{N}_{cr}} R_J(\mathbf{x}) \left(H(\mathbf{x}) - H(\mathbf{x}_J)\right) \mathbf{a}_J + \sum_{K \in \mathcal{N}_{tip}} R_K(\mathbf{x}) \sum_{\alpha=1}^{n_\alpha} \left(B_\alpha(\mathbf{x}) - B_\alpha(\mathbf{x}_K)\right) \mathbf{b}_{\alpha K}, \tag{6.18}$$

where the R_I, R_J, and R_K are NURBS basis functions, $H(\mathbf{x})$ and $B_\alpha(\mathbf{x})$ are Heaviside and crack-tip enrichment functions, respectively. While $\mathbf{q}_I$, $\mathbf{a}_J$, and $\mathbf{b}_{\alpha K}$ are variables associated with the control points and enrichments, n_α represents the number of crack-tip enrichment functions used. Meanwhile, $\mathbf{x}$ is now two-dimensional spatial components. It should be noted that the local enrichment functions R_J and R_K are not necessary to be the same as the shape function R_I which is used for the displacement approximation [150]. $\mathcal{N}$ is the set of all control points. Besides, $\mathcal{N}_{cr}$ represents the set of control points whose supports are bisected by the crack while $\mathcal{N}_{tip}$ is the set of all control points whose support contains the crack tip. As the integration gets less reliable results in the elements being cut by the crack path or element with crack tip, in this study, the full integration with subtriangle technique is used to improve the approximation in such elements. A brief description of different sets of control point and how enriched elements being segmented into subtriangles is provided in Fig. 6.1.

The Heaviside function which is employed to model the discontinuity in structure with cracks takes values of $+1$ if the point of interest in physical coordinate $\mathbf{x}$ is on one side the crack and -1 otherwise. Giving $\mathbf{x}^*$ is the closet point on the crack to $\mathbf{x}$ and $\mathbf{e}_n$ is the unit normal vector at $\mathbf{x}^*$, the function can be expressed

mathematically as follow [121]

$$H(\mathbf{x}) = \begin{cases} +1 & \text{if } (\mathbf{x}-\mathbf{x}^*).\mathbf{e}_n > 0, \\ -1 & \text{otherwise.} \end{cases} \tag{6.19}$$

Fig. 6.2 illustrates a simple representation of the Heaviside function and its effects on the basis functions in approximation of fields in which a crack at $\xi = 0.4$ is considered.

Meanwhile, the crack-tip enrichment functions improve the accuracy of the solution by spanning the near tip asymptotic field and reliably describing the singular stress field near the crack tip. The choice of the crack-tip enrichment functions depends on the original displacement description of the problem and how well the function can capture the near tip asymptotic field [121]. In this specific problem of the small-scale plates in which the RPT and SGT are employed, the enrichment functions should also account for the inclusion of high-order strain gradient terms [151]. They are defined in the local polar coordinates associated with the crack tip as follows

$$\mathbf{B} \equiv \begin{cases} \left[r^{3/2}\sin\frac{\theta}{2}, r^{3/2}\cos\frac{\theta}{2}, r^{3/2}\sin\frac{3\theta}{2}, r^{3/2}\cos\frac{3\theta}{2}, r^{3/2}\sin\frac{5\theta}{2}, r^{3/2}\cos\frac{5\theta}{2} \right] & \text{for } u_0, v_0, \\ \left[r^{3/2}\sin\frac{\theta}{2}, r^{3/2}\sin\frac{3\theta}{2}, r^{5/2}\sin\frac{\theta}{2}, r^{5/2}\cos\frac{\theta}{2}, r^{5/2}\sin\frac{3\theta}{2}, r^{5/2}\cos\frac{3\theta}{2}, r^{5/2}\sin\frac{5\theta}{2}, r^{5/2}\cos\frac{5\theta}{2} \right] & \text{for } w_b, w_s. \end{cases} \tag{6.20}$$

By substituting the approximation in Eq. (6.18) into the strains derived in Eqs. (6.1)-(6.3), the classical strain components can be expressed in terms of the basis functions and enrichment functions as follows

$$\boldsymbol{\varepsilon}_b = \begin{bmatrix} \boldsymbol{\varepsilon}_0^T & \boldsymbol{\kappa}_b^T & \boldsymbol{\kappa}_s^T \end{bmatrix}^T = \sum_A \begin{bmatrix} \left(\mathbf{B}_A^m\right)^T & \left(\mathbf{B}_A^{b1}\right)^T & \left(\mathbf{B}_A^{b2}\right)^T \end{bmatrix}^T \mathbf{q}_A, \tag{6.21a}$$

$$\boldsymbol{\varepsilon}_s = \sum_A \mathbf{B}_A^s \mathbf{q}_A, \tag{6.21b}$$

where $\mathbf{q}_A$ consists of both displacement and enrichment variables and the detailed expressions of $\mathbf{B}_A^m, \mathbf{B}_A^{b1}, \mathbf{B}_A^{b2}$, and $\mathbf{B}_A^s$ matrices are given in Appendix A.2.

Similarly, by using Eqs. (6.18), (6.4) and Appendix A.1, the strain gradient tensors can be expressed in the form of the following equations

$$\left[\begin{array}{ccccc} \left(\boldsymbol{\kappa}_i^0\right)^T & \left(\boldsymbol{\kappa}_i^1\right)^T & \left(\boldsymbol{\kappa}_i^2\right)^T & \left(\boldsymbol{\kappa}_i^3\right)^T & \left(\boldsymbol{\kappa}_i^4\right)^T \end{array} \right]^T = \sum_A \left[\begin{array}{ccccc} \left(\mathbf{B}_A^{i0}\right)^T & \left(\mathbf{B}_A^{i1}\right)^T & \left(\mathbf{B}_A^{i2}\right)^T & \left(\mathbf{B}_A^{i3}\right)^T & \left(\mathbf{B}_A^{i4}\right)^T \end{array} \right]^T \mathbf{q}_A, \tag{6.22}$$

where i represents three possibilities of $\{x, y, z\}$ and the detailed expressions of the matrices in the RHS are given in Appendix A.2.

The discretised systems of equations for the free vibration analysis using extented isogemetric analysis is

$$\left(\mathbf{K} - \omega^2 \mathbf{M}\right) \mathbf{q} = \mathbf{0}, \tag{6.23}$$

where the global stiffness and mass matrices are respectively given as

$$\mathbf{K} = \mathbf{K}_c + \left(\mathbf{K}_{gx} + \mathbf{K}_{gy} + \mathbf{K}_{gz}\right), \tag{6.24a}$$

$$\mathbf{M} = \mathbf{M}_c + \left(\mathbf{M}_{gx} + \mathbf{M}_{gy} + \mathbf{M}_{gz}\right), \tag{6.24b}$$

in which the subscript c indicates the matrices on RHS are associated with the classical terms while the remains are with the strain gradient terms. The element stiffness and mass matrices from which the global matrices are assembled are given in Appendix A.3 and Appendix A.4, respectively. It is worth noting that, as discussed, the derivatives of displacement variables with respect to z are identically zero yielding $\mathbf{M}_{gz}$ to be a zero matrix.

As a final note to close this section, observing from Appendix A.2, the third derivatives of the approximation functions are required in the extended isogeometric discretisation process which means the C^2-continuity between elements should be maintained. This requirement of highly smooth elements is not fulfilled in the platform of the traditional finite element methods. However, this issue can be addressed naturally and efficiently by using NURBS-based basis functions with polynomial order $p \geq 3$.

6.3 Numerical results and discussion

In this section, the numerical results of the vibration analysis of small-scale FG plates with cracks will be presented. The microplates are made of Al/Al_2O_3 in which the material properties are E_c = 380 GPa, E_m = 70 GPa, $\nu_c = \nu_m = 0.3$,

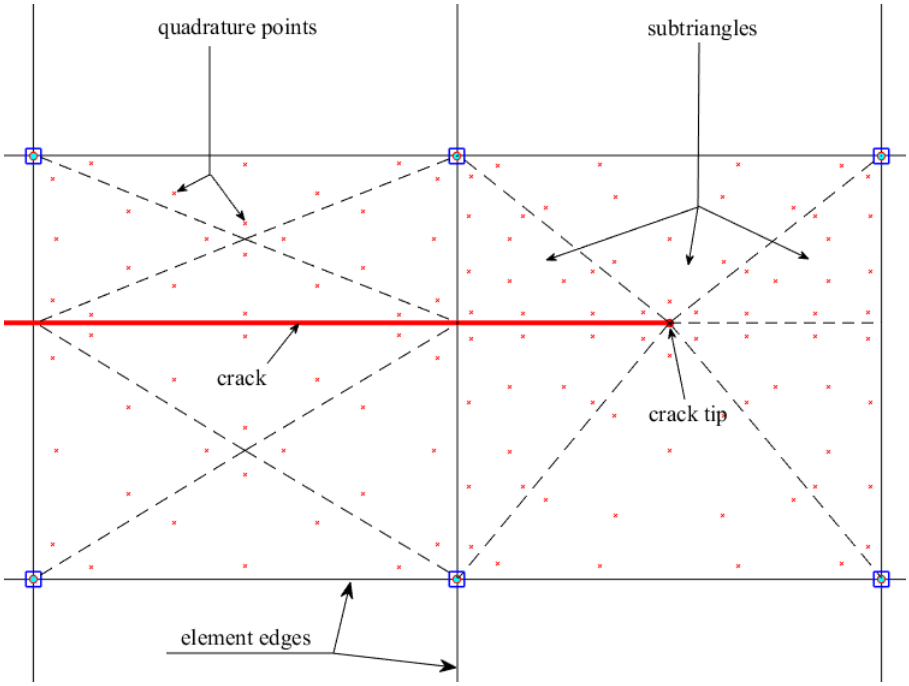

Fig. 6.1 Sub-triangles for element cut by crack path and tip element.

$\rho_c = 3800$ (kg/m^3), $\rho_m = 2707$ (kg/m^3). Unless specifically mentioned, the rule of mixture is employed to describe the distribution of the ceramic and metal phases for numerical analyses in this section. It should be noted that $\ell/h \equiv 0$ implies the analysis is conducted within the context of classical continuum, i.e. no size effects considered. As the formulation of the SGT-based vibration problems require at least C^2-continuity elements, the quartic basis functions ($p = 4$) which satisfy up to C^3-continuous requirements have been employed. Meanwhile, the boundary conditions are applied using similar techniques that have been discussed in the work of Nguyen et al. [84].

6.3.1 Convergence and validation

For the illustration of the convergence and validity of the proposed approach, a number of analyses for square plate with different parameters of element meshes have been tested. Since there are no results reported for the vibration of cracked FG microplates based on the SGT, the numerical results are first generated for the plates without the size-dependent effects. Fig. 6.3 shows the convergence of the fundamental frequency of the simply-supported Al/Al_2O_3 square plate with a crack. The frequency normalisation $\bar{\omega} = \omega \dfrac{a^2}{h}\sqrt{\dfrac{\rho_c}{E_c}}$ is used when presenting

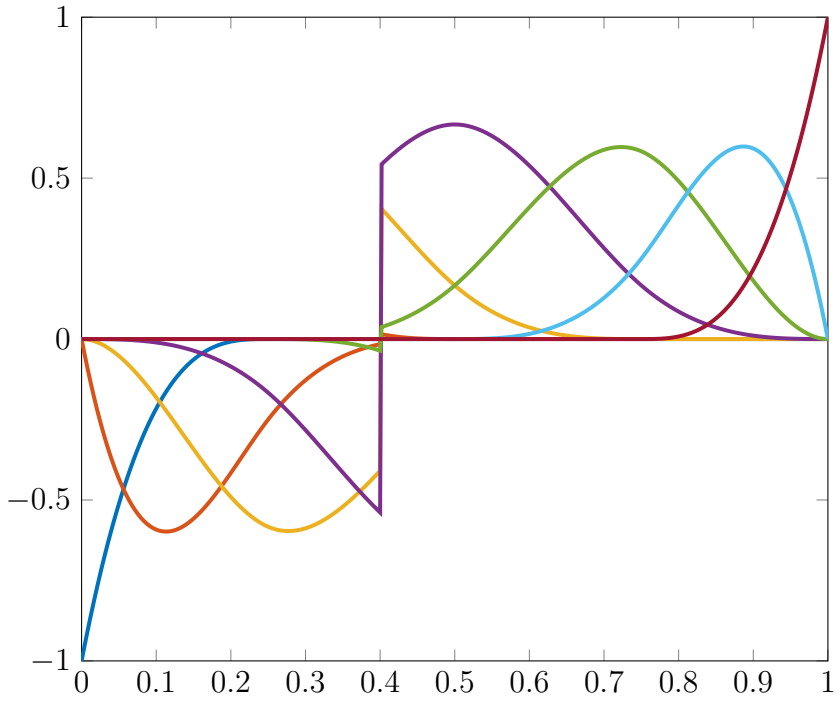

(a) The basis functions

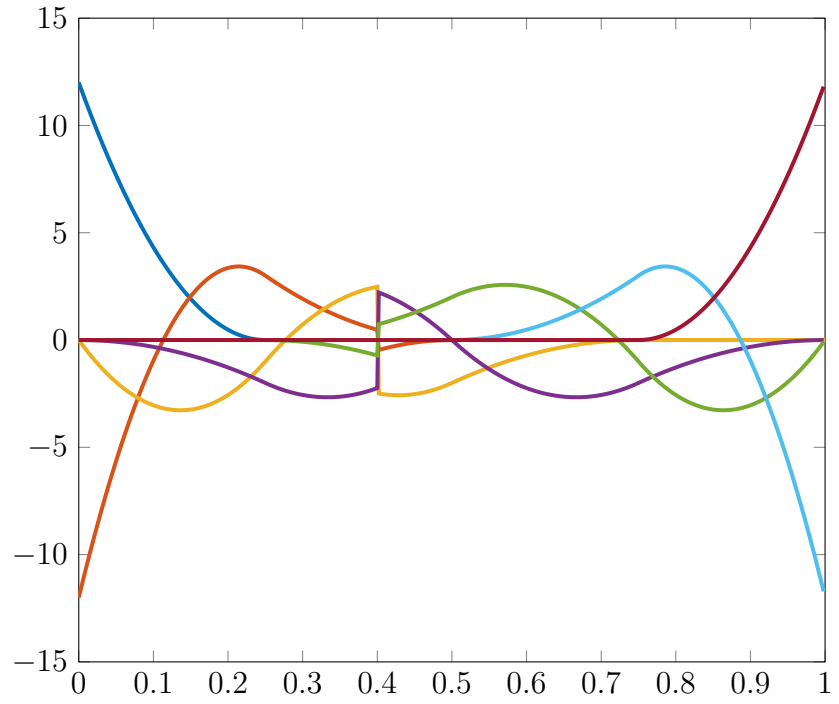

(b) The first derivatives of basis functions

Fig. 6.2 Product of the Heaviside function H at $\xi = 0.4$ with the B-spline basis functions and its derivatives with the knot vector $\boldsymbol{\Xi} = \left\{0,0,0,0,\frac{1}{4},\frac{1}{2},\frac{3}{4},1,1,1,1\right\}$.

the results. As can be observed, with the mesh of 17×17 elements, the solutions converge well to the reference 3D elasticity results, which were reported by Huang et al. [152].

Table 6.1 presents a complete comparison of the results generated from the proposed method and those of other approaches including 3D elasticity and Ritz method by Huang et al. [152], XFEM by Natarajan et al. [153], and XIGA using TSDT by Tran et al. [154]. As can be seen, for the case of absence of size effects, i.e. $\ell/h \equiv 0$, the present results of the first five natural frequencies of the plates are in good agreement with the existing analytical and approximate solutions in the literature.

In the next parts, investigations into the vibrational behaviours of square, circular, and annular microplates with edge cracks and center cracks will be presented.

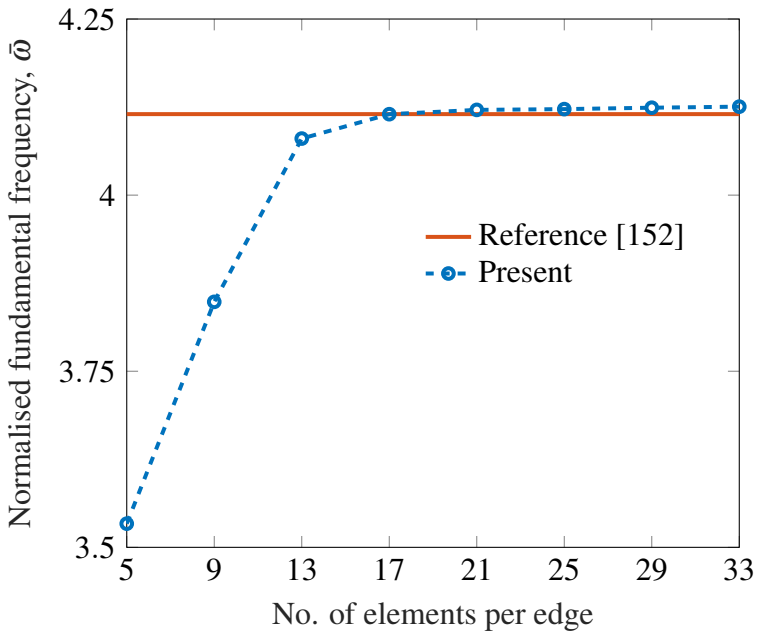

Fig. 6.3 Convergence of fundamental natural frequency of simply-supported Al/Al_2O_3 square plates with different meshes, $a/h = 10$, $c/a = 0.5$, $n = 0$.

Table 6.1 Normalised natural frequencies of SSSS Al/Al_2O_3 square plates with an edge crack

n	Method	ℓ/h	Mode				
			1	2	3	4	5
0	Ritz [152]		5.3790	11.4500	13.3200	16.1800	17.3200
	XFEM [153]		5.3870	11.4190	13.3590	—	
	XIGA-TSDT [154]		5.3643	11.4734	13.2801	16.2062	17.2927
	Present [149]	0	5.4013	11.6012	13.2822	15.3834	17.3216
		0.2	6.6548	14.8945	15.9156	16.3371	19.3573
		0.4	9.3819	16.5765	19.5058	21.2259	22.3737
		0.6	12.6181	17.0482	19.6141	23.8053	28.5286
		0.8	15.9933	17.4653	19.7264	24.9174	32.6846
		1	17.8595	19.3634	19.8416	25.8765	33.9185
1	3D elasticity [152]		4.1150	8.8360	10.2400	13.3300	13.5200
	Ritz [152]		4.1220	8.8560	10.2500	13.3100	13.4900
	XFEM [153]		4.1220	8.5260	10.2850		
	XIGA-TSDT [154]		4.1119	8.8791	10.2131	13.3103	13.4946
	Present [149]	0	4.1345	8.9400	10.2092	12.7727	13.3407
		0.2	5.2431	11.7900	12.9007	13.2175	16.0945
		0.4	7.5919	13.7657	16.2206	17.1983	18.5554
		0.6	10.3308	14.1609	16.3108	19.7674	23.3282
		0.8	13.1642	14.5086	16.4042	20.6946	27.1119
		1	14.8369	15.9821	16.5000	21.4940	28.1524
5	Ritz [152]		3.5110	7.3790	8.6210	10.4900	11.1700
	XFEM [153]		3.6260	7.4150	8.5660		
	XIGA-TSDT [154]		3.5018	7.3980	8.5912	10.4928	11.1511
	Present [149]	0	3.5289	7.5199	8.5991	9.9608	11.1737
		0.2	4.3602	9.7714	10.3137	10.6874	12.5581
		0.4	6.1475	10.7351	12.6574	14.0349	14.4805
		0.6	8.2635	11.0441	12.7279	15.4147	18.8640
		0.8	10.4694	11.3157	12.8007	16.1391	21.1315
		1	11.5719	12.6717	12.8755	16.7637	21.9454
10	Ritz [152]		3.3880	7.0620	8.2890	9.5690	10.7100
	XFEM [153]		3.4090	7.0590	8.2210		
	XIGA-TSDT [154]		3.3773	7.0792	8.2582	9.5750	10.6887
	Present [149]	0	3.4068	7.2173	8.2690	9.0874	10.7259
		0.2	4.1387	9.2388	9.4179	10.1306	11.4478
		0.4	5.7298	9.7933	11.5371	13.0854	13.2137
		0.6	7.6340	10.0738	11.6013	14.0628	17.4656
		0.8	9.6308	10.3210	11.6677	14.7221	19.2907
		1	10.5543	11.6304	11.7359	15.2906	20.0274

6.3.2 Square microplates with cracks

In this part, a number of numerical studies of vibration responses of square FG microplates with edge and center cracks are presented to demonstrate the effects of material length scale ratio ℓ/h, aspect ratio a/h, and material index n on the natural frequencies of the small-scale structures. The geometry configurations of the square plates with edge and center cracks are given in Fig. 6.4. In order to present the numerical results efficiently, unless otherwise stated, the normalisation of frequency mentioned in the previous section is used. As there are no results reported for the vibration of cracked microplates using the SGT, the solutions in this study can be used as benchmark references.

Fig. 6.5 presents the effects of the material length scale ratio ℓ/h on the frequencies of SSSS Al/Al_2O_3 microplates through the first five modes in which the crack is initialised in the middle of an edge. With constant values of aspect ratio a/h, crack ratio c/a, and material index n, it is observed that the growth of material length scale ratio ℓ/h meaning h decreases as ℓ fixed is followed by the increase of the natural frequency in each mode. This observation can also be made from Table 6.1 where the numerical results for cases with size effects, i.e. $\ell/h \neq 0$ are presented. The reason for this phenomenon is that as the consideration of the size-dependent effect gets more pronounced, i.e. larger ℓ/h, the contribution of the non-classical terms to the structure's strain energy density in Eq. (2.10) becomes proportionally significant. Therefore, the stiffness of the structure is considerably increased yielding higher vibrational frequencies as a result of the structural capacity improvement. It is worth commenting that the frequencies consistently increase as the modes change reflects the nature of the vibration problem regardless of size-dependent effects. For illustrative purposes, the first four mode shapes of simply-supported plates with an edge crack for specific geometry and material parameters of $a/h = 20, c/a = 0.5, \ell/h = 0.2, n = 5$ in which the size-dependent effects are considered are plotted in Fig. 6.6. As can be observed, with fixed boundary condition at the perimeter of the plate, the first mode displays a shape of half of sine wave with one peak and the crack is closed. Meanwhile, other modes yield a full sine wave with the crack opened and then closed.

Similarly, as a parametric study, while Fig. 6.7 shows the effects of the material length scale ratio ℓ/h on the the frequencies of clamped-free Al/Al_2O_3 microplates with an edge crack, those effects on Al/Al_2O_3 microplates with a

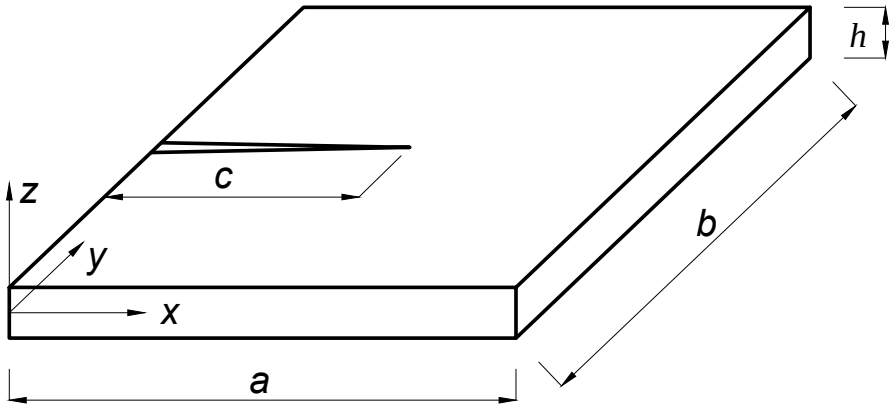

(a) Edge crack

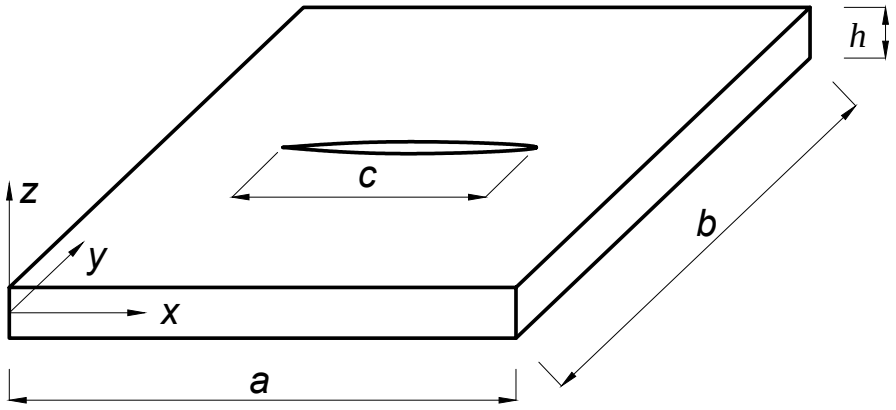

(b) Center crack

Fig. 6.4 Geometry of square plates with cracks.

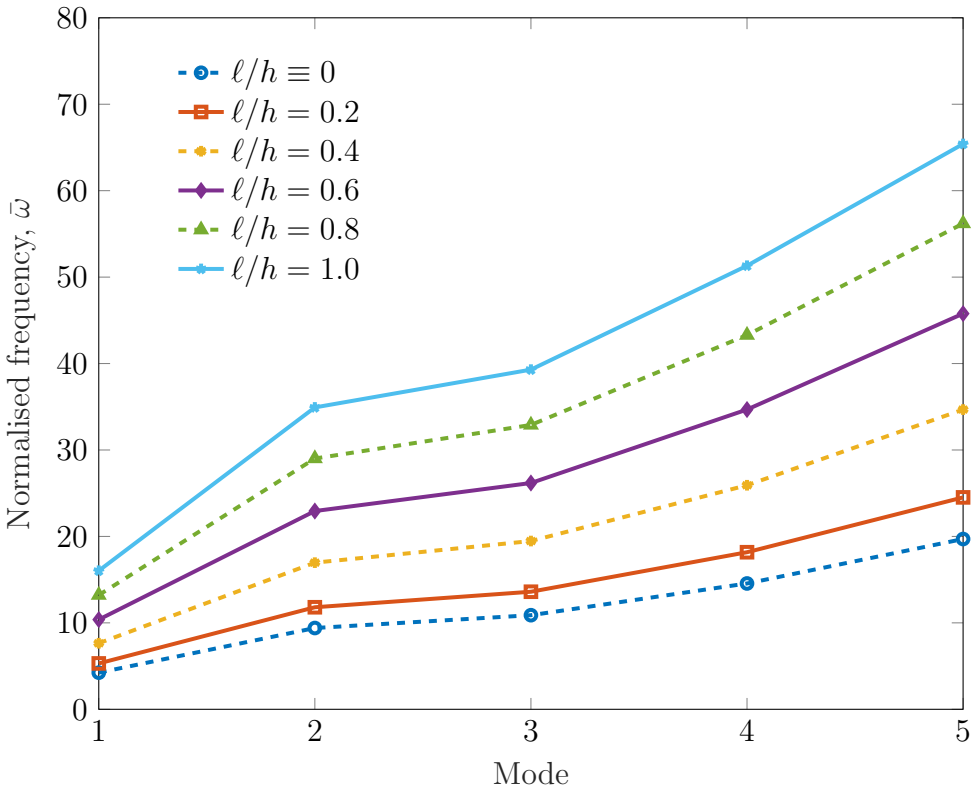

Fig. 6.5 Effects of material length scale ratio ℓ/h on the natural frequencies of SSSS Al/Al_2O_3 square plates with an edge crack ($a/h = 100$, $c/a = 0.5$, $n = 1$).

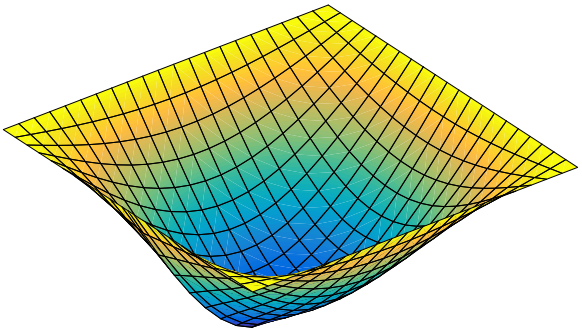

(a) Mode 1

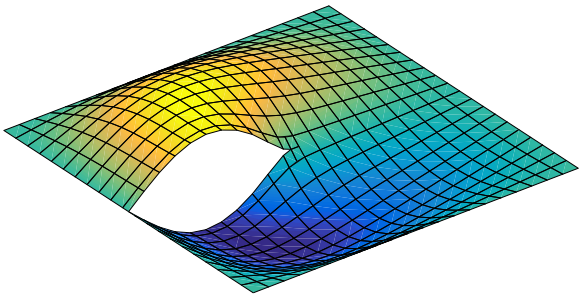

(b) Mode 2

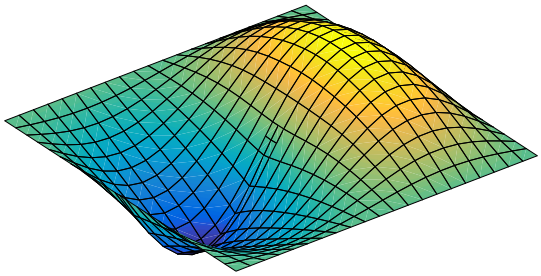

(c) Mode 3

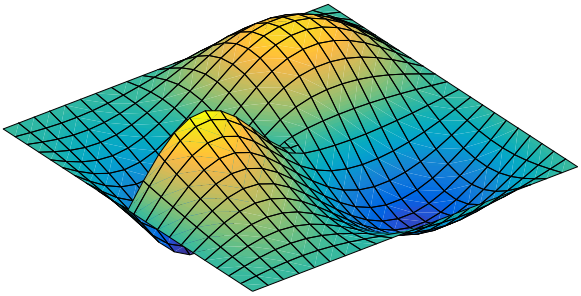

(d) Mode 4

Fig. 6.6 The first four mode shapes of SSSS Al/Al_2O_3 with an edge crack.

center crack are illustrated in Fig. 6.8. In the latter case, the plates are tested with different type of boundary conditions including simply-supported and clamped ones. As the clamped plates are enforced with more constraints, the natural frequencies reach higher magnitudes due to the increase of the structure's stiffness. Also, it is clearly shown that the change of material length scale ratio ℓ/h, i.e. the consideration of the size effects, significantly affects the frequencies of the plates.

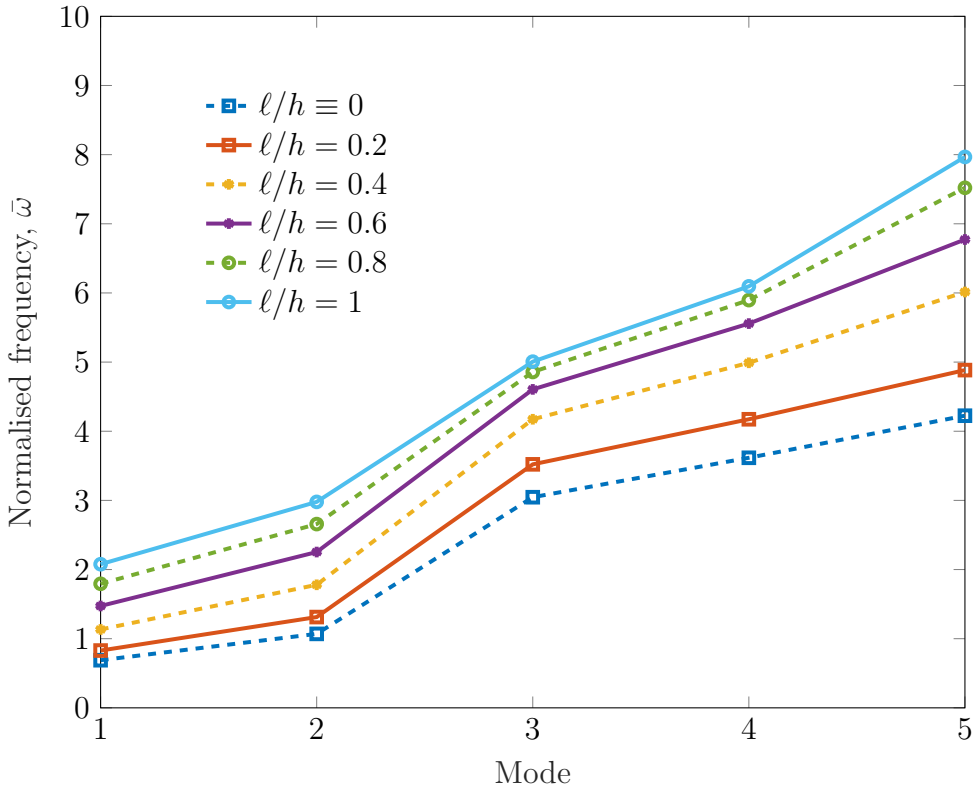

Fig. 6.7 Effects of material length scale ratio ℓ/h on the natural frequencies of CFFF Al/Al_2O_3 square plates with an edge crack ($a/h = 20$, $c/a = 0.5$, $n = 5$).

Fig. 6.9 demonstrates the effects of the crack ratio c/a and the material length scale ratio ℓ/h on the frequencies Al/Al_2O_3 microplates with center crack through modes ($a/h = 20, n = 1$). As it can be expected, although the variations of natural frequencies against the crack ratio are of similar trends, the results generated from cases with $\ell/h \equiv 0$ are 25% - 30% smaller than those calculated from the approach in which the SGT is considered to account for size-dependent effects ($\ell/h = 0.2$). Meanwhile, the increase of the crack ratio c/a which means a larger crack is prescribed in the plate is generally followed by the decline in vibrational frequencies as a result of the structure being weaken. In addition, one may notice that while the frequencies of the first and third modes vary slightly as crack length

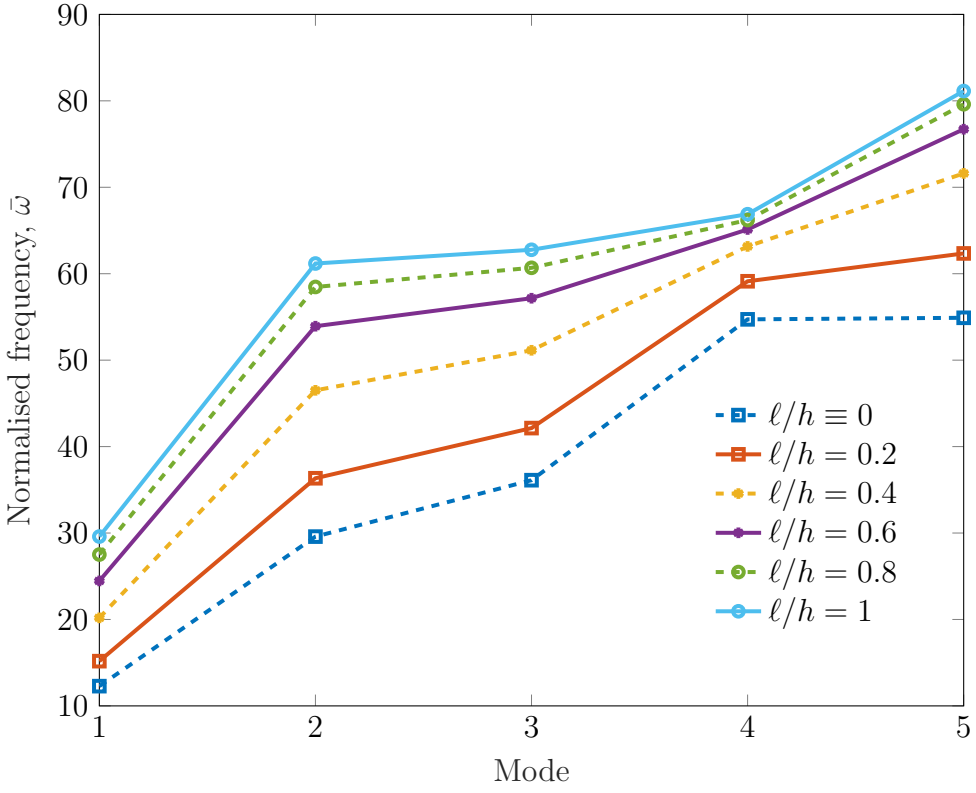

(a) Simply-supported plate

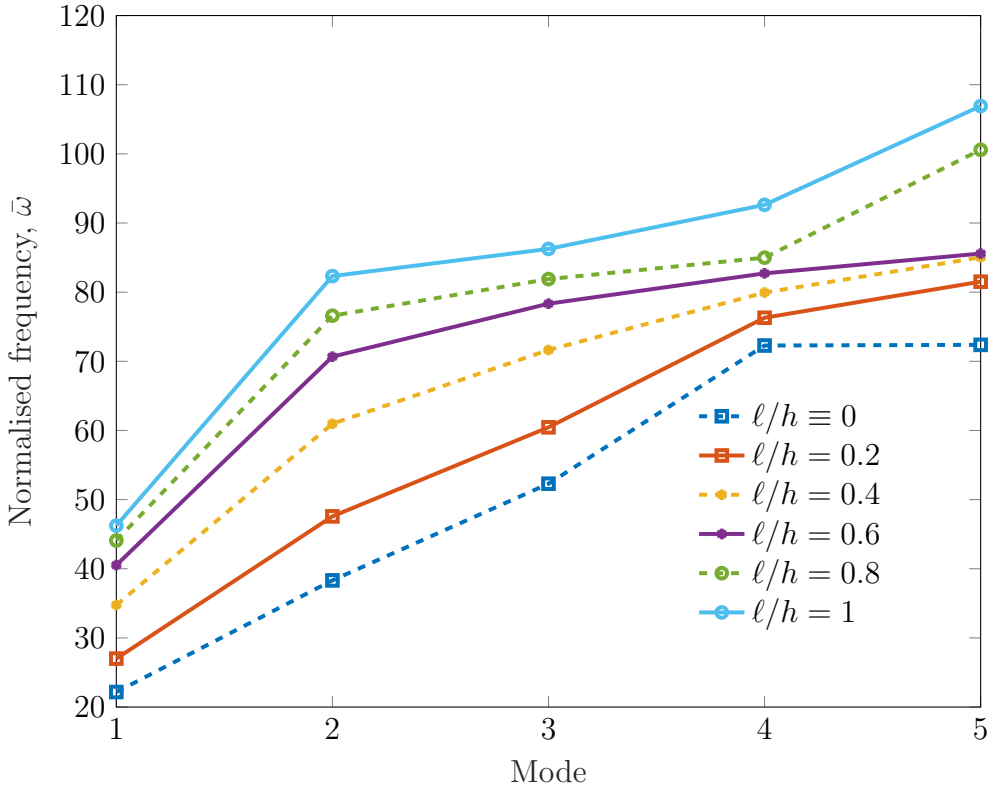

(b) Clamped plate

Fig. 6.8 Effects of material length scale ratio ℓ/h on the natural frequencies of Al/Al_2O_3 square plates with center crack ($a/h = 20$, $c/a = 0.5$, $n = 1$).

grows, those of the second and fourth modes drop significantly. This is due to the fact that the mode shapes in the latter case are of crack-opening configurations while the crack paths in the former cases remain closed.

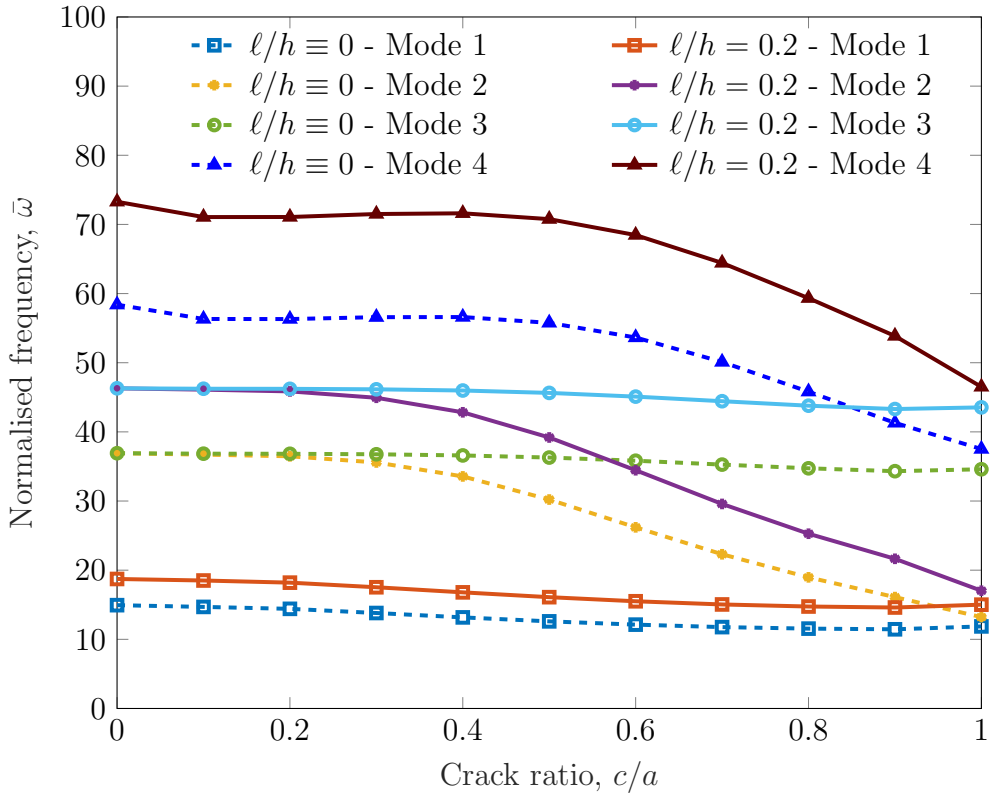

Fig. 6.9 Effects of center crack ratio c/a and material length scale ratio ℓ/h on the natural frequencies of SSSS Al/Al_2O_3 square plates with center crack, ($a/h = 20$, $n = 1$).

A more comprehensive illustration of the effects of the material length scale ratio ℓ/h, aspect ratio a/h, and material index n on the fundamental frequency of the plate can be found in Fig. 6.10. As can be further observed here, with other geometrical parameter fixed, the increase of the material index n weakens the structural stiffness which causes the decrease in vibrational frequencies. This is a results of the volume fraction or, in order word, the proportion of ceramic phase (Al_2O_3) being reduced and replaced by the metal phase (Al) with lower elasticity modulus as n increased. One can also interpret this trend by looking at the material distribution of FG plates which is, in this study, governed by the rule of mixtures shown in Eq. (2.16). For the purpose of visual illustration, Fig. 6.11 shows the first four mode shapes of a clamped-free plate with an edge crack while those of a fully-clamped plate with a center crack are plotted in Fig. 6.12.

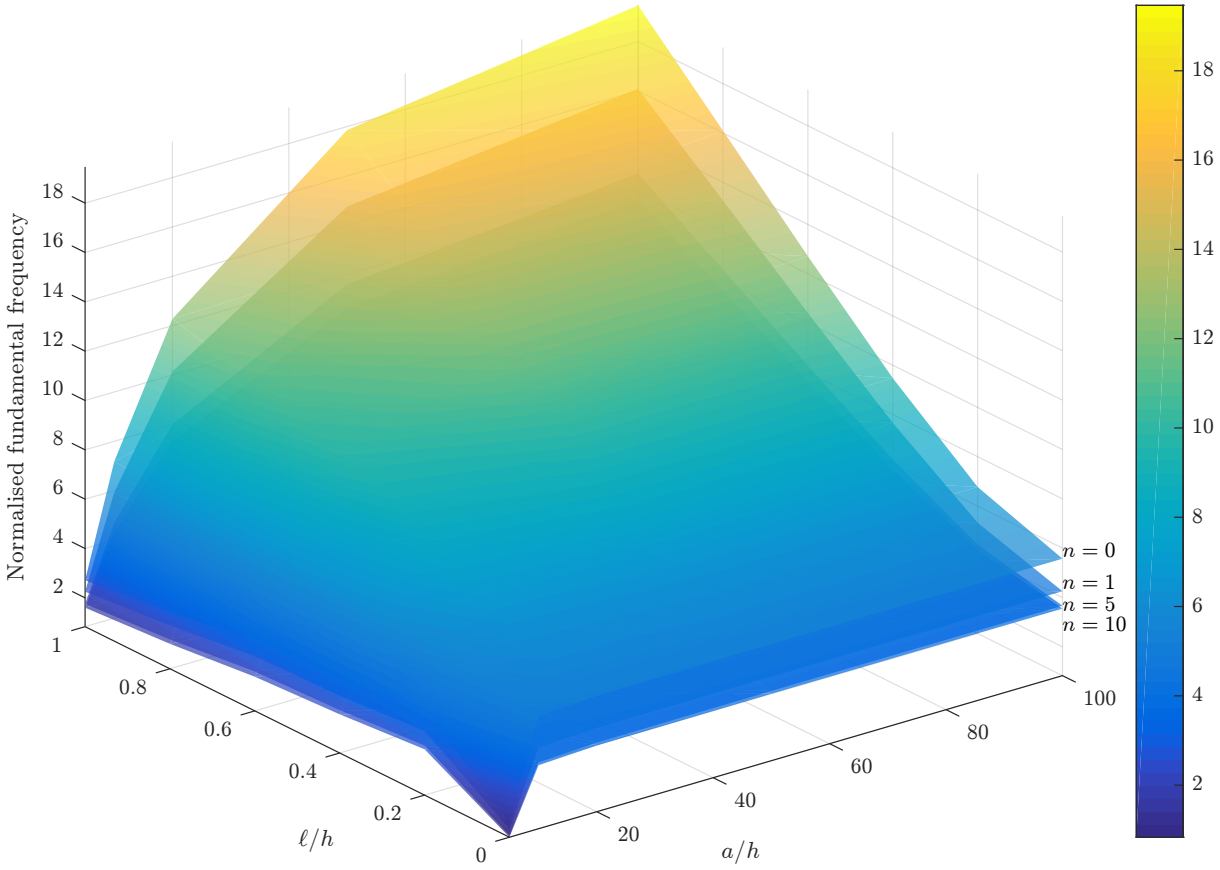

Fig. 6.10 Effects of $\ell/h, a/h, n$ on the fundamental frequencies of SSSS Al/Al_2O_3 square plates with an edge crack, ($c/a = 0.5$).

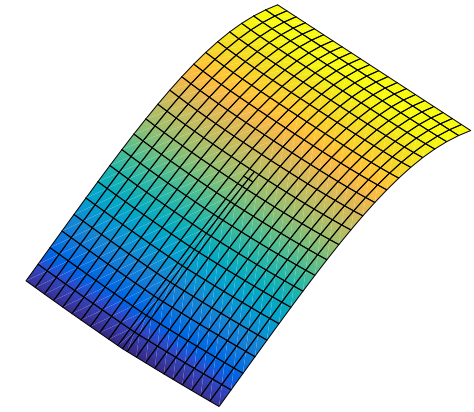

(a) Mode 1

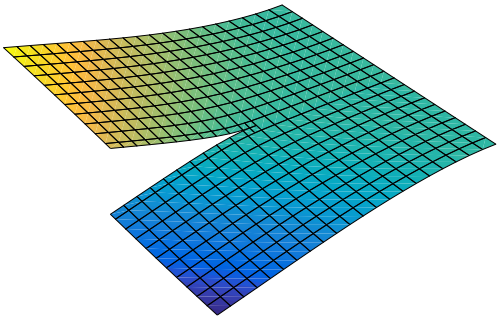

(b) Mode 2

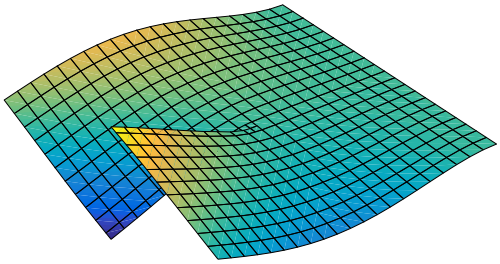

(c) Mode 3

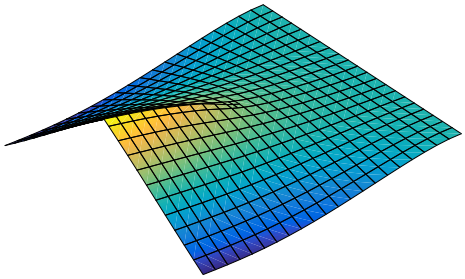

(d) Mode 4

Fig. 6.11 The first four mode shapes of clamped-free Al/Al_2O_3 with an edge crack.

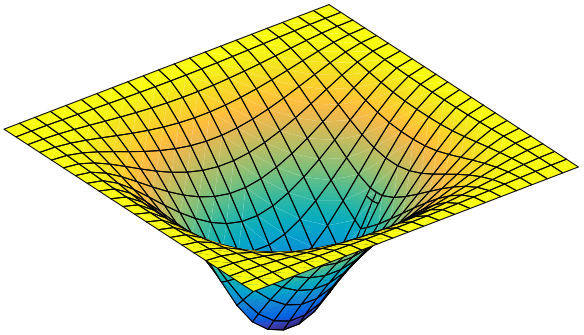

(a) Mode 1

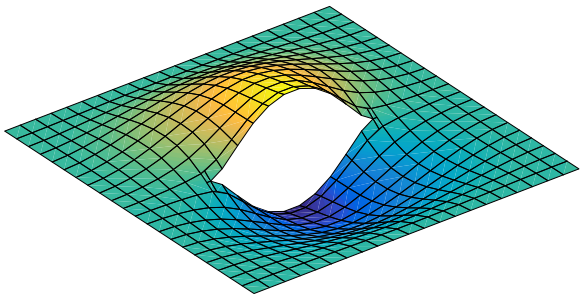

(b) Mode 2

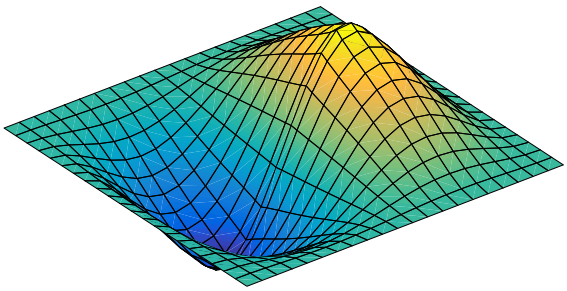

(c) Mode 3

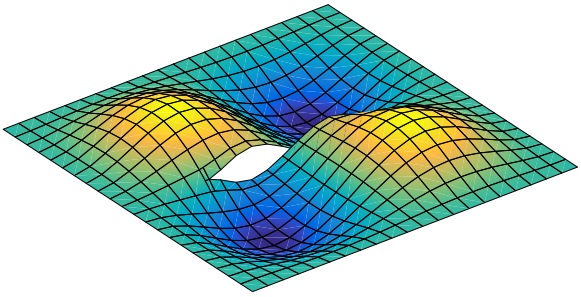

(d) Mode 4

Fig. 6.12 The first four mode shapes of clamped Al/Al_2O_3 with a center crack.

6.3.3 Circular and annular microplates with cracks

A number of numerical studies for the vibration behaviours of circular and annular small-scale FG plates with cracks whose geometries depicted in Fig. 6.13 will be discussed in this part of the section. In order to present the results in an efficient manner, this normalisation is employed $\bar{\omega} = \omega \frac{R^2}{h}\sqrt{\frac{\rho_c}{E_c}}$. Fig. 6.14 presents the effects of the material length scale ratio ℓ/h on the natural frequencies of the simply-supported circular plate with a center crack in which the material distribution follows the rule of mixture. Similar to the previous part where the rectangular plates are considered, the increase in material length scale ratio leads to the rise of the vibrational frequencies. This is attributed to the inclusion of the strain gradient terms in the strain energy density of the small-scale plates which increases the magnitude of the structural stiffness. For the illustration purposes of a general case, the first four mode shapes of the simply-supported microplates with a center crack and specific geometry and material parameters are plotted in Fig. 6.15. Similarly to the previous case, with the boundary condition applied at the perimeter of the plate, the first mode gives the shape of a half of a sine wave with one peak where as the other mode displays a full sine wave with one peak and one trough.

For annular plates, only one symmetric half of the structure is analysed due to the fact that this consideration significantly reduces the complexity of geometry representations in IGA and also the computational effort of solving procedure. Fig. 6.16 shows the effects of the material length scale ratio ℓ/h on the natural frequencies of the microplates in which the inner perimeter is free from constraints while the clamped boundary condition is apply at the outer circle of the annulus. In addition, Fig. 6.17 illustrates a more comprehensive observation of how geometry and material factors effect the vibrational behaviours in which the variation of the plate's fundamental frequencies against the changes of material length scale ratio ℓ/h, aspect ratio R/h, and material index n are given. As an illustration of a general case, Fig. 6.18 describes the first four mode shapes the annular plate subjected to clamped-free boundary condition with a center crack and specific geometry and material parameters. As can be observed, due to the clamped-free boundary condition, the first mode forms a shape with only one peak at the free end while other mode shapes displays at least one peak and one trough.

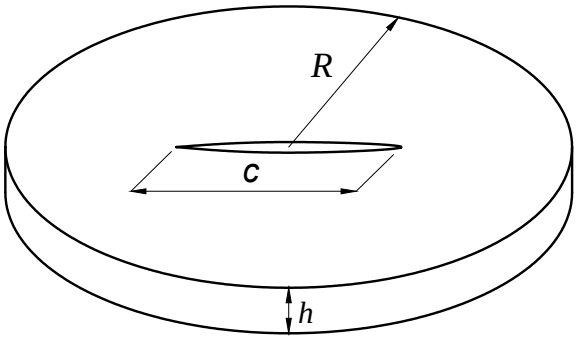

(a) Circular plate

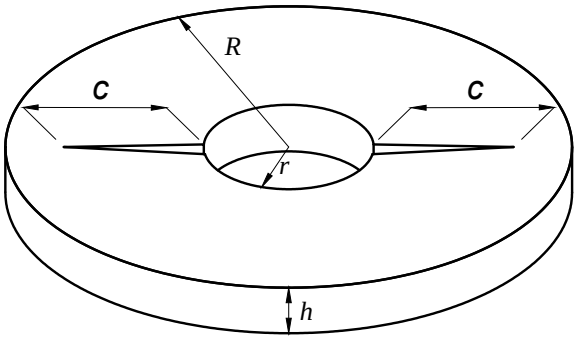

(b) Annular plate

Fig. 6.13 Geometry of circular and annular plates with center cracks.

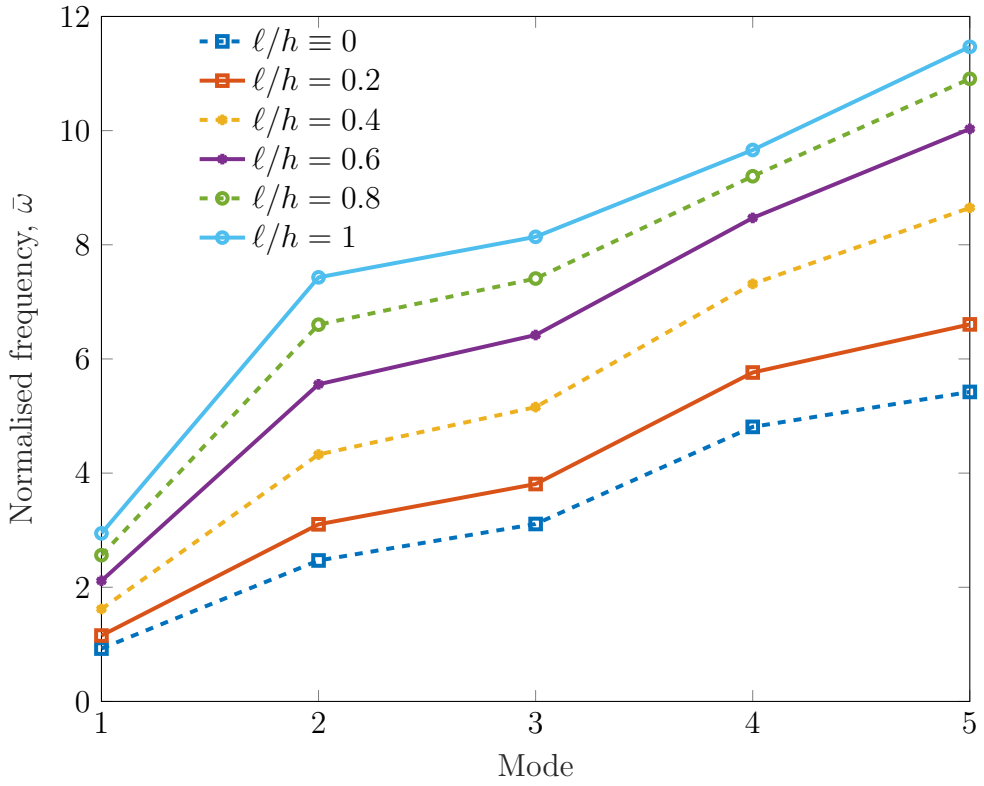

Fig. 6.14 Effects of material length scale ratio ℓ/h on the natural frequencies of simply-supported Al/Al_2O_3 circular plates with center crack, ($h/R = 0.05$, $c/R = 1, n = 1$).

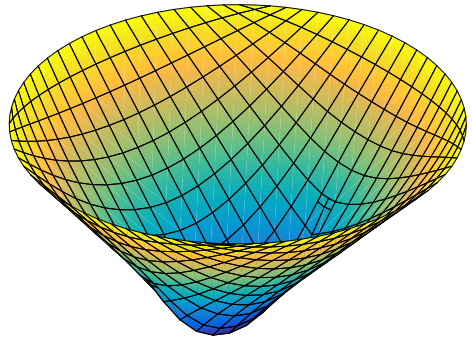

(a) Mode 1

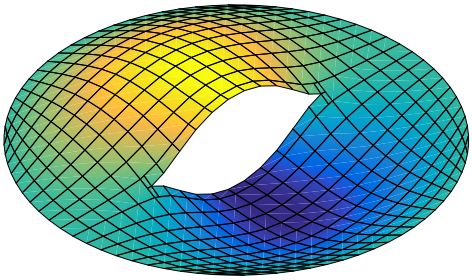

(b) Mode 2

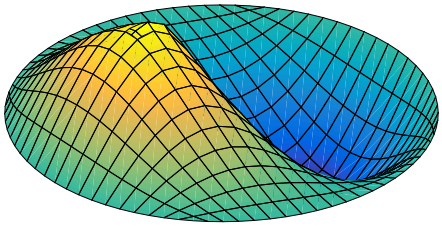

(c) Mode 3

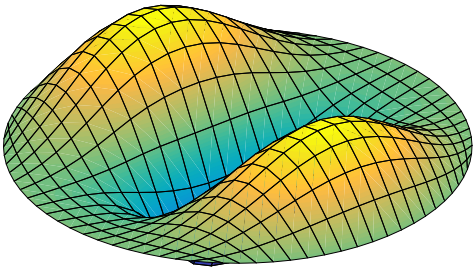

(d) Mode 4

Fig. 6.15 The first four mode shapes of simply-supported Al/Al_2O_3 circular with a center crack.

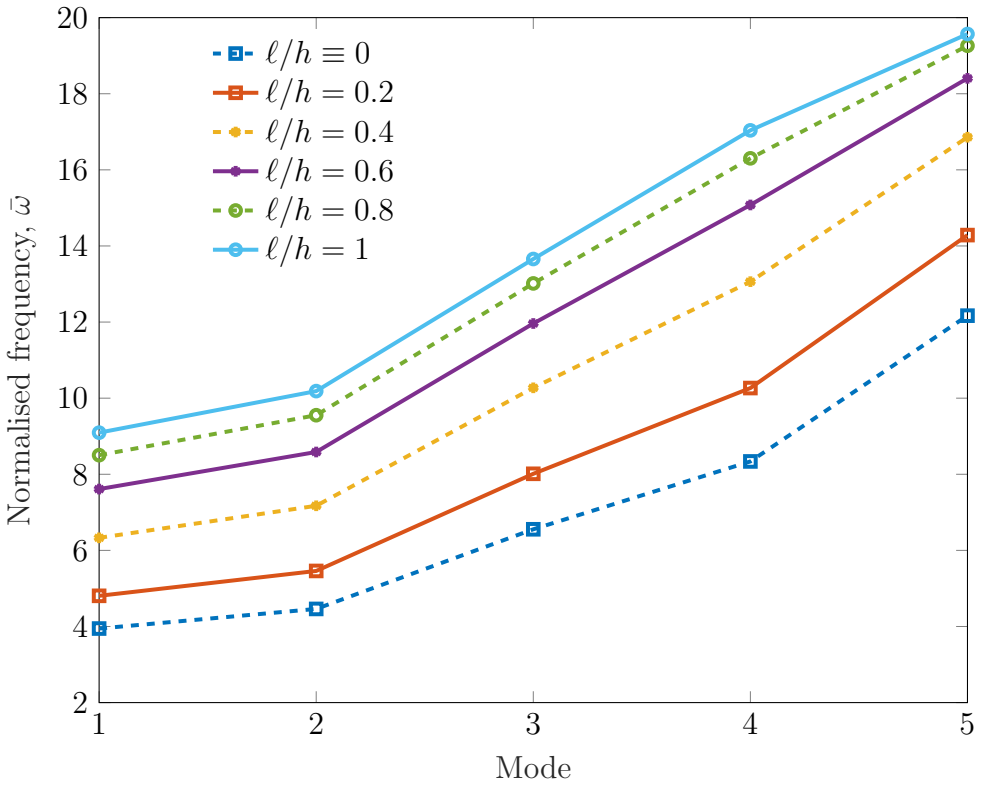

Fig. 6.16 Effects of material length scale ratio ℓ/h on the natural frequencies of Al/Al_2O_3 annular plates with center crack ($h/R = 0.05$, $r/R = 0.5$, $c/(R-r) = 0.5$, $n = 1$).

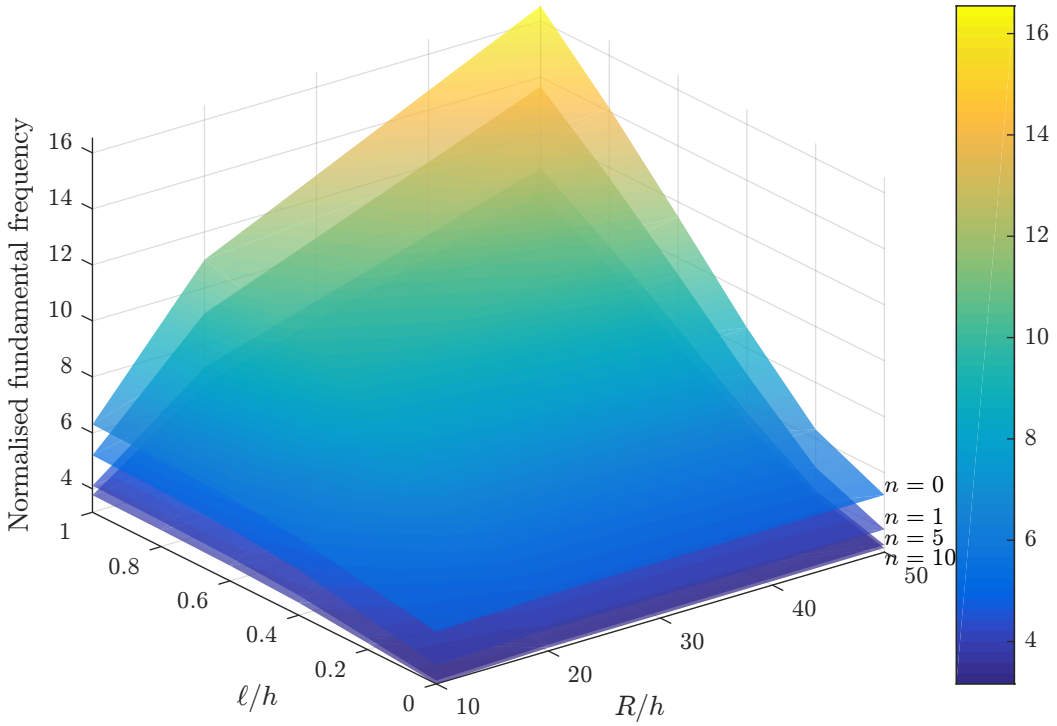

Fig. 6.17 Effects of $\ell/h, R/h, n$ on the fundamental frequencies of Al/Al_2O_3 annular plates with center crack ($c/a = 0.5(R-r)$).

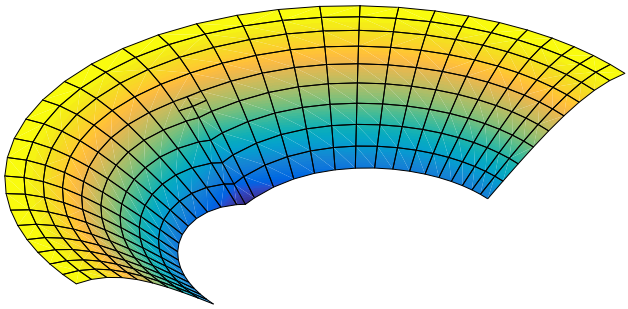

(a) Mode 1

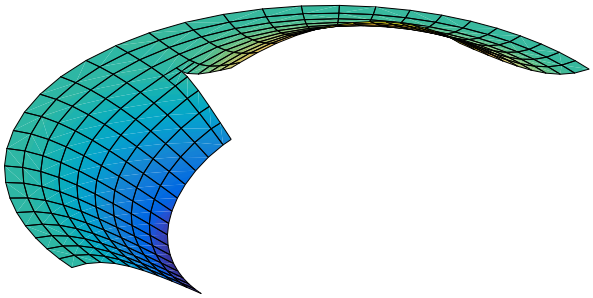

(b) Mode 2

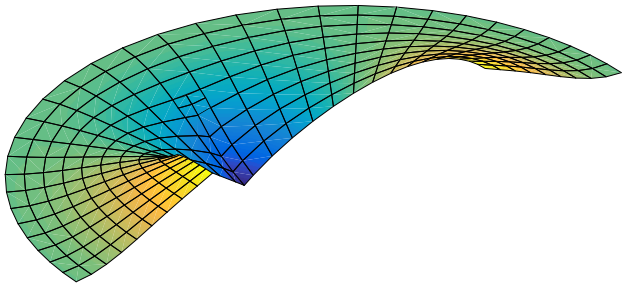

(c) Mode 3

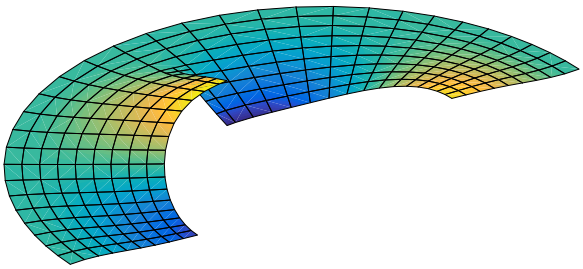

(d) Mode 4

Fig. 6.18 The first four mode shapes of clamped-free a Al/Al_2O_3 half annular plate.

Chapter 7

Conclusion and future work

7.1 Conclusion

In this thesis, effective computational approaches based on IGA and generalised continuum theories are presented to conduct linear, nonlinear, and crack analysis of plates with size-dependents effects. In the linear analysis, the mathematical model governing the bending, free vibration and buckling behaviour of the plates is constructed based on the MCST with only one material length scale accounting for the size dependency of small-scale plates. The presented quasi-3D approach not only considers shear deformations but also is able to accurately capture the thickness stretching effect which is neglected by other classical theories. The NURBS-based IGA is used to exactly describe the geometry and approximately construct the unknown field in which the higher-order continuity requirement of the proposed kinematical and constitutive theories is readily satisfied. Regarding the nonlinear analysis, the IGA associated with the four-unknown RPT is proposed to investigate the geometrically nonlinear bending responses of small-scale FG plates. The RPT which requires C^1 elements is used to construct the displacement fields before the nonlinear von Kármán strains are derived. Meanwhile, the size-dependent effects are efficiently captured by the MCST in which only length scale parameter is involved. While the NURBS-based IGA is successfully implemented to construct higher-order elements which are essentially required in refined plate and modified couple stress theories, the solutions of nonlinear problems are reliably obtained by means of Newton-Raphson iterative procedure. A number of convergence and validation studies confirm the validity and reliability of the proposed RPT-based IGA approach which is highly robust compared to other

HSDT-based FEA approaches in terms of computational efforts including the number of unknowns and element meshes. With respect to the crack analysis, the SGT with one material length scale parameter and an additional micro-inertia term was employed together with the XIGA to investigate the vibration behaviours of FG microplates with cracks. The combination of the SGT and RPT with four unknowns results in a sixth-order problem with C^2-continuity requirements. This condition was effectively fulfilled by the XIGA that possesses highly smooth basis functions of NURBS with new enrichment functions. Meanwhile, the size-dependent effects in small-scale plates which classical continuum theory failed to capture were efficiently predicted by the SGT.

A number of investigations including novel benchmark problems which have never been reported in the literature have confirmed the validity and efficiency of the proposed approaches. The results also reveal that increase of the material length scale parameter ratio raises the microplate's stiffness, especially when the material length scale ratio ℓ/h gets larger, which results in a decrease in the displacement and stresses and an increase in the natural frequency and buckling load. On the contrary, the increase of material index n of FGM leads to a completely different scenario in which the displacements are also risen. In addition, although the influence of the aspect ratio a/h on the bending responses is remarkable for thin plates, it becomes less pronounced when the thick plates are considered. Meanwhile, the benchmark results of crack analysis showed significant departure from those generated by the classical theory with size independence. The parametric studies imply that the inclusion of material length scale and the addition of micro-inertia term resulted in increases of vibration frequencies when the size of the plates become smaller. Furthermore, the vibration mode shapes had strong impacts on the corresponding natural frequencies when crack length increases, especially for open-crack cases. Meanwhile, those were less significant for configurations with cracks remained closed.

7.2 Future work

As can be inferred from Chapter 3, even though NURBS is robust and popular basis function for IGA, it has the limit in conducting local refinement due to the tensor product. Therefore, a different basis function with ability to do adaptive local refinement would improve the computational performance, especially for problems in which cracks are involved. One of the possibilities is the polynomial

splines over hierarchical T-meshes [113]. This basis function retains positive features of NURBS in geometry representation and field approximations including the high-order element continuity that are essentially required in generalised continuum theories presented in this thesis.

Appendix A

A.1 Strain gradient components

$$\boldsymbol{\kappa}_x = \begin{Bmatrix} \kappa_{xxx} \\ \kappa_{xyy} \\ 2\kappa_{xyz} \\ 2\kappa_{xxz} \\ 2\kappa_{xxy} \end{Bmatrix}, \boldsymbol{\kappa}_x^0 = \begin{Bmatrix} u_{0,xx} \\ v_{0,xy} \\ w_{s,xy} \\ w_{s,xx} \\ u_{0,xy} + v_{0,xx} \end{Bmatrix}, \boldsymbol{\kappa}_x^1 = \begin{Bmatrix} -w_{b,xxx} \\ -w_{b,xyy} \\ 0 \\ 0 \\ -2w_{b,xxy} \end{Bmatrix}, \boldsymbol{\kappa}_x^2 = \begin{Bmatrix} w_{s,xxx} \\ w_{s,xyy} \\ 0 \\ 0 \\ 2w_{s,xxy} \end{Bmatrix}, \boldsymbol{\kappa}_x^3 = \begin{Bmatrix} 0 \\ 0 \\ w_{s,xy} \\ w_{s,xx} \\ 0 \end{Bmatrix}, \boldsymbol{\kappa}_x^4 = \begin{Bmatrix} 0 \\ 0 \\ 0 \\ 0 \\ 0 \end{Bmatrix}, \tag{A.1}$$

$$\boldsymbol{\kappa}_y = \begin{Bmatrix} \kappa_{yxx} \\ \kappa_{yyy} \\ 2\kappa_{yyz} \\ 2\kappa_{yxz} \\ 2\kappa_{yxy} \end{Bmatrix}, \boldsymbol{\kappa}_y^0 = \begin{Bmatrix} u_{0,xy} \\ v_{0,yy} \\ w_{s,yy} \\ w_{s,xy} \\ u_{0,yy} + v_{0,xy} \end{Bmatrix}, \boldsymbol{\kappa}_y^1 = \begin{Bmatrix} -w_{b,xyy} \\ -w_{b,yyy} \\ 0 \\ 0 \\ -2w_{b,xyy} \end{Bmatrix}, \boldsymbol{\kappa}_y^2 = \begin{Bmatrix} w_{s,xyy} \\ w_{s,yyy} \\ 0 \\ 0 \\ 2w_{s,xyy} \end{Bmatrix}, \boldsymbol{\kappa}_y^3 = \begin{Bmatrix} 0 \\ 0 \\ w_{s,yy} \\ w_{s,xy} \\ 0 \end{Bmatrix}, \boldsymbol{\kappa}_y^4 = \begin{Bmatrix} 0 \\ 0 \\ 0 \\ 0 \\ 0 \end{Bmatrix}, \tag{A.2}$$

$$\boldsymbol{\kappa}_z = \begin{Bmatrix} \kappa_{zxx} \\ \kappa_{zyy} \\ 2\kappa_{zyz} \\ 2\kappa_{zxz} \\ 2\kappa_{zxy} \end{Bmatrix}, \boldsymbol{\kappa}_z^0 = \begin{Bmatrix} -w_{b,xx} \\ -w_{b,yy} \\ 0 \\ 0 \\ -2w_{b,xy} \end{Bmatrix}, \boldsymbol{\kappa}_z^1 = \begin{Bmatrix} 0 \\ 0 \\ 0 \\ 0 \\ 0 \end{Bmatrix}, \boldsymbol{\kappa}_z^2 = \begin{Bmatrix} 0 \\ 0 \\ 0 \\ 0 \\ 0 \end{Bmatrix}, \boldsymbol{\kappa}_z^3 = \begin{Bmatrix} w_{s,xx} \\ w_{s,yy} \\ 0 \\ 0 \\ 2w_{s,xy} \end{Bmatrix}, \boldsymbol{\kappa}_z^4 = \begin{Bmatrix} 0 \\ 0 \\ w_{s,y} \\ w_{s,x} \\ 0 \end{Bmatrix} \tag{A.3}$$

$$\kappa_{izz} = 0 \tag{A.4}$$

A.2 B matrices

$$\mathbf{B}_A^m = \begin{bmatrix} \bar{R}_{A,x} & 0 & 0 & 0 \\ 0 & \bar{R}_{A,y} & 0 & 0 \\ \bar{R}_{A,y} & \bar{R}_{A,x} & 0 & 0 \end{bmatrix}, \quad \mathbf{B}_A^{b1} = \begin{bmatrix} 0 & 0 & -\bar{R}_{A,xx} & 0 \\ 0 & 0 & -\bar{R}_{A,yy} & 0 \\ 0 & 0 & -2\bar{R}_{A,xy} & 0 \end{bmatrix}, \quad \mathbf{B}_A^{b2} = \begin{bmatrix} 0 & 0 & 0 & \bar{R}_{A,xx} \\ 0 & 0 & 0 & \bar{R}_{A,yy} \\ 0 & 0 & 0 & 2\bar{R}_{A,xy} \end{bmatrix}, \tag{A.5a}$$

$$\mathbf{B}_A^s = \begin{bmatrix} 0 & 0 & 0 & \bar{R}_{A,x} \\ 0 & 0 & 0 & \bar{R}_{A,y} \end{bmatrix}, \tag{A.5b}$$

$$\mathbf{B}_A^{x0} = \begin{bmatrix} \bar{R}_{A,xx} & 0 & 0 & 0 \\ 0 & \bar{R}_{A,xy} & 0 & 0 \\ 0 & 0 & 0 & 0 \\ 0 & 0 & 0 & \bar{R}_{A,xy} \\ 0 & 0 & 0 & \bar{R}_{A,xx} \\ \bar{R}_{A,xy} & \bar{R}_{A,xx} & 0 & 0 \end{bmatrix}, \quad \mathbf{B}_A^{x1} = \begin{bmatrix} 0 & 0 & -\bar{R}_{A,xxx} & 0 \\ 0 & 0 & -\bar{R}_{A,xyy} & 0 \\ 0 & 0 & 0 & 0 \\ 0 & 0 & 0 & 0 \\ 0 & 0 & 0 & 0 \\ 0 & 0 & -2\bar{R}_{A,xxy} & 0 \end{bmatrix}, \tag{A.6a}$$

$$\mathbf{B}_A^{x2} = \begin{bmatrix} 0 & 0 & 0 & \bar{R}_{A,xxx} \\ 0 & 0 & 0 & \bar{R}_{A,xyy} \\ 0 & 0 & 0 & 0 \\ 0 & 0 & 0 & 0 \\ 0 & 0 & 0 & 0 \\ 0 & 0 & 0 & 2\bar{R}_{A,xxy} \end{bmatrix}, \quad \mathbf{B}_A^{x3} = \begin{bmatrix} 0 & 0 & 0 & 0 \\ 0 & 0 & 0 & 0 \\ 0 & 0 & 0 & 0 \\ 0 & 0 & 0 & \bar{R}_{A,xy} \\ 0 & 0 & 0 & \bar{R}_{A,xy} \\ 0 & 0 & 0 & 0 \end{bmatrix}, \quad \mathbf{B}_A^{x4} = [\mathbf{0}], \tag{A.6b}$$

$$\mathbf{B}_A^{y0} = \begin{bmatrix} \bar{R}_{A,xy} & 0 & 0 & 0 \\ 0 & \bar{R}_{A,yy} & 0 & 0 \\ 0 & 0 & 0 & 0 \\ 0 & 0 & 0 & \bar{R}_{A,yy} \\ 0 & 0 & 0 & \bar{R}_{A,xy} \\ \bar{R}_{A,yy} & \bar{R}_{A,xy} & 0 & 0 \end{bmatrix}, \quad \mathbf{B}_A^{y1} = \begin{bmatrix} 0 & 0 & -\bar{R}_{A,xyy} & 0 \\ 0 & 0 & -\bar{R}_{A,yyy} & 0 \\ 0 & 0 & 0 & 0 \\ 0 & 0 & 0 & 0 \\ 0 & 0 & 0 & 0 \\ 0 & 0 & -2\bar{R}_{A,xyy} & 0 \end{bmatrix}, \tag{A.6c}$$

$$\mathbf{B}_A^{y2} = \begin{bmatrix} 0 & 0 & 0 & \bar{R}_{A,xyy} \\ 0 & 0 & 0 & \bar{R}_{A,yyy} \\ 0 & 0 & 0 & 0 \\ 0 & 0 & 0 & 0 \\ 0 & 0 & 0 & 0 \\ 0 & 0 & 0 & 2\bar{R}_{A,xyy} \end{bmatrix}, \quad \mathbf{B}_A^{y3} = \begin{bmatrix} 0 & 0 & 0 & 0 \\ 0 & 0 & 0 & 0 \\ 0 & 0 & 0 & 0 \\ 0 & 0 & 0 & \bar{R}_{A,yy} \\ 0 & 0 & 0 & \bar{R}_{A,xy} \\ 0 & 0 & 0 & 0 \end{bmatrix}, \quad \mathbf{B}_A^{y4} = [\mathbf{0}], \tag{A.6d}$$

$$\mathbf{B}_A^{z0} = \begin{bmatrix} 0 & 0 & -\bar{R}_{A,xx} & 0 \\ 0 & 0 & -\bar{R}_{A,yy} & 0 \\ 0 & 0 & 0 & 0 \\ 0 & 0 & 0 & 0 \\ 0 & 0 & 0 & 0 \\ 0 & 0 & -2\bar{R}_{A,xy} & 0 \end{bmatrix}, \quad \mathbf{B}_A^{z1} = [\mathbf{0}], \quad \mathbf{B}_A^{z2} = [\mathbf{0}], \tag{A.6e}$$

$$\mathbf{B}_A^{z3} = \begin{bmatrix} 0 & 0 & 0 & \bar{R}_{A,xx} \\ 0 & 0 & 0 & \bar{R}_{A,yy} \\ 0 & 0 & 0 & 0 \\ 0 & 0 & 0 & 0 \\ 0 & 0 & 0 & 0 \\ 0 & 0 & 0 & 2\bar{R}_{A,xy} \end{bmatrix}, \quad \mathbf{B}_A^{z4} = \begin{bmatrix} 0 & 0 & 0 & 0 \\ 0 & 0 & 0 & 0 \\ 0 & 0 & 0 & 0 \\ 0 & 0 & 0 & \bar{R}_{A,y} \\ 0 & 0 & 0 & \bar{R}_{A,x} \\ 0 & 0 & 0 & 0 \end{bmatrix}, \tag{A.6f}$$

where $\bar{R}$ can be either standard basis functions or enrichment functions.

A.3 Element stiffness matrices

$$\mathbf{K}_c^e = \int_{\Omega_e} \begin{Bmatrix} \mathbf{B}^m \\ \mathbf{B}^{b1} \\ \mathbf{B}^{b2} \end{Bmatrix}^T \begin{bmatrix} \mathbf{A} & \mathbf{B} & \mathbf{E} \\ \mathbf{B} & \mathbf{D} & \mathbf{F} \\ \mathbf{E} & \mathbf{F} & \mathbf{H} \end{bmatrix} \begin{Bmatrix} \mathbf{B}^m \\ \mathbf{B}^{b1} \\ \mathbf{B}^{b2} \end{Bmatrix} d\Omega_e, \tag{A.7}$$

$$\mathbf{K}_{gx}^e = \int_{\Omega_e} \begin{Bmatrix} \mathbf{B}^{x0} \\ \mathbf{B}^{x1} \\ \mathbf{B}^{x2} \\ \mathbf{B}^{x3} \\ \mathbf{B}^{x4} \end{Bmatrix}^T \begin{bmatrix} \mathbf{A}^g & \mathbf{B}^g & \mathbf{E}^g & \mathbf{G}^g & \mathbf{M}^g \\ \mathbf{B}^g & \mathbf{D}^g & \mathbf{F}^g & \mathbf{I}^g & \mathbf{N}^g \\ \mathbf{E}^g & \mathbf{F}^g & \mathbf{H}^g & \mathbf{J}^g & \mathbf{P}^g \\ \mathbf{G}^g & \mathbf{I}^g & \mathbf{J}^g & \mathbf{L}^g & \mathbf{Q}^g \\ \mathbf{M}^g & \mathbf{N}^g & \mathbf{P}^g & \mathbf{Q}^g & \mathbf{R}^g \end{bmatrix} \begin{Bmatrix} \mathbf{B}^{x0} \\ \mathbf{B}^{x1} \\ \mathbf{B}^{x2} \\ \mathbf{B}^{x3} \\ \mathbf{B}^{x4} \end{Bmatrix} d\Omega_e, \tag{A.8a}$$

$$\mathbf{K}^e_{gy} = \int_{\Omega_e} \begin{Bmatrix} \mathbf{B}^{y0} \\ \mathbf{B}^{y1} \\ \mathbf{B}^{y2} \\ \mathbf{B}^{y3} \\ \mathbf{B}^{y4} \end{Bmatrix}^T \begin{bmatrix} \mathbf{A}^g & \mathbf{B}^g & \mathbf{E}^g & \mathbf{G}^g & \mathbf{M}^g \\ \mathbf{B}^g & \mathbf{D}^g & \mathbf{F}^g & \mathbf{I}^g & \mathbf{N}^g \\ \mathbf{E}^g & \mathbf{F}^g & \mathbf{H}^g & \mathbf{J}^g & \mathbf{P}^g \\ \mathbf{G}^g & \mathbf{I}^g & \mathbf{J}^g & \mathbf{L}^g & \mathbf{Q}^g \\ \mathbf{M}^g & \mathbf{N}^g & \mathbf{P}^g & \mathbf{Q}^g & \mathbf{R}^g \end{bmatrix} \begin{Bmatrix} \mathbf{B}^{y0} \\ \mathbf{B}^{y1} \\ \mathbf{B}^{y2} \\ \mathbf{B}^{y3} \\ \mathbf{B}^{y4} \end{Bmatrix} d\Omega_e, \tag{A.8b}$$

$$\mathbf{K}^e_{gz} = \int_{\Omega_e} \begin{Bmatrix} \mathbf{B}^{z0} \\ \mathbf{B}^{z1} \\ \mathbf{B}^{z2} \\ \mathbf{B}^{z3} \\ \mathbf{B}^{z4} \end{Bmatrix}^T \begin{bmatrix} \mathbf{A}^g & \mathbf{B}^g & \mathbf{E}^g & \mathbf{G}^g & \mathbf{M}^g \\ \mathbf{B}^g & \mathbf{D}^g & \mathbf{F}^g & \mathbf{I}^g & \mathbf{N}^g \\ \mathbf{E}^g & \mathbf{F}^g & \mathbf{H}^g & \mathbf{J}^g & \mathbf{P}^g \\ \mathbf{G}^g & \mathbf{I}^g & \mathbf{J}^g & \mathbf{L}^g & \mathbf{Q}^g \\ \mathbf{M}^g & \mathbf{N}^g & \mathbf{P}^g & \mathbf{Q}^g & \mathbf{R}^g \end{bmatrix} \begin{Bmatrix} \mathbf{B}^{z0} \\ \mathbf{B}^{z1} \\ \mathbf{B}^{z2} \\ \mathbf{B}^{z3} \\ \mathbf{B}^{z4} \end{Bmatrix} d\Omega_e. \tag{A.8c}$$

A.4 Element mass matrices

$$\mathbf{M}^e_c = \int_{\Omega_e} \tilde{\mathbf{R}}^T \tilde{\mathbf{m}} \tilde{\mathbf{R}} d\Omega_e \tag{A.9}$$

$$\mathbf{M}^e_{gx} = \frac{1}{3} d^2 \int_{\Omega_e} \tilde{\mathbf{R}}^T_{,x} \tilde{\mathbf{m}} \tilde{\mathbf{R}}^T_{,x} d\Omega_e, \tag{A.10a}$$

$$\mathbf{M}^e_{gy} = \frac{1}{3} d^2 \int_{\Omega_e} \tilde{\mathbf{R}}^T_{,y} \tilde{\mathbf{m}} \tilde{\mathbf{R}}^T_{,y} d\Omega_e, \tag{A.10b}$$

$$\mathbf{M}^e_{gz} = \frac{1}{3} d^2 \int_{\Omega_e} \tilde{\mathbf{R}}^T_{,z} \tilde{\mathbf{m}} \tilde{\mathbf{R}}^T_{,z} d\Omega_e, \tag{A.10c}$$

where

$$\tilde{\mathbf{R}} = \begin{bmatrix} \mathbf{R}_1 \\ \mathbf{R}_2 \\ \mathbf{R}_3 \end{bmatrix}, \tag{A.11a}$$

$$\mathbf{R}_1 = \begin{bmatrix} \bar{R}_A & 0 & 0 & 0 \\ 0 & 0 & -\bar{R}_{A,x} & 0 \\ 0 & 0 & 0 & \bar{R}_{A,x} \end{bmatrix}, \quad \mathbf{R}_2 = \begin{bmatrix} 0 & \bar{R}_A & 0 & 0 \\ 0 & 0 & -\bar{R}_{A,y} & 0 \\ 0 & 0 & 0 & \bar{R}_{A,y} \end{bmatrix}, \quad \mathbf{R}_3 = \begin{bmatrix} 0 & 0 & \bar{R}_A & 0 \\ 0 & 0 & 0 & \bar{R}_A \\ 0 & 0 & 0 & 0 \end{bmatrix}. \tag{A.11b}$$

References

[1] Y. Fu, H. Du, W. Huang, S. Zhang, and M. Hu, "TiNi-based thin films in MEMS applications: a review," *Sensors and Actuators A: Physical*, vol. 112, pp. 395–408, May 2004.

[2] Z. Lee, C. Ophus, L. M. Fischer, N. Nelson-Fitzpatrick, K. L. Westra, S. Evoy, V. Radmilovic, U. Dahmen, and D. Mitlin, "Metallic NEMS components fabricated from nanocomposite Al–Mo films," *Nanotechnology*, vol. 17, no. 12, p. 3063, 2006.

[3] R. H. Baughman, C. Cui, A. A. Zakhidov, Z. Iqbal, J. N. Barisci, G. M. Spinks, G. G. Wallace, A. Mazzoldi, D. D. Rossi, A. G. Rinzler, O. Jaschinski, S. Roth, and M. Kertesz, "Carbon Nanotube Actuators," *Science*, vol. 284, pp. 1340–1344, May 1999.

[4] K.-T. Lau, H.-Y. Cheung, J. Lu, Y.-S. Yin, D. Hui, and H.-L. Li, "Carbon Nanotubes for Space and Bio-Engineering Applications," *Journal of Computational and Theoretical Nanoscience*, vol. 5, pp. 23–35, Jan. 2008.

[5] K. M. Liew, X. Q. He, and C. H. Wong, "On the study of elastic and plastic properties of multi-walled carbon nanotubes under axial tension using molecular dynamics simulation," *Acta Materialia*, vol. 52, pp. 2521–2527, May 2004.

[6] A. Menk and S. Bordas, "Influence of the microstructure on the stress state of solder joints during thermal cycling," in *10th International Conference on Thermal, Mechanical and Multi-Physics simulation and Experiments in Microelectronics and Microsystems, 2009. EuroSimE 2009*, pp. 1–5, Apr. 2009.

[7] N. A. Fleck, G. M. Muller, M. F. Ashby, and J. W. Hutchinson, "Strain gradient plasticity: Theory and experiment," *Acta Metallurgica et Materialia*, vol. 42, pp. 475–487, Feb. 1994.

[8] J. S. Stolken and A. G. Evans, "A microbend test method for measuring the plasticity length scale," *Acta Materialia*, vol. 46, pp. 5109–5115, Sept. 1998.

[9] D. Lam, F. Yang, A. Chong, J. Wang, and P. Tong, "Experiments and theory in strain gradient elasticity," *Journal of the Mechanics and Physics of Solids*, vol. 51, no. 8, pp. 1477 – 1508, 2003.

[10] A. C. Eringen, "Nonlocal polar elastic continua," *International Journal of Engineering Science*, vol. 10, pp. 1–16, Jan. 1972.

[11] R. D. Mindlin, "Micro-structure in linear elasticity," *Archive for Rational Mechanics and Analysis*, vol. 16, pp. 51–78, Jan. 1964.

[12] N. A. Fleck and J. W. Hutchinson, "A phenomenological theory for strain gradient effects in plasticity," *Journal of the Mechanics and Physics of Solids*, vol. 41, pp. 1825–1857, Dec. 1993.

[13] F. Yang, A. C. M. Chong, D. C. C. Lam, and P. Tong, "Couple stress based strain gradient theory for elasticity," *International Journal of Solids and Structures*, vol. 39, pp. 2731–2743, May 2002.

[14] R. D. Mindlin and H. F. Tiersten, "Effects of couple-stresses in linear elasticity," *Archive for Rational Mechanics and Analysis*, vol. 11, pp. 415–448, Jan. 1962.

[15] R. D. Mindlin, "Second gradient of strain and surface-tension in linear elasticity," *International Journal of Solids and Structures*, vol. 1, pp. 417–438, Nov. 1965.

[16] T. Hughes, J. Cottrell, and Y. Bazilevs, "Isogeometric analysis: Cad, finite elements, nurbs, exact geometry and mesh refinement," *Computer Methods in Applied Mechanics and Engineering*, vol. 194, no. 39–41, pp. 4135 – 4195, 2005.

[17] S. K. Park and X.-L. Gao, "Variational formulation of a modified couple stress theory and its application to a simple shear problem," *Zeitschrift für angewandte Mathematik und Physik*, vol. 59, pp. 904–917, May 2007.

[18] S. K. Park and X.-L. Gao, "Bernoulli–Euler beam model based on a modified couple stress theory," *Journal of Micromechanics and Microengineering*, vol. 16, no. 11, p. 2355, 2006.

[19] W. Xia, L. Wang, and L. Yin, "Nonlinear non-classical microscale beams: Static bending, postbuckling and free vibration," *International Journal of Engineering Science*, vol. 48, pp. 2044–2053, Dec. 2010.

[20] L.-L. Ke and Y.-S. Wang, "Size effect on dynamic stability of functionally graded microbeams based on a modified couple stress theory," *Composite Structures*, vol. 93, pp. 342–350, Jan. 2011.

[21] C. M. C. Roque, D. S. Fidalgo, A. J. M. Ferreira, and J. N. Reddy, "A study of a microstructure-dependent composite laminated Timoshenko beam using a modified couple stress theory and a meshless method," *Composite Structures*, vol. 96, pp. 532–537, Feb. 2013.

[22] H.-T. Thai, T. P. Vo, T.-K. Nguyen, and J. Lee, "Size-dependent behavior of functionally graded sandwich microbeams based on the modified couple stress theory," *Composite Structures*, vol. 123, pp. 337–349, May 2015.

[23] M. Salamat-talab, A. Nateghi, and J. Torabi, "Static and dynamic analysis of third-order shear deformation FG micro beam based on modified couple stress theory," *International Journal of Mechanical Sciences*, vol. 57, pp. 63–73, Apr. 2012.

[24] G. C. Tsiatas, "A new Kirchhoff plate model based on a modified couple stress theory," *International Journal of Solids and Structures*, vol. 46, pp. 2757–2764, June 2009.

[25] L. Yin, Q. Qian, L. Wang, and W. Xia, "Vibration analysis of microscale plates based on modified couple stress theory," *Acta Mechanica Solida Sinica*, vol. 23, no. 5, pp. 386 – 393, 2010.

[26] H. M. Ma, X.-L. Gao, and J. N. Reddy, "A non-classical Mindlin plate model based on a modified couple stress theory," *Acta Mechanica*, vol. 220, pp. 217–235, Apr. 2011.

[27] J. Chen and C.-J. Li, "A quadrilateral spline element for couple stress/strain gradient elasticity," *Computers & Structures*, vol. 138, pp. 133–141, July 2014.

[28] S. K. Park and X.-L. Gao, "Variational formulation of a modified couple stress theory and its application to a simple shear problem," *Zeitschrift für angewandte Mathematik und Physik*, vol. 59, pp. 904–917, May 2008.

[29] L. C. Trinh, H. X. Nguyen, T. P. Vo, and T.-K. Nguyen, "Size-dependent behaviour of functionally graded microbeams using various shear deformation theories based on the modified couple stress theory," *Composite Structures*, vol. 154, pp. 556–572, Oct. 2016.

[30] H.-T. Thai and T. P. Vo, "A size-dependent functionally graded sinusoidal plate model based on a modified couple stress theory," *Composite Structures*, vol. 96, pp. 376–383, Feb. 2013.

[31] J. N. Reddy, J. Romanoff, and J. A. Loya, "Nonlinear finite element analysis of functionally graded circular plates with modified couple stress theory," *European Journal of Mechanics - A/Solids*, vol. 56, pp. 92–104, Mar. 2016.

[32] J. Kim and J. N. Reddy, "A general third-order theory of functionally graded plates with modified couple stress effect and the von karman nonlinearity: theory and finite element analysis," *Acta Mechanica*, vol. 226, pp. 2973–2998, May 2015.

[33] M. Simsek, T. Kocaturk, and S. D. Akbas, "Static bending of a functionally graded microscale Timoshenko beam based on the modified couple stress theory," *Composite Structures*, vol. 95, pp. 740–747, Jan. 2013.

[34] A. Nateghi, M. Salamat-talab, J. Rezapour, and B. Daneshian, "Size dependent buckling analysis of functionally graded micro beams based on modified couple stress theory," *Applied Mathematical Modelling*, vol. 36, pp. 4971–4987, Oct. 2012.

[35] H.-T. Thai and S.-E. Kim, "A size-dependent functionally graded reddy plate model based on a modified couple stress theory," *Composites Part B: Engineering*, vol. 45, no. 1, pp. 1636 – 1645, 2013.

[36] H.-T. Thai and D.-H. Choi, "Size-dependent functionally graded kirchhoff and mindlin plate models based on a modified couple stress theory," *Composite Structures*, vol. 95, pp. 142 – 153, 2013.

[37] H.-T. Thai and T. P. Vo, "A size-dependent functionally graded sinusoidal plate model based on a modified couple stress theory," *Composite Structures*, vol. 96, pp. 376–383, Feb. 2013.

[38] L.-L. Ke, Y.-S. Wang, J. Yang, and S. Kitipornchai, "Free vibration of size-dependent Mindlin microplates based on the modified couple stress theory," *Journal of Sound and Vibration*, vol. 331, pp. 94–106, Jan. 2012.

[39] L.-L. Ke, J. Yang, S. Kitipornchai, and M. A. Bradford, "Bending, buckling and vibration of size-dependent functionally graded annular microplates," *Composite Structures*, vol. 94, pp. 3250–3257, Nov. 2012.

[40] L. He, J. Lou, E. Zhang, Y. Wang, and Y. Bai, "A size-dependent four variable refined plate model for functionally graded microplates based on modified couple stress theory," *Composite Structures*, vol. 130, pp. 107 – 115, 2015.

[41] J. N. Reddy and J. Kim, "A nonlinear modified couple stress-based third-order theory of functionally graded plates," *Composite Structures*, vol. 94, pp. 1128–1143, Feb. 2012.

[42] J. N. Reddy and J. Berry, "Nonlinear theories of axisymmetric bending of functionally graded circular plates with modified couple stress," *Composite Structures*, vol. 94, pp. 3664–3668, Dec. 2012.

[43] J. N. Reddy, J. Romanoff, and J. A. Loya, "Nonlinear Finite Element Analysis of Functionally Graded Circular Plates with Modified Couple Stress Theory," *European Journal of Mechanics - A/Solids*, 2015.

[44] A. C. M. Chong, F. Yang, D. C. C. Lam, and P. Tong, "Torsion and bending of micron-scaled structures," *Journal of Materials Research*, vol. 16, pp. 1052–1058, Apr. 2001.

[45] R. D. Mindlin, "Influence of couple-stresses on stress concentrations," *Experimental Mechanics*, vol. 3, pp. 1–7, Jan. 1963.

[46] E. C. Aifantis, "On the role of gradients in the localization of deformation and fracture," *International Journal of Engineering Science*, vol. 30, pp. 1279–1299, Oct. 1992.

[47] H. G. Georgiadis, I. Vardoulakis, and E. G. Velgaki, "Dispersive Rayleigh-Wave Propagation in Microstructured Solids Characterized by Dipolar Gradient Elasticity," *Journal of Elasticity*, vol. 74, pp. 17–45, Jan. 2004.

[48] H. Askes and E. C. Aifantis, "Gradient elasticity in statics and dynamics: An overview of formulations, length scale identification procedures, finite element implementations and new results," *International Journal of Solids and Structures*, vol. 48, pp. 1962–1990, June 2011.

[49] P. A. Gourgiotis, H. G. Georgiadis, and I. Neocleous, "On the reflection of waves in half-spaces of microstructured materials governed by dipolar gradient elasticity," *Wave Motion*, vol. 50, pp. 437–455, Apr. 2013.

[50] H. G. Georgiadis and D. S. Anagnostou, "Problems of the Flamant–Boussinesq and Kelvin Type in Dipolar Gradient Elasticity," *Journal of Elasticity*, vol. 90, pp. 71–98, Jan. 2008.

[51] M. Lazar and G. A. Maugin, "Nonsingular stress and strain fields of dislocations and disclinations in first strain gradient elasticity," *International Journal of Engineering Science*, vol. 43, pp. 1157–1184, Sept. 2005.

[52] P. A. Gourgiotis and H. G. Georgiadis, "Torsional and SH surface waves in an isotropic and homogenous elastic half-space characterized by the Toupin–Mindlin gradient theory," *International Journal of Solids and Structures*, vol. 62, pp. 217–228, June 2015.

[53] G. A. Maugin and A. Miled, "Solitary waves in micropolar elastic crystals," *International Journal of Engineering Science*, vol. 24, pp. 1477–1499, Jan. 1986.

[54] H. Gao, Y. Huang, W. D. Nix, and J. W. Hutchinson, "Mechanism-based strain gradient plasticity— I. Theory," *Journal of the Mechanics and Physics of Solids*, vol. 47, pp. 1239–1263, Apr. 1999.

[55] Y. Huang, H. Gao, W. D. Nix, and J. W. Hutchinson, "Mechanism-based strain gradient plasticity—II. Analysis," *Journal of the Mechanics and Physics of Solids*, vol. 48, pp. 99–128, Jan. 2000.

[56] P. A. Gourgiotis and H. G. Georgiadis, "Plane-strain crack problems in microstructured solids governed by dipolar gradient elasticity," *Journal of the Mechanics and Physics of Solids*, vol. 57, pp. 1898–1920, Nov. 2009.

[57] F. Putar, J. Sorić, T. Lesičar, and Z. Tonković, "Damage modeling employing strain gradient continuum theory," *International Journal of Solids and Structures*, vol. 120, pp. 171–185, Aug. 2017.

[58] S. Papargyri-Beskou and D. E. Beskos, "Static, stability and dynamic analysis of gradient elastic flexural Kirchhoff plates," *Archive of Applied Mechanics*, vol. 78, pp. 625–635, Aug. 2008.

[59] B. Altan and E. Aifantis, "On some aspects in the special theory of gradient elasticity," *Journal of the Mechanical Behavior of Materials*, vol. 8, no. 3, pp. 231–282, 1997.

[60] J. N. Reddy, "A Simple Higher-Order Theory for Laminated Composite Plates," *Journal of Applied Mechanics*, vol. 51, pp. 745–752, Dec. 1984.

[61] K. P. Soldatos, "A transverse shear deformation theory for homogeneous monoclinic plates," *Acta Mechanica*, vol. 94, pp. 195–220, Sept. 1992.

[62] N. R. Senthilnathan, S. P. Lim, K. H. Lee, and S. T. Chow, "Buckling of Shear-Deformable Plates," *AIAA Journal*, vol. 25, no. 9, pp. 1268–1271, 1987.

[63] B. Zhang, Y. He, D. Liu, Z. Gan, and L. Shen, "A non-classical Mindlin plate finite element based on a modified couple stress theory," *European Journal of Mechanics - A/Solids*, vol. 42, pp. 63–80, Nov. 2013.

[64] H.-T. Thai and S.-E. Kim, "A size-dependent functionally graded reddy plate model based on a modified couple stress theory," *Composites Part B: Engineering*, vol. 45, no. 1, pp. 1636 – 1645, 2013.

[65] L. He, J. Lou, E. Zhang, Y. Wang, and Y. Bai, "A size-dependent four variable refined plate model for functionally graded microplates based on modified couple stress theory," *Composite Structures*, vol. 130, pp. 107 – 115, 2015.

[66] C. A. Shankara and N. G. R. Iyengar, "A C0 element for the free vibration analysis of laminated composite plates," *Journal of Sound and Vibration*, vol. 191, pp. 721–738, Apr. 1996.

[67] J. N. Reddy, "Analysis of functionally graded plates," *International Journal for Numerical Methods in Engineering*, vol. 47, pp. 663–684, Jan. 2000.

[68] L. Zhang, B. Liang, S. Zhou, B. Wang, and Y. Xue, "An application of a size-dependent model on microplate with elastic medium based on strain gradient elasticity theory," *Meccanica*, vol. 52, pp. 251–262, Jan. 2017.

[69] S. J. V. Frankland, A. Caglar, D. W. Brenner, and M. Griebel, "Molecular simulation of the influence of chemical cross-links on the shear strength of carbon nanotube–polymer interfaces," *The Journal of Physical Chemistry B*, vol. 106, pp. 3046–3048, Mar. 2002.

[70] X. Ji, A. Li, and S. Zhou, "A comparison of strain gradient theories with applications to the functionally graded circular micro-plate," *Applied Mathematical Modelling*, vol. 49, pp. 124–143, Sept. 2017.

[71] S. Khakalo and J. Niiranen, "Form II of Mindlin's second strain gradient theory of elasticity with a simplification: For materials and structures from nano- to macro-scales," *European Journal of Mechanics - A/Solids*, vol. 71, pp. 292–319, Sept. 2018.

[72] S. Khakalo and J. Niiranen, "Gradient-elastic stress analysis near cylindrical holes in a plane under bi-axial tension fields," *International Journal of Solids and Structures*, vol. 110–111, pp. 351–366, Apr. 2017.

[73] E. Carrera, S. Brischetto, M. Cinefra, and M. Soave, "Effects of thickness stretching in functionally graded plates and shells," *Composites Part B: Engineering*, vol. 42, no. 2, pp. 123 – 133, 2011.

[74] J. L. Mantari and C. Guedes Soares, "A novel higher-order shear deformation theory with stretching effect for functionally graded plates," *Composites Part B: Engineering*, vol. 45, pp. 268–281, Feb. 2013.

[75] C. H. Thai, A. M. Zenkour, M. Abdel Wahab, and H. Nguyen-Xuan, "A simple four-unknown shear and normal deformations theory for functionally graded isotropic and sandwich plates based on isogeometric analysis," *Composite Structures*, vol. 139, pp. 77–95, Apr. 2016.

[76] A. M. Zenkour, "A simple four-unknown refined theory for bending analysis of functionally graded plates," *Applied Mathematical Modelling*, vol. 37, pp. 9041 – 9051, 2013.

[77] A. M. Zenkour, "Bending analysis of functionally graded sandwich plates using a simple four-unknown shear and normal deformations theory," *Journal of Sandwich Structures and Materials*, vol. 15, pp. 629–656, Nov. 2013.

[78] A. Neves, A. Ferreira, E. Carrera, C. Roque, M. Cinefra, R. Jorge, and C. Soares, "A quasi-3d sinusoidal shear deformation theory for the static and free vibration analysis of functionally graded plates," *Composites Part B: Engineering*, vol. 43, no. 2, pp. 711 – 725, 2012.

[79] J. L. Mantari and C. Guedes Soares, "Generalized hybrid quasi-3d shear deformation theory for the static analysis of advanced composite plates," *Composite Structures*, vol. 94, pp. 2561–2575, July 2012.

[80] H.-T. Thai and S.-E. Kim, "A simple quasi-3d sinusoidal shear deformation theory for functionally graded plates," *Composite Structures*, vol. 99, pp. 172–180, May 2013.

[81] T. N. Nguyen, C. H. Thai, and H. Nguyen-Xuan, "On the general framework of high order shear deformation theories for laminated composite plate structures: A novel unified approach," *International Journal of Mechanical Sciences*, vol. 110, pp. 242–255, May 2016.

[82] H. Nguyen-Xuan, L. V. Tran, C. H. Thai, S. Kulasegaram, and S. Bordas, "Isogeometric analysis of functionally graded plates using a refined plate theory," *Composites Part B: Engineering*, vol. 64, pp. 222 – 234, 2014.

[83] N.-T. Nguyen, D. Hui, J. Lee, and H. Nguyen-Xuan, "An efficient computational approach for size-dependent analysis of functionally graded nanoplates," *Computer Methods in Applied Mechanics and Engineering*, vol. 297, pp. 191 – 218, 2015.

[84] H. X. Nguyen, T. N. Nguyen, M. Abdel-Wahab, S. P. A. Bordas, H. Nguyen-Xuan, and T. P. Vo, "A refined quasi-3d isogeometric analysis for functionally graded microplates based on the modified couple stress theory," *Computer Methods in Applied Mechanics and Engineering*, vol. 313, pp. 904–940, Jan. 2017.

[85] L. C. Trinh, T. P. Vo, A. I. Osofero, and J. Lee, "Fundamental frequency analysis of functionally graded sandwich beams based on the state space approach," *Composite Structures*, 2015.

[86] T. P. Vo, H.-T. Thai, T.-K. Nguyen, A. Maheri, and J. Lee, "Finite element model for vibration and buckling of functionally graded sandwich beams based on a refined shear deformation theory," *Engineering Structures*, vol. 64, pp. 12–22, Apr. 2014.

[87] T. P. Vo, H.-T. Thai, T.-K. Nguyen, and F. Inam, "Static and vibration analysis of functionally graded beams using refined shear deformation theory," *Meccanica*, vol. 49, pp. 155–168, July 2013.

[88] M. Asghari, M. T. Ahmadian, M. H. Kahrobaiyan, and M. Rahaeifard, "On the size-dependent behavior of functionally graded micro-beams," *Materials & Design*, vol. 31, pp. 2324–2329, May 2010.

[89] V.-H. Nguyen, T.-K. Nguyen, H.-T. Thai, and T. P. Vo, "A new inverse trigonometric shear deformation theory for isotropic and functionally graded sandwich plates," *Composites Part B: Engineering*, vol. 66, pp. 233–246, Nov. 2014.

[90] H.-T. Thai and T. P. Vo, "A new sinusoidal shear deformation theory for bending, buckling, and vibration of functionally graded plates," *Applied Mathematical Modelling*, vol. 37, pp. 3269–3281, Mar. 2013.

[91] S. Natarajan, S. Chakraborty, M. Thangavel, S. Bordas, and T. Rabczuk, "Size-dependent free flexural vibration behavior of functionally graded nanoplates," *Computational Materials Science*, vol. 65, pp. 74–80, Dec. 2012.

[92] J. L. Mantari, "Refined and generalized hybrid type quasi-3d shear deformation theory for the bending analysis of functionally graded shells," *Composites Part B: Engineering*, vol. 83, pp. 142–152, Dec. 2015.

[93] J. Torabi, Y. Kiani, and M. R. Eslami, "Linear thermal buckling analysis of truncated hybrid FGM conical shells," *Composites Part B: Engineering*, vol. 50, pp. 265–272, July 2013.

[94] F. Tornabene, "Free vibration analysis of functionally graded conical, cylindrical shell and annular plate structures with a four-parameter power-law distribution," *Computer Methods in Applied Mechanics and Engineering*, vol. 198, pp. 2911–2935, Aug. 2009.

[95] T. Nakamura, T. Wang, and S. Sampath, "Determination of properties of graded materials by inverse analysis and instrumented indentation," *Acta Materialia*, vol. 48, pp. 4293–4306, Nov. 2000.

[96] T. Mori and K. Tanaka, "Average stress in matrix and average elastic energy of materials with misfitting inclusions," *Acta Metallurgica*, vol. 21, pp. 571–574, May 1973.

[97] J. A. Cottrell, T. J. R. Hughes, and Y. Bazilevs, *Isogeometric Analysis: Toward Integration of CAD and FEA*. Wiley Publishing, 1st ed., 2009.

[98] A. V. Vuong, C. Heinrich, and B. Simeon, "ISOGAT: A 2d tutorial MATLAB code for Isogeometric Analysis," *Computer Aided Geometric Design*, vol. 27, pp. 644–655, Nov. 2010.

[99] C. de Falco, A. Reali, and R. Vázquez, "GeoPDEs: A research tool for Isogeometric Analysis of PDEs," *Advances in Engineering Software*, vol. 42, pp. 1020–1034, Dec. 2011.

[100] V. P. Nguyen, C. Anitescu, S. P. A. Bordas, and T. Rabczuk, "Isogeometric analysis: An overview and computer implementation aspects," *Mathematics and Computers in Simulation*, vol. 117, pp. 89–116, Nov. 2015.

[101] C. H. Thai, A. J. M. Ferreira, E. Carrera, and H. Nguyen-Xuan, "Isogeometric analysis of laminated composite and sandwich plates using a layerwise deformation theory," *Composite Structures*, vol. 104, pp. 196–214, Oct. 2013.

[102] L. Beirão da Veiga, A. Buffa, C. Lovadina, M. Martinelli, and G. Sangalli, "An isogeometric method for the Reissner–Mindlin plate bending problem," *Computer Methods in Applied Mechanics and Engineering*, vol. 209–212, pp. 45–53, Feb. 2012.

[103] C. H. Thai, H. Nguyen-Xuan, N. Nguyen-Thanh, T.-H. Le, T. Nguyen-Thoi, and T. Rabczuk, "Static, free vibration, and buckling analysis of laminated composite Reissner–Mindlin plates using NURBS-based isogeometric approach," *International Journal for Numerical Methods in Engineering*, vol. 91, pp. 571–603, Aug. 2012.

[104] N. Valizadeh, S. Natarajan, O. A. Gonzalez-Estrada, T. Rabczuk, T. Q. Bui, and S. P. A. Bordas, "NURBS-based finite element analysis of functionally graded plates: Static bending, vibration, buckling and flutter," *Composite Structures*, vol. 99, pp. 309–326, May 2013.

[105] L. V. Tran, C. H. Thai, and H. Nguyen-Xuan, "An isogeometric finite element formulation for thermal buckling analysis of functionally graded plates," *Finite Elements in Analysis and Design*, vol. 73, pp. 65–76, Oct. 2013.

[106] C. H. Thai, A. J. M. Ferreira, S. P. A. Bordas, T. Rabczuk, and H. Nguyen-Xuan, "Isogeometric analysis of laminated composite and sandwich plates using a new inverse trigonometric shear deformation theory," *European Journal of Mechanics - A/Solids*, vol. 43, pp. 89–108, Jan. 2014.

[107] C. H. Thai, H. Nguyen-Xuan, S. P. A. Bordas, N. Nguyen-Thanh, and T. Rabczuk, "Isogeometric Analysis of Laminated Composite Plates Using the Higher-Order Shear Deformation Theory," *Mechanics of Advanced Materials and Structures*, vol. 22, pp. 451–469, June 2015.

[108] J. Kiendl, K. U. Bletzinger, J. Linhard, and R. Wüchner, "Isogeometric shell analysis with Kirchhoff–Love elements," *Computer Methods in Applied Mechanics and Engineering*, vol. 198, pp. 3902–3914, Nov. 2009.

[109] N. Nguyen-Thanh, J. Kiendl, H. Nguyen-Xuan, R. Wüchner, K. U. Bletzinger, Y. Bazilevs, and T. Rabczuk, "Rotation free isogeometric thin shell analysis using PHT-splines," *Computer Methods in Applied Mechanics and Engineering*, vol. 200, pp. 3410–3424, Nov. 2011.

[110] N. Nguyen-Thanh, N. Valizadeh, M. N. Nguyen, H. Nguyen-Xuan, X. Zhuang, P. Areias, G. Zi, Y. Bazilevs, L. De Lorenzis, and T. Rabczuk, "An extended isogeometric thin shell analysis based on Kirchhoff–Love theory," *Computer Methods in Applied Mechanics and Engineering*, vol. 284, pp. 265–291, Feb. 2015.

[111] T. W. Sederberg, J. Zheng, A. Bakenov, and A. Nasri, "T-splines and T-NURCCs," in *ACM SIGGRAPH 2003 Papers*, SIGGRAPH '03, (New York, NY, USA), pp. 477–484, ACM, 2003.

[112] Y. Bazilevs, V. M. Calo, J. A. Cottrell, J. A. Evans, T. J. R. Hughes, S. Lipton, M. A. Scott, and T. W. Sederberg, "Isogeometric analysis using T-splines," *Computer Methods in Applied Mechanics and Engineering*, vol. 199, pp. 229–263, Jan. 2010.

[113] J. Deng, F. Chen, X. Li, C. Hu, W. Tong, Z. Yang, and Y. Feng, "Polynomial splines over hierarchical T-meshes," *Graphical Models*, vol. 70, pp. 76–86, July 2008.

[114] N. Nguyen-Thanh, H. Nguyen-Xuan, S. P. A. Bordas, and T. Rabczuk, "Isogeometric analysis using polynomial splines over hierarchical T-meshes for two-dimensional elastic solids," *Computer Methods in Applied Mechanics and Engineering*, vol. 200, pp. 1892–1908, May 2011.

[115] S. Thai, H.-T. Thai, T. P. Vo, and V. I. Patel, "Size-dependant behaviour of functionally graded microplates based on the modified strain gradient elasticity theory and isogeometric analysis," *Computers & Structures*, vol. 190, pp. 219–241, Oct. 2017.

[116] D. J. Benson, Y. Bazilevs, M. C. Hsu, and T. J. R. Hughes, "Isogeometric shell analysis: The Reissner–Mindlin shell," *Computer Methods in Applied Mechanics and Engineering*, vol. 199, pp. 276–289, Jan. 2010.

[117] F. Tornabene, N. Fantuzzi, and M. Bacciocchi, "The GDQ method for the free vibration analysis of arbitrarily shaped laminated composite shells using a NURBS-based isogeometric approach," *Composite Structures*, vol. 154, pp. 190–218, Oct. 2016.

[118] H. Kapoor and R. K. Kapania, "Geometrically nonlinear NURBS isogeometric finite element analysis of laminated composite plates," *Composite Structures*, vol. 94, pp. 3434–3447, Dec. 2012.

[119] P. Phung-Van, T. Nguyen-Thoi, H. Luong-Van, and Q. Lieu-Xuan, "Geometrically nonlinear analysis of functionally graded plates using a cell-based smoothed three-node plate element (CS-MIN3) based on the C0-HSDT," *Computer Methods in Applied Mechanics and Engineering*, vol. 270, pp. 15–36, Mar. 2014.

[120] L. V. Tran, J. Lee, H. Nguyen-Van, H. Nguyen-Xuan, and M. A. Wahab, "Geometrically nonlinear isogeometric analysis of laminated composite plates based on higher-order shear deformation theory," *International Journal of Non-Linear Mechanics*, vol. 72, pp. 42–52, June 2015.

[121] N. Moes, J. Dolbow, and T. Belytschko, "A finite element method for crack growth without remeshing," *International Journal for Numerical Methods in Engineering*, vol. 46, no. 1, pp. 131–150, 1999.

[122] D. J. Benson, Y. Bazilevs, E. De Luycker, M.-C. Hsu, M. Scott, T. J. R. Hughes, and T. Belytschko, "A generalized finite element formulation for arbitrary basis functions: From isogeometric analysis to XFEM," *International Journal for Numerical Methods in Engineering*, vol. 83, pp. 765–785, Aug. 2010.

[123] E. De Luycker, D. J. Benson, T. Belytschko, Y. Bazilevs, and M. C. Hsu, "X-FEM in isogeometric analysis for linear fracture mechanics," *International Journal for Numerical Methods in Engineering*, vol. 87, pp. 541–565, Aug. 2011.

[124] S. S. Ghorashi, N. Valizadeh, and S. Mohammadi, "Extended isogeometric analysis for simulation of stationary and propagating cracks," *International Journal for Numerical Methods in Engineering*, vol. 89, pp. 1069–1101, Mar. 2012.

[125] J. N. Reddy, *Theory and Analysis of Elastic Plates and Shells*. CRC Press, 2nd ed., Nov. 2006.

[126] K.-J. Bathe, A. Iosilevich, and D. Chapelle, "An evaluation of the MITC shell elements," *Computers & Structures*, vol. 75, pp. 1–30, Mar. 2000.

[127] L. V. Tran, T. Nguyen-Thoi, C. H. Thai, and H. Nguyen-Xuan, "An Edge-Based Smoothed Discrete Shear Gap Method Using the C0-Type Higher-Order Shear Deformation Theory for Analysis of Laminated Composite Plates," *Mechanics of Advanced Materials and Structures*, vol. 22, pp. 248–268, Apr. 2015.

[128] F. Auricchio, L. B. da Veiga, A. Buffa, C. Lovadina, A. Reali, and G. Sangalli, "A fully "locking-free" isogeometric approach for plane linear elasticity problems: A stream function formulation," *Computer Methods in Applied Mechanics and Engineering*, vol. 197, no. 1–4, pp. 160 – 172, 2007.

[129] A. M. Zenkour, "Generalized shear deformation theory for bending analysis of functionally graded plates," *Applied Mathematical Modelling*, vol. 30, no. 1, pp. 67 – 84, 2006.

[130] S. Akavci and A. Tanrikulu, "Static and free vibration analysis of functionally graded plates based on a new quasi-3d and 2d shear deformation theories," *Composites Part B: Engineering*, vol. 83, pp. 203 – 215, 2015.

[131] J. L. Mantari and C. G. Soares, "A quasi-3d tangential shear deformation theory with four unknowns for functionally graded plates," *Acta Mechanica*, vol. 226, pp. 625–642, July 2014.

[132] S. S. Vel and R. Batra, "Three-dimensional exact solution for the vibration of functionally graded rectangular plates," *Journal of Sound and Vibration*, vol. 272, no. 3–5, pp. 703 – 730, 2004.

[133] H. Matsunaga, "Free vibration and stability of functionally graded plates according to a 2-d higher-order deformation theory," *Composite Structures*, vol. 82, no. 4, pp. 499 – 512, 2008.

[134] Z. Belabed, M. S. A. Houari, A. Tounsi, S. Mahmoud, and O. A. Bég, "An efficient and simple higher order shear and normal deformation theory for functionally graded material (fgm) plates," *Composites Part B: Engineering*, vol. 60, pp. 274 – 283, 2014.

[135] F. Alijani and M. Amabili, "Effect of thickness deformation on large-amplitude vibrations of functionally graded rectangular plates," *Composite Structures*, vol. 113, pp. 89 – 107, 2014.

[136] M. Mohammadi, M. Ghayour, and A. Farajpour, "Free transverse vibration analysis of circular and annular graphene sheets with various boundary conditions using the nonlocal continuum plate model," *Composites Part B: Engineering*, vol. 45, no. 1, pp. 32 – 42, 2013.

[137] L. Ma and T. Wang, "Relationships between axisymmetric bending and buckling solutions of {FGM} circular plates based on third-order plate theory and classical plate theory," *International Journal of Solids and Structures*, vol. 41, no. 1, pp. 85 – 101, 2004.

[138] A. Saidi, A. Rasouli, and S. Sahraee, "Axisymmetric bending and buckling analysis of thick functionally graded circular plates using unconstrained third-order shear deformation plate theory," *Composite Structures*, vol. 89, no. 1, pp. 110 – 119, 2009.

[139] L. V. Tran, A. Ferreira, and H. Nguyen-Xuan, "Isogeometric analysis of functionally graded plates using higher-order shear deformation theory," *Composites Part B: Engineering*, vol. 51, pp. 368 – 383, 2013.

[140] H. X. Nguyen, E. Atroshchenko, H. Nguyen-Xuan, and T. P. Vo, "Geometrically nonlinear isogeometric analysis of functionally graded microplates with the modified couple stress theory," *Computers & Structures*, vol. 193, pp. 110–127, Dec. 2017.

[141] J. N. Reddy, *An Introduction to Nonlinear Finite Element Analysis*. OUP Oxford, Mar. 2004.

[142] H. Nguyen-Van, *Development and application of assumed strain smoothing finite element technique for composite plate/shell structures*. PhD thesis, University of Southern Queensland, 2009.

[143] S. Levy, "Square plate with clamped edges under normal pressure producing large deflections," Tech. Rep. 740, National Advisory Committee for Aeronautics, Jan. 1942.

[144] A. Pica, R. D. Wood, and E. Hinton, "Finite element analysis of geometrically nonlinear plate behaviour using a mindlin formulation," *Computers & Structures*, vol. 11, pp. 203–215, Mar. 1980.

[145] T. Kant and J. R. Kommineni, "C0 Finite element geometrically non-linear analysis of fibre reinforced composite and sandwich laminates based on a higher-order theory," *Computers & Structures*, vol. 45, pp. 511–520, Oct. 1992.

[146] Y. Urthaler and J. N. Reddy, "A Mixed Finite Element for the Nonlinear Bending Analysis of Laminated Composite Plates Based on FSDT," *Mechanics of Advanced Materials and Structures*, vol. 15, pp. 335–354, Apr. 2008.

[147] G. N. Praveen and J. N. Reddy, "Nonlinear transient thermoelastic analysis of functionally graded ceramic-metal plates," *International Journal of Solids and Structures*, vol. 35, pp. 4457–4476, Nov. 1998.

[148] M. E. Golmakani and M. Kadkhodayan, "Nonlinear bending analysis of annular FGM plates using higher-order shear deformation plate theories," *Composite Structures*, vol. 93, pp. 973–982, Jan. 2011.

[149] H. X. Nguyen, E. Atroshchenko, T. Ngo, H. Nguyen-Xuan, and T. P. Vo, "Vibration of cracked functionally graded microplates by the strain gradient theory and extended isogeometric analysis," *Engineering Structures*, vol. 187, pp. 251–266, May 2019.

[150] S. Bordas, P. V. Nguyen, C. Dunant, A. Guidoum, and H. Nguyen-Dang, "An extended finite element library," *International Journal for Numerical Methods in Engineering*, vol. 71, pp. 703–732, Aug. 2007.

[151] G. Sciarra and S. Vidoli, "Asymptotic Fracture Modes in Strain-Gradient Elasticity: Size Effects and Characteristic Lengths for Isotropic Materials," *Journal of Elasticity*, vol. 113, pp. 27–53, Sept. 2013.

[152] C. S. Huang, O. G. McGee, and M. J. Chang, "Vibrations of cracked rectangular FGM thick plates," *Composite Structures*, vol. 93, pp. 1747–1764, June 2011.

[153] S. Natarajan, P. M. Baiz, S. Bordas, T. Rabczuk, and P. Kerfriden, "Natural frequencies of cracked functionally graded material plates by the extended finite element method," *Composite Structures*, vol. 93, pp. 3082–3092, Oct. 2011.

[154] L. V. Tran, H. A. Ly, J. Lee, M. A. Wahab, and H. Nguyen-Xuan, "Vibration analysis of cracked FGM plates using higher-order shear deformation theory and extended isogeometric approach," *International Journal of Mechanical Sciences*, vol. 96–97, pp. 65–78, June 2015.